

# ERL 2011

the 50th ICFA Advanced Beam Dynamics Workshop  
on Energy Recovery Linacs

KEK, Tsukuba, Japan  
October 16-21, 2011

<http://erl2011.kek.jp>

## International Organizing Committee

H. Kawata (chair), KEK  
R. Hajima (co-chair), JAEA  
S. Benson, TJNAF  
I. Ben-Zvi, BNL  
G. Hoffstaetter, Cornell U.  
K-J. Kim, ANL and the U. of Chicago  
J. Knobloch, HZB  
G. N. Kulipanov, BINP  
S. Smith, STFC/DL/ASTeC

## International Program Committee

R. Hajima (chair), JAEA  
W. Anders, HZB  
D. Angal-Kalinin, STFC/DL/ASTeC  
I. Bazarov, Cornell U.  
S. Belomestnykh, BNL  
J. Bisognano, SRC-U. Wisconsin-Madison  
M. Borland, ANL  
D. Douglas, JLAB  
B. Dunham, Cornell U.  
P. Evtushenko, JLAB  
T. Furuya, KEK  
C. Hernandez-Garcia, JLAB  
G. Hoffstaetter, Cornell U.  
A. Jankowiak, HZB  
T. Kamps, HZB  
D. Kayran, BNL  
K-J. Kim, ANL and the U. of Chicago

E-S. Kim, Kyungpook Natl. U.  
J. Knobloch, HZB  
Y. Kobayashi, KEK  
M. Liepe, Cornell U.  
V. N. Litvinenko, BNL  
K. Liu, Peking U.  
P. McIntosh, STFC/DL/ASTeC  
L. Merminga, TRIUMF  
J. Michael Klopff, Jefferson Lab  
B. L. Miltsov, STFC Daresbury Lab  
S. Sakanaka, KEK  
O. Shevchenko, BINP  
T. Smith, Stanford U.  
J. Teichert, HZDR  
A. Tribendis, BINP  
N. Vinokurov, BINP  
J. Wang, IHEP



Contact: [erl2011@kek.jp](mailto:erl2011@kek.jp)



# Contents

<b>Preface</b>	<b>i</b>
Contents . . . . .	iii
<b>Papers</b>	<b>iii</b>
PLT005 – An Oscillator Configuration of an X-Ray Free-Electron Laser for Exceptional Spectral Purity and Stability . . . . .	1
PLT008 – Applications of High-brightness Gamma-rays from ERLs . . . . .	5
WG1000 – ERL2011 Summaries of Working Group 1 . . . . .	10
WG1010 – High Brightness Thermionic Electron Gun Performance . . . . .	30
WG2000 – ERL2011 Summary of Working Group 2 Beam Dynamics . . . . .	36
WG2007 – Optics Layout for the ERL Test Facility at Peking University . . . . .	49
WG2009 – Design Studies on the ERL Test Facility at IHEP-Beijing . . . . .	52
WG2012 – Generation of High-Brightness Gamma-Rays from Energy-Recovery Linac . . . . .	56
WG2013 – Multiturn ERL X-ray Source (MARS) Feasibility Study . . . . .	60
WG2014 – Wake Fields and Energy Spread for the eRHIC ERL . . . . .	64
WG2017 – Calculation of CSR Impedance using Mesh Method . . . . .	68
WG2019 – Intra-beam Scattering and its Application to ERL . . . . .	73
WG2025 – Investigation of the Effect of Space Charge in the compact-Energy Recovery Linac . . . . .	78
WG3002 – Fabrication of Superconducting RF Cavity at MHI . . . . .	83
WG3003 – HOM Properties of Main Linac for cERL in Japan . . . . .	87
WG3006 – Development of Input Coupler for Compact ERL Main Linac . . . . .	91
WG3016 – Long-Term Monitoring of 3rd-period EP-electrolyte in STF-EP Facility at KEK . . . . .	97
WG3036 – Improved Heat Conduction Feedthroughs for HOM Couplers at DESY . . . . .	102
WG4000 – Closing Plenary Summary of Working Group 4 Instrumentation and Controls for ERL2011 . . . . .	105
WG4001 – Design and Performance of the Synchronization System and Beam Diagnostic Instruments for SACLA . . . . .	110
WG5003 – NSLS-II Beam Loss Monitor System* . . . . .	116
WG5005 – Brief Review of the Approaches to Elucidate the Mechanism of the Radiation-induced Demagnetization . . . . .	121
PSP001 – Lattice Design and Beam Dynamics of ERL-TF in IHEP, Beijing . . . . .	127
PSP007 – Individual Half-cells Frequency Measurements of a Dumbbell Cavity . . . . .	130
PSP019 – Charge Lifetime, Emittance, and Surface Analysis Studies of K <sub>2</sub> CsSb Photocathode in a JLab DC High Voltage Gun . . . . .	133
PSP020 – Recent Progress of an Yb-doped Fiber Laser System for an ERL-based Light Source . . . . .	137
PSP021 – Design of ERL Spoke Cavity for Non-destructive Assay Research . . . . .	140
<b>Appendices</b>	<b>145</b>
List of Authors . . . . .	145
Institutes List . . . . .	149
Participants List . . . . .	153



# AN OSCILLATOR CONFIGURATION OF AN X-RAY FREE-ELECTRON LASER FOR EXCEPTIONAL SPECTRAL PURITY AND STABILITY\*

K.-J. Kim, Argonne National Laboratory, Argonne, IL 60439, USA

## Abstract

A hard x-ray free-electron laser in oscillator configuration—an XFEL oscillator (XFELO)—will produce highly stable x-ray beams of ultra-high spectral purity and high average brightness, offering unique scientific opportunities. An XFELO is well suited for an energy recovery linac (ERL) facility. If combined with a high-gain amplifier, possibly with harmonic generation, an XFELO would constitute an ultimate x-ray machine.

## XFELO—AN X-RAY FEL IN AN OSCILLATOR CONFIGURATION

The recently successful LCLS [1] is the first x-ray free-electron laser operating in a self-amplified spontaneous emission (SASE) mode, in which the initial spontaneous emission is amplified to intense, quasi-coherent radiation in a single pass. High-gain XFELs are currently under vigorous development; several additional facilities are being constructed, the self-seeding scheme is being developed to improve the temporal coherence of a hard x-ray SASE [2], and seeded high-gain devices for soft x-rays have also been proposed [3].

An x-ray FEL oscillator (XFELO) is a qualitatively different device that will further enrich the era of x-ray FELs. In an XFELO, x-ray pulses are trapped in a high-Q optical cavity for repeated low-gain amplification, giving rise to highly stable, ultra-high spectral purity x-ray pulses. Oscillators were the first FELs built: they have been operated for many years for UV and lower photon energy regions where both low-loss, normal-incidence reflectors and accelerators producing the required beam qualities were readily available [4]. The concept for an XFELO that uses crystals as low-loss reflectors was first proposed in 1983 [5], at the same time that the x-ray SASE was proposed [6]. However, the concept did not receive its due attention until a recent, detailed study showed that an XFELO would be feasible with low-intensity, ultra-low-emittance electron bunches [7].

In the basic configuration shown in Fig. 1, an x-ray pulse is stored in an optical cavity consisting of two crystal reflectors and a grazing-incidence, curved mirror. Each time a pulse arrives at the undulator entrance it meets an electron bunch, and the pulse intensity becomes amplified as they travel together through the undulator. If the gain per pass is higher than the total loss, the pulse intensity increases steadily and the spectral shape narrows from pass to pass. Eventually, the gain decreases due to nonlinear effects, and the FEL reaches a steady state when the gain balances the loss. One of the crystals is made thin so that a fraction of the intra-cavity power is coupled out for users.

\*Work supported by U.S. Department of Energy, Office of Science, Office of Basic Energy Sciences, under Contract No. DE-AC02-06CH11357.

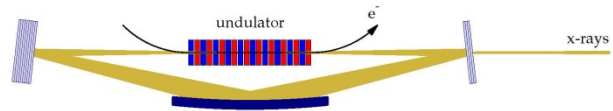


Figure 1: A basic scheme for optical cavities for XFELO which is not tuneable.

The tuning range of the basic scheme is severely limited because the curved mirror (necessary to control the transverse mode profile) efficiently reflects x-rays only when the grazing angle of incidence is less than a few mrad. Tuning can be achieved with the four-crystal scheme shown in Fig. 2 [8]. For this, the four crystals' Bragg angles are changed in unison while keeping a constant round-trip path length by a coordinated translation of the crystals. The four-crystal scheme also allows the use of one crystal material for all spectral regions of interest—an important advantage since we can then choose diamond, taking advantage of its excellent thermo-mechanical properties, as will be explained later.

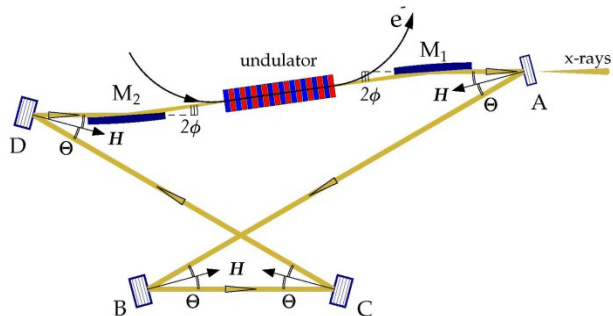


Figure 2: A tuneable cavity configuration in terms of four crystals.

The major parameters of an example XFELO are listed in Table 1. The electron beam parameters considered here are relatively conservative, as discussed below. XFELO parameters with higher beam qualities, lower bunch charge, and lower electron beam energy may also be feasible [9].

## UNIQUE CHARACTERISTICS

The distinguishing properties of an XFELO output are the exceptionally narrow bandwidth and the high pulse-to-pulse stability of the output. The narrow bandwidth is due to the repeated gain narrowing by the crystal reflectors. An XFELO is inherently stable since the pulse-to-pulse fluctuation is averaged out.

Although the output number of photons per pulse is three orders of magnitude less than the LCLS, the peak spectral brightness is similar due to the narrow bandwidth. Most importantly, the average brightness is higher due to the high repetition rate.

Table 1: Major Parameters

Electron Beam	
Energy	5 – 7 GeV
Bunch charge	25 – 50 pC
Bunch length (rms)	0.1 – 1 ps
Normalized rms emittance	0.2– 0.3 mm-mrad
Energy spread (rms)	$2 \times 10^{-4}$
Bunch repetition rate	$\sim 1$ MHz (constant)
Undulator	
Period length	$\sim 2$ cm
Deflection parameter K	1.0 – 1.5
Total length	30 – 60 m
Optical Cavity	
Configuration	2 – 4 diamond crystals and focusing mirrors
Total roundtrip reflectivity	$> 85\%$ (50% for 100A peak current)
XFEL Output	
Photon energy coverage	5 – 25 keV (plus the third harmonic)
Spectral purity	1 – 10 meV ( $10^{-6}$ – $10^{-7}$ in relative BW)
Coherence	Fully transverse and temporal
X-ray pulse length	0.1 – 1.0 ps
Tuning range	2 – 6 %
Number of photons/pulse	$\sim 10^9$
Pulse repetition rate	$\sim 1$ MHz
Peak spectral brightness	$10^{32} - 10^{34}$ ph/[s*mm <sup>2</sup> *mrad <sup>2</sup> *(0.1% BW)]
Average spectral brightness	$10^{26} - 10^{28}$ ph/[s*mm <sup>2</sup> *mrad <sup>2</sup> *(0.1% BW)]

The XFEL operation with Bragg reflectors will be difficult below 5 keV by enhanced photo-absorption in the crystal and above 20 keV by the small crystal bandwidth. Although the four-crystal configuration is tunable to any Bragg angle in the range from 90 to 45 degrees, the practical tuning range for a specific Bragg plane is limited to 2 – 6% because the angular acceptance can become smaller than the x-ray beam divergence at lower Bragg angles. We note that a few % is in fact rather broad when compared to its  $\sim 10^{-7}$  bandwidth.

An example of the radiation output from a tuneable, 4-mirror XFEL near the energy of 14.4 keV is shown in Fig. 3 [10]. In panel (a) the output radiation power as a function of time is indicated in red, with the electron beam current profile in green for reference. This power profile is obtained after 1000 passes, after which time it has saturated at approximately 2 MW. In panel (b) we

plot the corresponding output spectrum with a red line, showing that the spectral FWHM is approximately 1.8 meV, corresponding to a relative FWHM of  $\sim 1.3 \times 10^{-7}$ . Note that this bandwidth is much narrower than the reflectivity width of the Bragg crystals (the blue line) and approaches the Fourier transform of the electron bunch length.

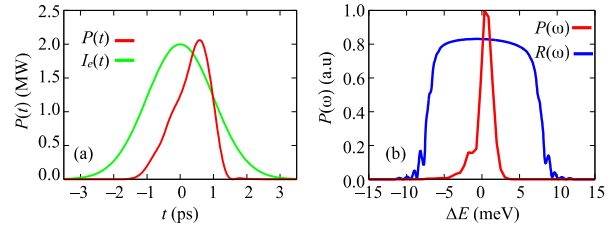


Figure 3: (a) The red line plots the temporal power profile of the XFEL output at 14.4 keV, showing peak powers  $\sim 2$  MW; the electron beam current is shown as a green line. (b) Spectrum of the XFEL output as a red line. The FWHM  $\sim 1.8$  meV is much narrower than that of the crystal reflectivity, shown in blue.

The number of passes to reach the steady state spectral shape, about 1000 passes, is relatively modest due to the small bandwidth of diamond reflection. If the bandwidth of the reflector were broad, say a few eV, it would take a much greater number of passes,  $> 10^{11}$ , to reach the transform-limited bandwidth, probably causing the FEL operation to be unstable.

An XFEL may be regarded to be a more natural extension of the third-generation sources. Currently the APS, one of the brightest sources in the hard x-ray range, produces  $10^9$  photons per second in the meV bandwidth, which will be increased a million-fold by an XFEL. Inelastic x-ray scattering and nuclear resonance scattering techniques, which are currently limited by the available flux in the desired bandwidth, can be revolutionized by an XFEL. Hard x-ray imaging will be feasible with nanometer resolution using multilayer Laue lenses that require x-ray bandwidth of less than  $10^{-5}$ . The intensity of an XFEL will also enable hard x-ray photoemission spectroscopy for time-resolved study of Fermi surfaces in bulk material. The temporally coherent photons at an average rate of  $10^{15}$  photons per second will be a game changer for x-ray photon correlation spectroscopy.

## ACCELERATOR SYSTEM

At the level of an individual bunch, the electron beam characteristics required for an XFEL (Table 1) have already been demonstrated, for example, by the LCLS accelerator system in its low-charge mode [11]. Producing ultra-low emittance bunches at a constant and high repetition rate is a challenge currently being actively addressed by several research groups, in particular those pursuing an ERL-based light source. These studies indicate that an injector with the bunch characteristics of Table 1 and a repetition rate in the MHz to GHz range is feasible. A variety of approaches based on laser-driven photocathodes, but employing either a DC voltage [12,

13] or a low-frequency radio frequency (rf) cavity [14] are in various stages of development.

The main accelerator for an XFEL-O should be of a cw superconducting type to accommodate a constant bunch repetition rate, with one or more recirculation paths to save cost. An XFEL-O is therefore a natural fit for a multi-GeV ERL-based light source facility. Various technical issues on ERL accelerator systems are being addressed in these proceedings, including the design of high-current, low-emittance injectors; beam mergers for the recirculation loop; cw superconducting linacs; and recirculation optics that preserve the electron beam quality [15]. The KEK-JAEA collaboration plans to construct a one-loop ERL with a 3-GeV superconducting linac in the first step. An XFEL-O operation is envisaged in the second step by adjusting the rf phase of the recirculation path to double the final energy to 6-7 GeV, as shown in Fig. 4 [16]. Note that energy recovery is not necessary for an XFEL-O due to its low average current.

A pulsed superconducting linac such as that being used for the European XFEL [17] can operate an XFEL-O in a pulsed mode. The macro-pulses in this linac are 1–2-ms long, accommodating 1000–2000 micropulses at a 1-MHz repetition rate, which is sufficient to drive an XFEL-O to saturation level.

can grow high-quality diamonds containing defect-free regions suitable for an XFEL-O. Experiments with 13.9-keV and 23.7-keV x-ray photons have established that the predicted reflectivity greater than 99% at near normal incidence is feasible [18, 19].

Temperature gradients that lead to gradients in the crystal lattice spacing can diminish the reflectivity. The simulation shows that the radiation heat load produced by an XFEL-O requires that the diamond crystal be cryogenically cooled to a temperature  $T \leq 100\text{K}$ . In this case, the diamond has sufficient time to conduct away the heat, so that the crystal temperature becomes homogeneous before the subsequent radiation pulse arrives. Low temperatures are favorable because diamond has an unmatched thermal diffusivity and an extremely small coefficient of thermal expansion for  $T < 100\text{K}$  as measured recently [20].

High radiation hardness is another desirable feature of diamond. The power density incident on diamond crystals in the XFEL-O cavity is  $\sim 4 \text{ kW/mm}^2$ , which is about 30 times higher than that of the undulator radiation used to test the first crystal at the APS. While it is encouraging that the APS crystals have survived one year of operation without an apparent decrease in performance, additional studies should be performed to understand the degree of

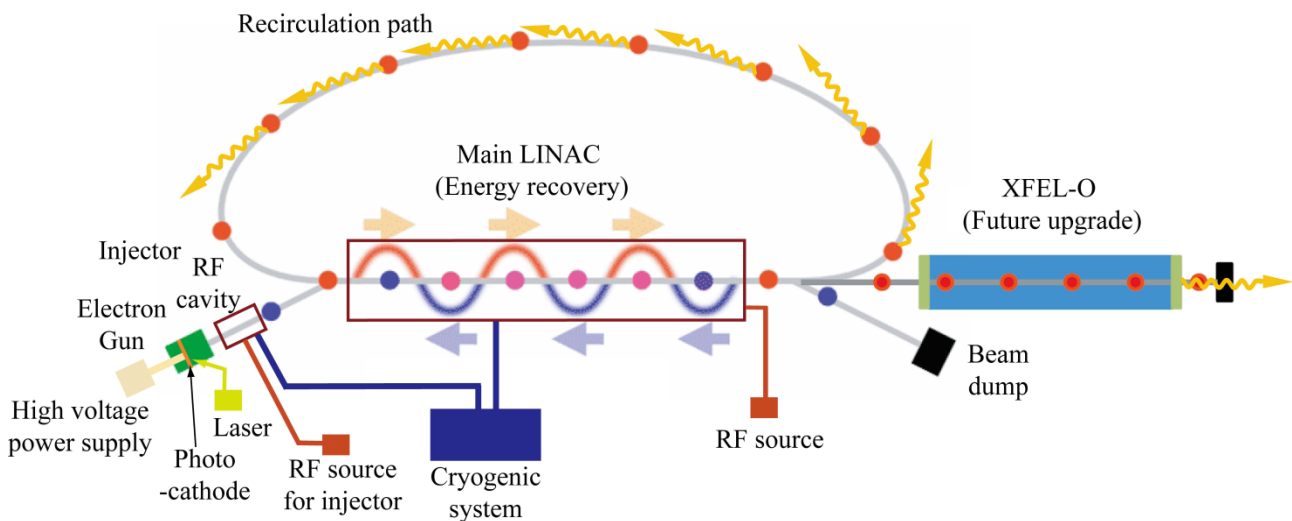


Figure 4: XFEL-O plan for the future KEK-JAEA 3-GeV ERL (courtesy of S. Sakanaka).

## X-RAY OPTICS

Diamond is a material whose superb physical qualities are well suited for an XFEL-O cavity: high mechanical hardness, high thermal conductivity, high radiation hardness, low thermal expansion, and chemical inertness. An exceptionally high  $\geq 99\%$  reflectivity is predicted in x-ray Bragg diffraction, higher than that from any other crystal due to the uniquely small ratio of the extinction length to the absorption length. The issue is then whether synthetic diamond crystals of sufficient size (active volume  $\sim 1 \text{ mm}^3$ ) and crystalline perfection required for high reflectivity can be manufactured. Working with several crystal growers, we found that modern techniques

irreversible radiation damage in diamond and how this damage affects its reflectivity.

Deviations of the crystal and focusing mirror surface from its ideal will disturb the x-ray wave-front, producing mode distortions and large-angle scattering. For diamond crystals, the surface error height  $\delta h$  should be a fraction of the x-ray wavelength times the difference of the index of refraction from unity  $\delta n$ . Since  $\delta n$  for hard x-rays is of the order of  $10^{-6}$ , the tolerance on  $\delta h$  is about a micron, which should be achievable. The tolerance of the grazing incidence mirror on the height error (contributing to diffusion) is about  $\delta h \leq 1 \text{ nm}$ , while the tolerance on figure error (contributing to mode distortion) is about  $0.1 \mu\text{m}$ . These tolerances are tight but are current state-of-the-art.

The requirements to stabilize the crystals and the mirrors in the cavity are stringent—better than 10-nrad (rms) angular stability and 3- $\mu\text{m}$  (rms) positional stability. The null-detection feedback technique employed at the Laser Interferometer Gravitational-Wave Observatory (LIGO) can stabilize several optical axes with a single detector, and therefore appears to be a promising approach. A pilot experiment with a high-resolution, six-crystal x-ray monochromator at the APS Sector 30 beamline succeeded in achieving an angular stability of 13 nrad (rms) [21]. We will need to improve the scheme to meet the XFEL requirements—a multiple-axis system with better than 10-nrad stability.

## CONCLUSIONS

The accelerator technology for an XFEL is essentially available in view of the active R&D program of the ERL projects. Several important advances have been made for the x-ray optics, such as the demonstration of near-perfect diamond reflectivity, the discovery of its low thermal expansion coefficient, and the success of a single-axis feedback for optical elements' mechanical stability. Issues that require further R&D include quantifying the radiation damage and preserving the wave-front after reflection from optical elements. However, we believe that there are good indications that these issues can be overcome.

An x-ray XFEL will provide capabilities outside the realm covered by high-gain x-ray FELs. After some development, it may be feasible to construct a low-power, compact XFEL providing seed radiation for a high-gain amplifier and producing very stable x-ray pulses with ultra-high spectral purity together with high intensity. With harmonic generation, the combination could produce “ultimate” x-ray beams up to 100 keV or higher.

## REFERENCES

- [1] P. Emma for the LCLS Team, Proc. of the 2009 Part. Accel. Conf., TH3PB101, p. 315 (2011).
- [2] G. Geloni, V. Kocharyan, and E.L. Saldin, J. Modern Optics 58, 1391 (2011); G. Geloni, V. Kocharyan, and E.L. Saldin, “Cost-effective way to enhance the

capabilities of the LCLS baseline,” DESY 10-133, August 2010.

- [3] J.N. Corlett et al., “A next generation light source facility at LBNL,” <http://escholarship.org/uc/item/81t3h97w>
- [4] For a review, see C. Brau, *Free-Electron Lasers* (Academic Press, New York, NY, 1990).
- [5] R. Colella and A. Luccio, Optics Comm. **50**, 41 (1984).
- [6] R. Bonifacio, N. Narducci, and C. Pellegrini, Opt. Commun. **50**, 373 (1984).
- [7] K.-J. Kim, Y. Shvyd'ko, and S. Reiche, Phys. Rev. Lett. **100**, 244802 (2008).
- [8] K.-J. Kim and Yu.V. Shvyd'ko. Phys. Rev. ST Accel. Beams **12**, 030703 (2009).
- [9] R. Hajima and N. Nishimori, Proc. of the FEL2009 (2009).
- [10] R. R. Lindberg et al., Phys. Rev. ST Accel. Beams **14**, 010701 (2011).
- [11] Y. Ding et al., PRL **102**, 254801 (2009).
- [12] I. Bazarov et al., Proc. of the 2009 Part. Accel. Conf., TU2GRI01, p. 683 (2011).
- [13] N. Nishimori et al., Proc. of the 2009 FEL Conf., TUPC17, p. 277 (2009).
- [14] F. Sannibale et al., Proc. of the 2010 FEL Conf., WEPB36, p. 475 (2010).
- [15] See presentations of the ERL Workshop, Tsukuba, Japan (October, 2011); <http://erl2011.kek.jp/>
- [16] K. Harada and ERL Project Team, J. of the Japanese Soc. for Synch. Rad. Res., **24**(5), 256 (2011) [in Japanese].
- [17] J. Zemella et al., presented at FLS2010 (SLAC, 2010).
- [18] Yu. V. Shvyd'ko et al., Nature Physics **6**, 96 (2010).
- [19] Yu. V. Shvyd'ko, S. Stoupin, V. Blank, and S. Terentyev, Nat. Photonics **5**, 539 (2011).
- [20] S. Stoupin and Yu. V. Shvyd'ko, Phys. Rev. Lett. **104**, 085901 (2010); S. Stoupin and Yu. V. Shvyd'ko, Phys. Rev. B **83**, 104102 (2011).
- [21] S. Stoupin et al., Rev. Sci. Instrum. **81**, 055108 (2010).

# APPLICATIONS OF HIGH-BRIGHTNESS GAMMA-RAYS FROM ERLS

T. Hayakawa, JAEA, Ibaraki 3191195 Japan

## Abstract

Progress in accelerator physics and laser physics has enabled us to generate a new generation of laser Compton scattering (LCS)  $\gamma$ -ray beam. The LCS  $\gamma$ -ray beam has been used for the study of fundamental science and industrial applications. We present examples of some applications using the LCS  $\gamma$ -ray beam and possibility using the next generation of high-intense LCS  $\gamma$ -ray beam provided from the ERLs.

## INTRODUCTION

The progress of the relativistic engineering (for example see Ref. [1]) provides a new  $\gamma$ -ray source with a MeV energy range. These  $\gamma$ -rays are generated by Compton scattering of relativistic electrons by laser photons (see Fig. 1) [2]. The LCS  $\gamma$ -ray beam has following advantages. The maximum energy is sharply determined in the basic QED process and that the  $\gamma$ -ray flux at high energy is relatively high. The energy can be changed with change of the energy of the electron beam and/or the wavelength of the laser. This method can generate almost 100% polarized  $\gamma$ -ray beam. The LCS  $\gamma$ -ray beam with the energy range of MeV have been provided for uses at the Duke Free Electron Laser Laboratory at Duke University [3], the National Institute of Advanced Industrial Science and Technology [4], and an electron storage ring NewSUBARU in SPring-8 [5]. They have been widely used for applications with photon-induced reactions [6, 7, 8]. Recently the next generation of high-brightness LCS  $\gamma$ -ray sources based on the ERLs have been proposed [9, 10]. In this paper we present examples of some applications using the LCS  $\gamma$ -ray beam.

## INDUSTRIAL APPLICATION

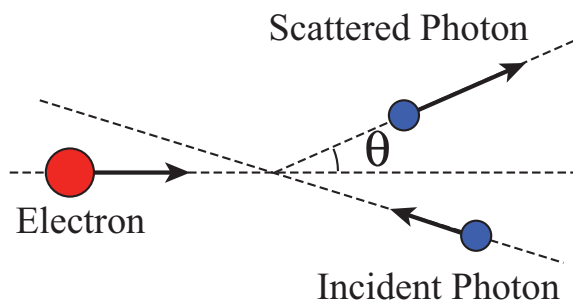


Figure 1: Schematic view of laser Compton scattering of laser photon and electron.

Detection of materials hidden by heavy shields are of im-

portance for many industrial applications: the detection of explosive materials hidden in a package or a cargo, and the management of special nuclear materials produced by nuclear power plants. Gamma-rays have been used as a probe to detect an isotope of interest with nuclear resonance fluorescence (NRF) for industrial applications [11]. Although Bremsstrahlung  $\gamma$ -rays have been widely used for NRF, Pruet *et al.* have proposed a novel non-destructive detection of  $^{235}\text{U}$  hidden in a cargo transporter by using NRF in conjunction with laser Compton scattering (LCS)  $\gamma$ -ray beam [12].

We have proposed an assay method of elemental and isotopic composition of materials hidden by heavy shields by measuring nuclear resonance fluorescence (NRF) scattering  $\gamma$ -rays with a LCS  $\gamma$ -ray beam provided from an ERL [9]. The NRF measurement with LCS  $\gamma$ -rays provides a unique finger print of each isotope. If the energy of the incident  $\gamma$ -ray is identical with the M1, E1, or E2 transition energy from the ground state of the nucleus of interest, the incident  $\gamma$ -ray is effectively absorbed in the nucleus and subsequently the nucleus de-excites by  $\gamma$ -ray emission. By measuring the NRF scattering  $\gamma$ -rays, we can detect the nuclear species of interest since the NRF  $\gamma$ -ray energies depend on the nuclear species as shown in Fig. 2. By measuring the energies of the NRF  $\gamma$ -rays, we can analyze nuclear species. The number of each isotope can be evaluated by the number of a NRF peak in the measured energy spectrum. Note that this method is applicable to detect both stable and unstable isotopes for most elements.

We demonstrated to detect isotope of interest concealed at the inside of a heavy shield with an available LCS  $\gamma$ -ray source at AIST [13]. A lead block was hidden by iron plates with a thickness of 15 mm. The position of the lead block was detected by measuring a 5512-keV  $\gamma$ -ray of  $^{208}\text{Pb}$  with the LCS  $\gamma$ -rays. Our proposed nondestructive assay method is demonstrated to be a powerful tool to detect isotopes of interest shielded deeply by materials.

## Detection of Nuclear Materials

Nondestructive assay (NDA) of plutonium in spent nuclear fuel is a key technology for safeguards of nuclear materials. The NDA of  $^{239}\text{Pu}$  in the nuclear fuel assembly has not been well established yet. First we should not only detect elements but also analyze each isotope of interest. However, the nondestructive detection of such an isotope in heavy materials is generally difficult. Second high- $Z$  element uranium in the nuclear fuel absorbs detection probes such as low-energy X-rays. Third the spent nuclear fuel is heated up due to the presence of the residual radioactivities. Thus, the spent fuel is often kept in a cooling water pool;

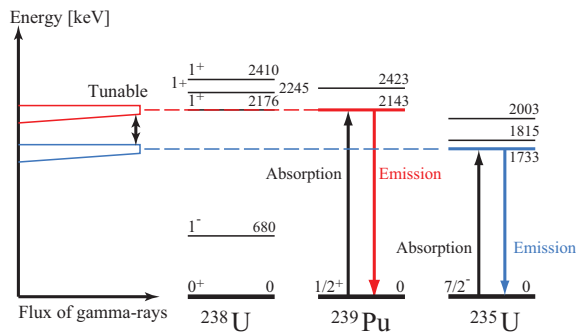


Figure 2: Schematic view of NRF measuring.

the water absorbs or scatters neutrons and low energy X-rays. We have proposed a nondestructive assay method for each isotope of uranium, plutonium, and minor actinides in spent nuclear fuel located in a water pool using NRF with  $\gamma$ -rays generated by a high-flux LCS source based on an ERL. This method has excellent advantages. Each isotope of elements located deeply in the nuclear fuel is detected by measuring the NRF  $\gamma$ -rays since high energy  $\gamma$ -rays of several MeV are used as the probe. In addition, the spent fuel can be analyzed with keeping in a water pool.

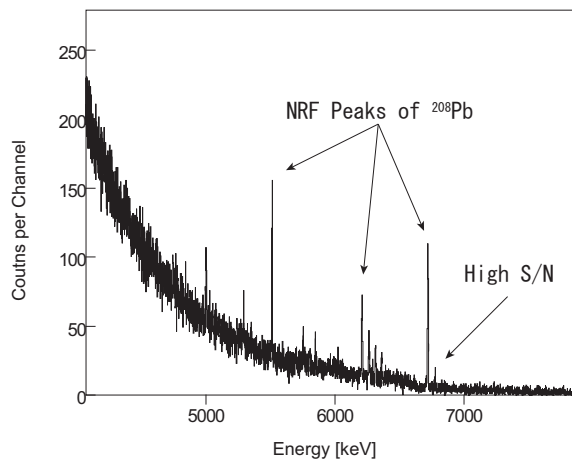


Figure 3: Example of measured NRF spectrum with LCS  $\gamma$ -rays.

For the nondestructive detection of materials in an industrial scale, we have designed a high-flux  $\gamma$ -ray facility utilizing a 350-MeV ERL equipped with a superconducting accelerator [14]. The high-flux  $\gamma$ -ray beams with energies of  $E_\gamma = 0.5\text{--}9$  MeV are generated from the Compton scattering with a ytterbium-doped fiber laser with a frequency of 80 MHz and a power of 100 W, which is similar to a system shown in the previous study [15]. For the most efficient interaction of laser photons and electrons, we set the root-mean-square (rms) size of laser power density profile equal to the rms size of electron beam at the collision point:  $w/2 = \sigma_e = 70$   $\mu\text{m}$ . The rms size of the laser power density profile at the mirrors of the laser super cavity becomes  $w(\text{at mirror}) = 2.3$  mm, which is small enough to keep the

high-Q configuration with mirrors of a practical diameter  $d \sim 10$  cm. The laser super cavity is assumed to have an amplification factor of 3000.

For detection of NRF  $\gamma$ -rays, a multi  $\gamma$ -ray detector array is used, which has been widely used for the study of the nuclear physics. This type of detector system typically consists of 20–120 high energy resolution  $\gamma$ -ray detectors (for example, see Refs. [16, 17]) such as high-purity germanium (HPGe) detectors. Figure 4 shows a schematic view of the detector system and a spent fuel assembly in a water pool. The  $\gamma$ -rays emitted from the spent fuel are measured with HPGe detectors. The spent fuel is stored in a water pool for cooling. The neutrons emitted from spontaneous fission of actinides in the nuclear fuel are absorbed by cooling water. The energy range of the incident LCS  $\gamma$ -ray beam is 1.7–2.5 MeV which is high enough to penetrate materials through shield water with a thickness of several ten centimeters.

An advantage of the use of NRF with high energy resolution HPGe detectors is to obtain the high signal-to-noise (S/N) ratio for the  $\gamma$ -ray peak. The energy resolution of the HPGe detectors is typically smaller than 0.2% (full width at half maximum (FWHM)) and resolve  $\gamma$ -ray peaks. In addition, the background is dominantly originated from the Compton scattering of the incident photons at the fuel assembly and the energies of the Compton scattered  $\gamma$ -rays are lower than the peak energy, and thus we can obtain high S/N ratio at NRF peak of a nucleus of interest. Figure 3 shows an example of measured NRF spectrum. One can see high S/N ratios around NRF peaks.

The nuclear fuel is vertically moved with a speed of 1 cm per 1 second to measure all the pellets. After a sequential measurement as a function of the vertical position of the fuel rods, the fuel assembly is horizontally moved for only a distance between two fuel rods. This measurements are repeated until the satisfactory data are accumulated for further computer analysis. In this manner, all the pellets in a fuel assembly can be measured for a period of 3000–4000 sec.

Here we estimate statistical uncertainty of the  $^{239}\text{Pu}$  detection. The peak count at 2143 keV is 36 photons for measurement time of 5 s. This suggests that we can detect the  $^{239}\text{Pu}$  NRF  $\gamma$ -rays at a rate of about 7 counts/s. For measurement duration of 4000 s, we can obtain a total count of  $2.8 \times 10^4$ . Note that, in the present calculation, we have assumed a spent fuel, of which  $\text{PuO}_2$  is highly concentrated compared with the typical expected concentration (1%). If the peak count is smaller than the present result by a factor of 10, the peak can be still observed because of the high S/N ratio. In this case we can obtain the total count of  $2.8 \times 10^3$  for the  $^{239}\text{Pu}$  NRF peak. This result suggests that we can detect  $^{239}\text{Pu}$  whose fraction of 1% in the spent fuel with statistical error of about 2%.

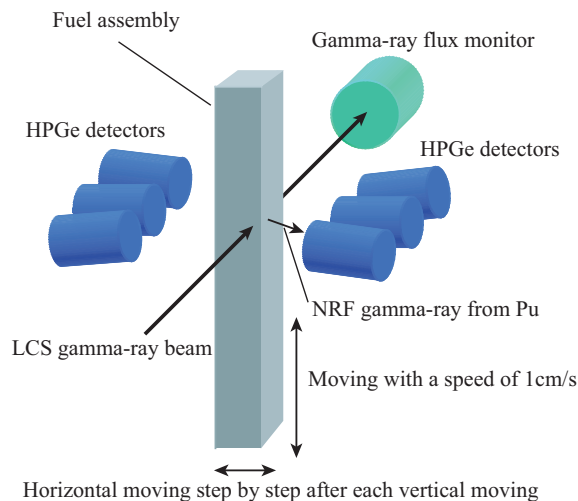


Figure 4: Schematic view of NRF measuring of  $^{239}\text{Pu}$  in fuel assembly.

### Measuring Chemical Material

We have proposed an extended non-destructive assay method for measuring molecules and chemical compounds hidden by heavy shields such as iron plates of a thickness of several centimeters [18]. The molecule or chemical compound consists of several elements and the elemental ratio depends on its chemical formula. By measuring the abundance ratio of key elements of the chemical compound of interest, we can detect the material inside heavy shields. For example, the chemical formula of melamine is  $\text{C}_3\text{H}_6\text{N}_6$  and the ratio of  $(\text{C}/\text{N})_{\text{melamine}}$  is 0.5.

## ASTROPHYSICS

### Photon-induced Reaction Nucleosynthesis in Supernova Explosions

Photons play an extremely important role in explosive nucleosynthesis, as might occur both in supernova explosions and in the Big-Bang. Massive stars that are at least eight times heavier than our Sun ultimately produce supernova explosions as the final stage of their evolution. High-energy photons at energies of an MeV or more are created in the extremely high-temperature environments that exist in this phase, and these photons can synthesize new isotopes, so-called "p-nuclei", by photon-induced reactions ( $\gamma$ -process) [19]. The p-nuclei are characterized by being at the neutron-poor extremes of the stable nuclides. Thus they cannot be produced by the two usual neutron capture processes (the rapid-neutron-capture-process, or r-process; and the slow-neutron-capture-process, or s-process), as  $\beta$ -decay to them is blocked by a stable isobar. Thus they are generally of very low abundance relative to the other isotopes of each element. The p-nuclei are thought to be produced by several different processes of nucleosynthesis, one of which is the  $\gamma$ -process, which proceeds by successive  $(\gamma, n)$  and  $(\gamma, \alpha)$  reactions operating on pre-existing

abundant heavier isotopes, interspersed with occasional  $\beta$ -decays (see Fig. 5). Woosley and Howard found [19] an anti-correlation between the solar abundances of the p-nuclei and their photo-induced reaction rates, which suggests that the photo-induced reaction rates on the p-nuclei, or on their nearest neighbors, are essential for understanding the  $\gamma$ -process. Recently evidence that some p-nuclei are synthesized in the photon-induced reactions in supernova explosions was found in the solar abundances [20]. Indeed, these processes often occur concurrently.

Thus, experimentally measured rates for photo-induced reactions are essential for accurate theoretical simulations of the  $\gamma$ -process. The  $(\gamma, n)$  reaction rates to giant dipole resonances have been measured, but the reaction rates at energies of astrophysical interest have been studied on several nuclei. The distribution of photons in supernovae is plankian, so the photon flux decreases sharply with increasing photon energy. Thus the energy at which the photons contribute to the abundances of the p-nuclei is typically a few hundred keV above the neutron separation energy, typically 7-9 MeV. The cross sections in this energy region are typically a few orders of magnitude smaller than those at the peaks of the giant dipole resonances.

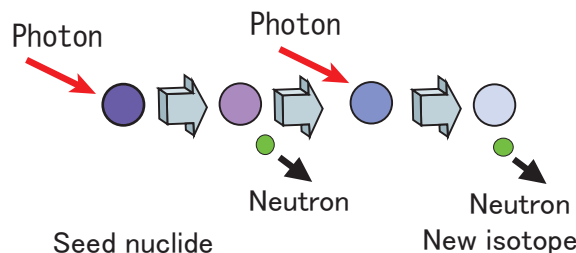


Figure 5: Schematic view of photon-induced reactions in supernova explosions.

### Neutrino-process in Supernovae

The interaction between neutrinos and nuclei plays an extremely important role for supernova explosions and their synthesis of nuclides. The question of how a star collapses and makes a supernova has challenged astrophysicists for decades. A huge number of neutrinos,  $10^{53}$  ergs, are produced from a core collapse supernova and the subsequent cooling phase of a proto-neutron star. Most of these neutrinos escape into the interstellar medium, but a small fraction of them transfer their energy to an outside exploding mantle and surrounding stellar envelope by neutrino-nucleus interactions such as neutral current reactions, charged current reactions, and inelastic neutrino-nucleus scattering. These neutrino nucleus interactions also are important for synthesis of several light isotopes, such as  $^7\text{Li}$ ,  $^{11}\text{B}$ , and  $^{19}\text{F}$ , as well as the heavy rare isotopes of  $^{138}\text{La}$  and  $^{180}\text{Ta}$  (see Fig. 6) [21]. However, very few neutrino reaction cross-sections are known with high accuracy since they are very difficult to measure, and their calculation depends on complex nuclear structures. The mag-

netic dipole (M1) and Gamow-Teller responses in nuclei are particularly important for the estimation of the inelastic neutrino-nucleus scattering and neutral current reaction cross-sections. Since the LCS gamma-ray sources can generate almost 100% linear polarized gamma-ray beam, and this has a strong experimental sensitivity to M1 transitions, LCS gamma-ray sources have enabled us to detect the fine structure of weak M1 transitions with high accuracy. These measurements have been carried out using LCS gamma-ray sources at the Duke Free Electron Laser Laboratory and at AIST (for example, see Ref. [8]).

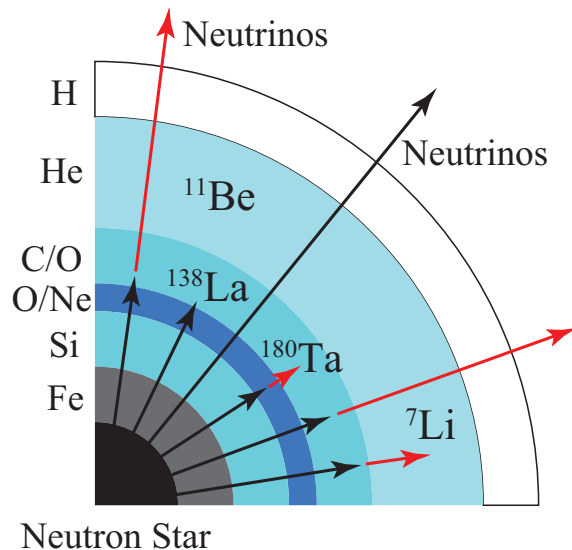


Figure 6: Schematic view of neutrino-induced reactions in supernova explosions.

## FUNDAMENTAL SCIENCE

Nuclear parity violation is caused by the weak interactions on the nucleon-nucleon (NN) interactions in nuclei. In the picture of meson exchange description, one meson-nucleon vertex is coupled to the other nucleon mediated by weak interaction. Parity doublets in nuclei are mixed with each other by this PNC NN interaction. Titov *et al.* have proposed a novel method to measure the nuclear parity violation using circularly polarized LCS  $\gamma$ -rays [22]. Their group measured PNC asymmetry in exciting the first excited state in  $^{19}\text{F}$  by using high intensity elliptically polarized synchrotron radiations generated by elliptical multipole wiggler at SPring-8. In case of  $^{19}\text{F}$ , the set of the ground ( $J^\pi = 1/2^+$ ) and 110 keV ( $J^\pi = 1/2^-$ ) excited states is a parity doublet. In the new method, the parity mixing is studied by NRF using a circularly polarized photon beam. The experiment has been carried out using hard x-ray synchrotron radiations (SR) from the elliptical multipole wiggler (EMPW) at SPring-8. In near future, extremely high-flux  $\gamma$ -ray beam can provide new information for the PNC NN interaction.

## CONCLUSION

The next generation of high-brightness LCS  $\gamma$ -ray sources based on the ERLs have been proposed. We have presented that these ERL-LCS  $\gamma$ -ray sources have high potential for the study of fundamental science and industrial applications.

## REFERENCES

- [1] G.A. Mourou, T. Tajima, S.V. Bulanov, *Rev. Mod. Phys.* 78, 309 (2006).
- [2] F.V. Hartemann, W.J. Brown, D.J. Gibson, S.G. Anderson, A.M. Tremaine, P.T. Springer, A.J. Wootton, E.P. Hartouni, C.P. Barty, *Phys. Rev. ST-AB* 8 (2005) 100702.
- [3] V.N. Litvinenko, B. Burnham, M. Emamian, N. Hower, J. M. J. Madey, P. Morcombe, P. G. O'Shea, S. H. Park, R. Sachtshale, K. D. Straub, G. Swift, P. Wang, and Y. Wu, *Phys. Rev. Lett.* 78, 4569 (1997).
- [4] H. Ohgaki, S. Sugiyama, T. Yamazaki, T. Mikado, M. Chiwaki, K. Yamada, R. Suzuki, T. Noguchi, and T. Tomimasu, *IEEE Trans. Nucl. Sci.* 38, 386 (1991).
- [5] K. Aoki, K. Hosono, T. Hadame, H. Munenaga, K. Kinoshita, M. Toda, S. Amano, S. Miyamoto, T. Mochizuki, M. Aoki and D.Li, *Nucl. Inst. Method. Phys. Res. A* 516, 228 (2004).
- [6] N. Pietralla, Z. Berant, V. N. Litvinenko, S. Hartman, F. F. Mikhailov, I. V. Pinayev, and G. Swift, M. W. Ahmed, J. H. Kelley, S. O. Nelson, R. Prior, K. Sabourov, A. P. Tonchev, and H. R. Weller, *Phys. Rev. Lett.* 88, 012502 (2002).
- [7] T. Hayakawa, S. Miyamoto, Y. Hayashi, K. Kawase, K. Horikawa, S. Chiba, K. Nakanishi, H. Hashimoto, T. Ohta, M. Kando, T. Mochizuki, T. Kajino, M. Fujiwara, *Phys. Rev. C* 74, 065802 (2006).
- [8] T. Shizuma, T. Hayakawa, H. Ohgaki, H. Toyokawa, T. Komatsubara, N. Kikuzawa, A. Tamii, and H. Nakada, *Phys. Rev. C* 78, 061303(R) (2008).
- [9] R. Hajima, T. Hayakawa, N. Kikuzawa, E. Minehara, *J. Nucl. Sci. Technol.* 45, 441 (2008).
- [10] V. N. Litvinenko, I. Ben-Zvi, E. Pozdeyev, T. Roser, *IEEE Trans. Plasm. Sci.* 36, 1799 (2008).
- [11] W. Bertozzi and R.J. Ledoux, *Nucl. Instrum. Methods B* 241 (2005) 820.
- [12] J. Pruet, D.P. McNabb, C.A. Hagmann, F.V. Hartemann, and C.P.J. Barty, *J. Appl. Phys.* 99 (2006) 123102.
- [13] N. Kikuzawa, R. Hajimam, N. Hishimori, E. Minehara, T. Hayakawa, T. Shizuma, H. Toyokawa, H. Ohgaki, *Applied Physics Express* 2, 036502 (2009).
- [14] R. Hajima, N. Kikuzawa, T. Hayakawa, E. Minehara, *Proc. 8th International Topical Meeting on Nuclear Applications and Utilization of Accelerators (AccApp-07)*, 2007, p.182.
- [15] T. Schreiber, C. Nielsen, B. Ortac, J. Limpert, and A. Tünnemann, "131 W 220 fs fiber laser system," *Optics Letters* 30, 2754 (2005).
- [16] K. Furuno, H. Oshima, T. Komatsubara, K. Furutaka, T. Hayakawa, M. Kidera, Y. Hatsukawa, M. Matsuda, S. Mitarai, T. Shizuma, T. Saitoh, N. Hashimoto, H. Kusakari, M. Sugawara, T. Morikawa, *Nucl. Inst. Meth. Phys. Res. A* 421, 211 (1999).

- [17] M. Devlin, L. G. Sobotka, D. G. Sarantites and D. R. LaFosse, Nucl. Inst. Meth. Phys. Res. A 383 (1999) 506.
- [18] T. Hayakawa, H. Ohgaki, T. Shizuma, R. Hajima, N. Kikuzawa, E. Minehara, T. Kii, H. Toyokawa, Rev. Sci. Inst. 80 (2009) 045110.
- [19] S.E. Woosley, W.M. Howard, Astrophys. J. Suppl. **36**, 285 (1978).
- [20] T. Hayakawa, N. Iwamoto, T. Shizuma, T. Kajino, H. Umeda, K. Nomoto, Phys. Rev. Lett. **93**, 161102 (2004).
- [21] S.E. Woosley, D.H. Hartmann, R.D. Hoffman and W.C. Haxton, Astrophys. J. **356**, 272 (1990).
- [22] A.I.Titov, M.Fujiwara, K.Kawase, J.Phys.(London) G32, 1097 (2006).

**ERL2011 SUMMARIES OF WORKING GROUP 1**

**ERL2011 SUMMARY OF WORKING GROUP 1:  
PROGRESS WITH DC PHOTOEMISSION ELECTRON SOURCES**

B. Dunham, et al.

**ERL2011 SUMMARY OF WORKING GROUP 1:  
PROGRESS WITH RF INJECTORS**

T. Rao, et al.

## ERL2011 SUMMARY OF WORKING GROUP 1: PROGRESS WITH DC PHOTOEMISSION ELECTRON SOURCES

B. Dunham, Cornell University, Ithaca, NY 14853, USA

S. Benson, C. Hernandez-Garcia, R. Suleiman, Jefferson Lab, Newport News, VA 23606, USA

N. Nishimori, JAEA, Tokai-mura, Ibaraki 319-1195, Japan

T. Rao, Brookhaven National Lab, Upton, NY 11973, USA

M. Yamamoto, KEK Tsukuba, Ibaraki 305-0801, Japan

### Abstract

This paper summarizes the recent progress made with DC photoemission electron sources for high average power Energy Recovery Linac-based light sources (ERL) and Free Electron Lasers (FEL). The progress during the past two years is discussed along with the remaining technical challenges for producing reliable, high-brightness, high average-power electron injectors.

### INTRODUCTION

Much progress has been made with DC photoemission guns and their associated RF injectors since the last ERL workshop. DC photoemission guns are the best fit for machines requiring low to intermediate bunch charges (up to 100's of pC) and from low to high average currents (up to 100's of mA). RF and SRF guns, with higher cathode field gradients, are better suited for high bunch charge applications. Emittance is also a key requirement, with many ERL and FELs desiring the lowest emittance (highest brightness) possible. In this paper, we will cover the latest improvements with DC photoemission sources.

In the previous workshop [1], several alternative insulator designs were discussed to overcome the problems with commonly used cylindrical insulator stacks. A number of the choices have been built and tested, demonstrating improved performance. One system has now worked at the 500 kV level, and others are soon to follow.

Cathodes are still the most important part of a photoemission gun, DC or RF/SRF. The cathode properties determine the maximum brightness one can obtain in the final beam from the injector, and the cathode lifetime will, in part, determine the reliability and up-time for the injector. Until this year, most groups have used GaAs cathodes, as they have the lowest intrinsic emittance of any known cathode. The first emittance measurements of alkali-type photocathodes were performed recently [2, 3], demonstrating that they generate only slightly larger thermal emittance beams than GaAs at 520 nm laser wavelength. This, combined with their longer lifetime (demonstrated by several labs), makes them the cathode of choice for the time being. In the previous workshop, many load-lock systems for cathode preparation and storage were introduced. Now, load-locks are common-place for all high performance photocathode guns.

Lasers are also a critical component for photocathode guns. A number of different designs are available,

depending on the frequency, wavelength and charge per bunch. A wavelength around 520 nm is often chosen for high quantum efficiency cathodes like GaAs and CsK<sub>2</sub>Sb. The frequency can vary greatly, from tens of MHz to 1300 MHz. Lower frequency lasers are often commercially available, while higher frequency systems are usually custom built.

As more DC photoemission guns with RF/SRF accelerating modules come on-line, operational issues are becoming of more interest to the DC gun community. How to deal with very high average power beams is still not well understood. Issues like beam halo, large dynamic range diagnostics, machine protection, beam dumps, and radiation safety become more important as we construct electron injectors in the 500 kW to 1 MW range.

This summary paper will cover the advances in each of these areas since the last ERL workshop in 2009.

### PHOTOCATHODES

#### *Bruce Dunham*

Cathodes are clearly the most important component of any photoemission gun, whether it is DC, RF or an SRF type. A number of recent photocathode workshops have been very well attended (<https://indico.bnl.gov/conferenceDisplay.py?confId=290>, <http://photocathodes2011.eurofel.eu/>). Much of the current knowledge is summarized in the review paper by Dowell [4].

For the high brightness, high-average current applications for ERLs and FELs, only semiconductor-type cathodes are considered, as the low quantum efficiency (QE) of metal cathodes precludes their use. There are several key parameters that a cathode must have for these high performance injectors. The first parameter for a cathode is high QE (5-10%) at an easily obtainable laser wavelength (520 nm, for instance) in order to reach 100's of mA average current. Second, a low thermal emittance is required (the lower the better) to generate bright beams. Early simulations showed that it is possible to nearly recover the cathode thermal emittance after accelerating the beam to 5-10 MeV [5], and these simulations have recently been verified experimentally [6]. Third, a very fast (sub-ps) electron response time is an integral part of reaching small emittances. Long tails lead to emittance growth, and limit the effectiveness of laser pulse shaping. Finally, the cathode must last a relatively long time while delivering

the desired beam current under operational conditions. Without this, one cannot build a reliable injector with good up-time.

GaAs and GaAs-like materials have been used as sources of polarized electrons for many years. GaAs has also been used for non-polarized applications, such as DC guns (at the Jlab FEL [7], for example). GaAs has a number of properties that make it attractive for non-polarized beams, but also has several that make its use difficult.

Obtaining high QE of 10-20% for GaAs is relatively straightforward for green laser wavelengths, making it a good candidate for obtaining high average currents with modest laser power. The QE falls off quickly for longer wavelengths. The response time for GaAs is quite fast (sub-ps) for green and shorter wavelengths [8] as long as the QE is below ~10%, but becomes much longer as the wavelength approaches the bandgap energy. GaAs also has the smallest measured intrinsic emittance of any known cathode [9], but this occurs at wavelengths approaching the bandgap where the QE becomes small. Thus, it is not possible to use GaAs to simultaneously get high QE, fast response time, and ultra-low intrinsic emittance. Finally, because the GaAs photoemission process is a surface phenomenon, extreme ultra-high vacuum is required, making it very sensitive to any vacuum excursions during operation. Continued R&D into GaAs-like materials will be very important for the future, in order to find a cathode with all of the key parameters needed for high-brightness, high average power injectors. It is important to note, that even with these difficulties, currents as high as 25 mA at 5 MeV have been produced using GaAs [6].

In the 1990's, alkali photocathodes were used in several photoemission guns as they were much more robust in terms of vacuum requirements. A CsK<sub>2</sub>Sb cathode was used to produce the highest average current beam to date [10]. They were not considered as candidates for high-brightness sources until recently, due to the assumption that the intrinsic emittance would not be as low as GaAs. Recent measurements [2, 3, 11] have dispelled that myth, demonstrating that alkali cathodes produce electrons with only a slightly higher transverse thermal energy than for GaAs around 520 nm. Much of the confusion in the past resulted from the misconception that GaAs could produce thermal or sub-thermal transverse energy electron beams at useful laser wavelengths. As discussed above, these sub-thermal beams are only generated using near band-gap radiation where the QE is low and the response time is slow, which is not compatible with high-power, high-brightness injectors. Using very thin GaAs samples can mitigate the problem with slow response time.

Due to these new measurements, a number of groups have switched to using alkali photocathodes for beam operations instead of GaAs. In addition, several groups have demonstrated long-term, stable cathode operation at 20 mA average currents (both DC beam at low energy (200 keV) [12], and CW beams at high energy (5 MeV)

[13]). QE values of 5-10% are readily achieved, and the response time is quite fast (<1 ps). There is still plenty of work to do to determine the optimum growth recipes, best substrate to use, and damage mechanisms during extended operations. The vacuum requirements are not as stringent as for GaAs, somewhat simplifying the design of load-locks and gun vacuum systems.

Having a robust cathode to use for commissioning high power injectors will free up cathode designers to concentrate on finding the ideal cathode for future light sources. Other possibilities include: engineered materials, like was done for polarized electron sources; GaN-like materials [14]; and improving the theoretical understanding of photoemission for NEA and PEA materials.

## HIGH VOLTAGE INSULATORS

*Nobuyuki Nishimori and Riad Suleiman*

Operation of DC photoemission guns at 500 kV or more has been a technological challenge to be faced since the first ERL workshop in 2005 [15]. The highest operational voltage has however stayed at 350 kV. The most serious problem is field emission from a cathode support electrode, which can lead to voltage breakdown, insulator punch-through and other problems on the ceramics. In order to solve this field emission problem, a segmented insulator, an inverted insulator and an insulator with a controlled bulk resistivity were proposed at the last ERL workshop in 2009 [1]. In this section, the progress of the segmented and inverted insulator developments over the past two years is summarized.

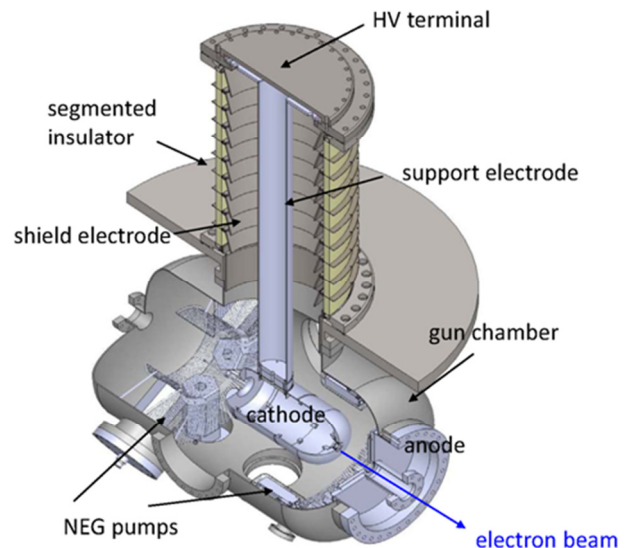


Figure 1: A DC photoemission gun with a segmented insulator at JAEA.

### *Segmented Insulators*

A segmented insulator has been widely used for DC electrostatic accelerators. The insulator consists of ceramics and metal rings alternatively stacked in series

Table 1: Parameters of Segmented Insulators for DC Photoemission Guns

Institute	HV(kV)	Segments	Ceramics	Support electrode	Shield electrode	Multiple insulators	Ref.
JAEA (existing)	500	10	99.8%Al <sub>2</sub> O <sub>3</sub> A99P 400 mm diameter 750 mm in height Rings are 65mm high x 20mm thick Ceramic by Shinagawa Fine ceramics Brazed by Hitachi Haramachi	Titanium 101.6 mm diameter	Titanium 290mm inner diameter	Single	[21]
Cornell (existing)	750	14	99.8% Al <sub>2</sub> O <sub>3</sub> Rings are 50mm high x 20mm thick Height: 448mm x 2 Ceramic by Friatec Brazed by Friatec	Stainless Steel 110 mm diameter	Copper, 363 mm inner diameter	Two	[22]
KEK (existing)	500	10	Al <sub>2</sub> O <sub>3</sub> based ceramic (TA010) 400mm diameter Height:398mmx2 Rings are 65mm high x 20mm thick Ceramic by Kyocera Brazed by Kyocera	Titanium 101.6 mm diameter	Titanium 290 mm inner diameter	Two	[23]
IHEP (planned)	500	10	Al <sub>2</sub> O <sub>3</sub> (Kyocera/CPI/other company) Detailed design is in progress	Titanium Detailed design is in progress	Titanium Detailed design is in progress	Two	[24]

(see Figure 1). This structure provides means to connect an additional electrode to the metal ring, which can shield ceramic surfaces from field emission cathode support electrode. The field emission current is drawn to ground through an external resistor connected between adjacent electrodes. These segmented insulators have been used for the 100 kV gun at NIKHEF [16], the 200 kV gun at Nagoya University [17] and the 230 kV gun at JAERI FEL [18]. The use of segmented ceramics for a 500 kV photoemission gun was proposed at JAEA and KEK in 2008 [19].

One of important parameters for the design of a segmented insulator is the surface electric field of a cathode support electrode, since the field emission generated from the support electrode may damage the ceramics. The surface field on the support electrode is roughly given by

$$E_r = \frac{V}{r \ln(R/r)},$$

where V is the potential difference between the support electrode with outer radius r and the additional shield electrode with inner radius R. Substitution of JAEA gun parameters r=50.8 mm and R=145 mm yields E<sub>r</sub>=9.38 MVm<sup>-1</sup> for V=500 kV. The surface electric field anywhere on the electrodes should be smaller than the voltage breakdown criteria. The breakdown criteria for large area electrodes decrease with increasing voltage due to total voltage effect. The criteria for V=500 kV is about 10 MVm<sup>-1</sup> [1, 20].

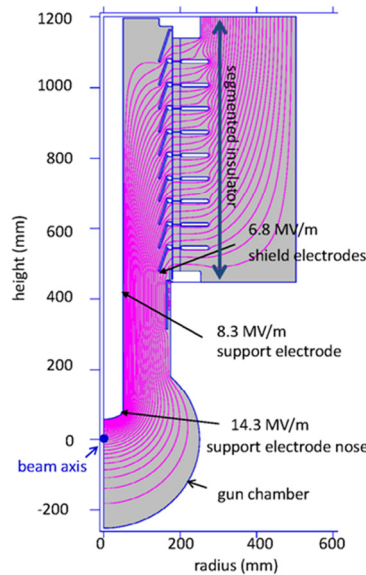


Figure 2: Static electric field calculation of segmented insulator with a support electrode and gun chamber at JAEA. The high voltage is 500kV.

The field emission from shield electrodes to the ceramic segments also needs to be avoided. This electrode is a cathode for the ceramic surface and an anode for the support electrode. The maximum field emission energy to the ceramic is equal to the total applied voltage divided by the number of segments. For a gun with ten segmented ceramics, the field emission energy is 50 keV for V= 500 kV. Since the voltage breakdown criteria at 50 kV is much higher than that at 500 kV, the damage on the ceramics caused by the field emission from shield electrodes will be small. Increasing

of the number of segments also helps to provide uniform electric field on the ceramic surface.

Figure 2 shows an example of the static electric field calculation for the segmented insulator at JAEA. The maximum electric field on the support and shield electrodes are  $8.3 \text{ MVm}^{-1}$  and  $6.8 \text{ MVm}^{-1}$ , respectively, which are smaller than the voltage breakdown criteria at 500 kV. The outer radius of the ceramics is determined to be 200 mm. Similar guns with segmented insulators have been developed in Cornell and KEK. Parameters of segmented insulators for DC photoemission guns under development or planned are listed in Table 1.

Multiple insulator stacks have been employed at Cornell and KEK. This helps to simplify installing shield electrodes inside the insulators and to avoid complete replacement of the insulators in case of failure of a single stack.

A segmented insulator was also used for the 1 MV bushing of the international thermonuclear experimental reactor (ITER) neutral beam injector (NBI) [25, 26, 27]. A negative deuteron ion beam of 40 A with duration of 3600 seconds at 1 MeV is required. The electrical bus bars and water cooling lines necessary for the negative ion source placed at -1.0 MV terminals are provided through the 1.0 MV bushing. The bushing therefore has a center conductor at -1.0 MV as an electrostatic shield. The structure is very similar to Fig. 1. High voltage conditioning up to 973 kV was demonstrated at Cadarache in France, when  $2 \times 10^{-2}$  Pa of hydrogen or helium gas was added in the high voltage chamber [26]. This additional gas is found to be very effective for high voltage conditioning.

### *Inverted Insulators*

The Jefferson Lab photocathode gun employs inverted insulator geometry [28] where a ceramic insulator extends into the vacuum chamber, as shown in Figure 3. The primary benefit of this approach is that a large metal structure is not required to support the cathode electrode. As a result, there is significantly less surface area biased at high voltage, and consequently there is less metal to generate electrons. The design also creates electrostatic field lines that tend to deliver field emitted electrons toward the grounded vacuum chamber, rather than to the insulator where damage can occur. Another appealing feature is that the insulator is a common element of medical x-ray sources, and therefore relatively inexpensive compared to cylindrical insulators purchased solely for accelerator electron gun applications. Finally, because there is no exposed high voltage, corona shields and a tank for dry nitrogen gas or  $\text{SF}_6$  are not required.

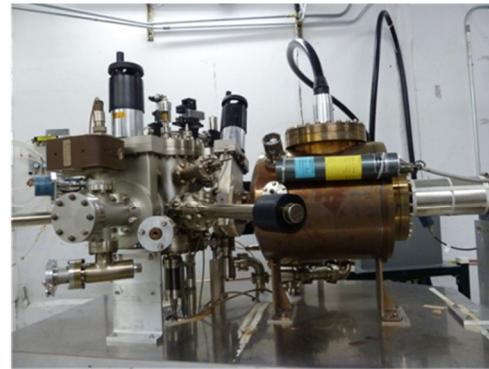
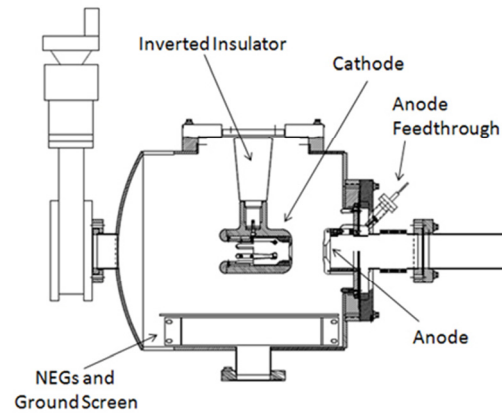


Figure 3: (Top) Cross section of the Jefferson Lab inverted gun HV chamber. (Bottom) The anode is electrically isolated and connected to a pico-ammeter to detect field emission. Commercial R28 HV cables connect the 225 kV Spellman HV supply to the gun through an oil tank. The oil tank allows for 100 M $\Omega$  resistor to be connected in series during HV conditioning the gun. An x-ray radiation detector is mounted on the side of the gun HV chamber.

Two guns have been built at Jefferson Lab based on the compact inverted insulator design [29]. One gun provides the polarized electron beam at the Continuous Electron Beam Accelerator Facility (CEBAF) and the other is used for more aggressive tests at a dedicated test facility. Both guns employ tee-shaped cathode electrodes. The CEBAF cathode electrode is made of 316L stainless steel polished to sub-micron finish using diamond grit. It was high voltage processed to 150 kV without field emission and now provides beam at 130 kV. The second gun uses a cathode electrode made of large-grain niobium and was successfully conditioned to 225 kV (the maximum voltage of the supply) without field emission. Efforts to build a 350 kV inverted gun using commercial R30 HV cables and connectors are underway. Simultaneously, we are working on a 500 kV inverted gun in collaboration with Jefferson Lab FEL. For this gun, commercial connectors are not available, so we are engineering appropriate HV connections, and considering means to allow for photocathode cooling.

## HIGH VOLTAGE CONDITIONING TECHNIQUES

*Carlos Hernandez-Garcia, Nobuyuki Nishimori and Riad Suleiman*

Electrodes in DC photoemission guns must be high voltage conditioned prior to normal operations at the desired voltage for reliability without field emission. Typically DC guns are conditioned 10% to 25% higher than the operational voltage to remove electron emission sites in a controlled manner. When precautions are taken towards producing smooth electrode surfaces and extreme high vacuum procedures implemented for cleaning and assembly, activity is not observed below 250 kV [30, 21]. Beyond this voltage, conditioning is usually performed at about 5-10 kV per hour to maintain the overall vacuum level below  $5 \times 10^{-6}$  Pa. This is typical for semiconductor photoemission guns where ultra-high vacuum conditions are necessary for good cathode lifetime, for other types of guns higher values may be acceptable. The high voltage power supply current is limited to a few  $\mu\text{A}$  above background to minimize damage to the electrode and/or to the current limiting resistor. Above 300 kV, voltage induced gas desorption slows down conditioning [1]. For example, in the JLAB FEL DC photoemission gun, it takes one hour for the vacuum to recover after each 1 kV increment, while the JAEA DC photoemission gun has been conditioned at a rate of 4 kV/hr.

It has also been observed that the higher the voltage, the longer it takes for the vacuum level to recover, assuming the incremental voltage steps are the same value [1]. In some instances the voltage is lowered to maintain the emission current at a few  $\mu\text{A}$  above the power supply's background for preventing damage, but at the same time the excess current needs to be sufficiently high to induce melting of the emitter by Joule heating. Often times this requires increasing the voltage beyond the last set point at which voltage induced gas desorption was last observed, therefore coupling field emission processing with voltage induced gas desorption processing.

Two results are noteworthy since the last ERL Workshop in 2009 [1]. The JAEA DC photoemission gun, built with a segmented insulator, has been conditioned to 550kV, and the CEBAF polarized source group has characterized various types of niobium electrodes in a high voltage test stand. In addition to those results, both the Cornell and the JLab FEL DC photoemission guns were rebuilt with cylindrical insulators of a new material (AL-970CD) from Morgan Advanced Ceramics that promised charge dissipation through some degree of conductivity embedded in the bulk. Unfortunately the new insulators in both the Cornell and the JLab FEL DC guns suffered punctures at  $\sim 450$  kV [30]. The leaks were sealed but re-processing was limited to  $\sim 400$  kV. The Cornell gun has been operating since then at 350 kV. Despite 100 hours of conditioning with Krypton gas, the JLab FEL gun has been operating at 325

kV [31]. Re-processing of both electron guns was limited by re-opening of the initial punch-through leak. The most likely mechanism is that field emitted electrons from the stem electrode, which is coaxial to the cylindrical insulator, accumulate charge in the bulk of the insulator. As the charge did not dissipate as advertised, the accumulated charge was high enough to violently discharge to ground, effectively vaporizing the material and causing micro holes, which after many events connect the vacuum side of the insulator to its outer surface letting  $\text{SF}_6$  into the vacuum environment.

### JAEA DC Gun 550kV Conditioning

The segmented insulator with a support electrode at JAEA was successfully high voltage processed up to 550 kV in 2009 [21]. In order to study the field emission effect from the support electrode, the cathode and anode electrodes and NEG pumps were not installed in the gun chamber initially. The ceramics and high voltage chamber were baked at 190 degree for eight hours prior to the processing. A  $1000 \text{ L s}^{-1}$  turbo molecular pump was used in this test and the base pressure was  $2 \times 10^{-8}$  Pa. Figure 4 shows the high voltage test results. The voltage started at 250 kV, and then took 15 minutes for each 1 kV step up to 500 kV. The processing speed becomes slower above 500 kV because of increased radiation.

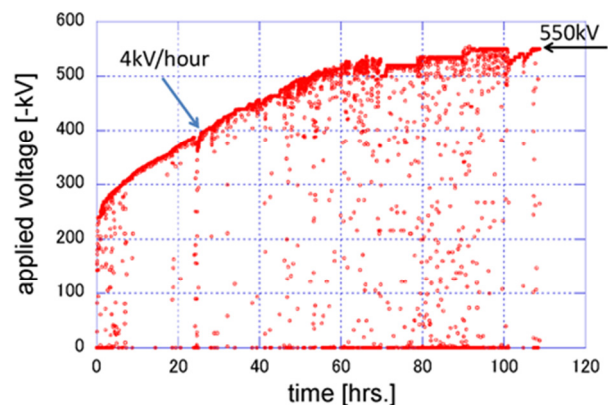


Figure 4: High voltage processing of a segmented insulator with a support electrode at JAEA [21].

Stable operation of the segmented insulator over eight hours was also demonstrated for the prospect of future light source applications, as shown in Figure 5. The top figure shows high voltage versus current as a function of time. The bottom shows radiation and vacuum pressure as a function of time. No indication of discharge or local heating due to dark current was observed. Thus 500 kV was applied between high voltage and ground terminals of the insulator. It is concluded that the segmented insulator with shield electrodes can solve the field emission problem from a support electrode at voltages up to at least 500 kV.

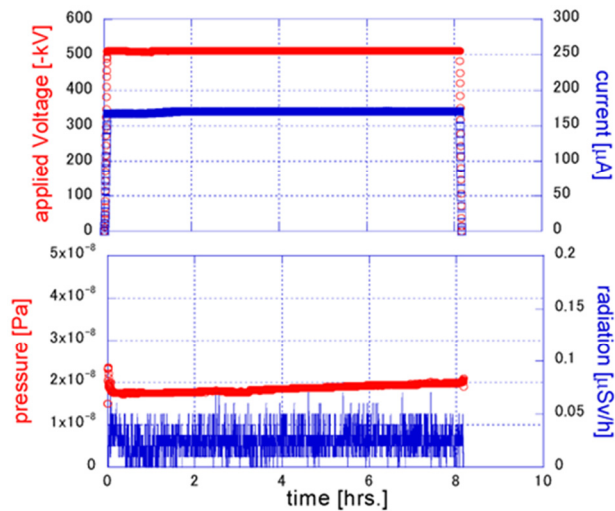


Figure 5: A long-time holding test for eight hours at JAEA [20]. The top figure shows applied voltage (red) and current of HV power supply (blue) as a function of time. The bottom figure shows pressure (red) and radiation (blue).

The next step was to repeat the same HV processing with electrodes and NEG pumps in place for beam generation. The cathode electrode should be designed for its maximum surface electric field to be less than voltage breakdown criteria at 500 kV. The maximum electric field of cathode electrode and field on the cathode center are  $10.3 \text{ MVm}^{-1}$  and  $6.7 \text{ MVm}^{-1}$ , respectively, at JAEA. The gap between cathode and anode electrodes is 100 mm. High voltage processing up to 526 kV was demonstrated in 2011 at JAEA [32].

The conditioning of the support electrode (without the cathode electrode) and the segmented insulator was mostly done manually. At voltages higher than 300 kV and when the HVPS tripped on vacuum or radiation, a few minutes of waiting time allowed the vacuum to recover before ramping up to the voltage set-point with a computer program. It takes another a few minutes to ramp back to the voltage set-point. Then the voltage was increased manually in 0.3 kV steps while monitoring vacuum, radiation, voltage and current. Once the vacuum and radiation exceeded their limit point, the HVPS was shut off by the computer program. The interlock limits were set to  $5 \times 10^{-6} \text{ Pa}$  for vacuum and to  $3 \times 10^{-6} \text{ Sv h}^{-1}$  with radiation monitors placed 50 cm from the vacuum chamber. The average current was limited to  $1 \mu\text{A}$  by the constant current circuit shown in Figure 6. If the average discharge current exceeds  $1 \mu\text{A}$ , the HVPS cannot maintain Constant Voltage mode and the voltage drops quickly. The voltage drop helps to reduce field emission current. Then the voltage recovers gradually as the power supply charges its capacitor back. Finally the operational mode returns to Constant Voltage mode. The time spent at voltage during processing from 250 kV to 550 kV was about 100 hours. Considering the vacuum recovery time it took a total of four weeks. There was no inert gas processing in the conditioning of the JAEA gun.

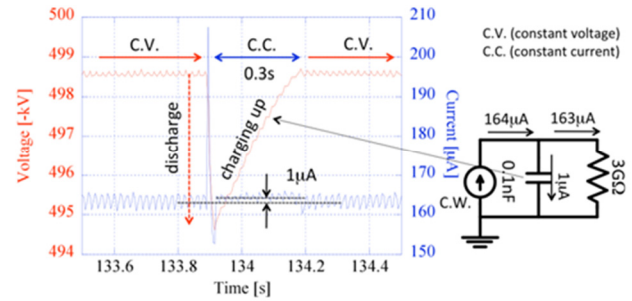


Figure 6: The circuit used in conjunction with the Cockcroft-Walton generator for high voltage processing in the JAEA gun.

When the cathode electrode was mounted to the support electrode (Figure 1) field emission made processing more difficult. Usually the conditioning of electrodes in DC photoemission guns is performed under ultra-high vacuum conditions achieved after thorough vacuum bakeout of the system at 125-250° C. This process nominally renders hydrogen dominated environment in the range of  $6 \times 10^{-8} \text{ Pa}$  to  $6 \times 10^{-9} \text{ Pa}$ . However, high voltage processing can be done without those stringent vacuum conditions. Once it was realized that electron emission was triggered by particulates falling from the NEG cartridges onto the cathode electrode, the gun was vented with dry nitrogen, the electrodes wiped off with lint-free tissue, and then the gun vacuum chamber evacuated without baking to  $3 \times 10^{-9} \text{ Pa}$  with NEG re-activation. High voltage processing continued until it was stopped again by falling NEG particulates. The cleaning process might be repeated, but the gun vacuum chamber was exposed to air for examination of NEG cartridges for source of falling particulates.

### Niobium Electrodes

Niobium is used to make superconducting RF cavities and there are many reports of field-emission free operation at field gradients exceeding  $30 \text{ MVm}^{-1}$ . Although these results were obtained at 2 K and with RF electric fields, it seemed reasonable to evaluate niobium in a DC photocathode gun at room temperature [33]. An appealing feature of niobium is that the cleaning procedures for producing good HV surfaces are well known from the SRF community. The niobium electrode was chemically etched in a mixture of hydrofluoric (49%), nitric (69%) and phosphoric (85%) acid with mixing ratio 1:1:1 at room temperature. This technique is referred to as buffered-chemical polishing (BCP). Besides taking advantage of BCP, other SRF techniques were adopted including high pressure rinsing with ultra-pure de-ionized water and 900°C vacuum degassing [34].

The first application of high voltage on the second inverted gun was disappointing, with field emission detected at voltage  $>140 \text{ kV}$ . By increasing the applied voltage, some field emitters were eliminated (Figure 7

(top), blue data points) but conditioning was limited to 225 kV. Figure 7 (bottom) shows the x-ray radiation measured during HV conditioning. Not surprisingly, photocathode lifetime was poor while delivering beam at 200 kV due to low level field emission which served to degrade the vacuum within the gun.

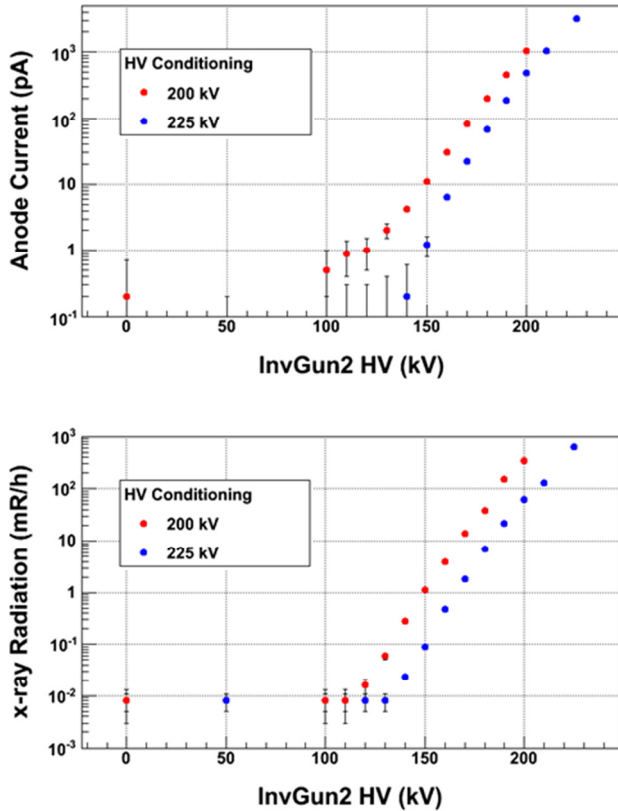


Figure 7: (Top) Field emission measurements during the initial HV conditioning of the second inverted gun. Going to higher voltage served to eliminate some field emitters (blue data points). (Bottom) The x-ray radiation measurements performed during HV conditioning.

The large-grain niobium electrode was removed from the gun and inspected, whereupon the surface finish was deemed too rough. Another BCP treatment was performed resulting in a cumulative removal of about 100  $\mu\text{m}$  of surface material (surface roughness < 0.5  $\mu\text{m}$ ). Upon re-installation of the cathode electrode into the gun and vacuum chamber bake-out, no field emission was detected at voltage up to 225 kV, see Figure 8. Similarly, no x-rays were detected and there was no vacuum activity in the gun chamber.

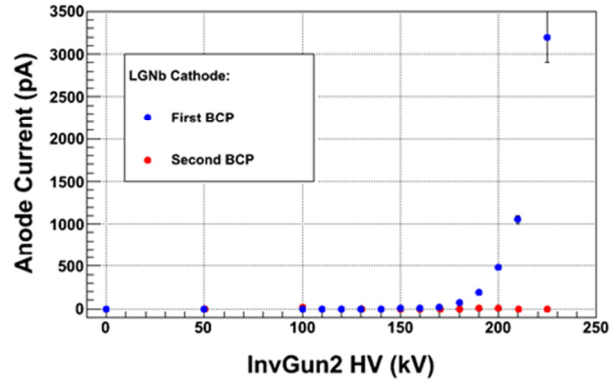


Figure 8: Field emission measurements during HV conditioning. A second BCP treatment successfully eliminated field emission to 225 kV.

## VACUUM TECHNIQUES

*M. Yamamoto*

A high brightness electron gun which utilizes a gallium arsenide (GaAs) photocathode requires an extreme high vacuum (XHV) condition to preserve a negative electron affinity state for a sufficiently long time under high current operation.

The ultimate pressure  $P$  is given by  $P=Q/S$ , where  $Q$  is a total outgassing rate of the system and  $S$  is the effective pumping speed. Therefore, all of the vacuum components in the gun system should have a low outgassing rate, and the pumps should function under XHV. The outgassing rate and the pumping speed of the actual gun vacuum system are important parameters to realize XHV condition.

At KEK, a 500 kV DC-gun was constructed with a segmented insulator as shown in Figure 9. The gun consists of a titanium chamber, a pair of segmented insulators and titanium guard ring electrodes, with surface areas of 2.39  $\text{m}^2$ , 1.26  $\text{m}^2$  and 2.02  $\text{m}^2$ , respectively. The total volume of the system is 0.333  $\text{m}^3$ .

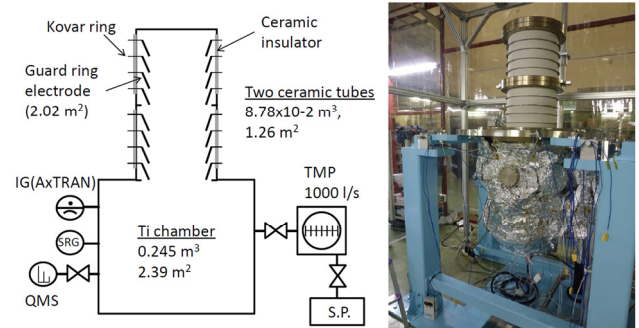


Figure 9: Schematic diagram of a KEK 500 kV DC gun vacuum system and its photograph.

The system was baked  $\sim 200\text{C}$  for 100 hours before the outgassing rate measurement. The total outgassing rate measurement was obtained with the rate-of-rise (RoR) method using a spinning rotor gauge (SRG). The ultimate pressure of the system reached  $7.2 \times 10^{-9}$  Pa (equivalent for nitrogen) after the bake-out process. The total outgassing rate of the system was estimated to be  $1.05 \times 10^{-10}$   $\text{Pa} \cdot \text{m}^3 \cdot \text{s}^{-1}$  equivalent for hydrogen as shown in Figure 10 [35].

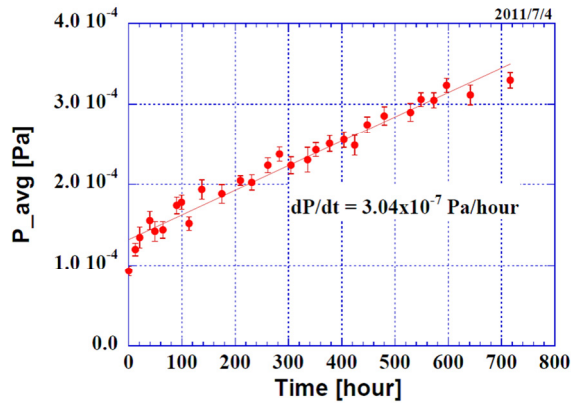


Figure 10: Result of the RoR measurement by the SRG for about 1 month. The value of pressure is equivalent for nitrogen.

At KEK, we demonstrated measurement of pumping speed of a bakeable cryopump, in which the G-M refrigerator is separated spatially from cryopump housing in order to bakeout the pump including cryopanel and adsorbent [36]. Such pumps have been reported to produce XHV conditions, without the usual arrays of NEG pumps. The apparatus is shown in Figure 11.

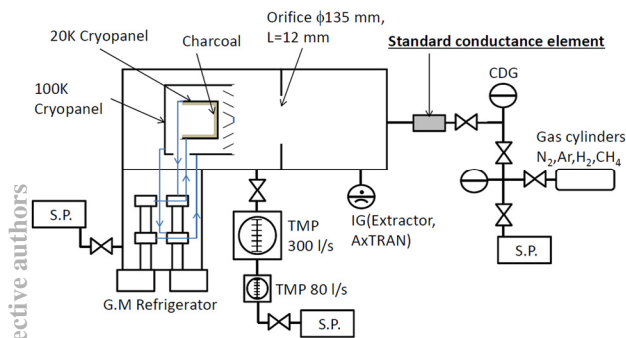


Figure 11: A 20 K bakeable cryopump and a pump speed measurement system with a precise gas flow control system using a standard conductance element.

One of the key issues for measuring pumping speed is to accurately control the gas flow to the test chamber. In this experiment, we use a standard conductance element [37]. The gas flow  $Q$  [ $\text{Pa} \cdot \text{m}^3 \cdot \text{s}^{-1}$ ] through the standard conductance element is estimated as

$$Q [\text{m}^3/\text{s}] = P_f [\text{Pa}] \cdot C [\text{m}^3/\text{s}] \sqrt{\frac{28}{M_a}} \sqrt{\frac{T [\text{K}]}{T_0}}$$

where  $P_f$  is the pressure in the inlet of the element measured by a capacitance diaphragm gauge (CDG),  $M_a$  is the molecular mass of gas,  $T$  is the temperature of the element,  $C$  [ $\text{m}^3/\text{s}$ ] is the experimentally determined conductance of the element for nitrogen at the temperature  $T_0$ . A conductance of  $3.01 \times 10^{-10}$   $\text{Pa} \cdot \text{m}^3 \cdot \text{s}^{-1}$  at the temperature of 300 K was used for the standard element.

The result of the effective pumping speed measurement of the 20 K bakeable cryopump is shown in Figure 12 [34]. The pumping speed was obtained for nitrogen, argon, methane, and hydrogen. The ultimate pressure was limited to  $1 \times 10^{-9}$  Pa by adsorption equilibrium of hydrogen in this experiment.

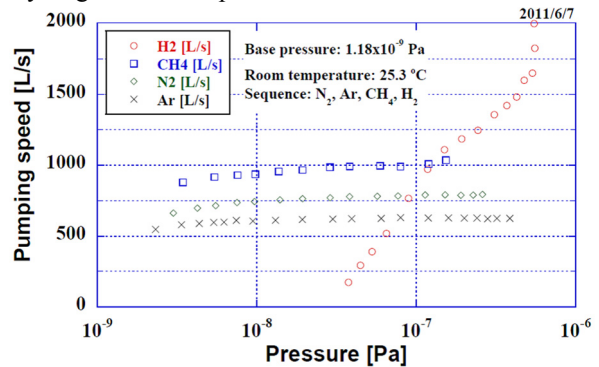


Figure 12: Result of the pumping speed of the 20 K bakeable cryopump for hydrogen, methane, nitrogen and argon.

## LASER SYSTEMS

*Triveni Rao and Bruce Dunham*

The parameters of the laser system driving photoinjectors are determined by the cathode's characteristics as well as those of the electron beam for the intended application, and hence, cover a wide range. Typically, for high current injectors, high QE cathodes irradiated with  $\sim 2$  eV photons are preferred, since laser systems meeting most of the specifications are available commercially. Until recently, most high current injectors relied on diode pumped solid state (DPSS) lasers. Lately, there has been sufficient progress with fiber lasers that they present a viable alternative to the DPSS laser systems. In the following sections, we will discuss the performance characteristics of both these devices.

Both these lasers have the same architecture: i) an oscillator (or an oscillator and modulator combination) that sets the operating wavelength, pulse duration, repetition rate, and timing stability, ii) an amplifier that maintains all the above parameters but increases the energy/pulse of the output beam, and iii) a non-linear medium that converts the  $\sim 1$  eV photons from the amplifier to  $\sim 2$  eV or  $\sim 3$  eV photons. A second modulator can be introduced between the amplifier and the nonlinear medium to accommodate the required pulse structure, while maintaining a constant thermal load on the

oscillator and amplifier, thereby, preserving the stability of laser output.

An example of a DPSS laser is the system for the BNL ERL program. It is designed to deliver up to 5 W at 355 nm, with pulse duration of  $\sim 10$  ps, repetition rate of 9.38 MHz, synchronized to an external 703.5 MHz master clock with a sub-picosecond jitter. A pulse selection system is incorporated to allow the ramp up from a single pulse to a series of micro pulses in a macro pulse with variable repetition rate (up to 10 kHz), and ultimately, to a continuous 10 MHz to facilitate the recovery of electron energy in the linac.

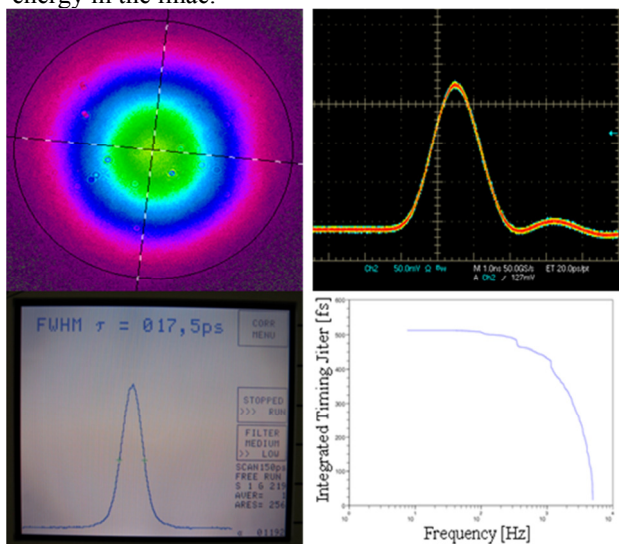


Figure 13: (clockwise from upper left) Transverse profile of the amplified beam; IR energy stability, contrast is better than 1:1800; pulse duration of the IR beam; jitter of the IR beam with respect to the master clock.

The oscillator consists of Nd:Vanadate crystal, a resonant cavity formed by a saturable absorber mirror (SAM) and an output coupler with 12% transmission. The  $4 \times 4 \times 6$  mm<sup>3</sup> laser crystal is end-pumped by an 18 W fiber-coupled diode laser operating at 808 nm. The key feature of the oscillator is its repetition rate, too low for conventional CW mode-locking and too high for cavity dumping. To meet the challenge, a folded cavity with a resonator length of 16 m was custom-designed and built. Such a long cavity makes the laser very sensitive to misalignments compared to conventional  $\sim 1$  m long resonators. To isolate the oscillator from mechanical- and thermal-instabilities, the oscillator is built on a monolithic metal-block and is sealed off from the rest of the system. The SAM is mounted on a stepper motor-driven translational stage with 25 mm travel range to accommodate slow drifts in the cavity length and the coarse tunability of the pulse's repetition rate. Another smaller mirror that is a part of the resonant cavity is mounted on a piezo-driven stage with 9  $\mu$ m travel range to compensate for fast changes in the cavity length and to preserve synchronization.

The double-pass amplifier consists of a vanadate crystal pumped by a 100 W diode laser operating at 888 nm. The weaker absorption at this wavelength reduces thermal problems, allowing a much higher pump power. The unabsorbed pump power in the first pass is reflected back into the crystal. A Faraday rotator changes the seed beam's polarization from vertical to horizontal after its second pass in the amplifier. The thin film polarizer and the Faraday rotator together inject the seed beam into, and extract it out of the amplifier. The entire pulse train from the oscillator is amplified to eliminate the time-dependent changes in the thermal load induced by the seed- and amplified-pulses. With 100 W pump power,  $>20$  W amplified power at 1064 nm  $\mu$ m was delivered from the amplifier. Figure 13 displays some performance characteristics of the amplified beam.

The pulse selector changes the repetition rate during the ramp-up process for the ERL and also alters its average current without changing the bunch charge. A BBO crystal is used as a Pockels cell, and, the pulses are picked by the polarizing beam-splitter cube (PBS) when the voltage is applied to the crystal, rather than when it is turned off. The BBO can handle the constant high voltage and can be oriented for the best contrast. The high voltage is triggered externally to deliver pulses from single shot to a micro pulse-macro pulse configuration with variable number of micro pulses within a macro pulse, and macro pulse repetition rate variable up to 10 kHz. The entire 9.38 MHz train also can be delivered to the cathode. Some possible configurations are illustrated in Figure 14.

The fundamental 1064 nm radiation is converted into 532 nm and 355 nm by a harmonic crystal for each conversion. The second harmonic crystal is a non-critically phase-matched LBO crystal maintained at 150 C. A vertically polarized beam at 1064 nm, focused to a beam waist of  $\sim 300$   $\mu$ m, is converted, with 50% efficiency, to horizontally polarized, 532 nm radiation.

The third harmonic crystal is a non-critically phase-matched LBO crystal maintained at 40 C. The vertically polarized 1064 nm and horizontally polarized 532 nm radiation, focused down to a beam waist of 300  $\mu$ m, deliver vertically polarized 355 nm beam with power levels of  $\sim 5$  W. Since the spot size in the crystal is very small and the average- and peak-powers are high, there is a very high probability for surface damage and UV-induced surface degradation. The UV module is purged constantly with hydrocarbon-free air to increase the lifespan of the optical components and coatings. The pointing stability of the beam was measured to be  $\sim 3$   $\mu$ rad over 2 hours, well within the range required for the application. The walk-off in the THG crystal causes the appearance of a halo in the transverse profile of the laser beam that must be filtered before it irradiates the cathode.

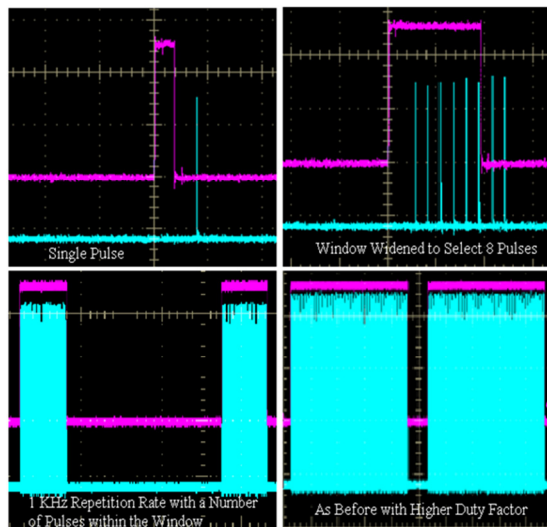


Figure 14: Different configurations of pulses from the pulse picker: Single micro pulse, multiple micro pulses, 1 KHz macro pulse with varying number of micro pulses within the macro pulse envelop. Magenta lines indicate the shape of the high voltage pulse.

The temporal profile of the 532 nm beam is shaped to nearly flat top profile using a stack of three birefringent crystals with lengths of 6, 12 and 24 mm. The conversion of spatial profile to a flat top is accomplished with a commercial shaper. The combined beam has been imaged onto the cathode located at  $\sim 9$  m from the laser with minimal modification of the profile. The spatial and temporal profiles at different locations from the laser, along with long/short term stability of the system are shown in Figure 15 [38].

Another example laser system for an ERL injector is the fiber laser at Cornell University. The parameters are quite different than the Brookhaven laser described above. For this injector, the operating frequency is 1300 MHz, the same as the RF system, as it is a true CW machine with each RF bucket filled with electrons. The laser must provide enough power to generate 77 pC per bunch at 1300 MHz, or 100 mA average power. For the worst case of a 1% QE cathode,  $\sim 20$  Watts at 520 nm delivered to the cathode is required. A pulse width of 1-2 ps FWHM is desired, which is then used to make a flat-top pulse in time with a series of birefringent crystals. A jitter of  $< 1$  ps is needed for stable injector operations.

A commercial optical clock (Pritel, Inc) is used as an oscillator to produce 8 ps rms chirped pulses. The output is synchronized to the RF master clock. The power is boosted in two preamplifier sections and one main amplifier, and then de-chirped to make the desired pulse length (Figure 16). The maximum power obtained is 110 Watts IR after de-chirping (with 220 Watts of pump power), and 65 Watts at 520 nm after passing through a second-harmonic generation crystal. The details of this laser are described in [39].

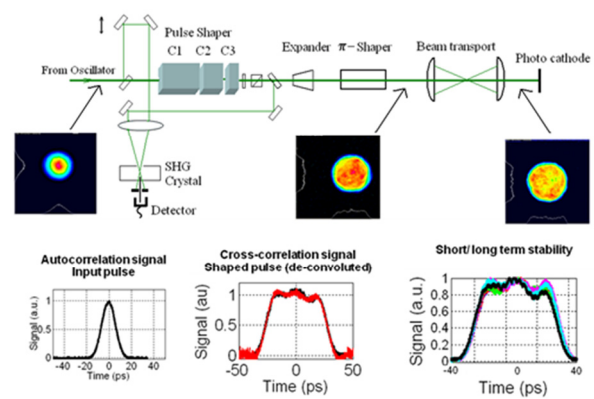


Figure 15: Spatial- and temporal-profile of the laser beam as it propagates along the beam transport. Left: Output of the laser; Middle: Spatially shaped by beam shaper and temporally shaped by beam stacker near the laser; Right: Shaped beam after relay imaging to the cathode location, 9 m away from the laser.

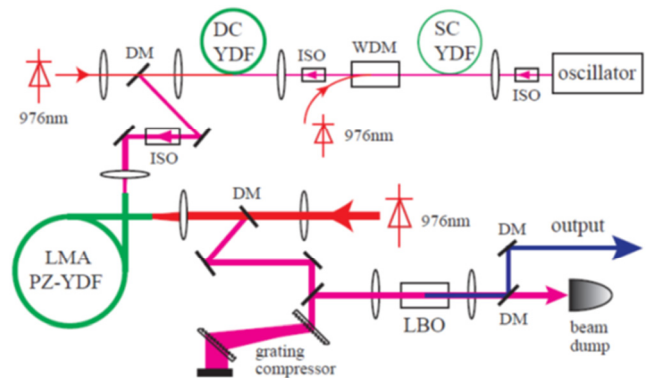


Figure 16: Schematic of the experimental setup: LMA, large mode area; PZ-YDF, single-polarization Yb-doped fiber; WDM, wavelength division multiplexer; SC, single-clad; DC, double-clad; ISO, optical isolator; DM, dichroic mirror.

## OPERATIONAL ISSUES

### Bruce Dunham

As more and more guns and injectors come on-line, operational issues are increasingly important to consider. This is an indication that intermediate bunch charge, high average power injectors comprised of DC photoemission guns coupled to RF boosters are becoming an accepted solution for many accelerators. In this section, a number of the operational issues encountered during machine commissioning at various labs will be discussed.

Beam halo in an injector is typically produced by different mechanisms than in the main accelerator. There are a number of sources of halo in an injector: field emission from HV electrodes; scattered light from the laser hitting the cathode outside the desired area; light from the main laser pulses (extinction ratio); and x-

rays/UV or visible light reaching the cathode from many different sources.

To reduce the effects of stray light producing electrons outside the desired cathode area, most groups now use techniques to keep the photo-emissive area as small as possible [40] (see Figure 17). This will definitely reduce halo due to stray light, but will also reduce the active area available for producing a beam after the previously used area decays.

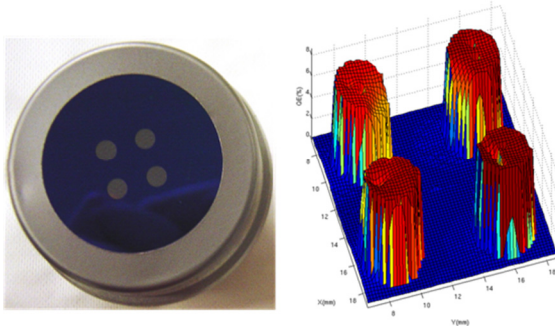


Figure 17: (left) A GaAs cathode is anodized over its entire surface to prevent emission (blue color), then stripped away to expose the clean surface (4 small, gray circles). The right picture shows a QE map of the cathode after use. For best results regarding halo, only one spot would be stripped clean on the left photo.

If a vacuum mirror is used to deflect the laser beam onto the cathode, the quality of the mirror is of critical importance. A mirror surface roughness of  $< 2$  nm-rms is required to keep the fraction of scattered light below  $10^{-5}$  to  $10^{-6}$ . It is not advisable to use dielectric mirrors as they can charge up from any scattered electrons that hit them, but one can purchase commercial mirrors on metal substrates with this surface finish (or better), or use silicon as a substrate.

For the injectors needed for ERLs and FELs, finding diagnostics to handle the huge dynamic range is a challenge. For example, at the high end we care about 100 mA currents, and at the low end maybe as little as 100 pA (for halo and beam loss), which is a dynamic range of  $10^9$ ! Some possibilities were discussed in working group 4 of this conference. One simple device is to use a fluorescent view screen with a hole in it: the main beam passes through the central hole while the halo is intercepted on the view screen (see Figure 18).

Feedback systems for high average power machines are important to reduce any transients generated by the beam, especially in the RF cavities. At the Cornell injector, we initially had difficulty exceeding 10 mA average current, as the RF cavities would trip off for currents great than this. This was caused by fast current transients that the RF controls could not correct for. The problem was traced to position jitter in the laser: as the laser passed through a small pinhole for transverse shaping, the position jitter was translated into power fluctuations after the pinhole. A digital fast-feedback system was used to correct for the fluctuations [41] (see Figure 19). The

necessary hooks for feedback should be included at an early stage in the injector design.

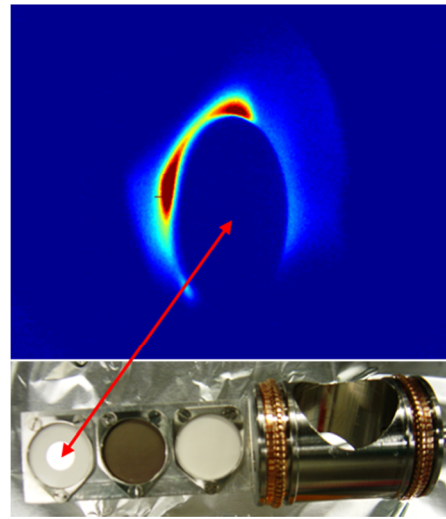


Figure 18: The lower photo shows a multiple view screen mechanism, where the left-most fluorescent screen has a 10 mm clear hole through it. The top picture shows halo hitting the edges of the view screen while the main beam passes un-impeded through the center.

These are a few examples of operational issues to consider during high average current operations.

### FUTURE NEEDS

We discussed various topics that need further research before the next ERL workshop, and list them here.

- GaN-like photocathodes, which may be more robust against vacuum excursions.
- Laser pulse pickers for GHz rep rate lasers, and how to ramp up the beam current for these systems.
- Pockels cells that can handle high average powers ( $>100$  Watts IR)
- Suppliers of optical coatings with high damage thresholds
- Continued work on pushing for higher gun voltages, inverted, segmented or otherwise
- Investigate using GaN diodes for blue light, where cathode QE's are higher
- Continued investigation of high voltage processing using noble gases
- Air core fibers for beam transport and for longitudinal shaping
- Methods for cooling cathodes during high power operation
- Recipe standardization for alkali cathodes
- Improved sources for alkali deposition
- Better diagnostics for halo and beam loss
- Wide dynamic range BPMs and CCD cameras
- Vacuum gauges with a fast response time ( $< 1$ ms)
- Easy to use fast DAQ and transient detection
- Fast, high dynamic range photodiodes to look between laser pulses for background light.

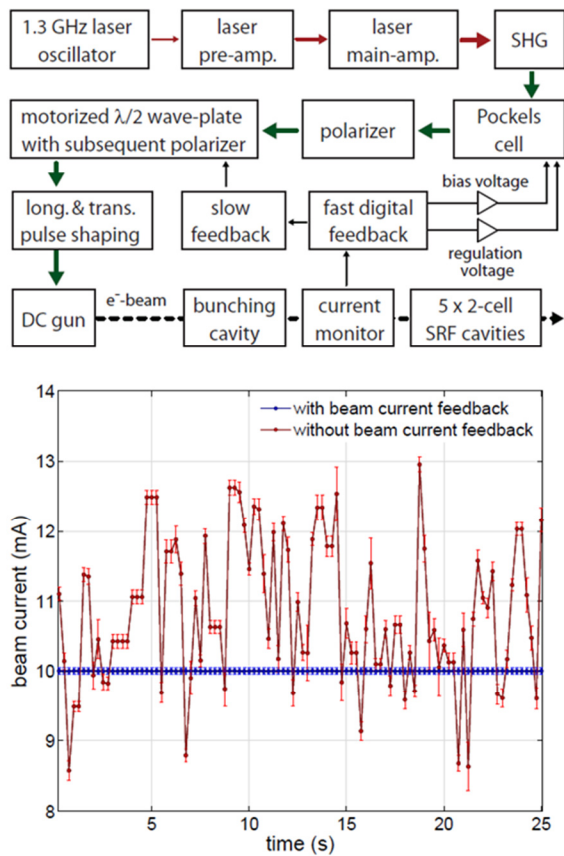


Figure 19: The top shows a block diagram of the digital fast feedback system. The bottom shows the beam current with and without feedback.

## CONCLUSIONS

DC photocathode guns have been in existence for several decades now, so it is exciting to see continued improvements over the past several years. Many in the accelerator community do not see DC guns as being very sexy, but these systems are now producing beam with parameters that were thought to be impossible only a few years ago. Thus, they are becoming the electron source of choice for intermediate range bunch charge machines with high average power and high brightness requirements.

## ACKNOWLEDGMENTS

The authors would like to thank the organizing committee and all of the contributors to the working group 1 presentation and discussion sessions.

Financial support for the JLab FEL electron gun was provided by the Office of Naval Research, the Army Night Vision Laboratory, the Air Force Research Laboratory, the Joint Technology Office, the Commonwealth of Virginia, and by the U.S. DOE Basic Energy Sciences under Contract No. DE-AC05-06OR23177. CEBAF work supported by the U.S. DOE under contract No. DE-AC05-84ER40150.

The CEBAF work is sponsored by Jefferson Science Associates under U.S. DOE Contract No. DEAC05-

06OR23177 and with funding from the DOE Office of High Energy Physics and the Americas Region ILC R&D program.

The JAEA work is supported by MEXT Quantum Beam Technology Program.

The Cornell work is sponsored by the National Science Foundation, Division of Materials Research grant number DMR-0807731.

Work at BNL is supported by DoE under Contract No. DE-AC02-98CH10886 with the U.S. DOE.

## REFERENCES

- [1] N. Nishimori, I. Bazarov, B. Dunham, J. Grames, C. Hernandez-Garcia, L. Jones, B. Militsyn, M. Poelker, K. Surlis-Law, and M. Yamamoto, "ERL09 WG1 Summary: DC Gun Technological Challenges," Proceedings of ERL09, Ithaca, NY, pp. 6-23 (2009).
- [2] I. Bazarov, L. Cultrera, A. Bartnik, B. Dunham, S. Karkare, Y. Li, X. Liu, J. Maxson and W. Roussel, "Thermal emittance measurements of a cesium potassium antimonide photocathode," Appl. Phys. Lett. **98**, 224101 (2011).
- [3] L. Cultrera, I. Bazarov, A. Bartnik, B. Dunham, S. Karkare, R. Merluzzi and M. Nichols, "Thermal emittance and response time of a cesium antimonide photocathode," Appl. Phys. Lett. **99**, 152110 (2011).
- [4] D.H. Dowell, I. Bazarov, B. Dunham, K. Harkay, C. Hernandez-Garcia, R. Legg, H. Padmore, T. Rao, J. Smedley and W. Wan, "Cathode R&D for future light sources," Nucl. Instr. Meth. A **622**, 685-697 (2010).
- [5] I. Bazarov, et al., "Multivariate optimization of a High Brightness DC Gun Photoinjector," Phys. Rev. ST Accel. Beams **8**, 034202 (2005).
- [6] personal communication, B. Dunham.
- [7] C. Hernandez-Garcia, T. Siggins, S. Benson, D. Bullard, H. F. Dylla, K. Jordan, C. Murray, G. R. Neil, M. Shinn, and R. Walker, "A High Average Current DC GaAs Photocathode Gun for ERLs and FELs", PAC05, Knoxville, Tennessee, 2005, p. 3117.
- [8] I. Bazarov, B. Dunham, Y. Li, X. Liu, D. Ouzounov, C. Sinclair, F. Hannon and T. Miyajima, "Thermal emittance and response time measurements of negative electron affinity photocathodes," J. Appl. Phys. **103**, 054901 (2008).
- [9] B. Dunham, L. Cardman and C. Sinclair, Proceedings of the 1995 Particle Accelerator Conference, Dallas, TX, pg. 1030 (1995).
- [10] D. H. Dowell et al., Appl. Phys. Lett. **63**, 2035 (1993).
- [11] T. Vecchione, I. Ben-Zvi, D. Dowell, J. Feng, T. Rao, J. Smedley, W. Wan, H. Padmore, "A low emittance and high efficiency visible light photocathode for high brightness accelerator-based X-ray light sources," Appl. Phys. Lett. **99**, 034103 (2011).
- [12] J. Grames, R. Suleiman, P. Adderley, J. Clark, J. Hansknecht, D. Machie, M. Poelker, and M. Stutzman, "Charge and fluence measurements of a dc

- high voltage GaAs photogun at high average current,” *Phys. Rev. ST Accel. Beams* **14**, 043501 (2011).
- [13] L. Cultrera, J. Maxson, I. Bazarov, S. Belomestnykh, J. Dobbins, B. Dunham, S. Karkare, et al., “Photocathode behaviour during high current running in the Cornell energy recovery linac photoinjector,” *Phys. Rev. ST Accel. Beams* **14**, 120101 (2011).
- [14] I. Bazarov, B. Dunham, X. Liu, M. Virgo, A. Dabiran, F. Hannon and H. Sayed, “Thermal emittance and response time measurements of a GaN photocathode,” *J. Appl. Phys.* **105**, 083715 (2009).
- [15] Charles K. Sinclair, “DC photoemission electron guns as ERL sources,” *Nucl. Inst. and Meth. A* **557** (2006) 69.
- [16] C.W. de Jager, V. Y. Korchagin, B.L. Militsyn, V.N. Osipov, N.H. Papadakis, S.G. Popov, M.J.J. van den Putte, Yu. M. Shatunov, Yu. F. Tokarev, “The Photocathode Gun of The Polarized Electron Source at NIKHEF,” *The Seventh International Workshop on Polarized Gas Targets and Polarized Beams*, AIP Conf. Proc. 421 (AIP, New York, 1998), 483.
- [17] Tsutomu Nakanishi, “Polarized electron source using NEA-GaAs photocathode”, *Proc. of LINAC2002*, Gyeongju, Korea, 811.
- [18] N. Nishimori, R. Nagai, R. Hajima, T. Shizuma, E.J. Minehara, “A Thermionic Electron Gun System for the JAERI Superconducting FEL,” *Proc. of EPAC00*, Vienna, Austria, 2000, 1672.
- [19] N. Nishimori, R. Nagai, H. Iijima, Y. Honda, T. Muto, M. Kuriki, M. Yamamoto, S. Okumi, T. Nakanishi, and R. Hajima, “Development of an electron gun for an ERL based light source in Japan,” *Proceedings of the 18th International Symposium on High Energy Spin Physics (SPIN2008)*, (Ref. [6]), 1094.
- [20] P.G. Slade, “The vacuum interrupter: theory, design, and application,” CRC Press, 2008.
- [21] R. Nagai, R. Hajima, N. Nishimori, T. Muto, M. Yamamoto, Y. Honda, T. Miyajima, H. Iijima, M. Kuriki, M. Kuwahara, S. Okumi, and T. Nakanishi, “High-voltage testing of a 500-kV dc photocathode electron gun,” *Rev. Sci. Instrum.* **81**, 033304 (2010).
- [22] B. Dunham, private communication.
- [23] M. Yamamoto, private communication.
- [24] Jiuqing Wang, private communication.
- [25] P. Massmann, H.P.L. de Esch, R.S. Hemsworth, T. Inoue, and L. Svensson, “The Cadarache 1 MV porcelain SINGAP bushing,” *Fusion Eng. Des.* **56-57**, (2001) 539-544.
- [26] L. Svensson, D. Boilson, H.P.L. de Esch, R.S. Hemsworth, A. Krylov, and P. Massmann, “Latest results from the Cadarache 1 MV SINGAP experiment,” *Fusion Eng. Des.* **66-68** (2003) 627-631.
- [27] A. Masiello, “Adaption of the 1MV bushing to the SINGAP concept for the ITER NB injector test bed,” *Nucl. Fusion* **46** (2006) S340-S351.
- [28] P. Adderley, J. Clark, J. Grames et al., *Phys. Rev. ST Accel Beams* **13**, 010101 (2010).
- [29] P. A. Adderley, J. Clark, J. Grames, et al., “CEBAF 200 kV Inverted Electron Gun,” *Proceedings of the 2011 Particle Accelerator Conference*, New York, NY. WEBODS3.
- [30] B. M. Dunham and K. W. Smolenski, “Voltage DC photoemission electron gun at Cornell University,” *Power Modulator and High Voltage Conference*, 2010 IEEE International, Atlanta GA, 23-27 May 2010.
- [31] C. Hernandez-Garcia, S. Benson, G. Biallas, D. Bullard, P. Evtushenko, K. Jordan, M. Klopff, D. Sexton, C. Tennant, R. Walker, and G. Williams, “DC High Voltage Conditioning of Photoemission Guns at Jefferson Lab FEL,” *Proceedings of the 18th International Symposium on High Energy Spin Physics (SPIN08)*, edited by D. Crabb, D. B. Day, S. Liuti, X. Zheng, M. Poelker and Y. Prok. 2009 AIP, p. 1071.
- [32] N. Nishimori, R. Nagai, H. Iijima, Y. Honda, T. Muto, M. Kuriki, M. Yamamoto, S. Okumi, T. Nakanishi, and R. Hajima, “Status of 500-kV DC gun at JAEA,” presented at ERL11, KEK, Japan, 2011.
- [33] M. BastaniNejad, P. Adderley, J. Clark, et al., “Field Emission measurements from Niobium Electrodes,” *Proceedings of the 2011 Particle Accelerator Conference*, New York, NY. WEB287.
- [34] P. Kneisel, “Cavity Preparation and Assembly Techniques and Impact on Q, Realistic Q-factors in a Module, Review of Modules,” *Proceedings of the ERL05 Workshop*.
- [35] M. Yamamoto et al., *Proc. International Particle Accelerator Conference (IPAC2011)*, San Sebastian, Spain, p.979.
- [36] H. Yamakawa, *Vacuum* **44**, (1993) 675.
- [37] H. Yoshida et al., “New leak element using sintered stainless steel filter for in-situ calibration of ionization gauges and quadrupole mass spectrometers,” *Vacuum* (2011), doi:10.1016/j.vacuum.2011.02.013 [in press].
- [38] A.K. Sharma, T. Tsang, and T. Rao, “Theoretical and Experimental Study of Passive Spatio-Temporal Shaping of Picosecond Laser Pulses,” *Phys. Rev. Special Topics* **12**, 033501 (2009).
- [39] Z. Zhao, in press.
- [40] C.K. Sinclair, P. Adderley, B. Dunham, J. Hansknecht, P. Hartmann, M. Poelker, J. Price, P. Rutt, W. Schneider and M. Steigerwald, “Development of a high average current polarized electron source with long cathode operational lifetime,” *Phys. Rev. ST Accel. Beams* **10**, 023501 (2007).
- [41] F. Loehl and P. Szypryt, “Active Beam Current Stabilization in the Cornell ERL Prototype Injector,” *Proceedings of the International Particle Accelerator Conference 2011*, San Sebastian, Spain, pp. 523-525.

## ERL2011 SUMMARY OF WORKING GROUP 1: PROGRESS WITH RF INJECTORS

T. Rao<sup>1</sup>, A. Arnold<sup>2</sup>, S. Belomestnykh<sup>1</sup>, D. Nguyen<sup>3</sup>, T. Quast<sup>4</sup>

<sup>1</sup>Brookhaven National Laboratory, Upton, NY 11973 USA

<sup>2</sup>Helmholtz-Zentrum Dresden-Rossendorf, Germany

<sup>3</sup>Los Alamos National Laboratory, Los Alamos, NM 87545 USA

<sup>4</sup>Helmholtz-Zentrum Berlin, Germany

### Abstract

This paper summarizes the progress made in the past two years with RF injectors as electron sources for high average power Energy Recovery Linacs (ERL).

### INTRODUCTION

Many ERL applications call for lowest emittance and highest brightness from electron injectors. The inherent capability of RF injectors to support high cathode field gradients makes them ideally suited for high bunch charge, low emittance applications. However, the price to be paid for the high gradient and high average current is the associated high thermal load and its management. Two different approaches have been adopted for thermal management: use of superconducting cavities that have inherently lower thermal load versus incorporation of elaborate cooling channels in normal conducting cavities. In the last two years there has been considerable progress towards the development of normal conducting RF (NCRF) and superconducting RF (SRF) guns to meet these challenges. Two additional major considerations in designing the gun are the RF power coupling and integration of the cathode in the gun. In this paper, we will discuss the latter topics and cover the latest developments with the NCRF and SRF guns.

### FUNDAMENTAL POWER COUPLERS FOR SRF GUNS

SRF electron guns based on elliptical cavities use traditional way of coupling RF power to SRF cavities via coaxial antennae connected to beam pipe ports. At lower RF power a single fundamental power coupler (FPC) is used [1, 2], while at high power two FPCs, symmetrically placed, are used to lower power load per coupler and eliminate transverse kick for beam on axis [3]. The latter FPCs (Fig. 1) were successfully tested in standing wave regime with full reflection up to 250 kW in pulsed mode and 125 kW in CW mode [4].

An alternative to the elliptical cavity design is the coaxial quarter-wave resonator (QWR) design. It has an advantage of smaller dimensions compared to elliptical cavities for the same frequency, or given the same size, the quarter-wave design operates at a lower frequency. QWR guns designed so far will operate with low average beam currents and hence low RF power. Due to the gun geometry and low frequency, the FPC design of choice is based on a coaxial beam tube at the beam exit [3, 5-6].

These couplers (Fig. 2) are axially symmetric and, if properly designed, should cause even less beam disturbance than two antenna-type couplers.

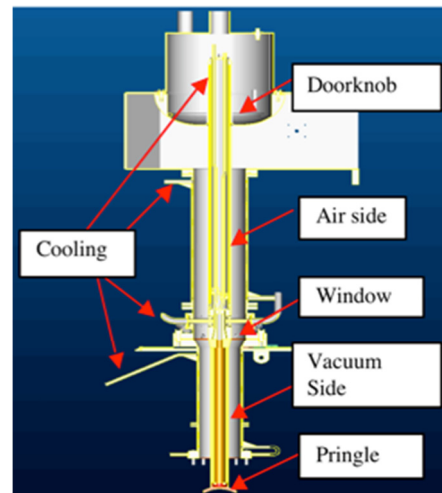


Figure 1: Coaxial antenna-type FPC for  $\frac{1}{2}$ -cell elliptical cavity SRF gun at BNL [4].

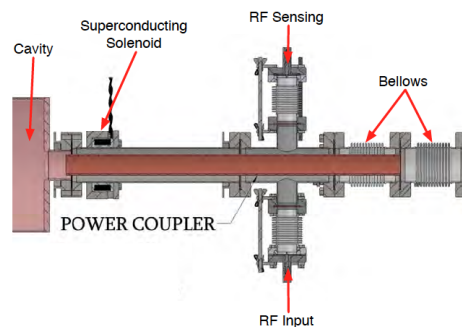


Figure 2: Coaxial beam line FPC for the quarter-wave resonator SRF gun at NPS [7].

### PHOTOCATHODE SELECTION AND INTEGRATION

The photocathodes for the high current operation has to meet a number of special requirements: they need to have quantum efficiency (QE) in the range of a few percent at a wavelength where high power lasers are readily available. In addition, they must be robust, prompt in electron emission, should have very high surface charge limit and insensitive to vacuum incursion that may occur in an

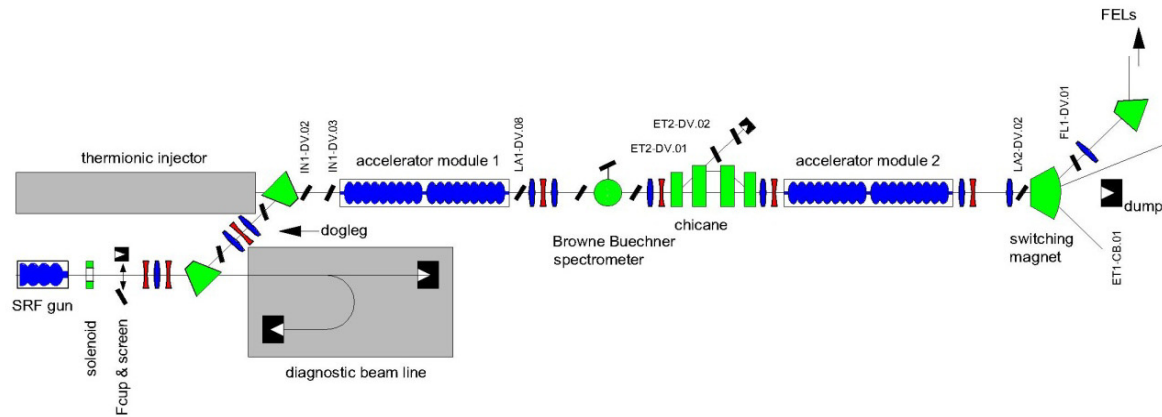


Figure 3: Beamline layout of the SRF gun, dogleg section, and ELBE linac.

operating gun environment. In a number of gun designs, it is preferable to characterize the gun at low average currents prior to operating it in its full capability. Different commissioning stages can then be decoupled from each other and the subsystems can be tested independently with minimal complications. As evidenced in the *BERLinPro* approach below, this characterization can be accomplished with a metal photocathode, which can later be replaced by a high QE one.

Incorporating the photocathode into the RF gun is still an evolving field, especially when a normal conducting cathode is used in a SRF injector. For average currents  $\ll 1$  mA, metal photocathodes are still a viable option. In such a case, a cathode (for example, a superconducting cathode such as lead) can be deposited onto the back wall of the cavity. For higher average currents, high QE cathodes need to be used. If the cathode life time is not long enough, care must be taken in the engineering of the cathode insertion so that the cavity stays superconducting while the spent cathode is being exchanged for a fresh one. One of the designs is described in [8]. In this, a batch of cathodes is prepared ex-situ in an ultra-high vacuum (UHV) chamber and is transported to an exchange chamber which is attached to the cryostat via an UHV transfer chamber. A cathode is then moved from the exchange chamber to the gun cavity by a transfer rod. An additional concern is the effective transport of the emitted electrons from the cathode to the booster cavity. Matching the beam radius to the booster cavity's gradient and exit energy must be done appropriately to minimize emittance growth.

Similar load-lock approach has been applied to NCRF injectors also, without the added complication of maintaining the cavity at superconducting temperatures.

## STATUS OF INJECTORS

### *Rossendorf SRF Gun: Operational Experience*

The SRF gun for the superconducting linear accelerator ELBE was developed within a collaboration of the German institutes BESSY/HZB, DESY, MBI and HZDR and put into operation in 2007. Details of the design have been published in [8]. During the first two years of

operation a lot of experience was gained using a separate diagnostic beamline [9]. Most of the results have been published in the summary paper of working group 1 of the 2009 ERL workshop [10].

Since 2010, the SRF gun is connected to the ELBE accelerator. The corresponding beam line layout is presented in Fig. 3. It consists of a solenoid for emittance compensation, followed by a screen station, a movable Faraday cup and a quadrupole triplet. The connecting dogleg is arranged about 1.5 m in front of the SRF gun exit using a  $45^\circ$  dipole magnet, which deflects the beam towards the ELBE linac, followed by a quadrupole triplet and ends with a second  $45^\circ$  magnet in front of the first acceleration module of ELBE. A photograph of the installation is shown in Fig. 4. Although the realized beam injection scheme with the dispersive part in the dogleg is disadvantageous since the gun produces high correlated energy spread, it can be compensated in the first acceleration module after the dogleg.



Figure 4: Photograph of the SRF gun with the beamline and dogleg.

The standard gun operation is continuous wave (CW). But to reduce the heat load and operate at higher gradient, the input RF is temporarily pulsed with repetition rate of 1 to 10 Hz, and the pulse length adjustable between 5 and 20 ms. Typical fields and gradients for both operations are listed in Table 1. In this mode the gun delivers an electron beam with the kinetic energy of 3 MeV,

accelerated by the peak electric field of 16.5 MV/m. Due to the lower field in the half-cell, the retracted photo cathode and the early launch phase with respect to the RF crest value ( $90^\circ$ ), the field at electron bunch emission is rather low (see Table 1).

In both CW and pulsed cases, a bias voltage of -5 kV is usually applied to the cathode. Although defocusing, this additional voltage increases the field at the cathode and improves slightly the beam quality.

Up to now, the maximum bunch charge injected and accelerated in ELBE is 120 pC, with a pulse repetition rate of 50 kHz (6  $\mu$ A). Energy spread of the beam has been measured in the ELBE beam line using Brown Buechner spectrometer. For CW operation with 6 MV/m accelerating gradient and 10 pC bunch charge, the energy spread is the lowest,  $\sim 20$  keV at a launch phase between  $0^\circ$  and  $10^\circ$ , as shown in Fig. 5. The longitudinal phase space ellipse has been measured in CW and pulsed mode with beam energies of 3.0, 3.5, 4.0 MeV and bunch charges between 10 and 100 pC. More details of the method are described elsewhere [11, 12]. The electron bunch length has been measured as a function of the

Table 1: Typical Parameters of the HZDR SRF Gun for CW and Pulsed Mode

Gun operation mode	CW	Pulsed RF
Accelerating gradient	6 MV/m	8 MV/m
Electron kinetic energy	3 MeV	4 MeV
Peak field on axis	16.5 MV/m	21.5 MV/m
Peak field at the cathode (2.5 mm retracted)	6.5 MV/m	8.4 MV/m
Cathode field at launch phase ( $10^\circ$ )	1.1 MV/m	1.5 MV/m
Cathode field at $10^\circ$ and -5 kV bias	2.2 MV/m	2.6 MV/m

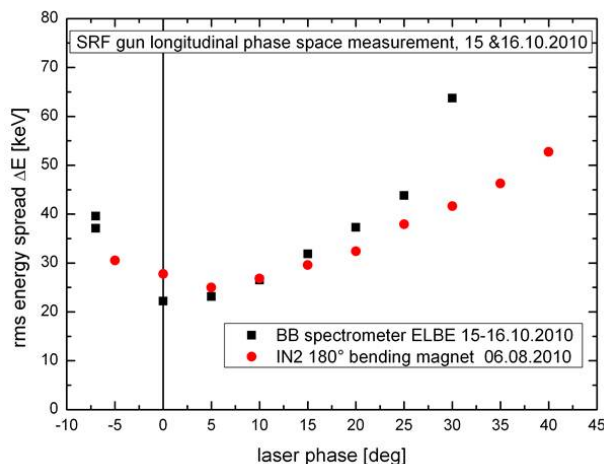


Figure 5: Energy spread measurements for 3 MeV and a bunch charge of 10 pC, using the Brown Buechner spectrometer in ELBE and the  $180^\circ$  bending magnet in the diagnostics beamline.

launch phase for 4 MeV beam energy and 10, 50 and 100 pC bunch charges. For optimum launch phase, the electron bunch lengths were approximately one half of the laser pulse duration of 6 ps.

### Cavity Performance

The  $Q$  of the cavity was measured in vertical tests as well as in the beam line, with and without the cathode inserted in the cavity. Although the intrinsic quality factor of  $Q_0 \approx 3 \cdot 10^9$  in the beam line is ten times lower than that in all vertical tests, the RF performance of the cavity did not change with the insertion of the cathode. It is assumed that contamination during clean room assembly is the most likely reason for the performance degradation between vertical tests and in the beam line.

Using the frequency shift during cool down, the coefficient of thermal expansion and the total change of the cavity length of  $\alpha_{20} = +6.8 \cdot 10^{-6} \text{ K}^{-1}$  and  $\Delta l/l = -0.155\%$  were established. The field distribution at a cryogenic temperature was calculated using algorithm published in [13] and found to be (-62% / 99.4% / -97.5% / 100%) starting in the half-cell, well within design parameters. The static helium and liquid nitrogen heat loads were measured to be  $\approx 7$  W and  $\approx 32$  W respectively, both within the specifications.

The frequency sensitivity with respect to helium pressure fluctuations was found to be  $\sim 150$  Hz/mbar, which is five times the value known for TESLA cavities. Nevertheless, this is not critical for operation due to the good helium pressure stability of  $\sim 0.1$  mbar and cavity bandwidth of  $\sim 160$  Hz. Since the Lorentz detuning was measured to be three times larger than known from TESLA cells due to the weak half-cell, an additional stiffener is used in the upgrade cavities [14].

Another important property of the cavity is its frequency detuning due to mechanical vibrations, known as microphonics. There are three main contributors: the helium refrigerator, the membrane pumps and the first mechanical cavity eigenmode. The residual phase error of  $\sigma_\phi = 0.05^\circ$  is more than sufficient for ELBE operation and does not depend on the gradient. The frequency error is calculated to be  $\sigma_f = -BW/2 \cdot \tan(K_p \cdot \sigma_\phi) \approx 6$  Hz, which is typical for TESLA cavities operated at ELBE. The typical closed loop gain and bandwidth during operation are  $K_p = 100$  and  $BW = 150$  Hz, respectively.

Finally, the cavity tuners have been characterized. Because of different mechanical properties, there is one tuner for the half-cell and another one for the TESLA cells. The tuner for the half cell has an excellent resolution of 0.3 Hz/step combined with a negligible hysteresis and a tuning range of  $\pm 78$  Hz. The second tuner is slightly worse but, because of its higher tuning range of  $\pm 225$  kHz, still good enough for rough cavity tuning.

### Photocathodes

Since 2005 the photocathode laboratory has been in operation at HZDR. The main goal is to prepare  $\text{Cs}_2\text{Te}$  photocathodes for the SRF gun. At the same time activities are directed towards new photocathode

materials with high QE for high current electron sources. A vacuum transport system with UHV is used to move the cathodes from the preparation lab to accelerator hall. Up to now, 31 Cs<sub>2</sub>Te photocathodes have been deposited and eight of them have been used in the SRF gun. The quantum efficiency of 1% and life time of months can be maintained during the gun operation.

Based on simulations, multipacting (MP) is expected in the gap between the cathode hole of the cavity and the cathode plug at the location of 5.5 mm behind the cathode surface. Negative cathode bias up to 5 kV is designed to prevent MP, which is efficient in most cases. A structure with multi rings on the cathode plug has been developed to minimize the risk of MP in this gap. However, cesium contamination of the cathode in the sensitive area, during deposition process could exacerbate the multipacting. This explanation is supported by the measurements that shows 30% increase in the field emission current from Mo/CsTe cathodes compared to bare metal cathodes as seen in Fig. 6.

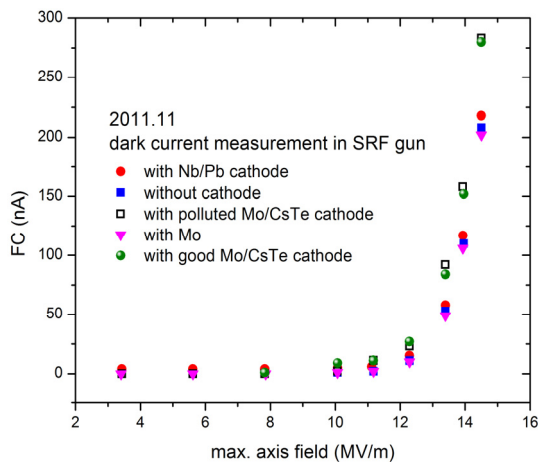


Figure 6: Dark current measured in the Faraday cup downstream of the gun versus maximum axis field. The blue squares show the cavity without a cathode. Four different cathodes have been measured in this experiment.

### BERLinPro SRF Gun at HZB

The final goal of the SRF injector at the BERLinPro is to deliver 100 mA current with repetition rate of 1.3 GHz and the emittance goal of 1mm-mrad at 1.5 MeV. In order to achieve this goal, a three-stage approach has been adapted. In the first phase, the focus is on the beam

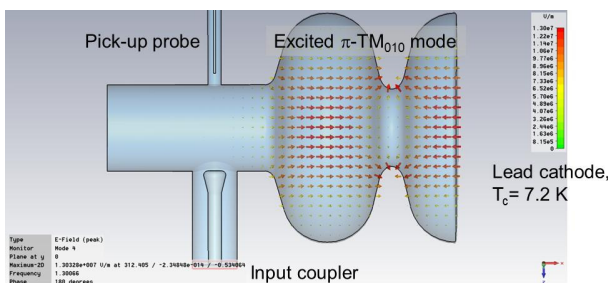


Figure 7: Schematic of the 1/2-cell, 1.3 GHz SRF gun.

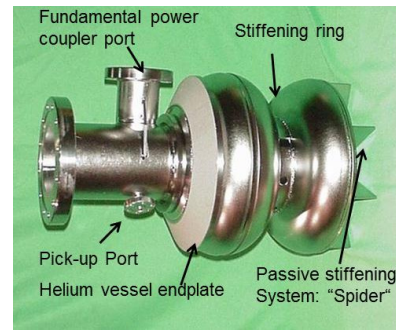


Figure 8: Photograph of the BERLinPro Stage 1 SRF gun.

dynamics of the SRF injector, with emphasis on RF performance and beam stability. The schematic design and a photograph of the 1/2 cell SRF gun, designed by J. Sekutowicz, DESY, are shown in Fig. 7 and 8 respectively.

Studies of field stability indicate that stiffening of the back plate of the cavity with a “spider” shaped support reduces the deformation to < 2 μm from > 8 μm for the unsupported cavity, resulting in reduced sensitivity to the fluctuations in He pressure. The Q<sub>0</sub> of this cavity prior to the cathode deposition, measured in a vertical test facility, was greater than 1×10<sup>10</sup> for peak E fields < 35 MV/m.

A lead cathode was deposited on to the central 5 mm of the cavity back wall using a plasma arc deposition set up with the cathode positioned at 30° to the source to minimize deposition of large droplets on the cathode as shown in Fig. 9. Both Q<sub>0</sub> and the threshold for field emission were reduced after Pb deposition. However, laser cleaning of the cathode, a necessary step to remove the adsorbed impurities, restored the field emission threshold from 12 MV/m at HoBiCaT to 18 MV/m.

The first photoemission beam of 50 nA current, 3-4 ps bunch length and 5-6 pC bunch charge was observed when the laser-cleaned cathode was irradiated with 258 nm laser beam [16]. The maximum electron energy, based on the dipole scan and simulations has been estimated to be ~1.8 MV. Work is underway to measure the intrinsic and beam emittances and to improve the cavity parameters.

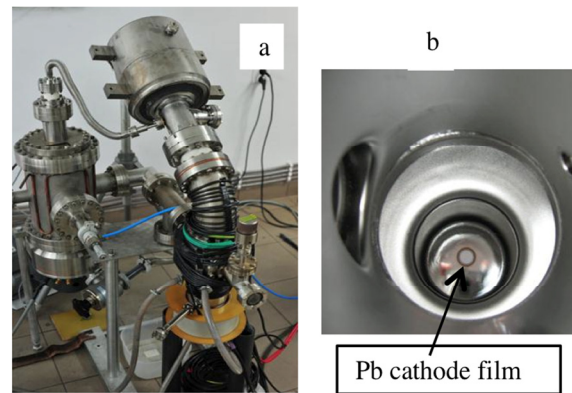


Figure 9: Photographs of the plasma arc deposition system (a) and Pb cathode film (b). The deposition was done by R. Nietubyc at NCBS.

### SRF Guns at BNL

Two SRF guns are under development at BNL [17]. The  $\frac{1}{2}$ -cell elliptical cavity gun belongs to the first generation of SRF guns. It was designed and fabricated by AES. The gun operates at 703.75 MHz and with the goal to produce high average current (up to 500 mA), high bunch charge (up to 5 nC) electron beams for the R&D ERL using  $K_2CsSb$  photocathode.

The gun cavity has been tested vertically several times in 2010. The fundamental power couplers (FPCs), manufactured by CPI/Beverly, have been conditioned recently with maximum RF power of 125 kW CW in full standing wave mode [18, 19]. The cavity has been cleaned and the cavity string assembled at JLab. Assembly of the cryomodule is in the progress at BNL (Fig. 10). The first cold test of the gun and subsequent beam generation are scheduled for 2012.

The second gun is a 112 MHz quarter-wave resonator, designed to generate 2 MeV, high bunch charge ( $>1$  nC), low repetition rate (78 kHz) beam for the Coherent electron Cooling (CeC) experiment, as well as for use in photocathodes studies.

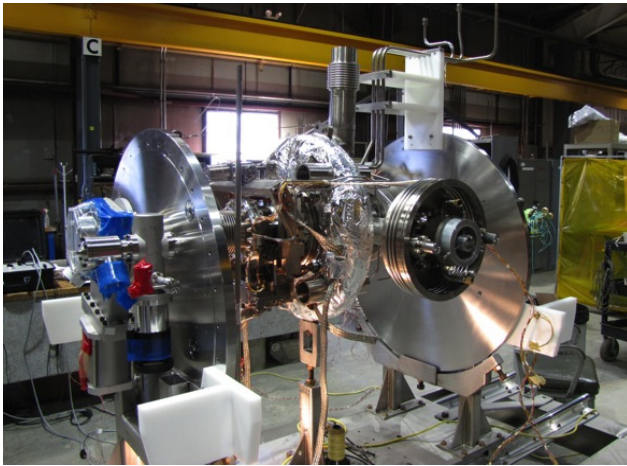


Figure 10: Photograph of the 704 MHz SRF gun cavity string being prepared for assembly into the cryomodule.

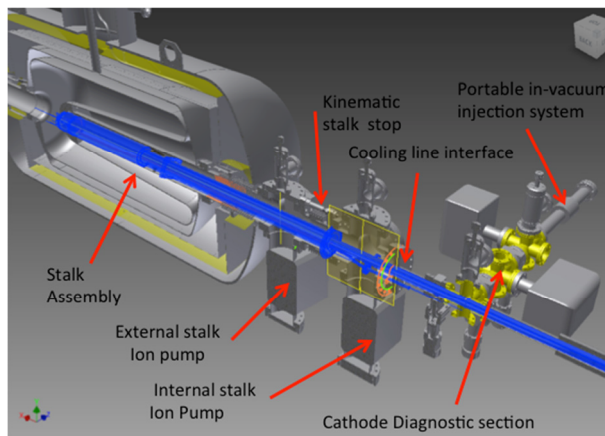


Figure 11: Cathode stalk and load lock system of the 112 MHz QWR electron gun.

The gun was developed by collaborative efforts of BNL and Niowave, Inc. and has been cold tested successfully [20]. It is now being modified for compatibility with the CeC experiment. A low-RF-loss cathode stalk and load lock system for multi-alkali photocathodes is designed (Fig. 11), and its fabrication has started. The gun will be equipped with a combine function FPC/tuner assembly [21]. The design of other upgrades and modifications is in progress.

### NCRF Gun at Los Alamos

The continuous-wave normal-conducting RF gun at Los Alamos has produced its first photoelectron beam with a  $K_2CsSb$  photocathode driven by a blue laser diode. The NCRF gun has undergone extensive testing with high-power RF to validate its thermal and RF integrity during CW operation. These tests have shown that in addition to heat removal from RF surfaces, the cooling and alignment of critical components such as the RF windows, photocathode plugs have to be properly implemented to ensure successful CW operation of the NCRF gun.  $K_2CsSb$  photocathodes with QE on the order of 1% and  $1/e$  lifetime of 20 hours are routinely prepared in an UHV deposition chamber. These  $K_2CsSb$  photocathodes are then transferred in vacuum to the NCRF gun for testing. The transfer of  $K_2CsSb$  photocathodes from the deposition chamber to the gun has to be carefully executed to minimize QE degradation and contamination to the gun that would otherwise increase field emission. Both photocurrent and dark current have been measured using a wall current transformer with typical dark current in the range of 10s of microamperes. Plans are underway to produce picosecond electron bunches at high repetition rates with  $K_2CsSb$  photocathodes driven by the green (second harmonic) pulses from a mode-locked Nd:YVO<sub>4</sub> laser in phase with the cavity RF signal.

### Other High Current RF Injectors

Beside the injectors mentioned above, there are a number of NCRF and SRF injectors under development.

The Naval Postgraduate School Mark I SRF injector, built by Niowave, Inc. and operated in collaboration with the Boeing Company, produced its first beam in June of 2010 [5]. The Mark I was intended primarily as a research and development tool to explore issues in designing and operating SRF guns in general, and quarter wave SRF guns in particular, although it can serve as an injector for the NPS Beam Physics Laboratory's linac. It uses an on-axis coaxial RF power coupler, and has a resonant frequency of 500 MHz. This low frequency allows operation at 4 K, thereby greatly simplifying the requirements to the cryogenic support system. Nominal beam energy is 1 MeV, with a maximum attained energy of 0.5 MeV to date.

The APEX/VHF NCRF gun [22] operating at 187 MHz has successfully undergone RF conditioning. The gun was run in continuous wave mode and at the nominal power of 100 kW for about 29 hours without faults. The installation

of the electron beamline with the low energy beam diagnostics is near completion.

University of Wisconsin has built a ~200 MHz SRF injector [23] that is expected to be cold tested in early 2012, with the final assembly scheduled for the summer of 2012 and the first beam anticipated in fall of 2012.

## REFERENCES

- [1] A. Arnold, "Rossendorf SRF Gun Operational Experience," this workshop.
- [2] K. Liu, et al., "DC-SRF photocathode injector for ERL at Peking University," this workshop.
- [3] S. Belomestnykh, "Status of BNL SRF guns," this workshop.
- [4] S. Belomestnykh and Wencan Xu, "Fundamental power couplers for the ERL prototype SRF gun at BNL," this workshop.
- [5] J. Harris, et al., "Design and operation of a superconducting quarter-wave electron gun," *Phys. Rev. ST Accel. Beams* **14** (2011) 053501.
- [6] R. Legg, et al., "Development of a Frequency Map for the WiFEL SRF Gun," Proc. SRF'11, 2011, Chicago, IL, to be published, MOPO032.
- [7] S. Niles, "Design and Analysis of an Electron Gun/Booster and Free Electron Laser Optical Theory," PhD dissertation, Naval Postgraduate School, Monterey, CA, 2010.
- [8] A. Arnold et al., "Development of a superconducting radio frequency photoelectron injector," *Nucl. Instrum. Meth A* **577** (2007) 440-454.
- [9] T. Kamps, et al., "Electron beam diagnostics for a superconducting radio frequency photoelectron injector," *Rev. Sci. Instrum.* **79** (2008) 093301.
- [10] J. W. Lewellen, et al., "ERL 2009 WG1 Summary Paper: Drive Lasers and RF Gun Operation and Challenges," Proc. ERL'09, 2009, Ithaca, NY, USA, 2009, p. 24-36.
- [11] D. H. Dowell, et al., "Longitudinal emittance measurements at the SLAC gun test facility," *Nucl. Instrum. Meth. A* **507** (2003) 331-334.
- [12] J. Teichert, et al., "Pulsed Mode Operation and Longitudinal Parameter Measurement of the Rossendorf SRF Gun," Proc. IPAC'11, 2011, San Sebastian, Spain, p. 262.
- [13] A. Arnold, et al., "Field Reconstruction by Passband Frequency Measurement at the Rossendorf SRF-Gun Cavity," Proc. SRF'07, 2007, Beijing, China, p. 689-691.
- [14] P. Murcek, et al., "Modified 3½-Cell SC Cavity Made of Large Grain Niobium for the FZD SRF Photoinjector," Proc. SRF'09, 2009, Berlin, Germany, p. 585-588.
- [15] T. Kamps, et al., "Status and perspectives of superconducting radio-frequency gun development for BERLinPro," *J.Phys.Conf. Ser.* **298:012009**, 2011.
- [16] T. Kamps, et al., "First Demonstration of Electron Beam Generation and Characterization with an all Superconducting Radiofrequency (SRF) Photoinjector," Proc. IPAC'11, 2011, San Sebastián, THPC109.
- [17] S. Belomestnykh, "Status of BNL SRF guns," this workshop.
- [18] W. Xu et al., "Conditioning fundamental power couplers for the ERL SRF Gun," Proc. SRF'11, 2011, Chicago, IL, to be published, TUPO010.
- [19] S. Belomestnykh and W. Xu, "Fundamental power couplers for the ERL prototype SRF gun at BNL," this workshop.
- [20] S. Belomestnykh, et al., "Superconducting 112 MHz QWR Electron gun," Proc. SRF'11, 2011, Chicago, IL, to be published, MOPO054.
- [21] T. Xin, et al., "Design of the fundamental power coupler and photocathode inserts for the 112 MHz superconducting electron gun," Proc. SRF'11, 2011, Chicago, IL, to be published, MOPO014.
- [22] F. Sannibale, et al., "Status of the LBNL normal-conducting CW VHF electron photo-gun," Proc. FEL'2010, Malmo, Sweden, 2010, p. 475-478.
- [23] R. Legg, et al., "SRF photoinjector R&D at University of Wisconsin," Proc. ERL'09, Ithaca, NY, USA, 2009, p. 45-49.

# HIGH BRIGHTNESS THERMIONIC ELECTRON GUN PERFORMANCE

H. P. Bluem, D. Dowell\*, A. M. M. Todd and L. M. Young\*,  
Advanced Energy Systems (AES), Medford, NY, USA

## Abstract

Commercial Off-The-Shelf (COTS) gridded thermionic cathode electron guns show promise for certain pulsed and CW electron beam applications. Accelerator systems utilizing these guns are presently being commissioned for pulse mode operation. Beam has been delivered to the IR wiggler of the Free Electron Laser (FEL) at the Fritz Haber Institute (FHI) der Max Planck Gesellschaft in Berlin [1] in advance of their October 28 Centennial. In the course of commissioning, we have performed emittance measurements that indicate the beam transverse rms emittance is 8-10mm-mrad at 20kV, consistent with our gun simulations. The nominal system operating voltage is 45kV. We have also studied the dependence of the extracted current as a function of RF power. After the initial low-level region, near linear behaviour is observed. The maximum value achieved was 806mA at 23.2kV and ~200W input RF, limited only by our available power supply. We find that pulsed beam applications must address the DC idle current that leaks from the cathode by utilizing grid or cathode pulsing. S-band systems are being commissioned at this time using both approaches. Lower frequency CW mode operation has also been proposed for high-power Energy Recovering Linacs (ERL) and FELs [2]. The above performance measurements indicate that adequate high-current thermionic gun beam quality is possible for IR FELs in such CW operation. The next step for this application, which is already in progress, is the design and testing of a gun with a normal-conducting pre-booster incorporating

solenoid focusing. This will raise the output energy to greater than 1 MeV so that the performance of the concept can be evaluated. The design must also consider ways to ameliorate beam scraping. Because the present COTS gun [3] is capable of delivering 5A, which greatly exceeds the requirements of all these applications, both CW and pulsed operation would benefit greatly from a redesigned gun with a smaller cathode and a reduced radius or totally eliminated cathode "hole". It remains to be seen if totally eliminating the "hole" is possible while maintaining a robust gun HV and RF design in the presence of ion back bombardment.

## INTRODUCTION

Standard thermionic guns for accelerator applications require complex, real-estate-consuming, bunching systems in order to produce high-quality electron beams and achieve low electron beam loss in the accelerating structures. Photocathode guns can be used to provide pre-modulated electron beams, but have not yet been shown to be practical for high-power CW systems, due principally to cathode lifetime issues at high current. In addition, they add their own, significant complexities to the system through the addition of the photocathode drive laser and the need for maintaining very good vacuum levels in the guns to avoid poisoning the cathodes. A gridded thermionic electron gun can provide a robust, economical, and compact solution to the provision of the high-performance, high-power electron beams required, when the grid is driven by an RF signal at the desired bunch

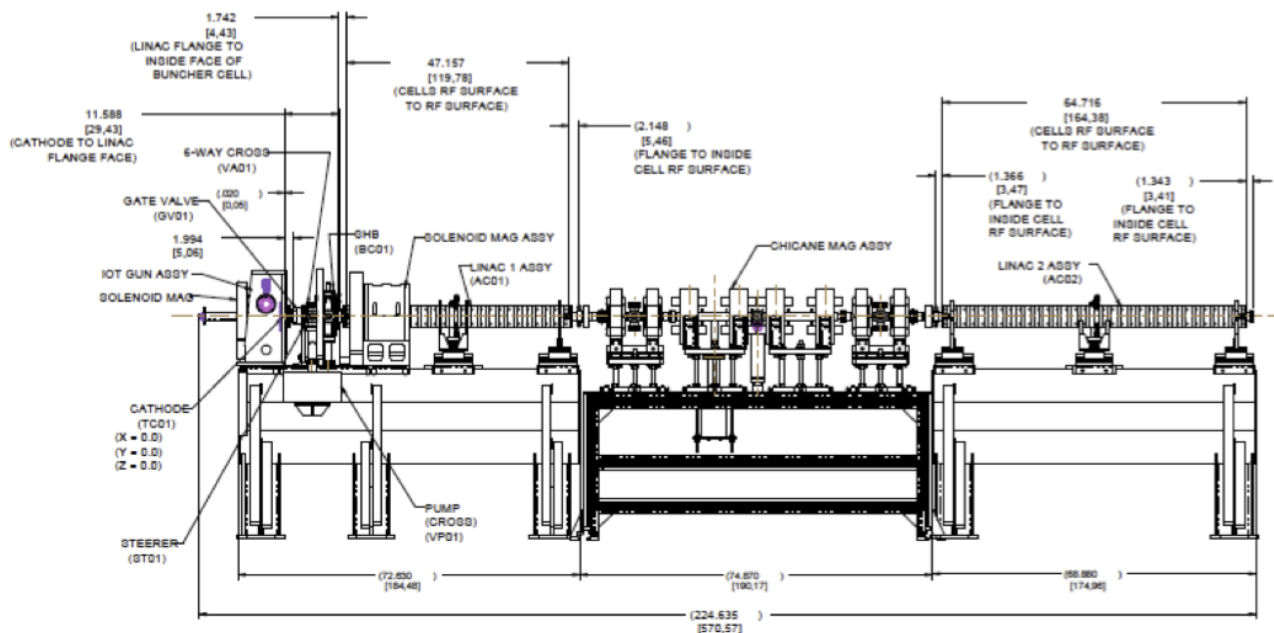


Figure 1: Layout of the FHI accelerator section from the gridded gun (left) to the second linac output (right).

\* Consultants to AES

frequency. Such a gun could find application in ERLs, compact FELs, and other areas that would benefit from a high-performance compact accelerator system. Two such guns are presently in use in AES accelerator systems [4], with one of them driving the FHI infrared FEL [5,6]. The layout of this accelerator for this device is shown in Figure 1.

The FEL consists of a 50MeV accelerator driven by a gridded thermionic gun with a beam transport system that feeds two undulators and a diagnostic beamline as shown in the schematic diagram of Figure 2. Two 2.998GHz S-band, normal-conducting electron linacs and the gun-to-

dump electron beam lines have been designed, fabricated, and installed by AES. The first linac accelerates the electron bunches to a nominal energy of 20 MeV, while the second one accelerates or decelerates the electrons to deliver any final energy between 15 and 50 MeV. A chicane between the structures allows for adjustment of the bunch length as required. A number of measurements and simulations have been performed on the gun indicating its potential for use in high-current, high-performance applications. Another group has also proposed using an identical gun for high-power ERLs and FELs [2].

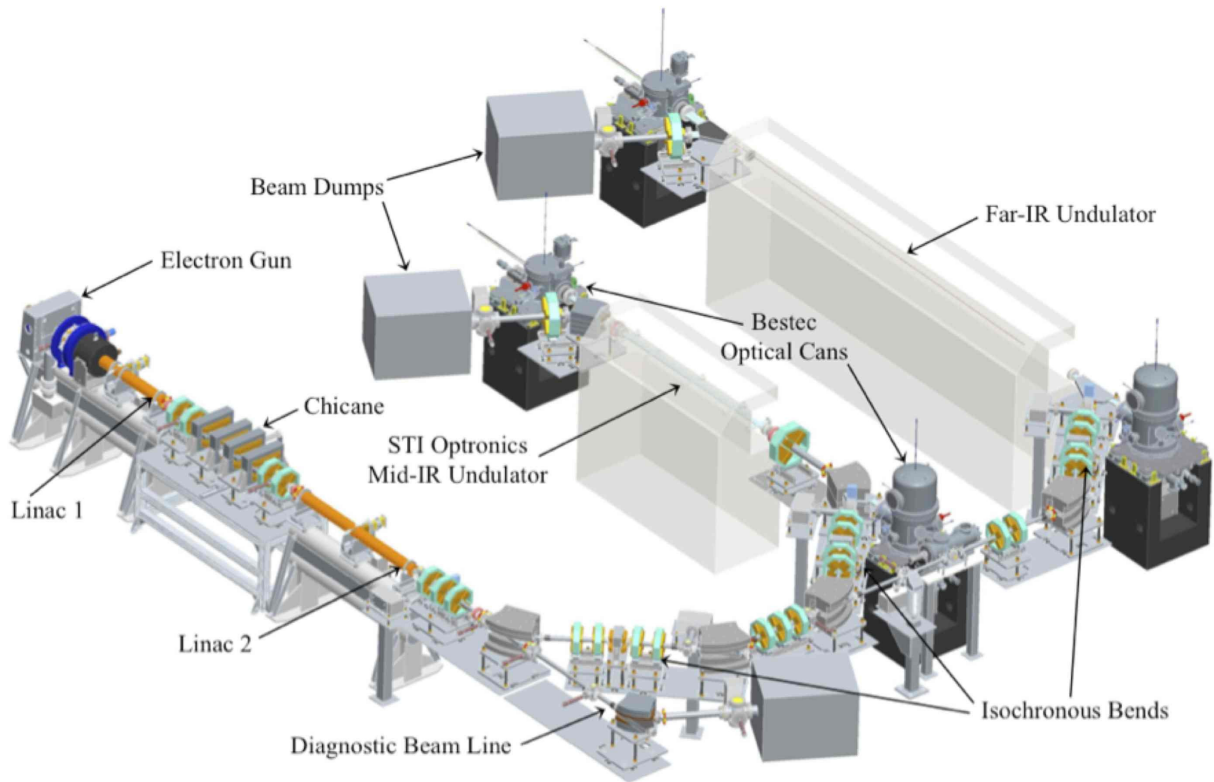


Figure 2: Schematic diagram of the FHI IR & THz FEL.

### INJECTOR DESIGN AND MODELING

Since the present guns are being used in conjunction with S-band accelerators, the RF drive to the gun is a sub-harmonic of the main 2.998 GHz accelerating frequency. Driving the grid at the third sub-harmonic produces a bunch length that is still too long for efficient capture so a sub-harmonic cavity is used to further compress the bunch length. The front-end design is shown in Figure 3. Solenoid focusing is required to confine the beam in this front-end section. Solenoid 1 in Figure 3 is a bucking coil to ensure zero magnetic field on the cathode.

We have performed simulations of this system. The RF fields with the biased gun grid are shown in Figure 4. The cathode is to the left and the anode to the right. The insert in the upper right is the axial solenoidal field employed. Figure 5 shows a TStep [7] simulation of bunch formation

where the beam pulse streaming through the grid can clearly be seen in the upper radial projection. We find there is a correlation between longitudinal beam position and cathode birth location in that electrons emitted at larger radius populate the front of the bunch and those emitted nearer the axis trail the bunch. The same behaviour is reported by Ref. [2]. In order to meet the FHI performance specifications of Table 1, it is necessary for us to scrape some of the electrons that populate the tail and the outer radii due to the unnecessary large diameter of the cathode. The key performance parameters from Table 1 at 50MeV and for a 200pC bunch are a transverse emittance  $< 20\text{mm-mrad}$  and longitudinal emittance  $\sim 50\text{keV-psec}$ . The latter requirement is particularly stressing but we achieve it in simulations.

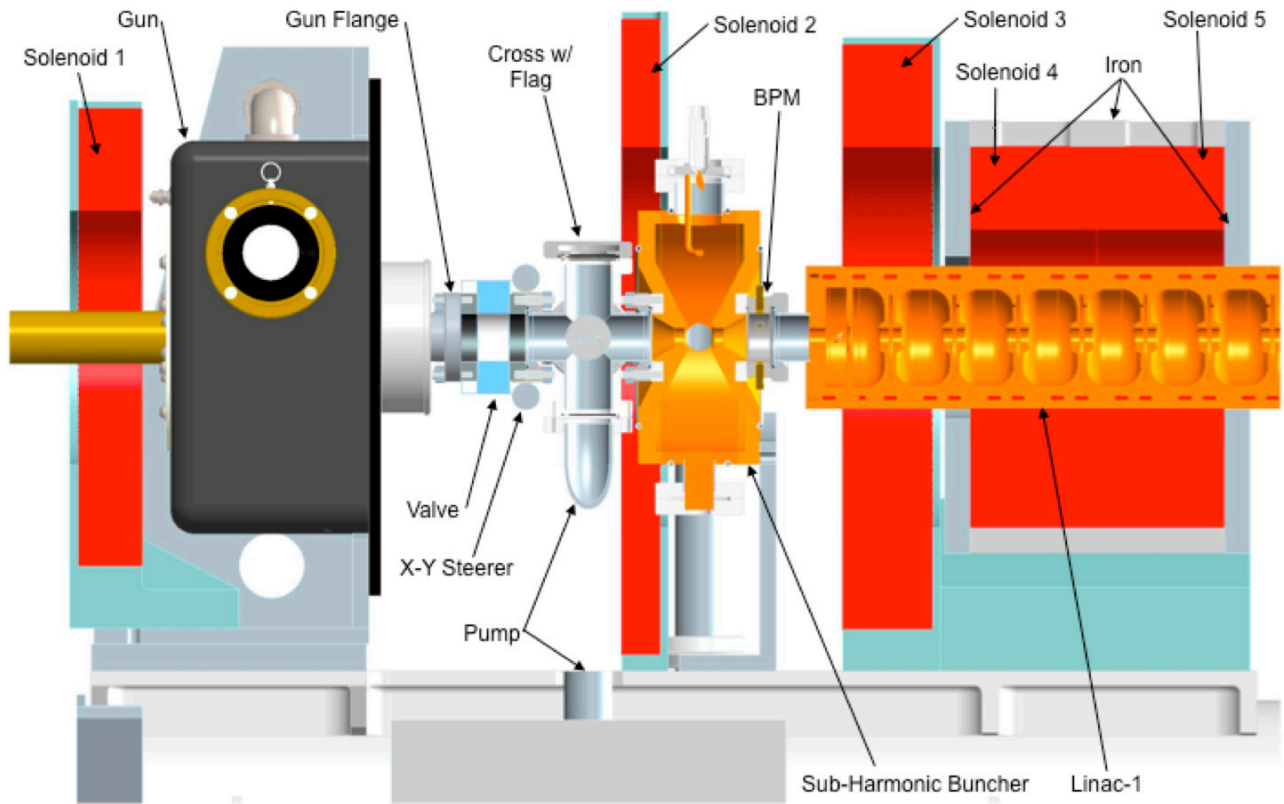


Figure 3: FHI FEL front-end configuration.

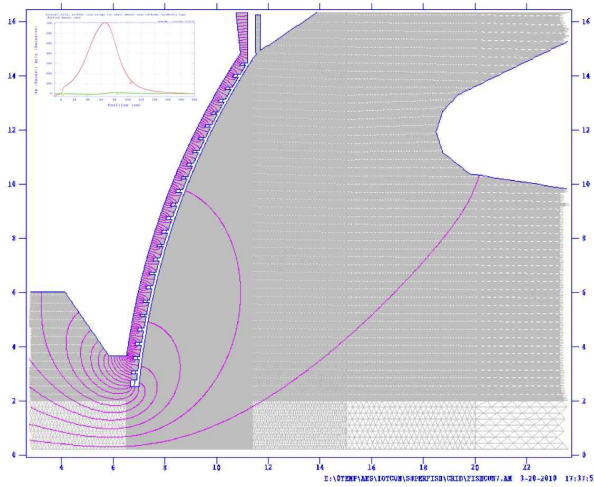


Figure 4: Gun biased grid RF fields.

Table 1: FHI FEL Electron Beam Parameters

Parameter	Unit	Specification	Target
Electron Energy	MeV	20 - 50	15 - 50
Energy Spread	keV	50	< 50
Energy Drift per Hour	%	0.1	< 0.1
Charge per Pulse	pC	200	> 200
Micropulse Length	psec	1 - 5	1 - 10
Micropulse Repetition Rate	GHz	1	1 & 3
Micropulse Jitter	psec	0.5	0.1
Macropulse Length	μsec	1 - 8	1 - 15
Macropulse Repetition Rate	Hz	10	20
Normalized rms Transverse Emittance	π mm-mrad	20	20

Figure 6 shows the delivered bunch at the end of the second linac with 3% of the bunch tail scrapped off. Upper left and right are the horizontal and vertical phase spaces respectively. The lower left and right are the transverse bunch distribution and the longitudinal phase space. Figure 7 reproduces the two lower plots of Figure 6 but projects out the longitudinal axial bunch and energy profiles.

In pulsed operation, we have measured 4mm-mrad transverse rms emittance at 14kV and 26mA. At 20kV and 100mA we obtained 8mm-mrad. Measurements at 45kV will be made shortly. Operation in this CW HV mode was limited by the available power supplies and the idle current produced by the gun. The idle current consists of electrons leaking through or around the grid when the HV is on even though the grid is biased negatively. There can be considerable power in the idle current. This is obviously not an issue in CW operation and is only a concern in macropulse operation mode.

### GUN PERFORMANCE IN PULSED MODE

Figure 8 shows the beam current as a function of grid RF power at lower levels of RF power. At 23.2kV we achieved 806mA with ~200W of RF grid power. Recently, at FHI, we achieved ~600mA with 200W of RF grid power at 45kV. Here, in both cases, we are only limited by the available 200W of our RF power supplies.

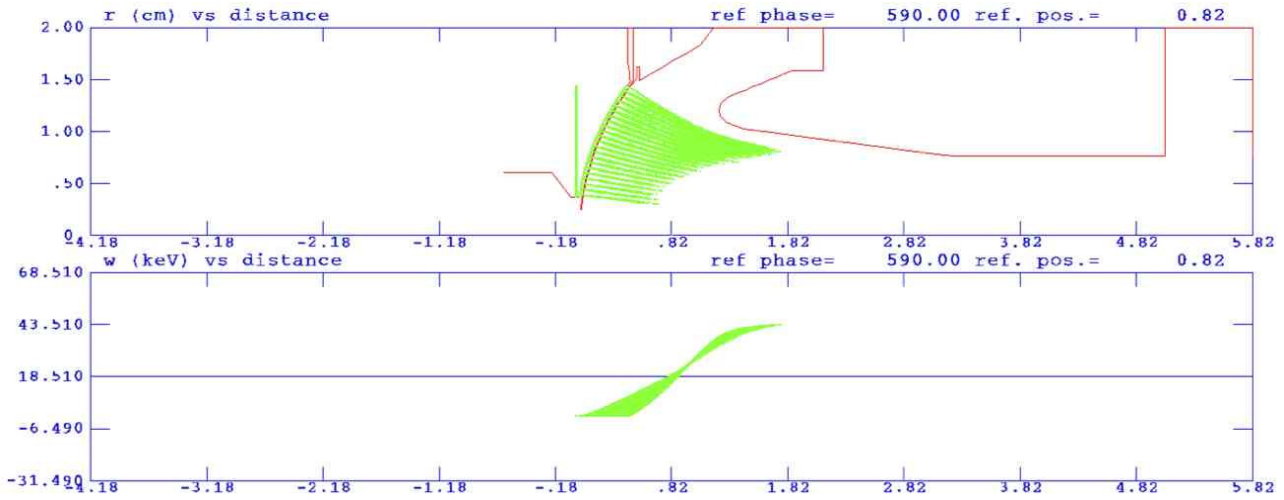


Figure 5: TStep radial projection (upper) and energy profile (lower) during bunch formation from the gun.

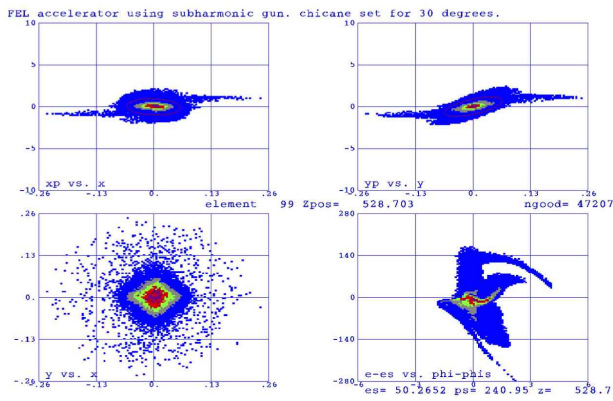


Figure 6: Phase space bunch profiles after the second linac.

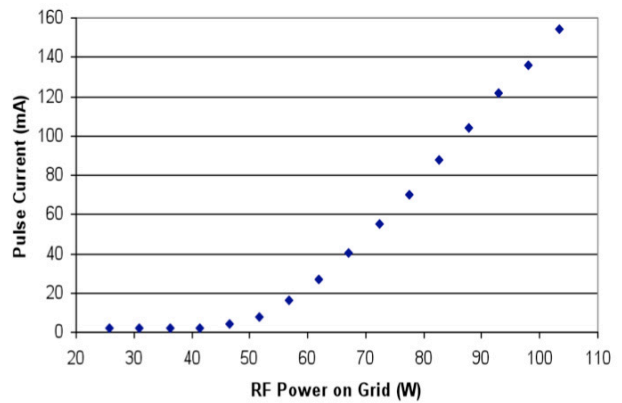


Figure 8: Pulse current with RF power on the grid.

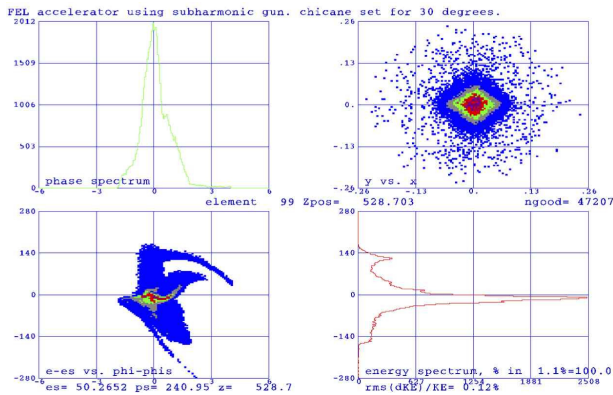


Figure 7: Longitudinal axial bunch and energy profiles after the second linac.

### HIGH-POWER ELECTRON INJECTORS

We have noted that Sprangle et al. [2] have proposed using such an electron source for high-power ERLs and FELs. Under these conditions, desired of future light sources and other systems, the reliability and power required of a photocathode drive laser is suspect, as are photocathode lifetimes at high-currents [8], given their high vacuum requirements.

In contrast, thermionic guns have demonstrated the required currents and operate comfortably with achievable vacuum levels in the  $10^{-8}$  Torr range. In this case we have to prove two things. Firstly, we must demonstrate that we can deliver the necessary beam quality for the application in question, in terms of transverse and longitudinal emittance. The reason photocathode systems have been preferred to date is that their achieved beam quality has been measurably better than thermionic systems. However, the intrinsic beam quality achievable with thermionic systems, ( $< 10\text{mm-mrad}$ ,  $< 100\text{keV-psec}$ ) is sufficient for some high-power applications such as IR FELs.

Secondly, we must demonstrate that we can entrain almost all of the emitted electrons in the bunch, since beam spill at high-power cannot be tolerated in a high-power accelerator system.

Figure 9 shows the installed front end of the FHI system that corresponds to Figure 2. Unfortunately, the orientation is inverted here with the gun to the right.

We have delivered beam to the FHI mid-IR beamline dump. Figure 10 shows the grid and heated cathode as imaged off the OTR screen before the first Linac. Figure 11 shows the beam imaged on this same screen.

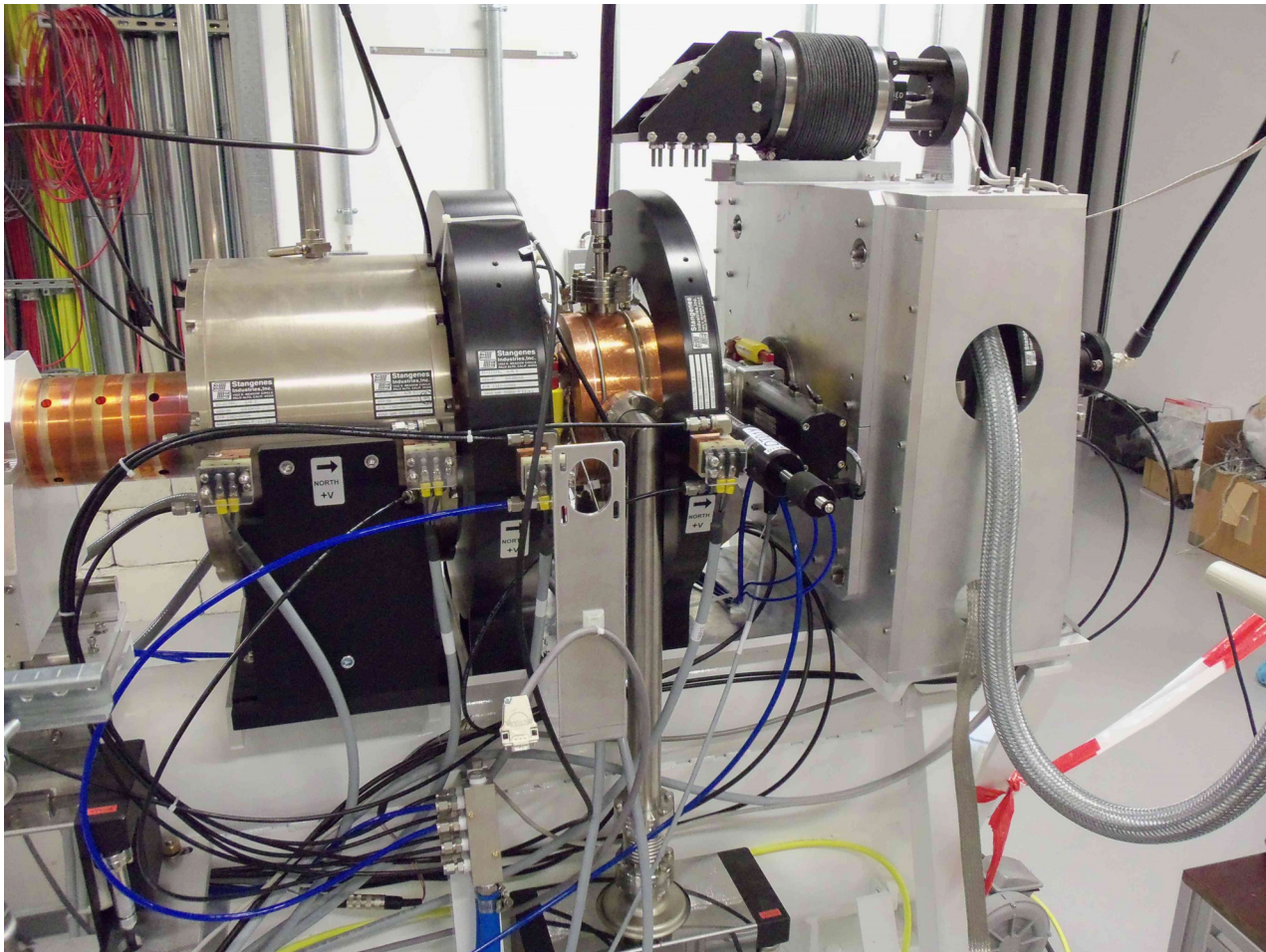


Figure 9: FHI gun, sub-harmonic buncher and first linac as installed in Berlin.

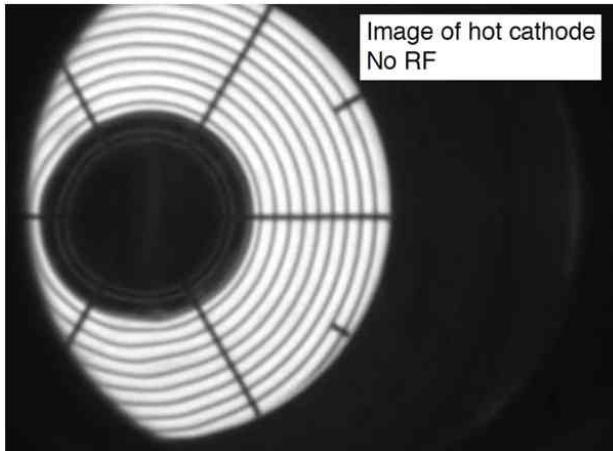


Figure 10: Gun filament and grid.

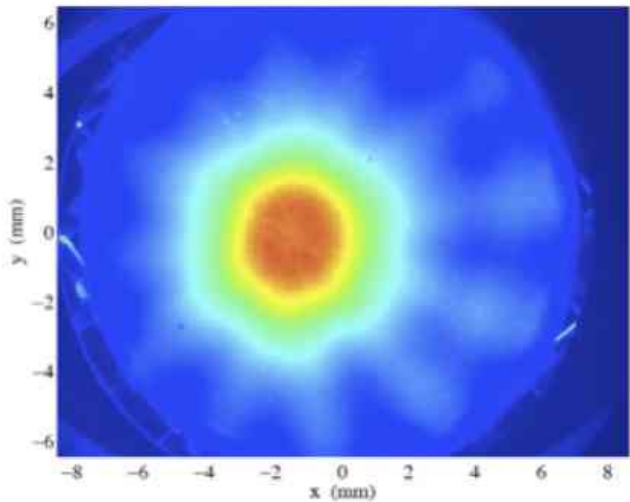


Figure 11: Beam imaged after the gun with the solenoids set for zero field on the cathode.

Figure 12, reproduced courtesy of Ref. [2], illustrates the concept. Firstly, they propose using both the fundamental RF frequency and the third harmonic on the gun grid to sharpen up the RF bucket and shorten the delivered electron bunch. This is illustrated in the lower right of Figure 12.

A bunch is produced by the gun and rapidly captured in a pre-booster cavity closely coupled to the gridded gun. A one and a half cell pre-booster is shown here. RF bunch

compression is arranged in the first half-cell of the pre-booster. The Ref. [2] simulations indicate that performance meeting the beam quality targets we need, can be achieved.

We have begun the physics and engineering design of such a close-coupled pre-booster and gridded gun. Our

initial analysis indicates that a simply-cooled copper cavity can be produced to validate this concept. We are proceeding to develop this work with a view to delivering a high-current > 1MeV electron beam for experimental performance measurements.

The lower left insert in Figure 12 shows the typical grid dimensions of the gun we are using. This gun can produce 5A, far exceeding the requirements of any of the applications in question. Consequently, given the observation of the correlation between birth radius and axial bunch position of the electrons, we would expect

better beam quality and electron entrainment to be achieved, not only in transverse phase space but also in longitudinal phase space, if we were to reduce the active size of the grid and cathode and reduce or eliminate the central hole in the grid as suggested by Ref. [2]. Whether the hole can be completely eliminated in the presence of ion back bombardment is to be determined. Hence, the electron source solution we seek is not precisely a COTS product but rather a slightly modified version for our applications.

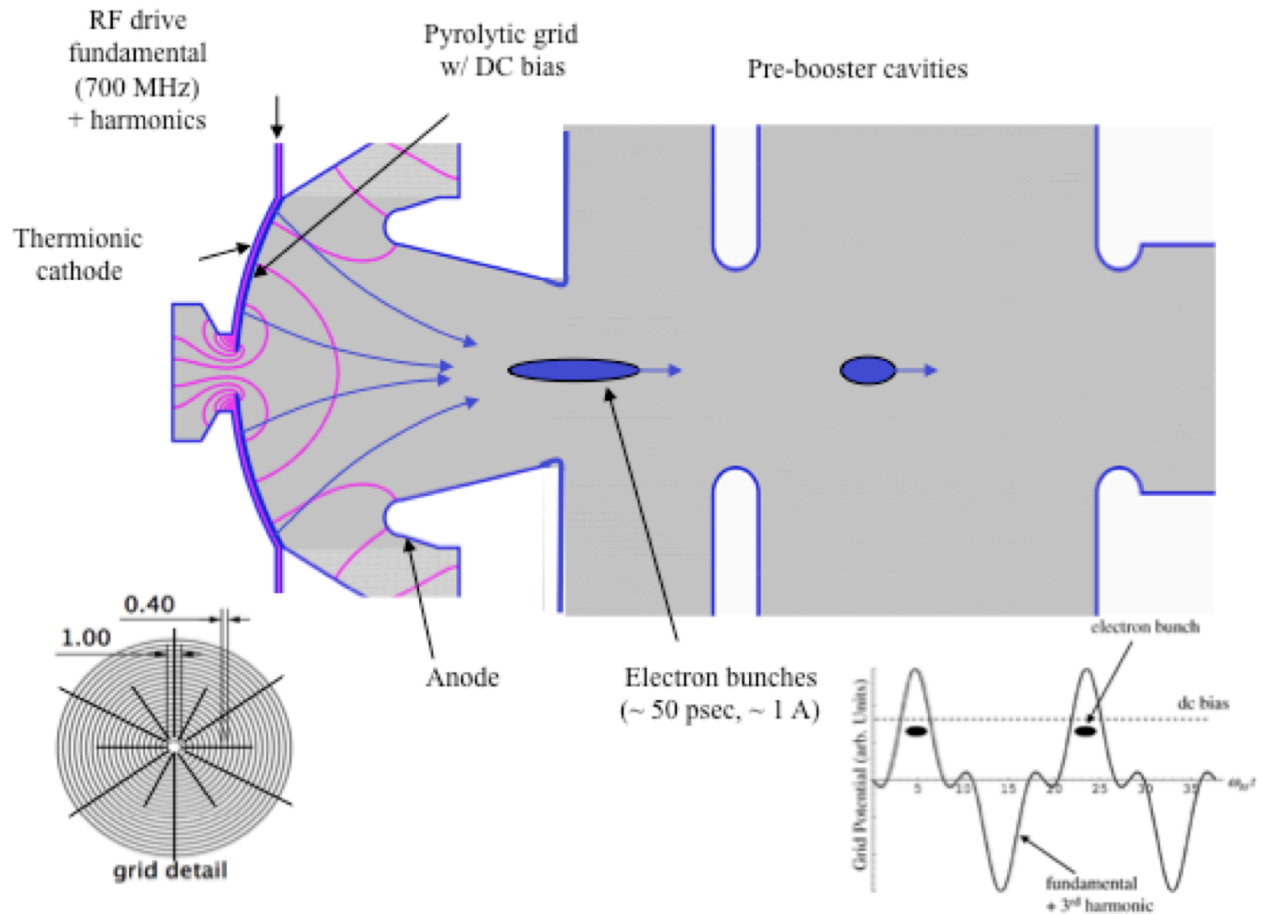


Figure 12: Ref [2] concept for a high-power gridded gun and pre-booster electron injector system.

### SUMMARY

COTS gridded thermionic cathode electron guns are being used for two accelerator systems that are presently being commissioned by AES. One is an IR and THz FEL and the other is a system for contraband detection. The predicted performance meets the requirements of the two systems and exceeds the performance of conventional DC gun designs within a more compact footprint. We are presently validating the predicted performance but initial results indicate we will meet the project targets. Lower frequency CW mode operation has also been proposed for high-power ERLs and FELs. We are presently designing a pre-booster/gun combination to measure and validate the performance of such an injector.

### REFERENCES

- [1] <http://www.fhi-berlin.mpg.de/mp/>
- [2] P. Sprangle et al., *Physical Review Special Topics - Accelerators and Beams* **14**, 020702 (2011).
- [3] <http://www.cpii.com>
- [4] A. M. M. Todd et al., Paper THP043, *Proc. PAC 2011*.  
<http://accelconf.web.cern.ch/AccelConf/PAC2011/>
- [5] H. Bluem et al., Paper MOPA09, *Proc. FEL 2010*.  
<http://accelconf.web.cern.ch/AccelConf/FEL2010/>
- [6] W. Schöllkopf et al., Paper TUPB30, *Proc. FEL 2011*.  
<http://accelconf.web.cern.ch/AccelConf/FEL2011/>
- [7] L. M. Young, priv. comm.
- [8] e.g. C. Dunham, these Proceedings.

## ERL2011 SUMMARY OF WORKING GROUP 2 BEAM DYNAMICS

C. Mayes, Cornell University, Ithaca, NY 14853, USA  
N. Nakamura, KEK Tsukuba, Ibaraki 305-0801, Japan

### Abstract

The 50<sup>th</sup> ICFA Advanced Beam Dynamic Workshop on Energy Recovery Linacs (ERL2011) was held on October 16-21, 2011 at KEK in Japan. Five working groups, Working Groups 1- 5, were organized in the workshop and Working Group 2 mainly covered topics and issues of beam dynamics for ERLs. This paper summarizes WG2 presentations and activities.

### INTRODUCTION

The number of existing and future ERL based accelerator projects are steadily increasing in North America, Europe, and Asia. In ERL2011, Working Group 2 (WG2) surveyed the optics designs of nearly all of these machines, and included operational experiences at existing machines. WG2 also addressed the critical issues of collective effects, beam instabilities, start to end simulation, simulation codes, halo formation, etc. in order to realize the excellent ERL performance such as ultra-low emittance bunches, ultra-short bunches, and high current.

There were 7 WG2 sessions in which 28 oral presentations were presented in total. The presentation time was set to 20 or 25 minutes including a 5-minute question time. Two of the sessions were held as joint sessions with Working Groups 1 (Electron Sources) and 5 (Unwanted Beam Loss). Two invited plenary talks relevant to WG2 were presented in the plenary sessions and several WG2 poster presentations were provided in the poster session. All these presentation slides can be seen in [1].

In order to make a summary report for WG2, we classified WG2 topics and issues for small collaboration reports as follows:

- 1) Design principles learned from existing ERLs
- 2) Test ERL designs
- 3) Lightsources ERLs
- 4) ERLs for high energy and nuclear physics
- 5) Code survey for ERL simulation
  - a) Space Charge
  - b) IBS/Touschek scattering
  - c) CSR
  - d) Surface physics/secondary electron production

We assigned each of them to one or several authors and encouraged to finally produce a set of stand-alone papers for these topics and issues. Separately we asked all of them to produce a one- or few-page manuscript (with figures) for making a summary paper and could receive manuscripts from some of the authors. Here we will present a WG2 summary based on these manuscripts.

### LESSONS FROM EXISTING ERLS

*Accelerator Transport Lattice Design Issues for High Performance ERLs: S. Benson and D. Douglas (JLAB)*

When designing an ERL there are some things that are good to remember:

1. ERLs are 6-dimensional systems. They are essentially time-of-flight spectrometers (well, maybe turned inside-out).
2. They are transport lines (not rings). The beam does not achieve equilibrium. The rms beam size  $\sigma$  is therefore not meaningful.
3. ERLs do not have closed orbits. The overall transport need not be betatron stable so there is no guarantee there are unique “matched” Twiss parameters. Therefore the actual beam envelope and the matched beam envelopes are not necessarily the same.
4. ERLs do not recover energy, they recover RF power – and power flow management is critical to their operation.

**Design Process** The design of an ERL should start with the user requirements, which flow down to the longitudinal match, which sets the RF drive requirements, and then the transverse match, which dominates acceptance. Chromatic/geometric aberration management is then carried out. Finally the collective effects and power flow are calculated, problems uncovered, and one iterates the process until one is satisfied.

**Longitudinal Matching in an ERL** Longitudinal matching requires the use of RF to compensate beam quality degradation and provide for energy compression during energy recovery. One must use the RF power to cover the user’s power draw. Note that the accelerated and decelerated beams may balance imperfectly during energy recovery. Because of this the beam dump energy is not necessarily the same as the injected energy.

The longitudinal scenario for the FEL at Jefferson Lab is as follows. Inject a long bunch to avoid space charge effects. Accelerate on the rising part of the RF waveform. Compress the bunch using both linear and non-linear momentum compactions ( $M_{56}$ ,  $T_{566}$ ,  $W_{5666}$ ). One then uses the linear and non-linear compactions of the exhaust arc to match the bunch from the FEL, which is still short but now has a large energy spread, into the linac and compress the energy spread to the dump. Note that the deceleration phase depends only on the exhaust full energy spread. This is because the entire bunch must

precede the trough of RF waveform. This means that the two beams are not necessarily 180° out of phase and not all the power is recovered. This is called incomplete energy recovery. Required phase bite is  $\cos^{-1}(1 - \Delta E_{\text{FEL}}/E_{\text{LINAC}})$ . At modest energy this is >25° at RF fundamental for 10% and >30° for 15%. With this large a phase spread one generally needs correction to third order (octupoles).

The longitudinal transport to the wiggler is essentially a parallel to point image while the wiggler to dump is point to parallel. Because of this, the energy and energy spread at the dump do not depend on the laser exhaust energy spread or efficiency. Finally note that chicanes are not necessary for bunch compression and that harmonic RF is not necessary for linearization of the longitudinal phase space.

Operationally the longitudinal match relies on bunch length measurements at full compression using a Martin-Puplett Interferometer, and longitudinal transfer function measurements of R<sub>55</sub>, T<sub>555</sub>, and U<sub>555</sub>. Such measurements are shown in Fig. 1 for a nominal bunch (red curve), for mis-matched R<sub>56</sub> (cyan and green curves), and for mismatched T<sub>566</sub> (purple and yellow curves).

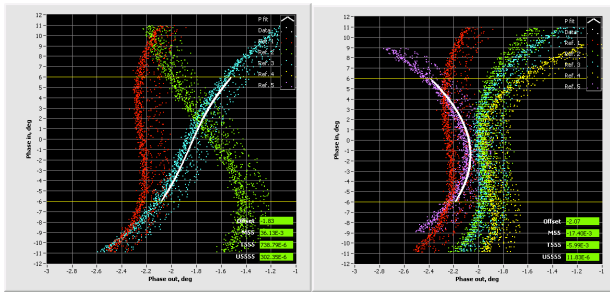


Figure 1: Phase transfer system measurements used to verify R<sub>55</sub>, T<sub>555</sub>, and U<sub>555</sub>.

**Transverse Matching** Since the transverse match is the key driver of the acceptance, one must suppress chromatic/geometric aberrations.

One “old school” but very effective way to check the aberrations is to do momentum and aperture scans. One evaluates the spatial transfer function (4x4 matrix,  $M(dp/p):(x_i, x'_i, y_i, y'_i) \rightarrow (x_f, x'_f, y_f, y'_f)$ ) and reference orbit  $((0,0,0,0) \rightarrow (x_o(dp/p), x'_o(dp/p), y_o(dp/p), y'_o(dp/p)))$  at numerous momenta over some range.

One then uses the result to propagate notionally matched beam envelopes for monoenergetic beam for each momentum. One then designs the system to keep  $\beta(dp/p)$ ,  $\alpha(dp/p)$ ,  $x(dp/p)$ ,  $x'(dp/p)$ ,... invariant over the full momentum range. One typically has to invoke multiple sextupole families and/or construct destructive interferences amongst quad telescopes. One must avoid introducing *geometric aberrations* when correcting chromatics. Chromatic scans for the IR-Demo accelerator are shown in Fig. 2.

Experience from the ERLs at Jefferson Lab has shown that low loss energy recovery is possible when these techniques are followed and that deviation from this setup leads to an energy spread dependent loss at the low energy end of the recovery transport where the orbits are adiabatically undamped.

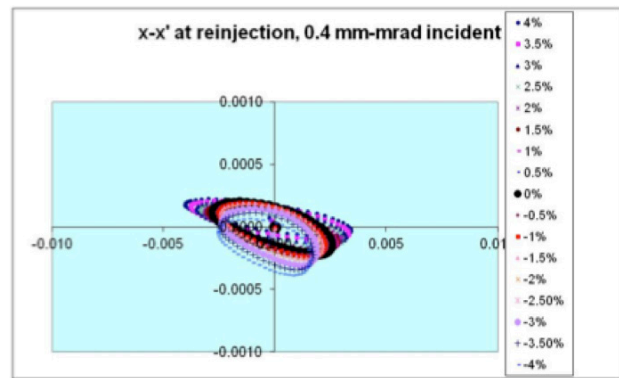
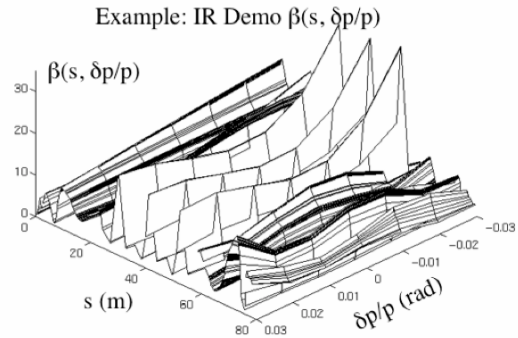


Figure 2: Momentum scans for the IR Demo FEL.

**Collective Effects** The whole reason to build an ERL is to generate high brightness, high power beams so collective effects are a logical consequence of that fact. Thus longitudinal space charge, coherent synchrotron radiation, resistive wall heating, and wakefields are always a problem. At higher currents, intrabeam scattering, Toushek effect, beam-gas scattering, and ion trapping will also be a problem. Halo is a major operational problem and has multiple sources, some of which might be the experiment itself (for example in nuclear and high energy physics applications). When designing an ERL one must provide locations to disentangle halo from core, large dynamic range diagnostics, and knobs for independent control of halo and core. For large systems one must also provide for collimation systems to protect long, small gap undulators. This must consist of multiple stages with appropriate phase separation.

**Issues for Large Systems** Large systems have to deal with multi-pass focusing & steering in linac. One must also make accommodations for beam dynamics (ISR, CSR, BBU, wakes, scattering, Halo). Another problem is the large dynamic range of the ERL, leading to the

potential for the longitudinal emittance exceeding the dump acceptance. A very important issue with large machines is magnetic field quality. This can provide significant obstacles to ERL performance. The basic idea is that differential field errors lead to differential angular kick which lead to differential betatron oscillations, which lead to accumulated path length error, leading to phase errors, leading to energy errors at the dump. This may have been source of performance-limiting loss in CEBAF-ER during operation with 20 MeV injection. When the full analysis is done one finds that the integrated magnetic field error tolerance is inversely proportional to the linac energy. One must provide a means to diagnose and correct the magnetic field errors.

**Conclusions** The path forward to higher power/higher energy/higher brightness is clear, but challenging.

### *Investigation of Beam Dynamics with Not-ideal Electron Beam on ALICE ERL: Y. Saveliev (Daresbury Laboratory)*

ALICE is a multifunctional R&D facility at Daresbury Laboratory operating currently for ten projects in four different generic setups both in energy recovery and non-energy recovery modes. The range of parameters is wide: beam energy 12-28 MeV, bunch charge 20-100 pC, required energy spread from ~10 keV to 100 keV, and the bunch length from several ps down to sub picoseconds. Two major operating modes are for generation of infrared light with an IR FEL (tunable with 8 $\mu$ m nominal wavelength) and for broadband coherent THz radiation.

Depending on mode of operation, the first superconducting (SC) cavity of the booster (BC1) in the injector is set to off-crest phases of -10 to -20 deg. Generally, setting the BC1 phase farther off-crest improves the overall “quality” of the longitudinal phase-space in terms of combined uncorrelated energy spread and all imperfections of the phase space. The second cavity, BC2, compensates the energy chirp from BC1 and is set +10 to +40 deg off-crest. Note the phases quoted are in terms of the RF wave, not the bunch. The main linac cavities phases are chosen to (i) minimize energy spread if required; (ii) compensate a positive energy chirp from the injector and (iii) introduce a specific negative energy chirp for further bunch compression in the magnetic chicane. The linac off-crest phases are normally 0 to +16 deg.

Switching the machine from one mode of operation to another is often required on nearly daily basis. The adopted strategy for ALICE is that the beam energy in the injector is always kept constant of 6.5 MeV. Restoring of the setups relies on accurate, within a degree, phasing of all five RF cavities - the NC buncher pillbox cavity and the booster and the main linac each containing two SC cavities. The buncher zero-crossing is accomplished using the downstream BPM as a time-of-arrival monitor. The SC cavities are crested using downstream non-zero dispersion sections and predefined off-crest phases are set with calibrated phase shifters.

Beam dynamics investigation at nominal 60 pC bunch charges is hampered by irregular shape of beam images on screens where “two beams” can be often identified. This feature was recently investigated in more detail. Transversely, the two beams emerging from the booster are characterized by different size and divergence. Setting the second booster cavity at zero-cross phase allowed to imprint a specific energy chirp upon the electron bunch thus, in combination with the energy spectrometer, providing a means for evaluating the longitudinal structure. The two beams were found to be separated longitudinally. An example with the buncher power set deliberately high is shown in Fig. 3 and the longitudinal distance between the beams was measured to be 27 ps.

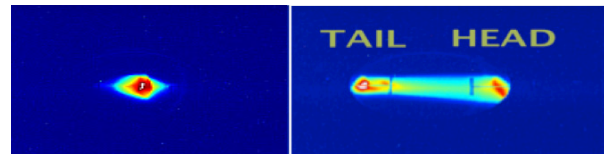


Figure 3: Two beams structure in non-zero dispersion section at high buncher power. Left – lower BC2 gradient just enough to equilibrate the energies of two beams. Right – at higher BC2 gradient to ensure energy separation between the two beams.

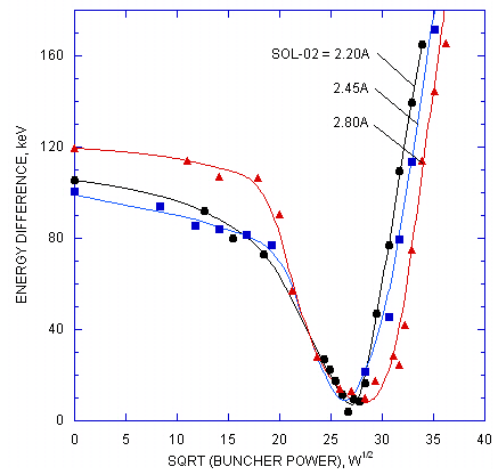


Figure 4: Energy difference between two beams in the injector as a function of buncher power at three different settings of the focusing solenoid. The energy chirp introduced by the second booster cavity BC2 is kept constant. Bunch charge is 60 pC.

The beams separation depends strongly on the buncher power (longitudinal compression) and on the strength of the solenoid located upstream of the booster (transverse focusing), see Fig. 4. This suggests that the space charge during the initial stage of the beam acceleration is an important factor in “two beams” formation and longitudinal separation between them. The other factor

could be temporally non-uniform laser pulse on the photocathode of the DC HV gun. ASTRA simulations suggest that the two beams could be formed with both, “flat” and “spiky”, laser pulses.

Currently, the formation of the two beams on ALICE could be amplified by low DC gun voltage of 230 kV and potentially non-uniform temporal laser pulse profile. Increasing the gun voltage should alleviate the problem but not eliminate it. The “two beams” could be therefore a feature of all injectors with DC photoelectron guns where acceleration in the first linac starts from non-relativistic electron energies (500 keV or lower).

Further experiments on ALICE will be conducted after installation of the large gun ceramic that will allow to increase the gun voltage to the design value of 350 kV. This will be complimented by measurements at various laser pulse profiles.

### COMPACT ERL TEST FACILITIES FOR LIGHT SOURCES

Currently there are no less than four ERL test facilities being planned or under construction in order to gather experience with ERL technology and prepare for large multi-GeV ERL light sources. There are two Chinese

projects, one at the Peking University [2] and one at the Institute for High Energy Physics (IHEP) also in Beijing [3]. KEK at Tsukuba, Japan is currently setting up a compact ERL extendable to a two-loop configuration [4] and *BERLinPro* at the HZB in Berlin, Germany, has been funded in October 2010 [5].

The common understanding is, that the ERL based radiation sources promise extremely attractive features, but that the technologies involved are so challenging, that they should be investigated and prepared in a test facility, which also covers the need for personal training. Common goals to all test facilities are to:

- Demonstrate high charge, low emittance bunches from the gun
- Gather experience with 1.3GHz superconducting accelerating structures
- Produce high average current, high brightness electron beams
- Demonstrate energy recovery
- Investigate high current effects like BBU, CSR, halo formation, space charge etc.

Table 1: Listing of Main Parameters of Four Compact ERL Projects

	units	Peking University	IHEP Beijing	KEK	BERLinPro
Gun		DC-SRF	DC 500KeV	DC 500keV	SRF
Bunch charge	pC	60	77	7.7-77	77
Current	mA	1.56	10	10-100	<100
Booster				3x2-cell	3x2cell
Merger		Dogleg 20° – sector dipoles	Chicane – 6 quads	Dogleg 16°– 2 quads	To be decided
Injection energy	MeV	6	5	5-10	5-10
Linac		1.3GHz 2x9cell TESLA	1.3GHz 2x7cell	1.3GHz (2-8)x9cell TESLA	1.3GHz 3x7cell
Energy	MeV	30	35	35-125/245	50
Emittance	mm mrad	4	2	0.01-1	<1
Energy spread	%	0.3	0.5	0.01-0.02	
Bunch length (rms) / compressed	ps	4 FWHM	2-4 / 0.2-0.5	1-3 / 0.1	2
R56 / T566		0.525/42.8	0.16-0.19	0.1 – 0.15	-0.4-0.4
Arc bends		4x45°	45°-90°-45°	4x45°	4x45°
Arc quads		5	3 x 2	3 x 2	7
Sextupoles		2	Under consideration	2 x 2	2
Insertion device	No of poles*period length[cm]	40*3	25*6	Laser Compton THz	Not in first stage

In Table 1, the main design parameters for the four projects are listed. The largest deviation between the projects can be found in the gun. While KEK and IHEP employ DC guns, Peking University puts much effort in developing a novel DC-SRF gun, and the HZB has set up a gun laboratory to develop an SRF gun. All guns, though, are expected to deliver the same 60-77 pC, 2-3 ps low emittance bunch, which is then accelerated to 5-10 MeV before it is injected into the recirculator. KEK and Peking University use a dogleg merger with quadrupoles and sector magnets respectively for dispersion

suppression. IHEP may proposes two different 3-4 dipole chicanes with two different injectors aiming at studying the possibility of accelerating the two beams from two gun simultaneously in the same main linac, one is directly for FEL experiment and another for ERL. However in the first phase of IHEP, only one DC-gun injector will be considered. The merger decision for *BERLinPro* is still open. The superconducting main linacs all run at 1.3 GHz, TESLA technology has been adopted in Peking University and an original 9-cell cavity with enlarged beam pipes and on-axis HOM absorbers has been

developed at KEK. The other projects focus on 7 cell structures. All recirculating arcs start with  $45^\circ$  dipoles to keep the dispersion low. While IHEP uses a  $90^\circ$  magnet at the center, KEK split this magnet into two  $45^\circ$  magnets. To control the path length up to half the RF wavelength the four  $45^\circ$  magnets are movable along the orbit for the upgrade to the two-loop configuration. BERLinPro and Peking University introduce one and three quadrupoles, respectively, between the two inner dipoles, providing more flexibility to fit  $R_{56}$  and the Twiss parameters simultaneously. Only the two Beijing projects include considerations for undulators/FEL operation from the beginning, while KEK has plans for laser-Compton scattering (LCS) x-rays and THz radiation without an undulator at the compact ERL.

Only a few contributions concerning nonlinear effects were made during this session. IHEP and BERLinPro comment on shaping the beta functions in the linac in order to suppress CSR and BBU, while BERLinPro sees matching difficulties between the second arc and the linac due to BBU conditions. KEK tries to minimize CSR effects by minimizing the betatron functions in the arc; IHEP uses Twiss parameter ( $\alpha_x$ ) matching in front of the first arc. Peking University and IHEP apply an energy spread suppression technique in the second arc to compensate the increase in energy spread due to the insertion devices.

#### *ERL Test Facility at Peking University: S. Huang (PKU)*

In slight deviation from the above mentioned goals, the focus of the ERL Test Facility at Peking University is to build an ERL-based radiation source (including an FEL) and especially to develop the superconducting photo-injector.

At present, the DC-SRF photo-injector and 2K cryogenic system have been installed. Preliminary beam loading tests on the injector agree well with dynamics studies and indicate that it is expected to produce electron beams with bunch charge of 60 pC, repetition rate of 26 MHz and normalized emittance better than 4 mm-mrad. The optics design for the ERL test facility has been carried out according to these characteristics.

The building to host the facility and the layout of the LHe transfer pipes pose constraints to the optics of the ERL test facility. The distance between the south straight section and north straight section is 4 m and the east arc is very close to the shielding wall, which leads to very compact arcs. However, as a test facility, the optics design gives as much flexibility for ERL and ERL-based FEL experiments as possible. For cost reason, the beta functions of the facility are controlled within 16 m, and the dispersion is within 1 m. Shown in Fig. 5 are the overall lattice, beta functions and dispersion.

Beam dynamics studies are ongoing. Further optimization of operation parameters for DC-SRF injector will be performed to improve the characteristics of the electron beam, especially to lower the transverse and longitudinal emittance.

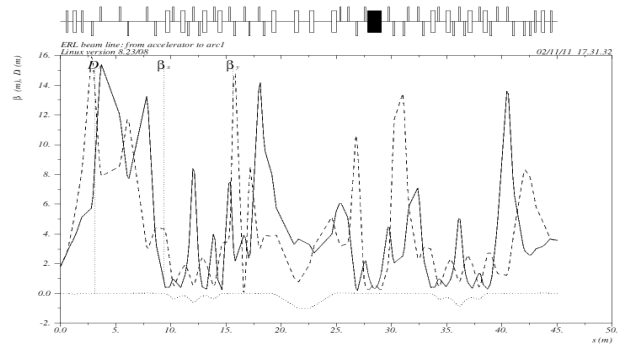


Figure 5: Beta functions and dispersion for the Peking University ERL test facility.

#### *ERL Test Facility at IHEP: J. Wang (IHEP)*

The layout of the 35 MeV, 10 mA ERL test facility at IHEP is as shown in Fig. 6. A 500 kV DC-gun and 5 MeV injector will provide the low emittance beam for the main linac. Two TBA arcs (each consist of  $45^\circ$ - $90^\circ$ - $45^\circ$  bending magnets, with some quads and sextupoles) and two long straight lines for the main linac and for the insertion device, respectively. The 77pC, 2ps bunch is compressed to 0.25-0.5ps with the 1<sup>st</sup> TBA arc to achieve high CSR-THz and/or THz-oscillator powers produced in a followed undulator. The emittance growth due to CSR during the bunch compression can be minimized to about 30% by employing envelope matching methods. The BBU threshold current could be higher than 260 mA by a code simulation. The energy spread minimization down to 1.5% of the decelerating beam is preliminarily studied by choosing the linac RF phase and  $R_{56}$  of the 2<sup>nd</sup> TBA arc. The 77pC, 5MeV, 2pS beam injection into the main linac is also preliminarily simulated with some beam emittance and bunch length growth mainly due to the space charge effect. Further studies are underway.

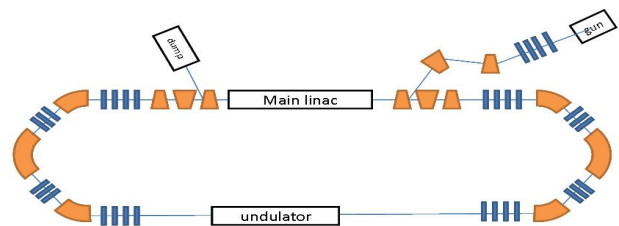


Figure 6: The layout of test ERL at IHEP, Beijing.

#### *Compact ERL Test Facility at KEK: M. Shimada (KEK)*

Also at KEK the long-term plan is to replace the photon factory by a combined ERL-XFEL-O facility. In a two stage approach, a 3 GeV ERL will be set up, which in a later stage and an electron beam accelerated twice to feed a 6-7 GeV XFEL-O without energy recovery. As a test

facility, the compact ERL extendable to 2-loop configuration is under construction in KEK site. For the first commissioning in 2013, one cryomodule including two 9-cell superconducting cavities will be installed in the one loop ERL. The full energy is 35 MeV. The compact ERL will be gradually upgraded to double loop scheme and the full energy of 245 - 250 MeV (injection energy is 5 - 10 MeV). The layout of the double loop is shown in Fig. 7.

Start-to-end (S2E) simulation is started to evaluate the beam quality and the emittance growth due to the space charge effect and CSR wake. Space charge effects, which are significant at low electron energy, are simulated by the code, General Particle Tracer (GPT). It is only used for injector and dump beam at less than 65 MeV because it consumes too much CPU time. The 6D electron distribution in the double loops is simulated by particle tracking code 'elegant' including the CSR wake.

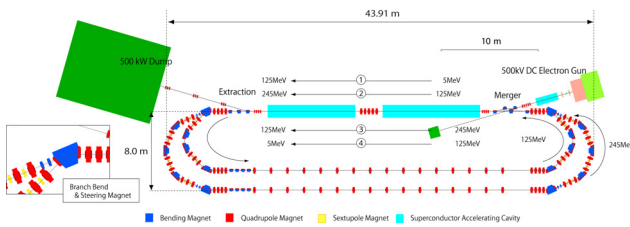


Figure 7: Layout of double loop compact ERL at KEK.

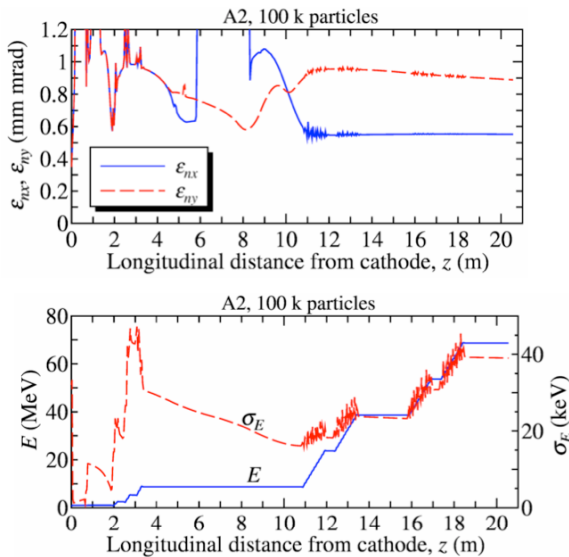


Figure 8: Optimization results of injector: transverse normalized emittance (upper) and electron energy and energy spread (lower).

Figure 8 shows simulation results of injector. The injection energy is 8.7 MeV and the electron charge is 77 pC. The normalized transverse emittance at 65 MeV is 0.54 mm-mrad[H] and 0.89 mm-mrad[V], which are restricted by the optical matching with the double loops shown in Fig. 9. The optical functions of double loops are

designed using dummy loops, which are composed of quads and drifts. The horizontal emittance increases at each arc in the double loops due to the CSR wake. It results in 5mm-mrad at the straight section in the outer loop. Further optics optimization will be done to reduce the horizontal emittance.

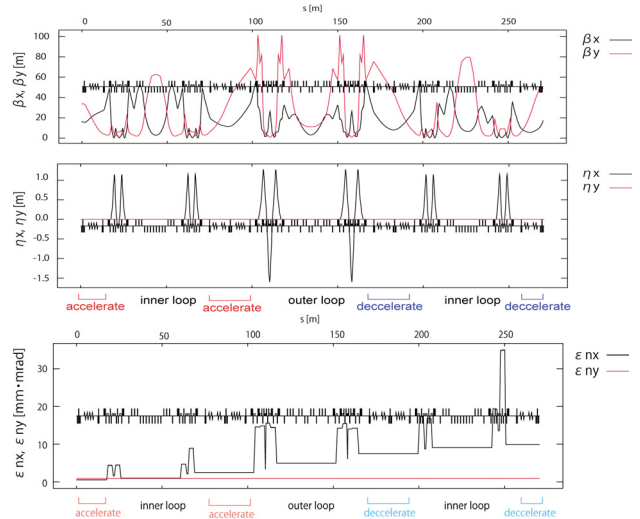


Figure 9: Betatron function (upper), dispersion function (middle) and transverse emittance of double loop compact ERL.

*BERLinPro – ERL Project in Berlin, Germany: B. Kuske (HZB)*

BERLinPro, a high current, low emittance ERL test facility at the HZB has been funded in October 2010. Due to the restricted financial frame, the project goals had to be de-scoped mainly by cutting down on the SRF systems. The layout of BERLinPro is shown in Fig. 10. The energy has been lowered to 50 MeV, which results in a severe cut in the radiation shielding requirements. The pulse-shaping unit for the cathode laser has been canceled. Figure 11 shows the effects of the pulse shaping on the bunch current profile and Figure 12 shows the bunch length dependence on laser pulse and bunch length development between the cathode and booster. The layout of BERLinPro could be adapted to the new requirements without severe performance degradation.

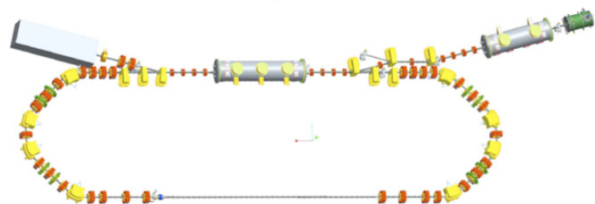


Figure 10: Layout of BERLinPro.

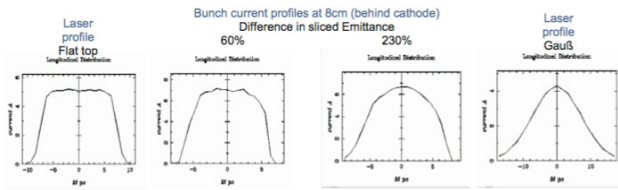


Figure 11: Laser pulse shape and current profile of the bunch behind the gun cavity for a flat top laser pulse (left) and a Gaussian laser pulse (right). The minor differences are further washed out and are negligible behind the booster longitudinally as well as in the transverse phase space.

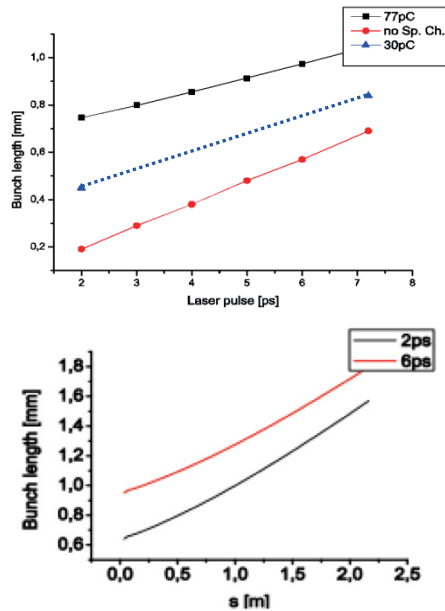


Figure 12: Upper: Bunch length as a function of the laser pulse length, behind the gun cavity for 77 pC (black) and without space charge (red); without space charge, velocity bunching shrinks the bunch to  $\sim 1/3$  of the laser pulse length. Space charge counteracts this process. Lower: Bunch length development between cathode and booster for a 2 ps and a 6 ps long laser pulse. The difference in bunch length is only  $\sim 15\%$ .

Beam dynamics studies for an injector with a half-cell SRF gun have been performed for low gun phases ( $10^\circ$  off zero phasing) and show that longitudinal bunch properties are dominated by velocity bunching and space charge rather than by the initial longitudinal laser profile or its length.

The reduction from 5 to 3 cavities in the booster module increases the RF focusing, as the injection energy remains at 5-10 MeV. The increased focusing can be compensated by a different solenoid setting. The first cavity can be used for velocity compression of the bunch. The two later cavities will have enough transmitter power for acceleration. The emittance behind the booster is 0.87 mm mrad for a 6 ps bunch.

It has been shown that for the 4 dipole chicane merger the number of quadrupoles necessary to keep the emittance below 1mm mrad grows with the shortening of the bunches, as space charge increases.

The BBU instability can be controlled by matching the beta functions in the linac. BBU conditions result in a minimum in both beta functions in front of the linac. To match these conditions, it seems helpful to keep the distance between the end of the second arc and the linac as short as possible and to provide high matching flexibility in the arc. For this reason an extra quadrupole has been introduced between the central  $45^\circ$  dipoles in the arc, and a scheme to include the last arc dipole into the chicane for the high energy beam is considered.

### LIGHTSOURCE ERLS

#### 3-GeV ERL at KEK: N. Nakamura(KEK)

KEK has a future project to construct an ERL-based light source as the successor of two existing SR sources at the Photon Factory, 2.5-GeV PF ring and 6.5-GeV PF-AR [6]. In the first stage of this project, a 3GeV ERL will be constructed with many insertion devices providing super-brilliant and/or ultra-short SR in the VUV to hard X-ray region. In the second stage, a 6-7 GeV XFEL-O, which can generate fully coherent X-rays, will be constructed. The schematic view of the ERL-based light source is shown in Fig. 13. In the XFEL-O operation, an electron beam is accelerated twice by the main linac without energy recovery and fed to the XFEL-O. The design study of the 3-GeV ERL was recently started. A test ERL, the compact ERL(cERL), is under construction in the KEK Tsukuba Campus and will be commissioned in 2013 to demonstrate excellent ERL performance toward the ERL-based light source project.

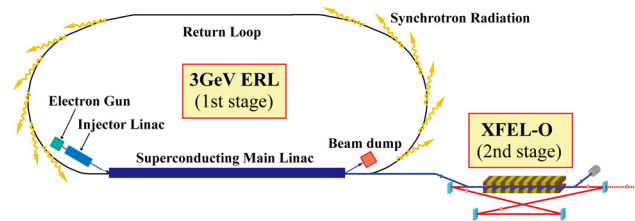


Figure 13: Schematic view of the ERL-based light source project at KEK.

Injector design and optimization of an ERL are very important for transporting high-current and low-emittance beams to the main linac without serious degradation of beam quality. The injector of the 3-GeV ERL will be designed based on design and operational experiences of the cERL injector. The cERL injector consists of a 500 kV photo cathode DC gun, two solenoid magnets, a buncher cavity, three superconducting RF cavities, five quadrupole magnets, and a merger consisting of three rectangular magnets with the bending angles of  $-16$ ,  $16$  and  $-16$  degrees, and two quadrupole magnets. By multi-

objective optimization with a genetic algorithm, the horizontal and vertical normalized emittances at the exit of the cERL injector were successfully optimized to be smaller than 0.6 mm mrad for the bunch length of 0.6 mm (2 ps), the beam energy of about 8.5 MeV and the bunch charge of 80 pC (more than 100 mA at 1.3 GHz repetition). In the injector of the 3-GeV ERL, the emittance should be reduced further to improve the light source performance. Higher injector energy and higher gun voltage are possible approaches, in addition to improving the injector design.

The main linac will consist of more than 200 superconducting (SC) 9-cell cavities, each of which has a moderate accelerating field of less than 15 MV/m to suppress field emission causing beam halo and radiation hazards. Quadrupole triplets are placed at every eight SC cavities for focusing. The optics of the main linac is mirror-symmetric for acceleration and deceleration and designed so that the betatron function is well suppressed for achieving a high BBU threshold current.

The return loop of the 3-GeV ERL have 28 TBA cells with 22 x 6 m and 6 x 30 m long straight sections for insertion devices. The bending radii of the bending magnets are sufficiently long to suppress emittance growth and increase of energy spread due to the incoherent synchrotron radiation (ISR) effects. Each of these cells is achromatic and isochronous and has a horizontal betatron phase advance of  $\pi$  per two cells so that CSR kicks to the beam can be considerably cancelled. Figure 14 shows preliminary optical functions of the main linac and the return loop. A bunch compression scheme should be studied by using off-crest acceleration in the main linac and non-zero  $R_{56}$  in the return loop in order to generate ultra-short bunches less than 100 fs. A chicane system changing a path length by a half RF wavelength is also needed for switching from energy recovery operation to XFEL-O operation. The tentative layout of the 3-GeV ERL with the XFEL-O in the KEK Tsukuba Campus is shown in Fig. 15.

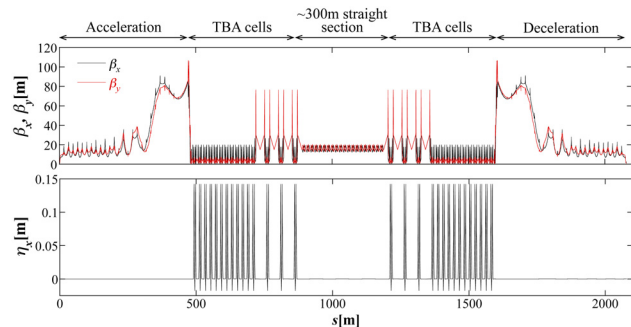


Figure 14: Betatron function (upper), dispersion function (bottom) of the main linac and the return loop of the 3-GeV ERL.

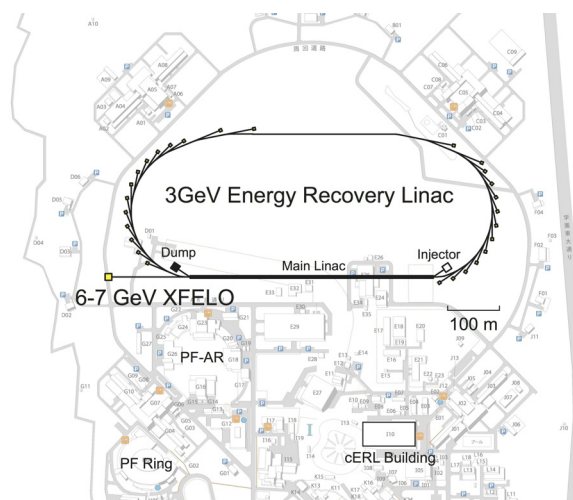


Figure 15: Tentative layout of the ERL-based light source in the KEK Tsukuba Campus.

### Cornell ERL: C. Mayes (Cornell U.)

The Cornell Laboratory for Accelerator-based Sciences and Education (CLASSE) is planning to build a hard x-ray ERL-based lightsource operating at 5 GeV at 1.3 GHz. The Cornell ERL will nominally provide three operating modes: High Flux operating at 100 mA, 0.3 mm-mrad normalized emittance and 2 ps bunch duration, High Coherence operating a reduced current of 25 mA with an enhanced normalized emittance of 0.08 mm-mrad, and Short Bunch operating at reduced current and short bunches of 100 fs duration.

This project is extensively documented in the Cornell ERL Project Definition Design Report (PDDR) [7], which begins with a chapter on the history and motivation for an ERL at Cornell. The accelerator chapter comprises the bulk of the PDDR, and includes sections on accelerator physics, the vacuum system, the injector, the linac, the RF systems, the electron transport lines, the beam stops, startup procedures, beam diagnostics and control, control system integration, and machine protection. A separate chapter outlines novel x-ray experiments and beamlines that are well-suited for ERL-quality beams. In addition to a chapter on conventional facilities, this document is supported by an economic impact report, a draft environmental impact report, a design for a new x-ray science building, a tunnel design and review, a proposal for the construction of the electron beamlines, and two proposals for the cryogenic system.

In preparation for this facility, CLASSE continues to perform essential research and development of key ERL technologies, and currently operates a prototype ERL injector, a dedicated photocathode laboratory, and an SRF laboratory. Novel insertion devices such as the ‘delta’ undulator are also being developed. Some recent achievements, including new world-record currents from the injector, are described in [8].

### Multi-turn ERL X-Ray Source (MARS):

G. Kulipanov (BINP)

A conception of the multi-turn accelerator-recirculator source (MARS) was proposed for realization of a fully spatially coherent X-ray source in 1997 [9]. The Novosibirsk ERL with two orbits and two FELs is operated towards MARS [10]. In order to generate fully spatially coherent undulator radiation with wavelength  $\lambda = 0.1\text{nm}$ , emittance of electron beam should be decreased to diffraction limit  $\varepsilon_{x,z} < \lambda/4\pi \approx 10^{-11}\text{m}$  at  $E = 5\text{-}6\text{ GeV}$ . Since high current up to 100 mA does not increase and even decreases the brightness sometimes, the average current does not need to be more than 10 mA. Radiation should be used only from three types of undulators with number of periods  $N_{u1}=100$ ,  $N_{u2}=1000$ ,  $N_{u3}=10000$ , not from bending magnets to keep the photon flux at the level of the 3<sup>rd</sup> generation sources.

The main disadvantage of the multi-turn ERL scheme with one accelerating structure is that two electron bunches (accelerating and decelerating) are circulated simultaneously at almost all the magnetic arcs. Radiation at an undulator in such an arc is generated by both accelerating and decelerating beams. This requires precise alignment and complicated control of the electron beams. Therefore, as shown in Fig. 16, it has been proposed to use scheme with two accelerating sections and separated magnetic arcs for accelerating and decelerating beams [10].

In this scheme, cascade injection system, which consists of two preliminary acceleration sections, is employed. This injection system accelerates electrons to energies 50 MeV and 400 MeV. This relatively high injection energy simplifies focusing of electron beams with different energies traveling simultaneously in the accelerating structure. Moreover, it increases the threshold current of the transverse beam breakup (BBU). For the same reasons, two asymmetrical main accelerating structures (0.7 and 1.9 GeV) are used. Use of the cascade injection and energy recovery decreases radiation hazard and the induced radioactivity due to the low energy of electrons at the dump (5-8 MeV), and leads to reduction in the cost of building and RF power supply for the injector.

Another advantage of the split accelerating structure is a possibility of servicing the multi-user community. A scheme with one undulator in Fig. 16 can be extended by installations of the long undulators into bending arcs 4. There are 7 undulators for 5.6 GeV, and 4 undulators for 3.7 GeV, 3 GeV and 1.1 GeV. To simplify the radiation output the magnetic arcs are separated both horizontally and vertically. A schematic view of MARS with these features is shown in Fig. 17.

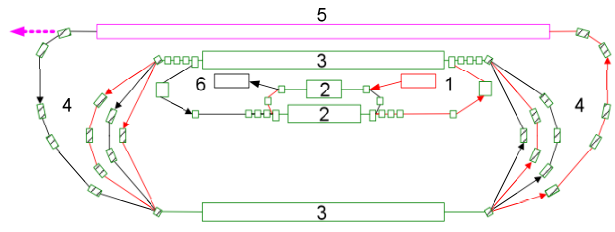


Figure 16: The simplest scheme of accelerator with 2 separated accelerating structures: 1-injector, 2 –two preliminary accelerating structures, 3 – two separated linacs, 4 – magnetic arcs, 5 – undulator, 6 – dump.

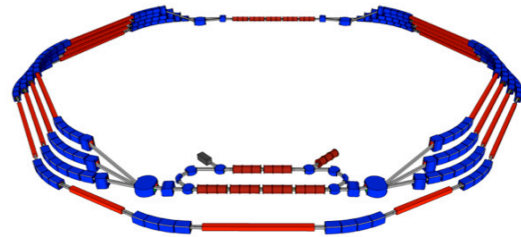


Figure 17: Scheme of MARS with main features: cascade injection, two accelerating structures, separated bending arcs, vertical separation of radiation beamlines.

Table 2: Parameters of MARS

Energy	5.6 GeV
Average current	10 mA
Peak current	10 A
Normalized emittance	0.1 mm mrad
Relative energy spread	$2.2 \cdot 10^{-5}$
SR sources	19 Undulators ( $N_u \sim 10^2$ , $N_u \sim 10^3$ , $N_u \sim 10^4$ )
Geometrical sizes	1x1 km

Since the magnetic structure of this accelerator is not an isochronous, all three types of beam-cavity interaction instabilities are excited (beam-loading, HOM transverse and longitudinal BBU). In the simplest case of single-cavity model, threshold current of transverse BBU was estimated and found that the threshold current of more than 10 mA can be achievable [11]. For beam-loading instability, simulations showed that there are areas of the stable accelerating phases. The main parameters of MARS are listed in Table 2.

*Laser Compton Scattered Gamma-ray Sources:*  
*R. Hajima(JAEA)*

The combination of an ERL and a high-power mode-locked laser realizes significant improvement of  $\gamma$ -ray sources based on laser Compton scattering (LCS) [12]. In order to obtain a high-flux  $\gamma$ -ray, it is necessary to increase the density of both electrons and photons at the collision point. An electron beam of small emittance and high-average current is essential to high-flux  $\gamma$ -ray generation via Compton scattering. The combination of an ERL and a laser enhancement cavity is, thus, a promising source of high-flux  $\gamma$ -rays. Figure 18 shows a schematic view of an ERL  $\gamma$ -ray source. At the collision point, electron bunches circulating the ERL loop collide with laser pulses stored in an enhancement cavity, which is a high-finesse Fabry-Perot optical resonator to stack a train of laser pulses from a mode-locked laser.

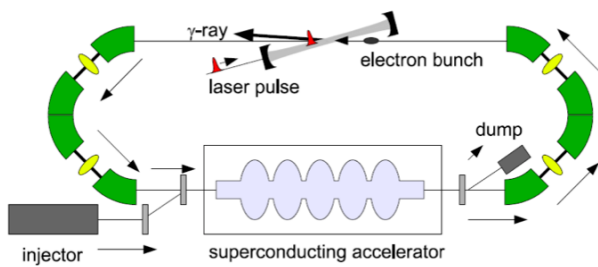


Figure 18: A schematic view of LCS  $\gamma$ -ray source based on an ERL and a laser enhancement cavity.

The effect of electron beam emittance on the broadening of  $\gamma$ -ray bandwidth becomes as small as the effect of laser diffraction when the normalized emittance  $\epsilon_n$  is equal to  $\lambda/4\pi$  ( $\lambda$ : laser wavelength). For a typical laser wavelength,  $1\mu\text{m}$ , the normalized emittance is  $0.08\text{ mm-mrad}$ , which is a similar value to the required emittance for ERL-based synchrotron radiation sources to obtain coherent hard X-rays.

Figure 19 shows the  $\gamma$ -ray spectrum calculated for a 2-MeV  $\gamma$ -ray source using a 350-MeV ERL in the narrow-bandwidth mode (10 pC, 0.1 mm-mrad, 130 MHz). For a 0.05-mrad aperture, the  $\gamma$ -ray bandwidth is 0.2% (FWHM). In the limit of small aperture at the narrow-bandwidth mode, the  $\gamma$ -ray bandwidth is restricted by the electron beam energy spread. Possible use of low-frequency spoke cavities achieves further reduction of LCS  $\gamma$ -ray bandwidth because of the smaller RF-correlated energy spread of electron beams. It should be noted that a LCS  $\gamma$ -ray source based on a storage ring has a limitation of  $\gamma$ -ray bandwidth resulting from a large energy spread of electrons at the equilibrium state, where the quantum excitation is balanced with the longitudinal damping.

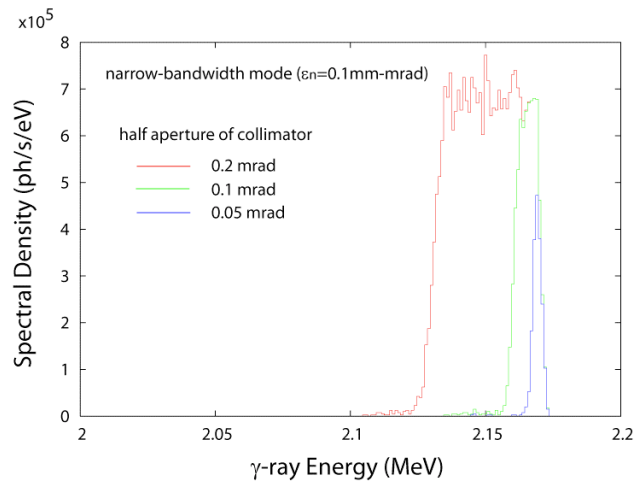


Figure 19: Calculated  $\gamma$ -ray spectrum from a 2-MeV  $\gamma$ -ray source using a 350-MeV ERL in the narrow-bandwidth mode (10 pC, 0.1 mm-mrad, 130 MHz) with various sizes of on-axis collimators. Collimator half aperture is 0.2 mrad, 0.1 mrad and 0.05 mrad.

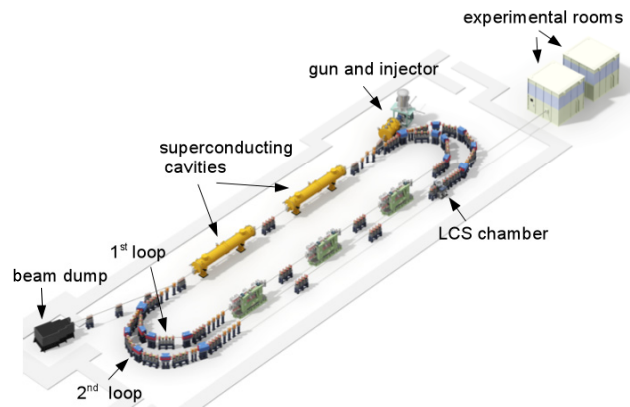


Figure 20: A schematic view of the LCS  $\gamma$ -ray experiment at the Compact ERL of KEK.

In order to demonstrate the performance of ERL  $\gamma$ -ray source and explore applications of ERL  $\gamma$ -ray sources to nuclear security and safeguards purposes, JAEA has launched a 3-year program (2011-2013) supported by Ministry of Education, Culture, Sports, Science and Technology (MEXT) in Japan. The program aims at generation of a high-flux and narrow-bandwidth  $\gamma$ -ray beam at the Compact ERL in collaboration with KEK. Application of the  $\gamma$ -ray to non-destructive measurement of isotopes is also planned. Figure 20 shows a schematic view of the proposed experiment at the Compact ERL.

## CODE SURVEY FOR ERL SIMULATION

*Survey on CSR codes - Contributors: G. Bassi, W. M. Fawley, R. Li, A. Novokhatski, K. Oide, J. Qiang, B. Terzic, J.-L. Vay, and D. Zhou*

The paper published by G. Bassi, et al. [13] gave a comprehensive overview of the CSR codes developed before 2006. Since then, tremendous efforts have been expended in developing new codes as well as investigating new numerical techniques. The present survey focuses on progresses of code developments since ERL2005. The purpose is to highlight the progresses of CSR code developments as well as new numerical techniques in the past several years. The new CSR codes are classified into 1D approach, Newton-Maxwell approach, approach with paraxial approximation, Vlasov-Maxwell approach, and Particle-In-Cell (PIC) approach. This classification is based on the numerical methods adopted by the CSR codes [14]. Another scheme is to classify the CSR codes into 1D, 2D, or 3D based on the simulated dimensions in real space.

**1D approach** CSR is included in the parallel beam dynamics code IMPACT [15]. In the code, the CSR model is a combination of the longitudinal CSR wake function to account for radiation fields and the three-dimensional short-range space charge fields [16]. The longitudinal wake function follows a physical model developed by Saldin et al. [17] and simplified by Borland [18] and by Stupakov et al. [19] under relativistic approximation. The line density function  $\lambda$  is obtained using a linear macroparticle deposition. This function and its derivatives are smoothed using a first-order Savitzky-Golay filter [20] or a custom designed local filter [21]. The CSR wake field is calculated following a direct double summation. The three-dimensional space-charge fields are calculated inside a locally rotated beam framework along the bending trajectory using the Green function method. The convolution is done numerically on a three-dimensional mesh using an FFT based method [22].

**Newton-Maxwell approach** Novokhatski developed a new 3D approach [23] to study CSR field dynamics. It is based on solving Maxwell's and Newton's equations. For this reason it can give fruitful information about the beam and field dynamics. It describes the radiation of a bunch in a metal chamber and includes geometrical wake fields. Another effect, especially important for the bunch compressors, is the acceleration or deceleration of a bunch due to the change of its shape and its position in a chamber. This method already predicted many new effects. The most important is the coherent energy spread. The numerical schemes are discussed in details in Refs. [24, 25]. The comparison with the THz measurements at ANKA is on the way.

**Approach with paraxial approximation** Since the mesh method by paraxial approximation was devised by Agoh and Yokoya [26], it has been extended by several

authors [27, 28, 29, 30] to calculate the CSR impedance in a single bending magnet or a series of bending magnets. By paraxial approximation, Maxwell's equations for CSR fields are simplified into a parabolic wave equations for the transverse electric fields.

Gillingham and Antonsen solved the parabolic equation in the time domain [27]. The space-charge effect was taken into account by keeping the dominant term of  $1/\gamma^2$  in the field equation. In their code, an unconditionally stable integration method with transparent boundary conditions was implemented. It allows the use of a minimally sized computational domain about the bunch. The causality condition was explicitly enforced so that no portion of the fields can propagate faster than the speed of light. Stupakov and Kotelnikov solved the parabolic equation in the frequency domain [28] using mode expansion method. The beam is assumed to be ultrarelativistic. In a vacuum chamber with uniform cross section, the electromagnetic fields generated by a bunched beam can be decomposed over the eigenmodes of the chamber. A computer code based on using the Mathematica programming environment [31] was developed to calculate the CSR impedance for a toroid of rectangular cross section. The mode expansion method is quite general and, in principle, is applicable to arbitrary cross section of the toroidal pipe.

Oide developed a new code independently [29]. The code is basically a Helmholtz solver using a finite difference method. It accepts arbitrary shapes of the beam pipe. The most important nature is that the coupling between  $E_x$  and  $E_y$  at the boundary is introduced via an expression of the Laplacian at the boundary. It is done by numerical fudge factors which are determined through comparison between numerical and analytic solutions for solvable cross sections, square and round pipes. Another characteristic of the code is that it is embedded in the SAD code [32] to utilize the object-oriented script language of SAD and incorporation with other accelerator calculations as well as graphics interfaces, etc. A new code CSRZ was developed by Zhou [30] to investigate the longitudinal coherent synchrotron radiation (CSR) impedance for a single or a series of bending magnets. To calculate CSR impedance, the mesh method developed by T. Agoh and K. Yokoya [26] was adapted to the case of a curved rectangular chamber with variable bending radius. In the code, the curvature of the beam trajectory can be set to be an arbitrary function of the distance along the beam orbit. Thus it allows calculating CSR impedance generated by a single bending magnet, a series of bending magnets interleaved with drift chambers, or a wiggler.

**Vlasov-Maxwell approach** Vlasov-Maxwell solvers aim to study the electrodynamics evolution of the system self-consistently with a mean field theory approximation, i.e. the system is evolved under the influence of its own electromagnetic fields generated by the macroscopic, or mean, charge/current densities. With this approximation, microscopic or collisional effects are neglected. Bassi et al. developed a self-consistent 4D Vlasov-Maxwell

Monte Carlo code VM3@A (Vlasov-Maxwell Monte-carlo Method @ Albuquerque). Because the source comes from the Vlasov equation the (Maxwell) self-field is a mean field. Significant progress has been made since the previous overview on CSR codes [23]. A parallel self-consistent algorithm has been developed and applied to study CSR effects and the microbunching instability in bunch compressors [33, 34, 35, 36, 37].

**PIC approach** Terzic and Li developed a new 2D code for self-consistent simulations of coherent synchrotron radiation (CSR) in beams [38]. The new code is based on the 2D CSR code developed by Li [39, 40] but is of the particle-in-cell (PIC) variety: the beam bunch is sampled by point-particles, which are deposited on the grid. The corresponding forces on the grid are then computed using retarded potentials according to causality, and interpolated so as to advance the point-particles in time. The retarded potentials are evaluated by integrating over the path history of the bunch, with the charge and current densities at the retarded time obtained from interpolation of the particle distributions recorded at discrete time steps. Vay and Fawley proposed a numerical scheme to speed up the CSR calculation. It is based on a suitable choice of the proper Lorentz boosted frame [41]. Orders-of-magnitude improvement on CPU-time has already been demonstrated for simulations from first principles of laser-plasma accelerators [42], free electron lasers [43], and particle beams interacting with electron clouds [44]. In [45], it is shown that this approach can be utilized in CSR calculations to remove the imbalance between the different scales in space and time of the problem by performing the calculation in a suitable Lorentz-boosted frame. Unlike some other lab-frame based approaches [26] no approximation of the Maxwell equations is required. The boosted-frame scheme is implemented in the parallel PIC code Warp [46]. Their results to date suggest that fully electromagnetic and accurate simulation of beam compressors is possible in regimes of great interest for design of linac-based short wavelength free electron lasers.

## CONCLUSIONS

Lessons from two existing ERLs, the JLAB ERL and ALICE at Daresbury Laboratory, are very instructive and we should learn design principles and operational experiences from the existing ERLs including the Novosibirsk ERL at BINP, the first multi-turn ERL in the world, which was presented in the WG2 session.

There are four test ERL projects for light sources being planned or under construction at Peking U., IHEP, KEK and HZB. Various parameters related to beam dynamics are listed for comparison of these ERLs and optics design and/or beam dynamics studies of each test ERL are also shown here. It is noted that a high-current test ERL for high-energy and nuclear physics is under construction at BNL. It may be effective for these facilities to share experiences of optics design and beam simulation,

because their accelerator energies, structures and scales are very similar.

Unlike the test ERLs, light-source ERLs have variety in their features. While the 3-GeV KEK ERL is a single-turn ERL with one accelerating structure and a 6-7 GeV XFEL-O, the 5-GeV Cornell ERL includes the existing ring CESR and two main accelerator sections. MARS project at BINP is a multi-turn 5-6 GeV ERL with split accelerating structure, a cascade injection system and separated magnetic arcs for accelerating and decelerating beams. Although these multi-GeV ERLs have many common beam dynamic issues for generating high brightness SR, they also have to solve issues peculiar to their projects. Gamma-ray ERL sources based on laser Compton scattering (LCS) are rather similar to test ERLs in many features and can share major beam dynamics issues with them. ERL projects for high energy and nuclear physics such as MESA, eRHIC and LHeC were also hot topics in this workshop and their beam dynamics issues should have been compared to one another and those of the other ERLs, though they are not described here.

Several simulation codes on CSR, space charge, IBS/Touschek scattering and field emission in a cavity and their simulation results were reviewed or presented in the plenary and WG2 sessions. CSR codes are systematically surveyed in this paper.

## ACKNOWLEDGMENTS

We would like to thank the ERL2011 committees, all the contributors to the presentations and discussions in Working Group 2, and those who provide material for this paper.

## REFERENCES

- [1] <http://erl2011.kek.jp>
- [2] S. L. Huang et al., "Optics Layout for the ERL Test Facility at Peking University", these proceeding.
- [3] S. H. Wang et al., "Design Studies on the ERL Test Facility at IHEP-Beijing", these proceedings.
- [4] M. Shimada et al., Proc. of IPAC11, San Sebastian, pp.1909-1911.
- [5] A. N. Matveenko et al., Proc. of IPAC11, San Sebastian, pp.1500-1502.
- [6] Energy Recovery Linac Preliminary Design Report (2012); N. Nakamura, Proc. of IPAC12, New Orleans, pp.1040-1044.
- [7] Cornell Energy Recovery Linac Project Definition Design Report, G. Hoffstaetter, S. Gruner, M. Tigner, eds. <http://erl.chess.cornell.edu/PDDR/> (2012).
- [8] C. Mayes *et al.*, Status of the Cornell ERL, ICFA Beam Dynamics Newsletter 58, pp. 112-118 (2012).
- [9] G. N. Kulipanov, A. N. Skrinsky, N. A. Vinokurov, J. of Synch. Rad. **5** (1998) 176.
- [10] N. A. Vinokurov et al., Proc. of IPAC10, Kyoto, pp.2427-2429.

- [11] G. N. Kulipanov et al., "Multi-turn ERL X-ray Source (MARS) Feasibility Study", these proceedings.
- [12] R. Hajima, "Laser Compton Scattered Gamma-ray Sources", these proceedings.
- [13] G. Bassi, et al., Nucl. Instrum. Methods Phys. Res., Sect. A 557, 189 (2006).
- [14] M. Dohlus, EPAC 2006, p.1897.
- [15] J. Qiang, R. Ryne, S. Habib, V. Decyk, J. Comp. Phys. vol. 163, 434, (2000).
- [16] J. Qiang, R. D. Ryne, M. Venturini, A. A. Zholents, I. V. Pogorelov, Phys. Rev. ST Accel. Beams, 12, 100702 (2009).
- [17] E. L. Saldin, E. A. Schneidmiller, and M. V. Yurkov, Nucl. Instrum. Methods Phys. Res., Sect. A398, 373 (1997).
- [18] M. Borland, Phys. Rev. Special Topics - Accel. Beams 4, 070701 (2001).
- [19] G. Stupakov and P. Emma, "CSR Wake for a Short Magnet in Ultrarelativistic Limit," SLAC-PUB-9242, 2002.
- [20] W. Press, S. Teukolsky, W. Vetterling, and B. Flannery, Numerical Recipes in FORTRAN, Cambridge University Press, New York, 1992.
- [21] I. Pogorelov, J. Qiang, R. D. Ryne, M. Venturini, A. Zholents, R. Warnock, in Proceedings of 9<sup>th</sup> Int. Comp. Accel. Physics Conf., p. 182, 2006.
- [22] J. Qiang, S. Lidia, R. D. Ryne, C. Limborg-Deprey, Phys. Rev. Special Topics - Accel. Beams 9, 044204, (2006).
- [23] A. Novokhatski, Phys. Rev. ST Accel. Beams 14, 060707 (2011).
- [24] A. Novokhatski and M. Sullivan, IPAC'10, TUPEB028.
- [25] A. Novokhatski, PAC'11, TUOAN1.
- [26] T. Agoh and K. Yokoya, Phys. Rev. ST Accel. Beams, 7(5):054403 (2004).
- [27] D. R. Gillingham and T. M. Antonsen, Jr, Phys. Rev. ST Accel. Beams 10, 054402 (2007).
- [28] G. V. Stupakov and I. A. Kotelnikov, Phys. Rev. ST Accel. Beams 12, 104401 (2009).
- [29] K. Oide, et al., PAC'09, MO3RAI01.
- [30] D. Zhou, Ph.D. thesis, KEK/SOKENDAI, Sep. 2011.
- [31] Stephen Wolfram, The Mathematica Book, 5<sup>th</sup> ed. (Wolfram Media, 2003).
- [32] SAD home page: <http://acc-physics.kek.jp/SAD/>
- [33] G. Bassi, J. A. Ellison, K. Heinemann, and R. Warnock, Phys. Rev. ST Accel. Beams 12, 080704 (2009).
- [34] G. Bassi, J. A. Ellison, K. Heinemann, and R. Warnock, Phys. Rev. ST Accel. Beams 13, 104403 (2010).
- [35] B. Terzic and G. Bassi, Phys. Rev. ST Accel. Beams 14, 070701 (2011).
- [36] G. Bassi, J. A. Ellison and K. Heinemann, Proceedings of ICAP09, San Francisco, September, 2009. See Jacow for ICAP09.
- [37] K. Heinemann, Two topics in particle accelerator beams: A Vlasov-Maxwell treatment of coherent synchrotron radiation and topological treatment of spin polarization, PhD dissertation, Math&Stat, University of New Mexico, May 2010. Archived on ProQuest.
- [38] B. Terzic and R. Li, PR ST-AB, in preparation, 2012.
- [39] R. Li, Nucl. Instrum. Meth. Phys. Res. A, 429:310, 1999.
- [40] R. Li, Proc. of The Second ICFA Advanced Accelerator Workshop on the Physics of High Brightness Beams, 1999.
- [41] J.-L. Vay, Phys. Rev. Lett. 98 (2007) 130405.
- [42] J.-L. Vay, C.G.R. Geddes, E. Cormier-Michel, D.P. Grote, Phys. Plasmas 18 (2011) 030701.
- [43] W. Fawley, J.-L. Vay, AIP Conf. Proc. 1086 (2009) 346.
- [44] J. L. Vay, Phys. Plasmas 15 (2008) 056701.
- [45] W.M. Fawley, J.-L. Vay, Jacow Conf. Proc. IPAC10 (2010) 1874.
- [46] D.P. Grote, A. Friedman, J.-L. Vay, and I. Haber, AIP Conf. Proc. 749 (2005), 55.

# OPTICS LAYOUT FOR THE ERL TEST FACILITY AT PEKING UNIVERSITY\*

S. L. Huang, K. X. Liu, S. W. Quan, L. Lin, F. Zhu, J. E. Chen,  
IHIP, School of Physics, Peking University, Beijing 100871, China

## Abstract

An ERL test facility will be built at Peking University, which incorporates the compact DC-SRF photo-injector, a superconducting module composed of two 9-cell TESLA-type cavities and a high average power IR FEL oscillator. Physical design of the test facility has been updated according to the expected characteristics of the DC-SRF photo-injector and accelerating module. In this work we will describe the physical issues in detail, especially the latest optics for the facility.

## INTRODUCTION

An ERL (Energy Recovery Linac) test facility is under construction at Peking University, with the primary goals to study energy recovery, to demonstrate ERL-based FEL, and to develop the related technologies for ERL, especially those technologies on superconducting photo-injector and superconducting accelerator.

The test facility incorporates the compact DC-SRF photo-injector [1], a superconducting linac composed of two 9-cell TESLA-type cavities and a high average power IR FEL oscillator. The DC-SRF photo-injector, which integrates a DC pierce gun and a 3.5-cell superconducting RF cavity, was designed to produce 6 MeV electron beams with bunch charge of 60 pC, repetition rate of 26 MHz and normalized emittance less than 2 mm-mrad. At present, the DC-SRF photo-injector and 2K cryogenic system have been installed. Preliminary beam loading tests on the injector agree well with dynamics studies and indicate that it is expected to deliver electron beams with bunch charge of 60 pC, repetition rate of 26 MHz and normalized emittance better than 4 mm-mrad.

The single-pass superconducting linac will accelerate the electron beam to full energy of 30 MeV. After bunch compression to 4 ps (FWHM), the electron beam will be used to drive the IR FEL oscillator. The recirculated electron beam, after FEL interaction, is decelerated by the same linac 180 degrees out of the accelerating phase, which leads to energy recovery. Due to cost reason, the ERL test facility is designed to operate in long pulse mode, with a macro pulse length of 2 ms and repetition rate of 10 Hz.

The IR FEL oscillator is designed to lase within 5-10  $\mu\text{m}$ . Calculations show that out-coupled macro pulse power of hundreds watts can be achieved. FEL lasing within middle IR to THz regime is also under consideration, which may be realized by reducing the ERL full energy and using wigglers with longer period

length. A list of the baseline parameters for the ERL-based IR FEL is shown in Table 1.

Table 1: Baseline Parameters for the ERL-based FEL at Peking University

Electron Beam Parameters	
Energy [MeV]	30
Energy spread, FWHM	0.32%
Bunch charge [pC]	60
Normalized emittance [mm-mrad]	4
Bunch length, FWHM [ps]	4
Micro pulse repetition rate [MHz]	26
Macro pulse length [ms]	2
Macro pulse repetition rate [Hz]	10
Wiggler Parameters	
Period length [cm]	3
Gap [mm]	12 (21)
Kw, rms	1.14 (0.41)
Number of wiggler periods	40
Beta function @ wig centre, horiz. [m]	0.346
Beta function @ wig centre, vert. [m]	0.245 (0.677)
Alpha @ wiggler centre, horiz.	0
Alpha @ wiggler centre, vert.	0
Optical Cavity Parameters	
Cavity length [m]	11.5305
Rayleigh range [m]	0.8
Mirror radius of curvature [m]	5.876
g1.g2	0.93
Extraneous loss	2%
Out-coupling	8% (1%)
FEL Parameters	
Wavelength [ $\mu\text{m}$ ]	10.03 (5.1)
Gain	0.30 (0.10)
Out-coupled peak power [MW]	2.12 (0.97)
Out-coupled macro pulse avg power [W]	220.7 (101.2)
Out-coupled avg power [W]	4.4 (2.0)
Intra-cavity peak power [MW]	26.53 (97.31)
Intra-cavity avg power [W]	55.2 (202.4)

\*Work supported by National Basic Research Program of China (2011CB808304).

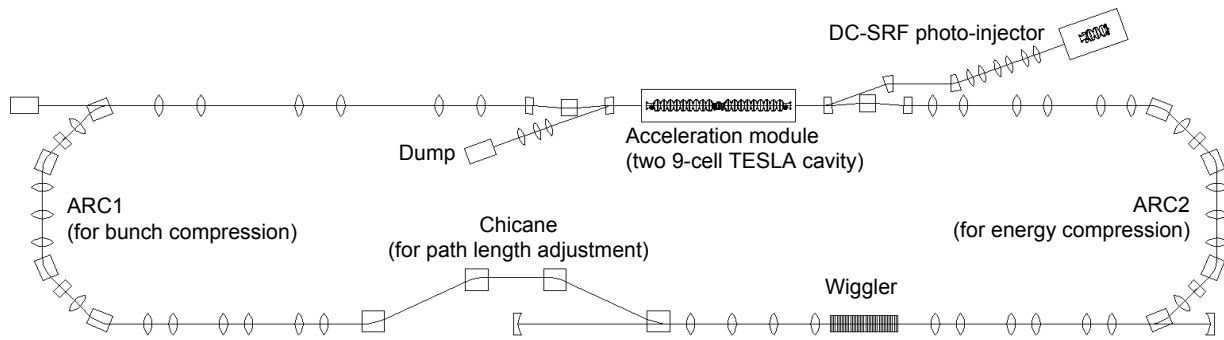


Figure 1: Optics for the ERL test facility at Peking University.

**OPTICS FOR THE ERL TEST FACILITY**

Shown in Figure 1 is a schematic layout of the overall optics for the ERL test facility, which is essentially a revision of [2]. The building to host the facility and the layout of the LHe transfer pipes pose stringent constraints to the optics of the ERL test facility. The distance between south straight section and north straight section is 4 m and the return arc is very close to the shielding wall, which leads to very compact arcs. The FEL oscillator is placed opposite the linac for both cost consideration and space limitation. A 4-dipole chicane is used for path length adjustment, while the outward arc (ARC1) is used to compensate R56 for optimized bunch compression of electron beam in FEL operation. The return arc (ARC2), which has a similar optics layout as ARC1, is used for bunch decompression and energy spread compression of electron beam after FEL interaction. Optics design were performed with MAD8 [3]. At full energy of 30 MeV, analytical calculation and ASTRA [4] tracking show that space charge effect can be neglected.

*Injection*

The injection line, which transports electron beam from the DC-SRF injector into ERL beam line, consists of three doublets and a 3-dipole achromatic dog-leg. The injection

angle is chosen to be 20 degrees due to space limitations. The three doublets are used to match electron beam into the linac, which allow variation of injector parameters. Beta functions and dispersion through the injection line are shown in Figure 2.

*Chicane*

The 4-dipole chicane is used for path length adjustment. By tuning the bending angles of dipoles between 24.4 and 25.6 degrees, the path length can be changed by 3.74 cm, corresponding to an RF phase change of about 60 degrees. The according R56 of the chicane is between -0.785 and -0.883 m. During the path length adjusting, Twiss parameter does not change much, as shown in Figure 3. Path length adjustment outside this tuning range can be realized by moving the second and third dipoles towards/against each other.

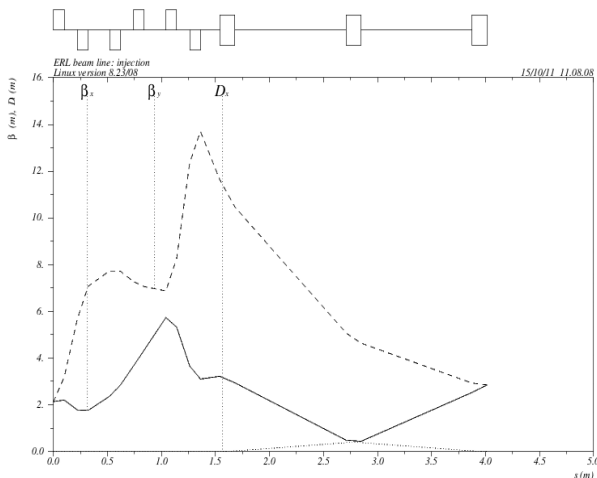


Figure 2: Beta functions and dispersion through the injection line.

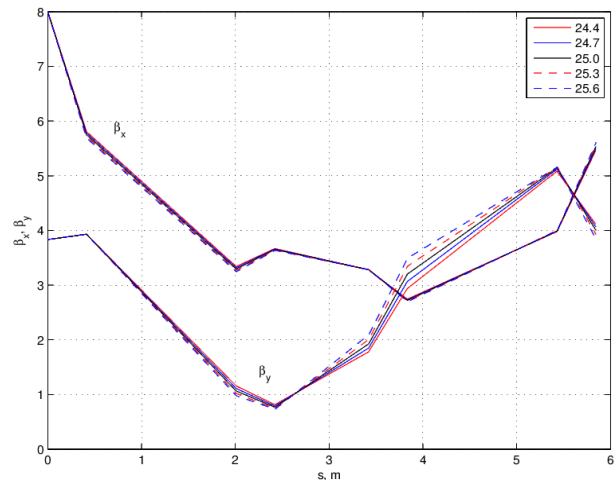


Figure 3: Beta functions through the chicane for different bending angles.

*Arcs*

The outward arc (ARC1) and return arc (ARC2) have similar optics layout; each consists of four 45-degree rectangular dipoles, three sets of quadrupoles for R56 adjustment and two sextupoles for T566 adjustment. When adjusting the path length of electron beam with the chicane, R56 of the outward arc is tuned accordingly for optimized bunch compression. With this arc design,

quadrupole strength does not change much during the R56 tuning when path length is adjusted by about 6 cm (corresponding to an RF phase change of about 90 degrees), which diminishes the effects exerted on transverse phase space by the longitudinal phase space tuning. To compensate R56 from the chicane for optimized bunch compression of electron beam in FEL operation, R56 of the outward arc will be tuned between 0.25 and 0.37 m. The optics is accordingly optimized so that beta functions do not change much at the arc exit for different R56s, as shown in Figure 4. R56 of the return arc is 0.525 m, which makes the entire transport approximately isochronous.

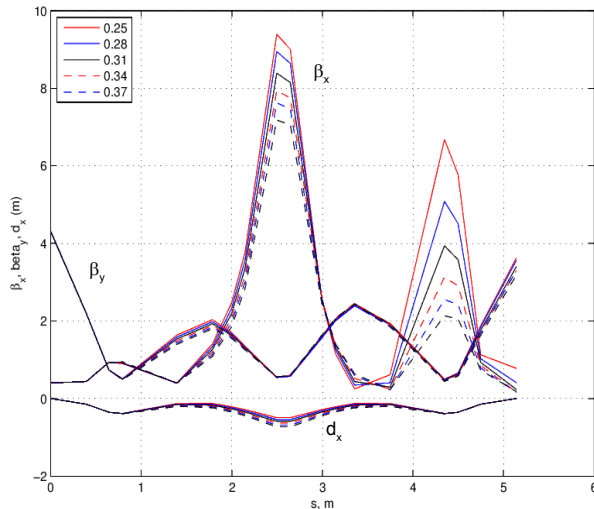


Figure 4: Beta functions and dispersion through the outward arc (ARC1) for different R56s.

### Matching Optics

The transfer line from the linac to the outward arc composes a symmetric extraction chicane and a straight section of about 7.5 m long, on which are located three doublets for electron beam matching into the outward arc. The extraction chicane consists of three dipoles; on both ends are sector bends, while in between is a rectangular bend.

The transfer line from the outward arc to the 4-dipole chicane consists of three doublets for electron beam matching into the chicane and beam envelop controlling. The transfer line from the chicane to the wiggler consists of four quadrupoles, which are used to optimize the transverse phase space of electron beam for FEL operation.

The transfer line from the wiggler exit to the return arc consists of three doublets, which are used to match the electron beam after FEL interaction into the return arc and control the beam envelop.

The transfer line from the return arc to the linac is very similar to that from the linac to the outward arc. It comprises three doublets for electron beam matching into the linac and a symmetric 3-dipole chicane with sector bend at both ends and rectangular bend in between.

The overall beta functions and dispersion for the test facility are shown in Figure 5.

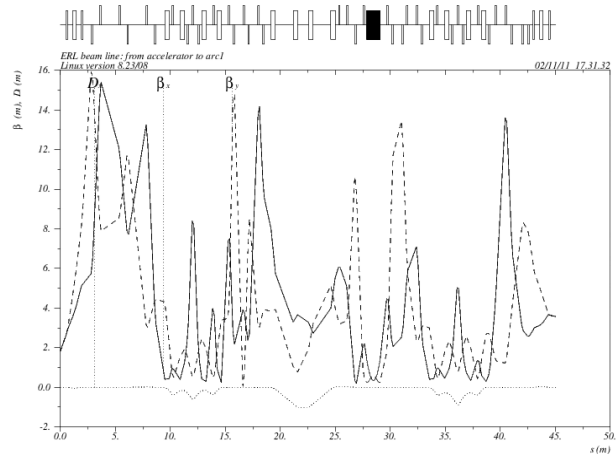


Figure 5: Beta functions and dispersion for the ERL test facility. Bending angle of the chicane dipoles is 25 degrees; R56 of ARC1 is 0.308 m, R56 of ARC2 is 0.525 m, R56 of the chicane is -0.833 m.

## SUMMARY

The optics design for the ERL test facility at Peking University has been updated according to the expected characteristics of DC-SRF photo-injector and accelerating module. The constraints to optics from the building to host the ERL test facility and the layout of LHe transfer pipes have been taken into account in the design.

As a test facility, the optics design gives as much flexibility for ERL and ERL-based FEL experiments as possible.

Study on beam dynamics is on-going. Further optimization of operation parameters for DC-SRF injector will be performed to improve the characteristics of the electron beam, especially to lower the transverse and longitudinal emittance.

## REFERENCES

- [1] F. Zhu, et al, Chinese Physics C, 31 (5), p. 496 (2007).
- [2] G. M. Wang, PhD Dissertation, Peking University, June, 2008.
- [3] H. Grote and F. Christoph Iselin, The MAD Program User's Reference Manual, CERN/SL/90-13 (AP) (Rev. 5).
- [4] G. Poeplau, et al, Proceedings of EPAC 2006, Edinburgh, Scotland, WEPCH121, p. 2203 (2006).

# DESIGN STUDIES ON THE ERL TEST FACILITY AT IHEP-BEIJING

S.H.Wang, J.Q.Wang, S.Y. Chen, Y.L.Chi, G.W. Wang, J.S. Cao, S.G. Liu, J.Gao, J.Y. Zhai, W.B.Liu, X.H.Cui, J.Q. Xu, Z.S. Zhou, X.P. Li, H.H. Lu, Q. Xiao  
Institute of High Energy Physics, CAS, Beijing 100049, China

## Abstract

A compact ERL test facility has been proposed at IHEP-Beijing. The design study is briefly presented, including the main parameters, essential lattice and the features of the key components, such as photo-cathode DC gun and CW superconducting accelerating structures. Some important beam physics issues such as space charge effects, coherent synchrotron radiation (CSR) effect and beam break-up (BBU) effects are described with the simulation results.

## INTRODUCTION

The linac based Free Electron Laser (FEL), and the Energy Recovery Linac (ERL) based light source are the two major types of the 4th generation light source. FEL has higher brightness, shorter pulse length and higher coherent features, but with a minor photon beam lines. ERL combines the good beam performance of the linac and good operation efficiency of the storage ring machine, although its brightness and coherent degree not as higher as FEL, but with many (more than 30) photon beam lines. Hence, both FEL and ERL cannot be replaced each other, we really need both of them. Based on this point, IHEP has proposed a suggestion of “one machine two purposes”, both FEL and ERL will share a same super-conducting (SC) linac for having a high efficiency [1]. The design study on the ERL-FEL Test Facility (ERL-TF) has been started at IHEP and being well progressed.

A compact ERL Test Facility is proposed at IHEP-Beijing, aiming at studying the ERL's key technology, such as photo-cathode high voltage DC gun, low emittance injector, merger system, CW multi-cell SC cavity and some beam physics problems including CSR, BBU effects and so on. The main parameters of the test facility are listed in Table 1. Figure 1 shows the ERL-TF layout. A 500 keV photo-cathode DC gun followed by a 5 MeV injector provide electron beam for the SC linac, with bunch length of (2~4) ps and normalized emittance of (1~2) mm-mrad. Two 1.3 GHz 7-Cell SC cavities accelerate the 10 mA beam to 35 MeV. The beam circulating loop consists of two TBA arc sections and two straight sections. As beam passing through the 1st TBA, the bunch length may be compressed to 0.5 ps (as one of the options), and then get into a wiggler at south straight section to produce a coherent THz wave with very high average power. Then beam passes the 2nd TBA and gets into the linac again to recover its beam energy to the structure at the deceleration RF phase. Then the 5 MeV beam gets into the beam dump. Table 1 shows the main parameters of the ERL-TF.

Table 1: Main Parameters of the Test Facility

Beam energy	35 MeV
Beam current	10 mA
Bunch charge	77 pC
Normalized emittance	(1~2) mm-mrad
RMS energy spread	0.5% ~ 1.0%
Bunch length	(2~4) ps
Bunch frequency	130 MHz
RF frequency	1300 MHz
Beam energy	35 MeV

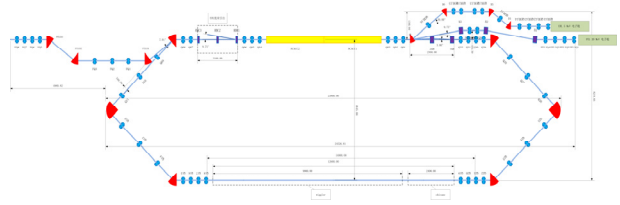


Figure 1: L Layout of the test facility.

## INJECTOR DESIGN

The injector for the ERL test facility includes a 500 keV DC gun with GaAs photo-cathode, two solenoids, a 1.3GHz normal conducting RF buncher, and two 2-cell superconducting RF cavities as energy booster. The layout is shown in Figure 2.

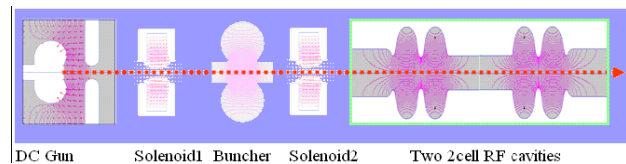


Figure 2: Injector Layout.

### Photo-cathode DC Gun

To steady support a 500 keV high voltage between cathode and anode for the DC gun, besides employing an optimized ceramic insulator, avoiding the emitted electrons on the ceramic insulator is also very important. In our gun body design, the KEK/JAEA option is adopted [2], in which a segmented insulator structure with guard rings between every two adjacent segments is employed to effectively avoid the emitted electrons toward the ceramic insulator and hence to mitigate field emission, as shown in Figure 3. The gun body and the guard rings are made of titanium alloy to minimize the gassing rate and to keep a very high vacuum in the gun. For a 500 kV high voltage, if the gap between cathode and anode is 12 cm, then the maximum field gradient on the cathode surface is

5.48MV/m and the maximum gradient along z axis is 6.45MV/m [3]. Recently, IHEP has decided to fund this gun's construction.

Table 2: Main Parameters of the DC Gun

High voltage	350 ~ 500 kV
Cathode material	GaAs:Cs
Quantum efficiency	5-7% (initial) , 1%
Live time	20 h
Driven laser	2.3W, 530nm
Repetition rate	130MHz , 1.3GHz*
Nor. emittance	(1~2)mm.mrad@77pC/bunch; (0.1~0.2)mm.mrad@7.7pC/bunch
Bunch length	20ps
Bunch charge	77pC
Beam current	(5~10) mA
High voltage	350 ~ 500 kV

\* Two operation modes:

- (1) 130MHz-10mA-77pC, (2) 1300MHz-10mA-7.7pC.

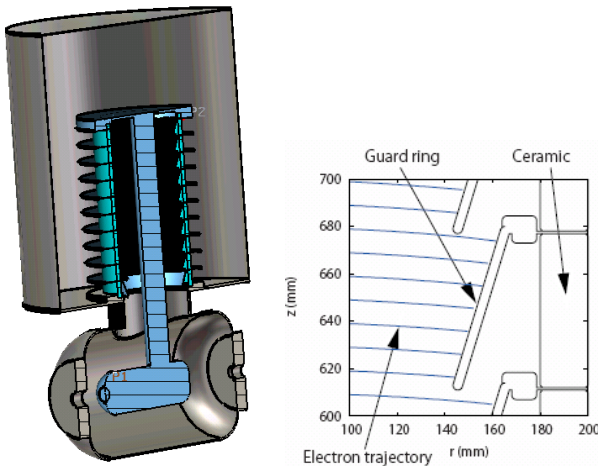


Figure 3: DC gun with segmented insulators (left) and guard rings(right).

### 2-cell Superconducting RF Cavity

The 2-cell cavity's parameters are listed in Table 4. The electric field distribution is shown in Fig. 4

Table 3: ERL-TF 2-cell SC Cavity Parameters

Wave mode	Standing wave
Operation mode	TM010, $\pi$ -mode
Fundamental mode frequency	1300.000 MHz
Accelerating gradient	15 MV / m
$Q_0$	$1 \times 10^{10}$
Effective length	0.2292 m
Geometry factor ( $G$ )	274.5 $\Omega$
$R / Q$	214.2 $\Omega$
$G \cdot R / Q$	58776 $\Omega^2$
$E_{peak} / E_{acc}$	2.02
$B_{peak} / E_{acc}$	4.2 mT / ( MV / m )
Wave mode	Standing wave

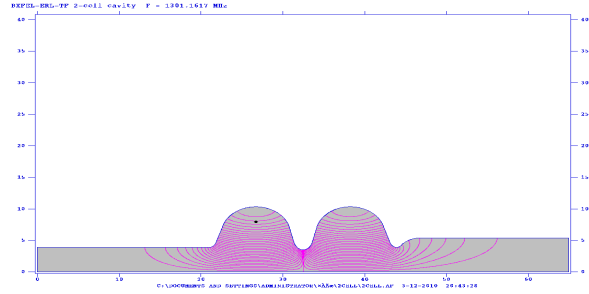


Figure 4: Electric field distribution in 2-cell cavity.

Due to the high average beam current (10 mA) , low accelerating gradient (5 ~ 15 MV/m) and small cell numbers, we firstly consider the HOMs (Higher Order Modes) suppression and to lower the surface field in the structure, then to lower the cryogenic loss of the fundamental mode (i.e. increase the  $G \cdot R / Q$ ). The cavity shape is based on the TESLA design but with one-side beam pipe enlarged, so that most of the HOMs with frequencies higher than the cut-off frequency of the pipe (except a few quadrupole modes) can propagate to the HOM absorbers. The diameter of the beam pipe on the main coupler side is 78 mm (same as TESLA cavity), and in the other side the beam pipe is increased from 78 mm to 108 mm. The transition between the cavity and large beam pipe is made with two arcs of  $R = 6$  mm and  $R = 30$  mm with multi-pacting free geometry [4]. To avoid Q-value decrease of the fundamental mode by the HOM absorbers, the beam pipe length is relatively long (210 mm).

### Injector Beam Simulation

The injector beam simulation aims at having small emittance, short bunch length, small energy spread and compact structure. Because the field gradient in this gun is low, the space charge is the dominated effect to the beam quality of a 77pC bunch. The optimised parameters for simulation are as following: Laser RMS beam size is 1.2mm with longitudinal flat-top of 20ps long, rise and down time are all 2ps. In the photoemission process, GaAs cathode is illuminated by 532nm laser. Photoelectrons have initial kinetic energy of 0.2eV. The thermal emittance due to the initial energy is taken into account in the simulation.

The two solenoids are used to have a reasonable transverse beam size in the buncher and in the energy booster. A little bit emittance compensation effect can be made by them also. The bunching phase is so chosen so that a good velocity modulation can be achieved for the original long bunch. The normal conducting RF cavity buncher can operate in CW mode with a water cooling system.

The two 2-cell SC RF cavities accelerate the beam from 0.713MeV to 5MeV. The maximum field gradient should be set to 20MV/m. All components of the injector are designed and optimized with SUPERFISH and POISSON code. The beam simulation along the injector

is performed with ASTRA code. The beam parameters at the injector exit are listed in Table 4.

Table 4: Beam Parameters at the Injector Exit

Beam energy	5 MeV
Current	10 mA
Normalized emittance	1.49 mm-mrad
RMS bunch length	0.67 mm (2.2 ps)
RMS energy spread	0.72%
Total injector length (from cathode to the cryomodule exit)	3.2 m

## PRELIMINARY STUDIES ON THE ERL-TF BEAM PHYSICS

As shown in Figure 1 two small emittance TBA arc sections, each composed of 450-900-450 three bends, are adopted to easily adjust the beam transport matrix elements of R56 and T556 for meeting the right phase of the re-circulated beam at the linac entrance, and to easily adjust T166 and T266 to control the beam emittance. The accelerating structures are placed in the north straight section and the insertion device is placed in the south straight section for high power THz wave productions. The focusing strength of the quads in the acceleration area are optimised both for accelerating and decelerating beams. A so called “Graded Gradient” method [5] is used for this purpose, which makes the optics fully matching to the lower energy beam (due to its larger geometry emittance), and properly chose the beta function to control the beam envelope of the higher energy beam (due to its smaller geometry emittance).

To have a higher averaged power of the THz-FEL, the bunch length should be compressed before it arrives at the entrance of the insertion device. First let the beam to be accelerated at the RF phase of about  $15^\circ$  to increase the beam energy spread as well, then using the 1st TBA to compress the bunch length from 2 ps to about 0.3 ps with a TBA's R56 of 0.165, making the peak current to be increased by a factor of higher than 6. The emittance growth caused by the bunch compression is about 35%. With a 1.5 m long wiggler, a THz coherent synchrotron radiation with high average power of 270 W can be obtained, or a THz-FEL with average power of 9 kW by using an optical oscillator cavity. The electron beam parameters, insertion device parameter and the THz wave performance are listed in Table 5.

Aiming at high average beam power, some major key issues of the ERL-TF are studied and briefly described in the following sections.

### Space Charge Effects

It plays an important role in the low energy injector system, in which the 500 keV beam from the gun is bunched with a single bunch cavity and is boosted to 5 MeV by two 2-Cell SC cavities and with some focusing elements as well. The PARMELA simulation shows the beam emittance is increased from  $1\mu\text{m}$  to about  $1.5\mu\text{m}$  (with bunch length of 2 ps and bunch charge of 77 pC)

due to the space charge effect. The further optimisation on this issue is under the way.

### Coherent Synchrotron Radiation (CSR) Effect

A high current and short bunch beam could be affected by the CSR in the bending magnet, in which the CSR produced by the head part of the bunch may affects on the tail part of the bunch after a bending magnet and causes an emittance growth. Our simulation result with ELGENT code [6] shows that with beam parameters of 77pC-2ps - 1mm-mrad-10 mA the CSR effects in the TBA sections are not so important, and by properly optimising some optics parameters, the emittance growth can be controlled within about 2%. However, for the CSR mode operation the test facility, the bunch length should be suppressed to about 0.2ps. In this case, the CSR effect will cause emittance growth. The so called “envelop matching method [6]” is used. Detailed is described in [7]. The preliminary results show that the emittance growth is about 30% due to CSR with the orientation of the phase ellipse set parallel to the CSR kick by scanning the Twiss parameters at the arc exit.

Table 5: THz Performance and Beam Parameters

FEL Mode		CSR	Oscillator
Beam	Energy (MeV)	20	35
	Bunch length (ps)	0.5	4
	Emittance ( $\mu\text{m}$ )	2	2
	Energy spread (%)	0.5	0.5
	Peak current (A)	62	20
ID	Period length (mm)	60	60
	Gap (mm)	9-23	23-32
	Length (m)	1.5	1.5
FEL	Wave length ( $\mu\text{m}$ )	0.15-1	21-50
	Freq. (THz)	0.3-2	
	Peak power (MW)	2	7
	Average power (kW)	0.27	9

### Beam Break-Up (BBU) Effect

In the high average current SC linac, the BBU effect caused by some HOMs in the SC cavity may be one of the most critical issues to limit the beam current. To suppress this effect, the most effective way is to well control the R/Q of the HOMs and well optimizes the beam optics. Our simulation results with a BBU-code for ERL [8] shows that with HOM's parameters of JLab 7-cell ERL SC cavities [9] and with our ERL-TF parameters the BBU current limitation could be higher than 200mA. For the BBU effects the simulation and experimental results can be well agreed with each other at JLab's ERL facility and many labs worldwide have done a lot of studies on above effects, and obtained their positive results to cure these effects [11-13].

### Energy Compression with Return ARC

Downstream the undulator, the beam energy spread is enlarged. While decelerated through the Linac, relative energy spread is increasing. This energy spread can be

reduced by rotating the bunch in the longitudinal phase space, as so called Energy Compression [14]. In our ERL-TF, energy compression [7] is done by setting the return arc (2nd TBA arc) non-isochronous, and tuning the deceleration phase in the linac. To stretch the bunch length,  $R56 = -0.16$  is set in the return arc, with RF phase around  $193^\circ$ , the energy spread could be controlled down to  $\sim 1.5\%$ .

### PRELIMINARY DESIGN STUDIES ON THE ERL-TF 7-CELL SC CAVITIES

For the design of the SC cavities of the main linac, the following factors are considered: 1) Lower the cryogenic loss with large  $G \cdot R / Q$ ; 2) Lower the HOM impedance (which is related to the cavity configuration and the location of the HOM absorber) about one order of magnitude than the ILC and XFEL cavities, and to avoid HOM frequencies around the multiples of the fundamental mode; 3) small electromagnetic surface field; 4) Large bandwidth of dipole modes, to decrease the frequency error due to fabrication error; 5) Magnetic field shielding (less than 10 mG). The preliminary parameters of the cavity are listed in Table 6. The cavity shape and HOM impedance will be further optimised according to the beam dynamics requirements.

Table 6: ERL-TF 7-cell SC Cavity Parameters

Fundamental frequency $f_0$	1.3 GHz
Cavity voltage $V_c$	15 MV
Effective length $L_{\text{eff}}$	0.8 m
Accelerating gradient $E_{\text{acc}}$	18.8 MV / m
$Q_0$	$> 10^{10}$
$Q_L$	$2 \times 10^7$
Bandwidth	65 Hz
$R / Q$	800 $\Omega$
Iris diameter	72 mm
Large beam pipe diameter	110 mm
Small beam pipe diameter	78 mm
Geometry factor ( $G$ )	270 $\Omega$
$E_{\text{peak}} / E_{\text{acc}}$	2.06
$B_{\text{peak}} / E_{\text{acc}}$	4.2 mT / ( MV / m )

\* with bunch length 0.6 mm.

### SUMMARY

In this paper we briefly described the major issues of the design studies on the ERL-FEL Test Facility at IHEP-Beijing, including the design parameters, essential lattice and the features of the key components, such as photocathode DC gun and CW superconducting accelerating structures. Some important beam physics issues such as space charge effects, CSR and BBU effects are described with the simulation results. A Concept Design Report on the ERL-FEL Test Facility [15] and a 500 kV-DC Gun Preliminary Design Report [16] are prepared. They

described all aspects of the test facility, such as beam physics, accelerating structure, RF power supply and LLRF, cryogenic system, magnet and power supply, vacuum system, beam instrumentation and control system, radiation protection and some utilities. These studies results established essential foundations to further promote the ERL-FEL studies at IHEP.

### REFERENCES

- [1] CHEN Senyu, ZHU Xiongwei and WANG Shuhong, "Towards one machine two purposes: using a common SC linac for XFEL and ERL simultaneously", Chinese Physics C 34. 1, Jan., 2010.
- [2] R. Nagai, et al, "High-Voltage Test of a 500-kV Photocathode DC Gun for the ERL Light Sources in Japan", Proceedings of IPAC'10, Kyoto, Japan.
- [3] LIU Shengguang and XU Jinqiang, Design Studies on a 500 kV DC gun photo-injector for the BXFEL test facility, Chinese Physics C 35. 1, Jan. 2011.
- [4] S. Belomestnykh, V. Shemelin, Multipacting-free transitions between cavities and beam-pipes. Nuclear Instruments and Methods in Physics Research A 595 (2008) 293–298.
- [5] Douglas D., Design Consideration for Recirculating and Energy Recovering Linac, JLAB-TN-00-027, November 2000.
- [6] Borland M. "elegant: A Flexible SDDS-Compliant Code for Accelerator Simulation," Advanced Photon Source LS-287, sept. 2008.
- [7] R. Hajima, APAC2004.
- [8] X.H. Cui, this workshop.
- [9] JIAO Yi, A BBU code developed with C language implanted in Matlab environment, private communication.
- [10] Mayes C.E. and Hoffstaetter G.H, Coherent Synchrotron Radiation Simulation for the Cornell ERL, Proceedings of IPAC 2010, TUPE-097, Kyoto, Japan.
- [11] Merminga L. et al, High Average Current Effects In Energy Recovery Linacs, Proceedings 2001 Particle Accelerator Conference, Chicago, IL, 18-22 June 2001.
- [12] Douglas D., "Operational" Beam Dynamics Issues, Talk to ERL-09, Cornell, 2009.
- [13] Campisi I.E. et al, Beam Backup Simulations for the Jefferson Lab FEL Upgrade, Proceedings of 1999 Particle Accelerator Conference, NY, USA 27 March-2 April 1999.
- [14] P. Pilot, et al, Phys. Rev. ST Accel. Beams 6 (2003) 0.0702)
- [15] Concept Design Report on the IHEP-ERL-FEL Test Facility (CDR-0, in Chinese), 2010.10.
- [16] Preliminary Design Report on the IHEP-500kV-DC-Gun (in Chinese), 2011.2.

# GENERATION OF HIGH-BRIGHTNESS GAMMA-RAYS FROM ENERGY-RECOVERY LINAC

R. Hajima, JAEA, Ibaraki 3191195 Japan

## Abstract

Energy-recovery linac (ERL) to generate an electron beam of small emittance and high-average current is a suitable driver for laser Compton scattered  $\gamma$ -ray sources (LCS  $\gamma$ -ray). A combination of an ERL and a laser enhancement cavity will improve the performance of LCS  $\gamma$ -ray significantly in comparison with existing LCS  $\gamma$ -ray sources based on linac and storage rings. Accelerator technologies relevant to ERL LCS sources, small-emittance gun and superconducting cavities, are same as ERL X-ray sources. We plan to demonstrate high-brightness LCS photon generation at the Compact ERL.

## LASER COMPTON SCATTERED GAMMA-RAY SOURCES

The combination of an energy-recovery linac and a high-power mode-locked laser realizes significant improvement of  $\gamma$ -ray sources based on laser Compton scattering (LCS).

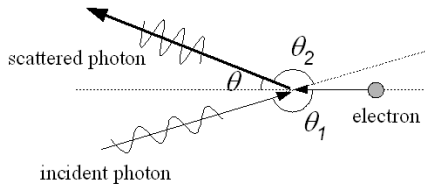


Figure 1: Laser Compton scattering.

Figure 1 shows a schematic representation of laser Compton scattering, where a high-energy photon ( $\gamma$ -ray) is generated via the Compton back-scattering of an incident laser photon with a relativistic electron [1]. The energy of the scattered  $\gamma$ -ray photon,  $E_g$ , is a function of the incident photon energy,  $E_L = hc/\lambda$ , electron energy  $E_e = \gamma mc^2$ , and scattering geometry, and approximated for a head-on collision:

$$E_g \approx \frac{4\gamma^2 E_L}{1 + (\gamma\theta)^2 + 4\gamma E_L / (mc^2)} \quad (1)$$

The above equation shows that the  $\gamma$ -ray energy has a correlation to the scattered angle. Therefore, monochromatic  $\gamma$ -rays can be obtained by putting a collimator to restrict the  $\gamma$ -ray divergence at the downstream. Owing to the energy tunable monochromatic  $\gamma$ -ray generation, LCS  $\gamma$ -ray sources have been developed by using storage rings and linacs [2-5].

A  $\gamma$ -ray flux from Compton scattering at an ideal head-on geometry integrated over the entire scattering angle is given by

$$F_{total} = \frac{fN_e N_L \sigma_C}{A}, \quad (2)$$

where  $f$  is the collision frequency,  $N_e$  is the number of electrons in an bunch,  $N_L$  is the number of photon in a laser pulse,  $\sigma_C$  is the cross-section of Compton scattering,  $A$  is the effective sectional area of beams at the collision point. In order to obtain a high-flux  $\gamma$ -ray, it is necessary to increase the density of both electrons and photons at the collision point. As seen in the above equation, an electron beam of small emittance and high-average current is essential to high-flux  $\gamma$ -ray generation via Compton scattering. The combination of an ERL and a laser enhancement cavity is, thus, a promising source of high-flux  $\gamma$ -rays [6,7].

Figure 2 shows a schematic view of an ERL  $\gamma$ -ray source. At the collision point, electron bunches circulating the ERL loop collide with laser pulses stored in an enhancement cavity, which is a high-finesse Fabry-Perot optical resonator to stack a train of laser pulses from a mode-locked laser [8].

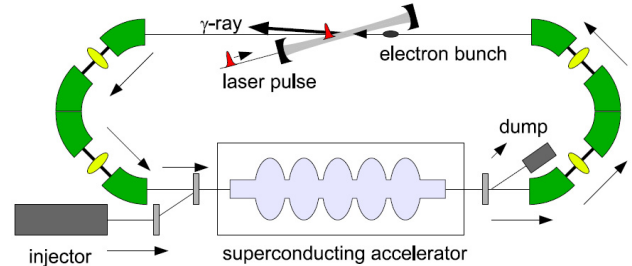


Figure 2: A schematic view of LCS  $\gamma$ -ray source based on an ERL and a laser enhancement cavity.

As shown in Eq. (1),  $\gamma$ -ray energy has a correlation with the scattering angle. However, this correlation becomes imperfect due to inhomogeneous effects of electron and laser beams. In the case of the head-on collision, the bandwidth of scattered  $\gamma$ -rays observed on the electron beam axis,  $\theta=0$ , can be calculated by assuming the laser spot size  $w$  ( $1/e^2$  radius) and the electron beam spot size  $\sigma$  ( $1/e$  radius) as follows [9]:

$$\left(\frac{\Delta E_g}{E_g}\right)^2 = \left(\frac{\Delta E_L}{E_L}\right)^2 + \left(\frac{2\Delta E_e}{E_e}\right)^2 + \frac{1}{4}\left(\frac{\lambda}{\pi w}\right)^2 + 4\left(\frac{\epsilon_n}{\sigma}\right)^4 \quad (3)$$

where the first term in the right-hand side is the spectral broadening due to the bandwidth of the incident laser pulse, the second term is the electron beam energy spread, the third term is the divergence of the laser beam, and the last term is the divergence of the electron beam due to a finite emittance.

The effect of electron beam emittance on the broadening of  $\gamma$ -ray bandwidth becomes as small as the effect of laser diffraction, when we have a normalized emittance:  $\varepsilon_n = \lambda/4\pi$ . From this criterion, we can define the “diffraction limited” electron beam. For a typical laser wavelength,  $1\mu\text{m}$ , the diffraction limited electron beam for LCS  $\gamma$ -ray sources has a normalized emittance of  $0.08\text{ mm-mrad}$ , which is a similar value to the required emittance for ERL-based synchrotron radiation sources to obtain coherent hard X-rays. Consequently, we can share accelerator components such as electron injector and accelerator for both ERL-based X-ray sources and ERL-based  $\gamma$ -ray sources.

Table 1: Parameters for a 2-MeV  $\gamma$ -ray source. Two operation modes are considered: high-flux mode (100 pC, 1 mm-mrad) and narrow-bandwidth mode (10 pC, 0.1 mm-mrad).

ERL electron beam		Laser	
Energy (MeV)	350	Wavelength (nm)	1064
Bunch charge (pC)	10 / 100	Pulse energy ( $\mu\text{J}$ )	1.5
Repetition (MHz)	130	Repetition (MHz)	130
Bunch length (rms, ps)	3	Pulse length (rms, ps)	3
Norm. emittance (mm-mrad)	0.1 / 1.0	Enhancement	2000
Energy spread (rms)	0.03%	Intracavity power (kW)	400
Collision spot (rms, $\mu\text{m}$ )	10	rms Collision spot (rms, $\mu\text{m}$ )	10
Collision angle (degree)	3.5		

Table 1 shows an example set of parameters for 2-MeV  $\gamma$ -ray source designed for nuclear material measurement [10]. The  $\gamma$ -ray source is operated at two different modes: high-flux mode (100 pC, 1 mm-mrad, 130 MHz) and narrow-bandwidth mode (10 pC, 0.1 mm-mrad, 130 MHz). The collision laser is assumed to be a 200 W average power and the laser cavity has an enhancement factor of 2000, which accumulates 400 kW intra-cavity laser power. The collision spot size is  $10\mu\text{m}$  (rms) for the electron and laser beams. In the high-flux mode, the LCS source produces a  $\gamma$ -ray with a total flux of  $1.0 \times 10^{13}$  ph/s as shown in Fig. 4, where the  $\gamma$ -ray spectrum is calculated

by Monte Carlo simulation code CAIN [11]. Narrowband  $\gamma$ -rays are obtained by placing an on-axis collimator on the  $\gamma$ -ray beam line. Figs. 4 and 5 show  $\gamma$ -ray spectra with various sizes of collimators for the high-flux and narrow-bandwidth modes, respectively. It is clearly seen that the diffraction-limited electron beam (normalized emittance of  $0.1\text{ mm-mrad}$ ) contributes to the significant improvement in the  $\gamma$ -ray bandwidth. In the narrow-bandwidth mode with a  $0.05\text{-mrad}$  aperture, the  $\gamma$ -ray bandwidth is  $0.2\%$  (FWHM). In the limit of small aperture at the narrow-bandwidth mode, the  $\gamma$ -ray bandwidth is restricted by electron beam energy spread. Possible use of low-frequency spoke cavities achieves further reduction of LCS  $\gamma$ -ray bandwidth because of the smaller RF-correlated energy spread of electron beams [12].

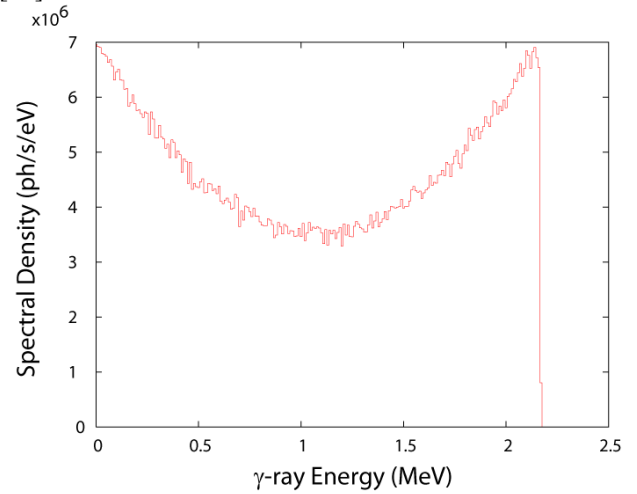


Figure 3: Calculated  $\gamma$ -ray spectrum for the high-flux mode of the designed ERL  $\gamma$ -ray source. The total flux is  $1.0 \times 10^{13}$  ph/s.

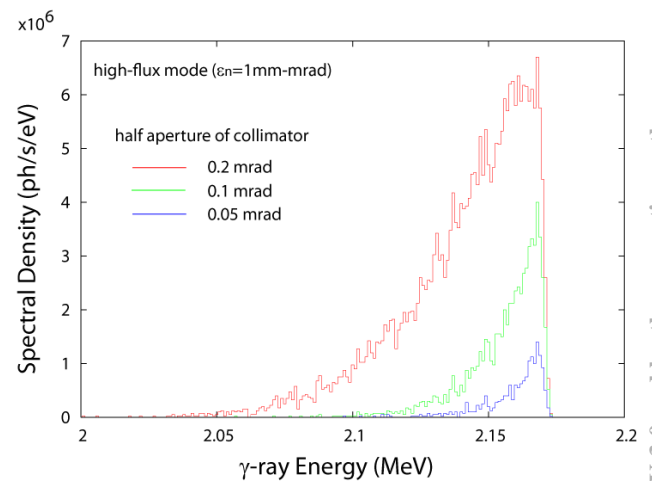


Figure 4: Calculated  $\gamma$ -ray spectrum for the high-flux mode with various sizes of on-axis collimators. Collimator half aperture is  $0.2\text{ mrad}$ ,  $0.1\text{ mrad}$  and  $0.05\text{ mrad}$ .

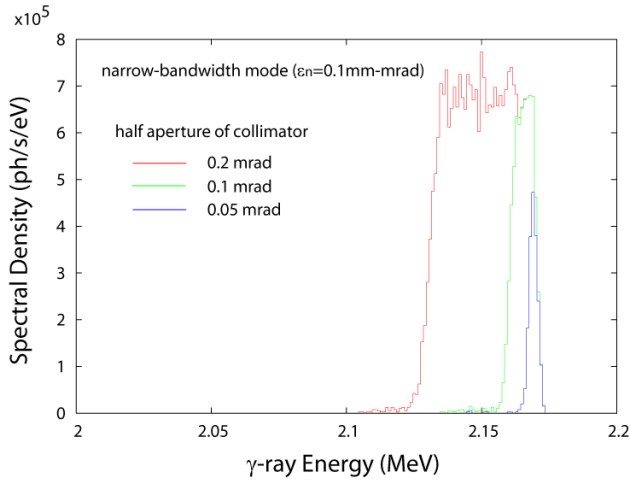


Figure 5: Calculated  $\gamma$ -ray spectrum for the narrow-bandwidth mode with various sizes of on-axis collimators. Collimator half aperture is 0.2 mrad, 0.1 mrad and 0.05 mrad.

An electron beam in a LCS  $\gamma$ -ray source suffers from quantum excitation from collision with laser photons. This quantum excitation causes growth of emittance and energy spread of the electron beam. Degradation of electron beam quality, growth of emittance and energy spread, is summarized in ref [13]. The growth of normalized emittance after a collision is given by

$$\Delta(\varepsilon_n) = \frac{3}{10} \frac{\lambda_c}{\lambda_L} \frac{\Delta E_\gamma}{E} \beta^* , \quad (4)$$

where  $\lambda_c = h/mc = 2.43 \times 10^{-12}$  m is the Compton wavelength of the electron,  $\lambda_L$  is the laser wavelength,  $\beta^*$  is the betatron function at the collision point,  $\Delta E_\gamma$  is the energy loss of the electron after the collision. For the designed 2-MeV  $\gamma$ -ray source operated at the narrow-bandwidth mode, we find  $\Delta E_\gamma = 2.0$  keV and  $\Delta(\varepsilon_n) = 2.7 \times 10^{-12}$  m-rad.

The electron energy spread induced by laser Compton scattering is calculated by

$$\Delta(\sigma_E) = \sqrt{\frac{7}{10} \hbar \omega_m \Delta E_\gamma} , \quad (5)$$

where  $\omega_m = 4\gamma^2 \omega_L$  is the maximum  $\gamma$ -ray photon frequency. For the designed 2-MeV  $\gamma$ -ray source operated at the narrow-bandwidth mode, we have  $\Delta(\sigma_E) = 56$  keV.

The above estimation of spent beam quality suggests that we may install multiple interaction points along an ERL return loop to accommodate several  $\gamma$ -ray beam lines without degradation of  $\gamma$ -ray brightness and bandwidth.

Note that a LCS  $\gamma$ -ray source based on a storage ring has a limitation of  $\gamma$ -ray bandwidth resulting from a large energy spread of electrons at the equilibrium state, where the quantum excitation is balanced with the longitudinal damping. The electron energy spread at the equilibrium state of a storage ring is given by [13]

$$\left( \frac{\sigma_E}{E} \right)_{eq} = \sqrt{\frac{7}{5} \frac{\lambda_c}{\lambda_L}} \gamma . \quad (6)$$

In a 350-MeV storage ring operating with a 1  $\mu$ m laser to produce 2-MeV  $\gamma$ -rays, the electron energy spread at the equilibrium state is calculated to be 4.6% (rms).

As we have seen, ERL is an ideal electron accelerator for laser Compton scattering light source to produce  $\gamma$ -rays of high flux and narrow bandwidth. Electron beams of small emittance and high-average current available from ERLs realize unprecedented light sources in photon energies of MeV,  $\gamma$ -rays, as well as X-rays. The improvement of  $\gamma$ -ray performance from the existing LCS  $\gamma$ -ray sources includes the enhancement of flux by 5-8 orders and the bandwidth narrowing by 1-2 orders. Such  $\gamma$ -ray sources are of great use in many scientific and industrial applications: nuclear physics [14], nuclear astrophysics [15], hadron physics [16], management of nuclear waste [17], nuclear security and safeguards [18].

In order to demonstrate the performance of ERL  $\gamma$ -ray source and explore applications of ERL  $\gamma$ -ray sources to nuclear security and safeguards purposes, JAEA has launched a 3-year program (2011-2013) supported by Ministry of Education, Culture, Sports, Science and Technology (MEXT) in Japan [19]. The program aims at generation of a high-flux and narrow-bandwidth  $\gamma$ -ray beam at the Compact ERL in collaboration with KEK. Application of the  $\gamma$ -ray to non-destructive measurement of isotopes is also planned. Figure 6 shows a schematic view of the proposed experiment at the Compact ERL.

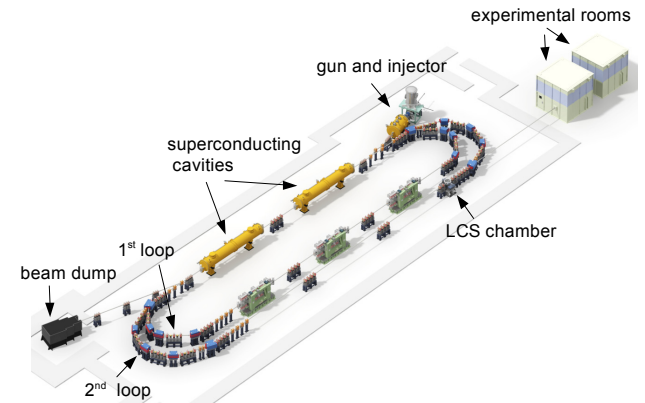


Figure 6: A schematic view of the LCS  $\gamma$ -ray experiment at the Compact ERL.

## REFERENCES

- [1] G.A. Krafft and G. Priebe, “Compton Sources of Electromagnetic Radiation”, *Rev. Acc. Sci. Tech.*, **3** (2010) 147–163.
- [2] H. Ohgaki et al., “Generation and application of laser-Compton gamma-ray at ETL”, *Nucl. Inst. Meth.* **A455** (2000) 54–59.
- [3] V.N. Litvinenko et al., “Gamma-ray production in a storage ring free-electron laser”, *Phys. Rev. Lett.* **78** (1997) 4569–4572.

- [4] H.R. Weller et al., “Research opportunities at the upgraded HIγS facility”, *Prog. Part. Nucl. Phys.* **62** (2009) 257–303.
- [5] F. Albert et al., “Design of narrow-band Compton scattering sources for nuclear resonance fluorescence”, *Phys. Rev. ST-AB* **14** (2011) 050703.
- [6] R. Hajima et al., “Energy-recovery linac for a high-flux quasi-monochromatic gamma-ray source”, *Proc. AccApp07* (2007) 182–188. ISBN: 0-89448-054-5.
- [7] V.N. Litvinenko et al., “Potential use of ERL-based  $\gamma$ -ray sources”, *IEEE Trans. Plasma Sci.* **36** (2008) 1799–1807.
- [8] K. Sakaue et al., “Development of a laser pulse storage technique in an optical super-cavity for a compact X-ray source based on laser-Compton scattering”, *Nucl. Instr. Meth.* **A637** (2011) S107–S111.
- [9] W.J. Brown and F.V. Hartemann, “Three-dimensional time and frequency-domain theory of femtosecond x-ray pulse generation through Thomson scattering” *Phys. Rev. ST-AB* **7** (2004) 060703.
- [10] R. Hajima et al., “Detection of radioactive isotopes by using laser Compton scattered  $\gamma$ -ray beams”, *Nucl. Instr. Meth.* **A608** (2009) S57–S61.
- [11] P. Chen et al., “CAIN: Conglomérat d’ABEL et d’Interactions Non-Linéaires”, *Nucl. Instr. Meth.* **A355** (1995) 107–110.
- [12] M. Sawamura et al., “Design Optimization of Spoke Cavity of Energy-Recovery Linac for Non-Destructive Assay Research”, to be published in *Proc. 15<sup>th</sup> Int. Conf. on RF Superconductivity* (2011).
- [13] Z. Huang and R. Ruth, “Laser-electron storage ring”, *Phys. Rev. Lett.* **80** (1998) 976–978.
- [14] T. Shizuma et al., “Fine structure of the magnetic-dipole-strength distribution in  $^{208}\text{Pb}$ ”, *Phys. Rev. C* **78** (2008) 061303(R).
- [15] T. Hayakawa et al., “Half-life of  $^{184}\text{Re}$  populated by the  $(\gamma, n)$  reaction from laser Compton scattering  $\gamma$  rays at the electron storage ring NewSUBARU”, *Phys. Rev. C* **74** (2006) 065802(R).
- [16] A.I. Titov, M. Fujiwara and K. Kawase, “Parity non-conservation in nuclear excitation by circularly polarized photon beam”, *J. Phys. G* **32** (2006) 1097–1103.
- [17] R. Hajima et al., “Proposal of nondestructive radionuclide assay using a high-flux gamma-ray source and nuclear resonance fluorescence”, *J. Nucl. Sci. and Tech.* **45** (2008) 441–451.
- [18] T. Hayakawa et al., “Nondestructive assay of plutonium and minor actinide in spent fuel using nuclear resonance fluorescence with laser Compton scattering  $\gamma$ -rays”, *Nucl. Instr. Meth.* **A621** (2010) 695–700.
- [19] R. Hajima et al., “Research and Development Program on Nondestructive Measurement of Isotopes by Using Laser Compton Scattered Gamma-rays”, *Proc. 52<sup>nd</sup> INMM Annual Meeting* (2011).

## MULTITURN ERL X-RAY SOURCE (MARS) FEASIBILITY STUDY

G.N. Kulipanov, Ya.V. Getmanov, O.A. Shevchenko, A.N. Skrinsky, A.G. Tribendis, V.N. Volkov,  
Budker INP, Novosibirsk, Russia

N.A. Vinokurov

Budker INP, Novosibirsk, Russia and Korea Atomic Energy Research Institute, Daejeon, Korea

### Abstract

Multiturn energy recovery linacs (ERL) looks very promising for making ERLs less expensive and more flexible, but have serious intrinsic problems. At this time only one multiturn ERL exists. This Novosibirsk ERL operates with two orbits and two free electron lasers now. The conception of Multiturn Accelerator-recuperator Radiation Source (MARS) was proposed in 1997 by G.N. Kulipanov, A.N. Skrinsky and N.A. Vinokurov. The use of the two-linac ERL (D. Douglas, 2001) makes multiturn operation much easier. The feasibility study for such ERL-based high brightness x-ray source is presented.

### INTRODUCTION

In the recent years, Russian government and scientific society have been coming gradually to an understanding the way of development science in Russia. Government have accepted a program of building one of the six mega-science projects, and one of them can be a new 4-th generation x-ray light source based on accelerator-recuperator.

At the last 30 years development of the synchrotron radiation (SR) sources have been aiming to different purposes. The main ones are the increasing of spectral brightness and energy of generated quanta, using of specific properties of SR radiation (coherence, polarization, time structure, etc.). Also, it is very important that each SR source has been used by a large number of users groups (up to 60) from different areas of science and has worked for 7000 hours a year.

Today, the SR sources of the 3rd generation available and those under construction (APS, ESRF, Spring-8, SLS, ELETTRA, DIAMOND, SOLEIL, PETRA-III, ALBA ...) are the efficient factories for generation of the new knowledge, new technologies and new materials.

### REQUIREMENTS TO SR SOURCES

In the last two decades, there were active discussions on the development of SR sources of the 4<sup>th</sup> generation. The world's physical community worked out the requirements to these sources and suggested several ways for the development of such sources [1]:

- full spatial coherence;
- the highest temporal coherence ( $\Delta\lambda/\lambda < 10^{-4}$ ) without additional monochromatization;
- the averaged brightness of the sources is to exceed  $10^{23}$ - $10^{24}$  photons  $s^{-1}mm^{-2}mrad^{-2}$ (0.1% bandwidth)<sup>-1</sup>;
- the full photon flux for the 4<sup>th</sup> generation sources must be at the level of the 3<sup>rd</sup> generation SR sources;

- high peak brightness of the order of  $10^{33}$  photons  $s^{-1}mm^{-2}mrad^{-2}$  (0.1% bandwidth)<sup>-1</sup> is important for some experiments;
- electron bunch length up to 1 ps; and if a specialized technique is used, the X-ray pulses become smaller than 100 fs;
- high long-term stability; generation of linear, left-right circular polarized radiation with fast switching of the polarization type and sign; constant heat load on chambers and optics, etc.;
- servicing the multi-user community.

During the last 30 years, the brightness of the X-ray SR sources based on storage rings increased by a factor of  $10^9$ . Nevertheless, on the modern sources, the flux of coherent quanta is only  $10^{-3}$  of the total flux. Therefore, in spite of successful demonstrating X-ray holography, it has not become an efficient technique for structural studies of real objects of mostly noncrystalline structure. Even for crystalline structures, the speckle spectroscopy, which is accessible only in coherent light, is very important. Therefore, obtaining a fully spatially coherent flux of quanta with full photon flux at the level of the 3<sup>rd</sup> generation SR sources is the most important from all the requirements to SR sources of the 4<sup>th</sup> generation. A possibility of obtaining undulator radiation with a monochromaticity of  $10^{-3} \div 10^{-4}$  without using monochromators, which as a rule spoil the beam spatial coherence, is also of great importance.

It is impossible to satisfy all requirements for the 4-th SR sources using only one type of sources. High peak brightness and femtosecond length of light pulses can be achieved by using x-ray free electron lasers based on linacs with high pulse current ( $I_p > 1$  kA). The first XFEL - LCLS is in operation since 2009 with 10 fs x-ray pulses at 1 Å wavelength and the second one, SPring-8, has started operation in 2011. In the next years x-ray FELs will start to work in Europe and Korea.

Other requirements are implemented easier and cheaper by using radiation from long undulators installed on the accelerator-recuperator.

To generate full spatially coherent undulator radiation with wavelength  $\lambda = 0.1$ nm it is necessary to decrease emittance of electron beam at  $E = 5 \div 6$  GeV to diffraction limit  $\varepsilon_{x,z} < \lambda/4\pi \approx 10^{-11}$ . Therefore, the charge in one bunch should be no more than  $10^{-11}$  C. For the RF frequency 1.3 GHz that corresponds to the average current 10 mA. The version suggested for some single-turn ERL projects - using current up to 100 mA for keeping the photon flux - seems to be far from optimum, since with such an increase in current the brightness does not increase and even decreases sometimes. To compensate the decrease in

the current value compared with that of the 3<sup>rd</sup> generation SR sources, we shall use radiation only from three types of undulators with number of periods  $N_{u1}=100$ ,  $N_{u2}=1000$ ,  $N_{u3}=10000$ , not from bending magnets. In this case, we solve the problem of full spatial coherence and at the same time keep the photon flux at the level of the 3<sup>rd</sup> generation sources.

### ACCELERATOR SCHEME

A conception of accelerators-recirculators with one accelerating structure was proposed for realization a fully spatially coherent X-ray source in 1997 [2,3]. The main disadvantage of this scheme is that two electron bunches (accelerating and decelerating) are circulated simultaneously at every magnetic arc except the last one. Due to this, in undulators of the lower-energy orbits radiation is generated by both accelerating and decelerating electrons. Therefore the precise alignment of both beams is required. Moreover, this complicates the control of electron beams. Therefore, it has been proposed to use scheme with two accelerating sections (see Fig. 1) and separated magnetic arcs for accelerating and decelerating beams ([4], [5]).

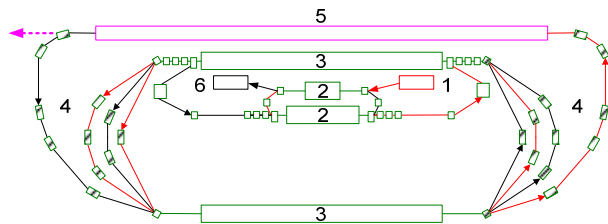


Figure 1: The simplest scheme of accelerator with 2 separated accelerating structures: 1 – injector, 2 – two preliminary accelerating structures, 3 – two separated linacs, 4 – magnetic arcs, 5 – undulator, 6 – dump.

Principle of operation is the following: electrons with energy 8 MeV from injector 1 pass two preliminary accelerating RF sections 2 (42 MeV and 350 MeV) and come to first main accelerating structure 3 (0.7 GeV). Then, magnetic structure 4 bends electrons to the second main RF structure 3 (1.9 GeV). After 2 passes through each accelerating structure 3, electrons gain final energy 5.6 GeV and pass to the undulator 5. Used electrons are decelerated at the same RF structures. In this case, accelerating and decelerating bunches pass through different magnetic arcs. Decelerated particles drop to the dump 6.

The main features of facility are the following.

**Injection.** Cascade injection system consists of two preliminary acceleration sections, which accelerate electrons to energies 50 MeV and 400 MeV. This relatively high injection energy simplifies focusing of particles with different energies traveling simultaneously in the accelerating structure. Moreover, it increases the threshold current of the transverse beam breakup (BBU). For the same reasons, we use two asymmetrical main accelerating structures (0.7 and 1.9 GeV). The using of the cascade injection and energy recovery decreases

radiation hazard and eliminates the induced radioactivity due to the low energy of electrons at the dump (5-8 MeV). It leads to reduction in the cost of building and RF power supply for the injector.

**Radiation.** It was already mentioned, that to achieve full spatial coherence with conservation of photon flux on the level of the third generation sources it is necessary to use long undulators. Thus, another advantage of split accelerating structure is a possibility of servicing the multi-user community. A scheme with one undulator (Fig.1) can be extended by installations of the long undulators into bending arcs 4 (see Fig. 2). There are 7 undulators for 5.6 GeV, and 4 undulators for 3.7 GeV, 3 GeV and 1.1 GeV. To simplify the radiation output the magnetic arcs are separated both horizontally and vertically.

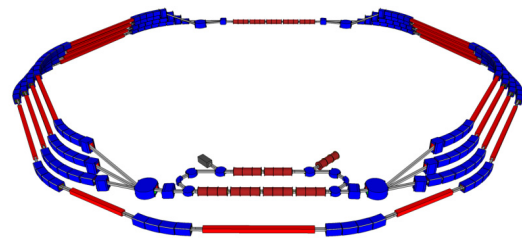


Figure 2: Scheme of MARS with main features: cascade injection, two accelerating structures, separated bending arcs, vertical separation of radiation beamlines.

The radiation parameters comparison of MARS (I=10 mA) and the best of existing third generation SR sources SPring-8 (100 mA) is presented in the table 1

Table 1: Comparison of SR Sources MARS and SPring-8

facility	Number of undulator periods	Number of channels	Brightness	Flux
MARS	$10^2$	48	$10^{22}$	$7.7 \cdot 10^{13}$
	$10^3$	12	$10^{23}$	$7.7 \cdot 10^{14}$
	$10^4$	4	$10^{24}$	$7.7 \cdot 10^{15}$
SPring-8	Bending magnets	23	$10^{16}$	$10^{13}$
	130	34	$3 \cdot 10^{20}$	$2 \cdot 10^{15}$
	780	4	$10^{21}$	$1.2 \cdot 10^{16}$

**Magnetic structure** of the each orbit (4 at Fig.1) consists of six 60-degree achromatic bending arcs with 26 magnets in each. Quantum fluctuations of SR practically do not increase energy spread and transverse emittances. For this, at the last turn bending radius should be more than 60m. To simplify the vacuum chamber elements, the same radius is used at all orbits. At the maximum energy (last orbit) the growth of the horizontal emittance limits «invariant» of the dispersion function:  $\gamma_T \eta^2 + 2\alpha_T \eta \eta' + \beta \eta'^2 < 3 \text{ cm}$ , where  $\gamma_T, \beta, \alpha_T$  are the Twiss parameters, and  $\eta$  is the horizontal dispersion function.

To control the longitudinal motion bending arcs are not isochronous. Longitudinal motion should provide low energy spread ( $2 \cdot 10^{-5}$ ) and low bunch length ( $< 0.1$  ps). This requires longitudinal emittance less than 5 keV·ps. Furthermore, longitudinal focusing should provide low bunch length at the last arcs. Limit of «invariant» of horizontal dispersion function also limits the longitudinal dispersion  $R_{56} = \pi \bar{\eta} / 3$  (0.18 m for the 60-degree arcs of the last turn). For the energy spread  $2 \cdot 10^{-5}$  this corresponds to bunch lengthening 11 fs only. It means that two last turns cannot be used for bunching. At the two first turns the growth of emittance due to quantum fluctuations is less; therefore it is possible to increase the transverse and so the longitudinal dispersion.

**RF structure.** To achieve the energy 5.6 GeV electrons it is planned to use two main accelerating superconducting RF structures with energy gain 0.7 GeV and 1.9 GeV and two preliminary ones for 42 MeV and 350 MeV. There are four electron beams (two accelerating and two decelerating) with average current 10 mA in each main linac simultaneously. Consequently, the main goal is not to get high acceleration rate, but a stability of the bunch.

Since the magnetic structure of accelerator is not an isochronous, all three types of beam-cavity interaction instabilities are excited (beam-loading, HOM transverse and longitudinal BBU). In the simplest case of single-cavity model, threshold current of transverse BBU can be estimated as [6]

$$I_{th} \approx 0.14 I_A \frac{\lambda \sqrt{\gamma_1 \gamma_2}}{Q \sqrt{\beta_1 \beta_2}},$$

where  $I_A = 17$  kA,  $\gamma_1$  and  $\gamma_2$  are the Lorentz factors of electrons at the first and the second passes through the cavity,  $\beta_1$  and  $\beta_2$  are the corresponding beta-functions of the beams. Therefore, for the current 10 mA,  $\lambda_{RF} = 0.23$  m and  $Q_{load} = 10^6$  it is enough to have  $\sqrt{\beta_1 \beta_2} / \sqrt{\gamma_1 \gamma_2} < 0.06$  m. So, for energies at the entrance of the first main accelerating structure 400 MeV and 3 GeV this gives  $\sqrt{\beta_1 \beta_2} < 120$  m, which is easily achievable.

Beam-loading instability may take place, as the  $R_{56}$  elements of transport matrices between accelerating structures are not zero. There are four electron beams in each linac simultaneously. So, in the single cavity model, the necessary condition for the longitudinal stability is [7]

$$\begin{aligned} & e \rho_1 I \sin(2\Phi_1) \sum_{n=0}^{N-1} \sum_{k=0}^{N-1} S_{4N-2n-1, 2k} + \\ & + e \rho_2 I \sin(2\Phi_2) \sum_{n=0}^{N-1} \sum_{k=0}^{N-1} S_{4N-2n-2, 2k+1} < \frac{1}{Q_1} + \frac{1}{Q_2}. \end{aligned}$$

Here  $I$  is the beam current,  $S_{nk}$  is the  $R_{56}$  transport matrix element between  $k$ -th and  $n$ -th passage through the accelerating structures,  $\rho$  and  $Q$  are the characteristic

impedances and loaded qualities for the fundamental mode ( $TM_{010}$ ), and  $\Phi_{1,2}$  are phases of the acceleration in the first and the second accelerating structures. Of course, threshold current depends on phases of acceleration  $\Phi_{1,2}$ , which are also determined by requirements of the bunch longitudinal focusing. Simulations show that there are areas of the stable accelerating phases (left part of the stability condition is negative).

The main parameters of the ERL are listed in Table 2.

Table 2: The Accelerator Parameters

Energy	5.6 GeV
Average current	10 mA
Peak current	10 A
Normalized emittance	0.1 mkm
Relative energy spread	$2.2 \cdot 10^{-5}$
SR sources	19 Undulators ( $N_u \sim 10^2$ , $N_u \sim 10^3$ , $N_u \sim 10^4$ )
Geometrical sizes	1x1 km

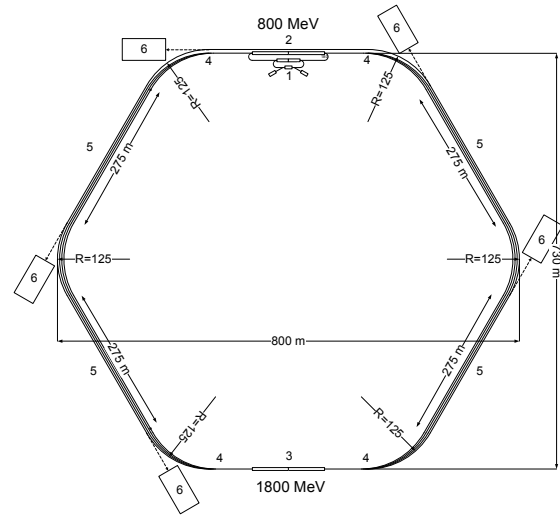


Figure 3: Scheme of MARS in scale: 1-injector and preliminary accelerating sections, 2,3– two separated linacs, 4 – magnetic arcs, 5 – undulator, 6 – user stations.

## CONCLUSION

The use of long undulators with the high-quality electron beam of ERL is the solution for the fourth-generation x-ray sources. The accelerating schemes and most of the systems, which make the basis of the projects, have already been tested in many laboratories (Jefferson Laboratory, DESY, MAMI, LEP, Budker INP, KEK, MAX). There are no any essential physical problems in the development of the 4th generation SR sources on the base of accelerators-recuperators with average current 10

mA. The main problem is the cost of such SR source and its further maintenance.

The main ideas of MARS design allow to reduce significantly the cost of facility and energy consumption, providing the servicing of many users simultaneously. These ideas are simple and clear:

1) Emittance of the electron bunch with energy  $E = 5 \div 6$  GeV is less, than  $10^{-11}$  m · rad, which corresponding to the normalized emittance  $\varepsilon_n < 10^{-7}$  m · rad.

2) Bunch charge should not exceed  $Q = 7.7 \cdot 10^{-12}$  C. That corresponds to a current value of 10 mA.

3) Photon flux from source proportional to the average current  $I$  of accelerator  $\Phi \sim I \cdot N$ ,  $N$  is a number of emitters in the source. To compensate the current decreasing in 10-50 times, it is necessary to use the radiation from undulators and wigglers with number of periods  $N_u > 100$ .

4) To provide a low level of radiation hazard and eliminate induced radioactivity, the bunch energy should not exceed 5-8 MeV in the beam dump.

5) To provide easily achievable conditions for simultaneous movement of the electron bunches with different energies in accelerating (decelerating) RF structures, it is necessary to use cascade scheme of injection.

6) For simultaneous multi-users servicing a scheme with two separated accelerating structures can be used. This eliminates the main disadvantage of the scheme with single linac, where accelerating and decelerating bunches create two radiation sources in each undulator, and simplifies the control of the beam.

7) Magnetic structure should contain long interspaces ( $L \sim 200$  m) for mounting a large number of undulators with number of periods  $N_u = 10^2 \div 10^4$ .

8). Energy spread of electron bunch at low energy should not exceed  $\Delta E/E = 10^{-4}$ .

## REFERENCES

- [1] Scientific Needs for Future X-Ray Sources in the U.S., A White Paper, LBNL, SLAC, 2008.
- [2] G.N. Kulipanov, A.N. Skrinsky, N.A. Vinokurov, Synchrotron light sources and recent development of accelerator technology. J. of Synchrotron Radiation –1998 V.5 pt.3 P.176); MARS - recirculator-based diffraction limited X-ray source, Budker INP preprint No 97-103 (1997).
- [3] G.N. Kulipanov, A.N. Skrinsky, N.A. Vinokurov, MARS a project of the diffraction-limited fourth generation x-ray source based on supermicrotron, Nucl. Instr. and Meth. A 467-468 (2001).
- [4] D. Douglas, A Generic Energy-Recovering Bisected Asymmetric Linac (GERBAL), ICFA BD-NI 26 (2001)40.
- [5] N.A. Vinokurov et al., Proc. IPAC'10.
- [6] N.A. Vinokurov et al., Proc. SPIE 2988 (1997) 221.
- [7] Ya.V. Getmanov, O.A. Shevchenko, N.A. Vinokurov, Longitudinal Stability of ERL with Two Accelerating RF Structures, Proc. IPAC'11.
- [8] G.N. Kulipanov, A.N. Skrinsky, N.A. Vinokurov, Multi-pass accelerator recuperator (MARS) as coherent x-ray SR source, SRI-2006, Daegu, Korea.

# WAKE FIELDS AND ENERGY SPREAD FOR THE eRHIC ERL\*

A.V. Fedotov<sup>#</sup> and D. Kayran, BNL, Upton, NY 11973, USA

## Abstract

Wake fields in high-current ERLs can cause significant beam quality degradations. Here we summarize effects of coherent synchrotron radiation, resistive wall, accelerating cavities and wall roughness for ERL parameters of the eRHIC project. A possibility of compensation of such correlated energy spread is also presented. An emphasis in the discussion is made on the suppression of coherent synchrotron radiation due to shielding and a possible reduction of wall roughness effects for realistic surfaces.

## INTRODUCTION

In this report we discuss the wake fields with a focus on their effect on the energy spread of the beam. Other effects of wake fields are addressed elsewhere. An energy spread builds up during a pass through a very long beam transport in the eRHIC ERL under design [1]. Such energy spread become important when beam is decelerated to low energy, and needs to be corrected.

Several effects, such as Coherent Synchrotron Radiation (CSR), Resistive Wall (RW), accelerating RF cavities (RF) and Wall Roughness (WR) were considered. In this paper, we briefly summarize major contributions to energy spread from the wake fields for eRHIC parameters, and present possible energy spread compensation for decelerated beam. In the rest of the report we discuss effects which we believe are suppressed for the eRHIC parameters.

## SOURCES OF ENERGY SPREAD FOR eRHIC ERL

For the eRHIC project, electron beam with high peak current has to go through the present tunnel of the Relativistic Heavy Ion Collider (RHIC) 6 times to reach the top energy (at which electron beam will collide with the ion beam) and then additional 6 times to be decelerated before going to the dump. To save on the cost of the vacuum chambers and magnets very small aperture of vacuum chambers are considered. As a result, such effects as RW and WR are strongly enhanced.

For the first stage of the eRHIC, the maximum top energy is presently 5 GeV, for the second stage the energy is upgradable to 20 and 30 GeV by adding additional RF cavities. For the second stage of the eRHIC, the highest bunch current is for 20 GeV energy. In Figs. 1 and 2 we show total longitudinal wake potential for the 5 GeV and 20 GeV scenarios for parameters shown in Tables 1 and 2, respectively. Table 3 shows summary of major contributions to the energy spread for the 20 GeV case.

\*Work supported by the U.S. Department of Energy

<sup>#</sup>fedotov@bnl.gov

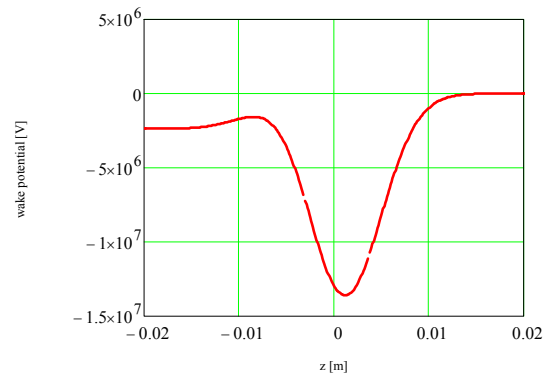


Figure 1: Longitudinal wake potential (contribution from RF cavities and Resistive Wall) for 1<sup>st</sup> stage 5 GeV eRHIC parameters in Table 1.

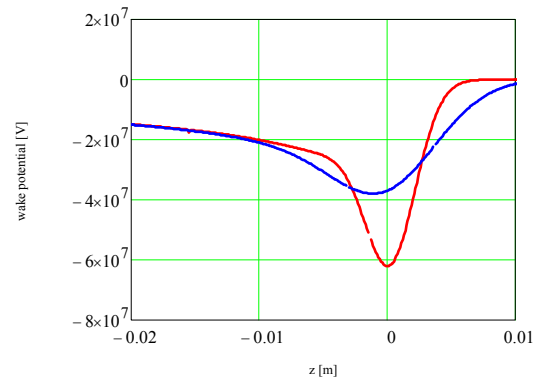


Figure 2: Longitudinal wake potential (contribution from RF and Resistive Wall) for 20 GeV eRHIC parameters in Table 2 for rms bunch length of 4 mm (red) and 2 mm (blue).

Table 1: Beam Parameters used for 1<sup>st</sup> Stage 5 GeV eRHIC ERL

Total length of beam transport (12 passes), km	46
Bunch charge, nC	3.5
Beam pipe diameter (low-energy passes), mm	8
Beam pipe diameter (high-energy passes), mm	5
Total number of RF cavities per pass	48
Rms bunch length, mm	4

Table 2: Beam Parameters used for 20 GeV eRHIC ERL

Total length of beam transport (12 passes), km	46
Bunch charge, nC	3.5
Beam pipe diameter (low-energy passes), mm	8
Beam pipe diameter (high-energy passes), mm	5
Total number of RF cavities per pass	240
Rms bunch length, mm	2-4

Table 3: Total Wake Field Contribution to the Energy Spread for the 20 GeV eRHIC for Rms Bunch Length of Electron Beam 2 mm

	Energy loss, MeV	Rms energy spread, MeV
CSR	suppressed	suppressed
Resistive wall	14 (Aluminum)	14.7
RF cavities	36	14.4
Wall roughness	suppressed	< 2

In this paper all values are shown for the Gaussian longitudinal distribution of electron beam. In Figs. 1-2 and Table 3, it is assumed that contribution from CSR and WR is suppressed. Such assumptions are discussed in the following sections.

The resulting energy spread is too large, even for the case of 1<sup>st</sup> stage 5 GeV eRHIC (+/-6.7 MeV) for which longer bunch length with 4 mm rms was already chosen, to go through the final low-energy beam transport to the dump. In the absence of various decoherence effects, such as synchrotron radiation or intrabeam scattering, for example, one can assume that accumulated energy spread is well correlated and thus its correction could be possible. In Fig. 3, we show an example of such correction for the 5 GeV case. The correction is done after beam is decelerated to 100 MeV energy and goes into eRHIC injector. The beam is first stretched by introducing longitudinal dispersion of 0.3 m with a subsequent adjustment of the phase of the injector linac. The resulting energy spread at 10 MeV is +/-3.7 MeV (green line in Fig. 3) and could be already satisfactory to go all the way to the dump. Compensation of energy spread for the 20 GeV eRHIC (which is significantly larger, as shown in Fig. 2) is under study and will be reported elsewhere.

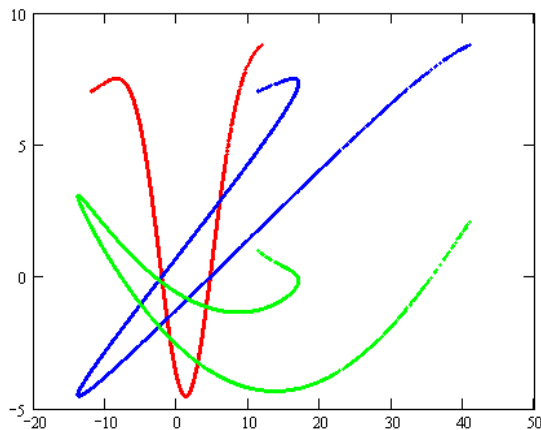


Figure 3: Compensation of correlated energy spread for 5 GeV eRHIC. Horizontal axis: longitudinal position within the bunch in mm; vertical axis – energy in MeV. Red – initial wake potential; blue – after stretching the beam; green – after adjusting the phase of the injector linac.

## CSR SHIELDING

Simple estimates of CSR effect for eRHIC shows that electron beams would have significant energy spread and energy loss if one does not take into account the shielding effect of the beam pipe walls. However, when the walls of vacuum chamber are conducting, induced charges will decrease the EM fields created directly by the bunches. This phenomenon is known as shielding of CSR and is the stronger the closer the induced charges. Analytic theory of CSR shielding suggests that CSR can be suppressed if beam-pipe dimension is small or the bunch length is large. A suppression factor involves bunch length, pipe dimension and radius of the curvature and is different for energy loss and energy spread suppression.

Theoretical studies of shielding goes back to the work by Schwinger [2] with subsequent work by many others starting with Ref. [3]. In accelerator community analytic expressions for the coupling impedance of vacuum chambers of various geometries for a particle moving on a circular orbit were obtained by Warnock [4]. A simplified form for the coupling impedance was given, for example, in Ref. [5]. In terms of the wake functions closed form expressions were derived in Ref. [6]. A direct summation of image charges was recently used in Ref. [7], which showed suppression of both energy loss and energy spread but by a very different degree. Such a different degree of suppression of the energy loss and energy spread follows directly from the closed form expression for the impedance as well [5], which has both real and imaginary parts. One can see that the real part of the impedance has very strong exponential suppression while the imaginary part does not, and thus less suppression is expected for the energy spread than for the energy loss.

For the eRHIC parameters the bunch length of electron beam is relatively long, and estimates based on the expression for the coupling impedance from Ref. [5] show that both energy loss and energy spread due to CSR will be completely suppressed for present vertical size of the vacuum chamber of 5 mm, due to a very large suppression factor.

Until recently [7], shielding of CSR was mostly discussed with regard to the suppression of the power or energy loss rather than its effect on the energy spread of the beam. Also, no experiments which directly address effect of shielding on the energy spread was found. Therefore, to address this question experimentally, a series of dedicated measurements of shielding of CSR were recently performed at BNL's Accelerator Test Facility which observed suppression of both CSR-induced energy loss and energy spread [8].

## WALL ROUGHNESS

Contribution of WR to the coupling impedance (wake potential) can become important especially when the size of the vacuum chamber is small and length of the electron bunch is very short. Several theoretical models were developed in the past which showed rather different importance of this effect. Some experimental studies of

the wall roughness are also available. Here we briefly review the models and discuss their application to realistic surface roughness.

An effect of the wall roughness was first estimated based on the impedance of small protrusions of different configurations and orientations [9]. In this model, impedance is purely inductive and thus there is no effect on the energy loss, just on the energy spread. Such a model is referred to as “inductive”. The inductive model was first used to estimate the wall roughness effect for the LCLS design which set very strict requirements on the surface polishing since the effect was estimated to be very strong. However, for realistic surfaces the length of the protrusions is significantly larger than their height, and thus the impedance is reduced (similar to the impedance of a long slot vs. impedance of a hole). As a result, an estimate based on this model gives result which overestimates the impedance and imposes over conservative tolerances in terms of the rms height of the roughness.

The length of the protrusions along the surface (referred to as the “correlation length”) was taken into account in a model developed by Stupakov [10], which reduced the coupling impedance significantly for typical surfaces with large correlation length. Such model is referred to as “statistical”. Its comparison with “inductive” model was given in [11]. Discussion and measurement of the surface roughness as well as arguments that the “statistical” model is a better description of realistic wall surfaces can be found in Ref. [12], for example.

Another model for the wall roughness was introduced by Novokhatski [13, 14]. In this model the presence of roughness is equivalent to a pipe with a thin dielectric layer or periodic corrugation on the smooth wall surface. This model is referred to as the “resonator” model. In the resonator model the coupling impedance has also resistive part. As a result, one may need to worry about energy loss in addition to the energy spread.

A detailed comparison of the “resonator” and “inductive” models was given in [14]. Estimates done with the resonator model can result in even stronger effect from the wall roughness especially if the bunch length is small or comparable to the length of the protrusion (period of corrugation) or the longitudinal profile of the bunch is not smooth. The resistive part of the impedance is associated with the mode which can be excited by the beam and can propagate synchronously with the beam (“synchronous” mode). However, the model becomes invalid when the correlation length (or period of corrugation) is significantly larger than the height of the protrusion.

An extension of the theory to shallow corrugations showed that the low-frequency synchronous mode becomes suppressed for the large aspect ratios of the correlation length to the height of the protrusion, as shown in a subsequent work by Stupakov [15, 16].

In addition to theoretical models of the wall roughness, dedicated experimental studies were conducted as well. In Ref. [17] existence of the synchronous modes was

confirmed, while in Ref. [18] suppression of the synchronous modes was demonstrated for the surface roughness with large aspect ratios, in agreement with theory [16] and numeric simulations [19].

For the present estimate for the eRHIC, we thus assume that suppression of the synchronous modes will occur for large aspect ratios of the wall roughness, and that we can use expression from Ref. [16] to calculate the suppression factor for our parameters. To minimize the wall roughness effect we would also like to have a vacuum chamber surface with the aspect ratio of the wall roughness as large as possible. Therefore, extruded aluminum vacuum chambers were suggested for the eRHIC design.

Since we were not able to find measurements for extruded aluminum surfaces with a detailed characterization of the wall roughness, we attempted such measurements ourselves [20]. For these measurements, a small sample of an unpolished extruded aluminum NSLS-II vacuum chamber was used. Using commercial “PocketSurf-1” device, measured rms height of the grooves on the surface was about 3-4 microns, which is slightly higher than in similar measurements done at NSLS-II [21]. The measurements of the correlation length were done at BNL’s Instrumentation Division using an optical microscope which gave about 3 mm length for such waves/grooves in the direction of extrusion.

Using measured aspect ratio of 3000/3 (length to height) for the wall roughness, the suppression factor from Ref. [16] is  $3 \cdot 10^{-10}$  for design parameters of eRHIC. Therefore, we assume that there should be no energy loss due to the suppression of the low-frequency synchronous mode for our parameters. However, for such long protrusions the bunch length is no longer larger than the correlation length, and thus excitation of high-frequency synchronous modes may need to be considered. On the other hand, experimental study in Ref. [18] seems to indicate suppression of the synchronous modes even for this regime of parameters.

The large aspect ratio of the roughness also suppresses inductive part of the impedance thus decreasing energy spread due to the wall roughness. As an example, Fig. 4 shows resulting energy spread due to the wall roughness for the eRHIC design calculated using expression from Ref. [10] where long correlation length is taken into account.

Based on this estimate, for our parameters with the vacuum chamber full size of 5 mm, expected contribution to the energy spread appears to be less important than from the RF and RW effects. As a result, we presently do not impose additional requirement of polishing of the vacuum chambers to a high degree. If needed, the effect of the wall roughness can be further minimized by increasing bunch length and increasing the size of the vacuum chamber.

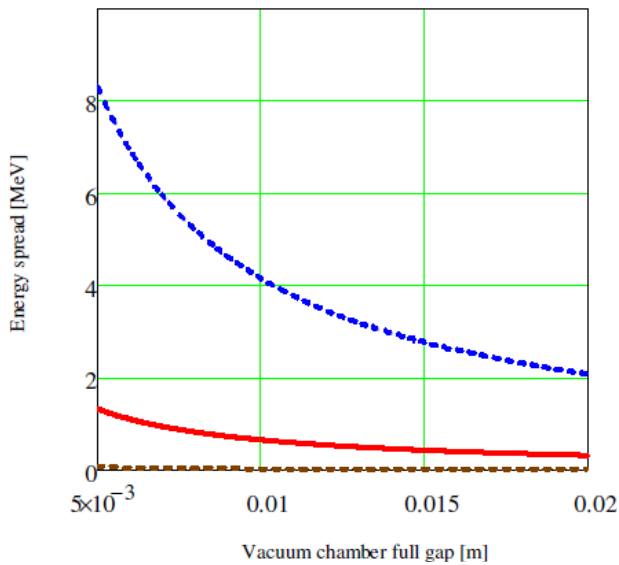


Figure 4: Calculated energy spread due to wall roughness for eRHIC design (for rms bunch length of 2 mm) assuming measured correlation length of 3 mm for several rms heights of the wall roughness: Blue (dashed upper curve) – 10  $\mu\text{m}$ ; red (solid middle curve) – 4  $\mu\text{m}$ ; brown (dashed low curve) – 1  $\mu\text{m}$ .

As discussed in this section, wake fields due to the wall roughness can have a very strong effect on the eRHIC design depending on the assumption used. Our present understanding of the subject, and assumptions used, suggest that this effect may be mitigated with the vacuum chamber surface which has very large aspect ratios of the wall roughness. However, discussion presented here should be regarded as work in progress, and further studies of this subject will continue.

### SUMMARY

For the eRHIC design, effect on the energy spread from the longitudinal wake fields was estimate from the RF cavities, Resistive Wall, Coherent Synchrotron Radiation and Wall Roughness. The largest contribution comes from the RF cavities and resistive wall.

Most of the discussions in this report were devoted to the effects which appear to be less settled such as suppression of CSR due to shielding and possible suppression of WR effects for surfaces with the large aspect ratios of the roughness.

### ACKNOWLEDGMENTS

We would like to thank S. Belomestnykh, I. Ben-Zvi, A. Blednykh, C. Hetzel, V. Litvinenko, G. Mahler, V. Ptitsyn, T. Rao and other members of eRHIC team for useful discussions and help.

### REFERENCES

- [1] V. Ptitsyn et al., Proc. of IPAC2011 (San Sebastian, Spain, 2011), p. 3726, THPZ019.
- [2] J. Schwinger, Phys. Rev. 75, 1912 (1949); “On Radiation by Electrons in a Betatron” (1945, unpublished) transcribed by M. Furman: LBNL-39088/CBP Note 179.
- [3] J. Nodvick, D. Saxon, Phys. Rev. 96, p. 180 (1954).
- [4] R. Warnock, SLAC-PUB-5375 (1990).
- [5] T. Agoh and K. Yokoya, Phys. Rev. ST Accel. Beams 7, 054403 (2004).
- [6] J. Murphy, S. Krinsky, R. Gluckstern, Proc. of PAC95 (1995); Part. Accel. 57, 9 (1997).
- [7] C. Mayes, G. Hoffstaetter, Phys. Rev. ST Accel. Beams 12, 024401 (2009).
- [8] V. Yakimenko et al., “CSR shielding experiment”, Proc. of PAC11 (New York, NY, 2011), WEP107.
- [9] K. Bane et al., Proc. of PAC97 (Vancouver, Canada, 1997), p. 1738.
- [10] G. Stupakov, Phys. Rev. ST Accel. Beams 1, 064401 (1998).
- [11] K. Bane and G. Stupakov, SLAC-PUB 8023 (1998).
- [12] G. Stupakov et al., Phys. Rev. ST Accel. Beams 2, 060701 (1999).
- [13] A. Novokhatski and A. Mosnier, Proc. of PAC97, p. 1661; A. Novokhatski, M. Timm, T. Weiland, “The surface roughness wake field effect”, Proc. of ICAP98 (Monterey), DESY Report TESLA 99-17.
- [14] K. Bane, A. Novokhatskii, SLAC-AP-117 (1999).
- [15] G. Stupakov, SLAC-PUB-8208 (1999).
- [16] G. Stupakov, SLAC-PUB-8743 (2000).
- [17] M. Huening et al., PRL 88, 074802 (2002).
- [18] F. Zhou et al., PRL 89, 174801 (2002).
- [19] A. Novokhatski, private communications.
- [20] A. Fedotov, G. Mahler, T. Rao et al., Measurements of the surface roughness for a sample of extruded aluminum vacuum chamber (2011).
- [21] A. Blednykh, C. Hetzel, private communications.

# CALCULATION OF CSR IMPEDANCE USING MESH METHOD

D. Zhou\*, KEK, 1-1 Oho, Tsukuba, Ibaraki 305-0801, Japan

## Abstract

A new code CSRZ was developed to investigate the longitudinal coherent synchrotron radiation (CSR) impedance for a single or a series of bending magnets. To calculate CSR impedance, the mesh method developed by T. Agoh and K. Yokoya [1] was adapted to the case of a curved rectangular chamber with variable bending radius. The method is based on the integration of the parabolic equation in the frequency domain in a curvilinear coordinate system. In the code CSRZ, the curvature of the beam trajectory can be set to be an arbitrary function of the distance along the beam orbit. Thus it allows calculating CSR impedance generated by either a single bending magnet or a series of bending magnets. In this paper, we first describe the code and formalism for CSR calculation. Then we apply the code to calculate the longitudinal CSR impedance using an example appearing in the compact energy recovery linac (cERL) project at KEK.

## INTRODUCTION

The mesh method was devised by Agoh and Yokoya and has been used to calculate the longitudinal CSR impedance in a single bending magnet [1]. The most important idea was based on paraxial approximation of Maxwell's equations. A simplified set of parabolic equations was found to describe the evolutions of CSR fields, i.e.

$$\frac{\partial \vec{E}_\perp}{\partial s} = \frac{i}{2k} \left[ \nabla_\perp^2 \vec{E}_\perp - \frac{1}{\epsilon_0} \nabla_\perp \rho_0 + 2k^2 \left( \frac{x}{R(s)} - \frac{1}{2\gamma^2} \right) \vec{E}_\perp \right], \quad (1)$$

where  $\vec{E}_\perp$  is the transverse electric field, and  $R(s)$  is the bending radius at distance  $s$  along the beam orbit.  $\epsilon_0$  is the vacuum permittivity.  $\gamma$  is the Lorentz factor, representing the beam energy. The term of  $1/\gamma^2$  indicates the normal space-charge effect. The beam is assumed to be rigid, i.e. the beam charge density  $\rho_0$  does not vary along  $s$ . Equation (1) also describes the field evolution in a straight chamber where the inverse bending radius is zero. With paraxial approximation, the longitudinal electric field is approximated by

$$E_s = \frac{i}{k} \left( \nabla_\perp \cdot \vec{E}_\perp - \mu_0 c J_s \right), \quad (2)$$

where  $\mu_0$  is the vacuum permeability,  $c$  is the speed of light in vacuum, and  $J_s = \rho_0 c$  is the current density.

The spatially discretized version of Eq. (1) was solved by an iterative procedure on a uniform grid. It was pointed out in Ref. [1] that this mesh method is very flexible and can be extended in a number of ways.

The original motivation of developing an independent code, i.e. CSRZ, was intended to study the multi-bend CSR interference in a storage ring. In CSRZ, the beam is assumed to have a point charge form in the longitudinal direction. Then the longitudinal CSR impedance is calculated by directly integrating  $E_s$  over  $s$

$$Z_\parallel(k) = -\frac{1}{q} \int_0^\infty E_s(x_c, y_c) ds \quad (3)$$

where  $(x_c, y_c)$  denotes the center of the beam in the transverse  $x-y$  plane. The appearance of the minus sign in Eq. (3) is due to the convention of the beam instability formalism.

The code CSRZ has been used to investigate the multi-mode interference in a long bending magnet with toroidal pipe [2], the multi-bend interference in a series of bending magnets [3], the coherent undulator radiation impedance [4], and the CSR field profiles inside a vacuum chamber [5]. In this paper, the main features of CSRZ are presented first. Then CSR impedance in a single magnet of cERL return loop [6] is calculated. The numerical results are compared with the analytical models.

## MAIN FEATURES OF CSRZ

The code CSRZ inherits main features of Agoh's method as described in Ref. [7]. As shown in Eq. (1), the beam trajectory defined by  $R(s)$  is assumed to be an arbitrary functions of  $s$ . This assumption indicates the most significant feature of CSRZ. The beam trajectory can be generated by a single bending magnet, by a series of bending magnets, or by an undulator or a wiggler. Consequently, the vacuum chamber having a uniform rectangular cross-section adopts the same curvature of the beam trajectory. Freeing  $R(s)$  allows CSRZ to investigate the CSR interference between consecutive bending magnets, even coherent wiggler or undulator radiation.

The total field is separated into two parts: the beam self-field in free space and the radiation field inside the vacuum chamber. For an ultra-relativistic beam, the beam field is transverse to the beam orbit and its analytic solution for a bi-Gaussian distribution is known and is independent of  $s$ . The boundary conditions should also be modified due to this field separation. The resistive-wall effects has also been taken into account by applying Leontovich boundary condition at the metal chamber surface.

\* dmzhou@post.kek.jp

The fields before the beam enters the curved chamber are given by the steady-state Coulomb field of the relativistic beam established in the straight chamber. By solving Poisson's equation of electric potential, the initial conditions are determined. Consequently, the entrance transient effect of CSR is naturally included.

Regarding to the discretization of the field evolution equation, finite-difference scheme is adopted. To avoid numerical oscillations as well as numerical damping, the fields are sampled on a staggered grid with ghost points outside the chamber wall surface introduced to enforce the boundary conditions. The transient effect at the final exit of the curved chamber is treated by connecting an infinite long straight chamber. The CSR fields entering this straight section are decomposed into the sum of simple eigenmodes in a uniform rectangular waveguide. Then the total wake potential is obtained by integrating these modes semi-analytically [8].

The capability of CSRZ is mainly limited by the mesh sizes in the  $x - y$  plane and step size in the  $s$  direction. With explicit discretization scheme, the mesh and step sizes should be proportional to  $k^{-2/3}$  and  $k^{-1/3}$  respectively, due to necessary numerical stability conditions [1]. To obtain CSR impedance at extremely high frequency, the computations become unacceptably expensive. The next limitation factors are bending radius and chamber cross-section. Smaller bending radius and larger chamber cross-section lead to longer computing time and more computer memory.

## APPLICATION TO COMPACT-ERL AT KEK

The cERL is a test facility under construction at KEK for demonstrating key technologies of GeV-class ERLs. The beam energy with one acceleration is 35 MeV in the first commissioning and will be 125 MeV finally [6]. The rms bunch length is 1-3 ps for normal operation and 0.1 ps or less for bunch compression mode. The bunch charge is 7.7 to 77 pC for normal operation and 77pC or more for bunch compression. The vacuum chamber of the cERL loop basically has a round shape with diameter of 50 mm.

The CSR impedance for a single bend is calculated at different beam energy, as depicted in Fig. 1. The vacuum chamber cross-section is approximated by a square with full size of 50 mm. The bending radius and bending angle for one bend are 1 m and  $\pi/4$ , respectively. The beam is assumed to locate at the center of the chamber, with transverse beam sizes of  $\sigma_x = 0.2$  mm and  $\sigma_y = 0.1$  mm. The numerical results are compared with steady-state models in free space [9] and with parallel-plates shielding [1]. From the figures, both numerical and analytical results show that at frequencies lower than  $k_{th} = \pi\sqrt{R/b^3}$  [10], the CSR waves are strongly shielded, mainly due to the existence of the upper and lower chamber walls. The outer-wall of the chamber reflects the trailing radiation fields back to the beam and causes fluctuations

in the impedance. The inner-wall of the chamber shields the overtaking fields and changes the slope of the imaginary part of the impedance [2]. The imaginary impedances show remarkable difference in the slope at beam energies of  $E = 35$  MeV and  $E = 125$  MeV. This difference is due to the normal space-charge effect related to the  $1/\gamma^2$  term. It suggests that normal space-charge effects can be comparable to CSR effects at the beam energy of 35 MeV. At beam energy of 125 MeV or higher, normal space-charge effects are fairly negligible.

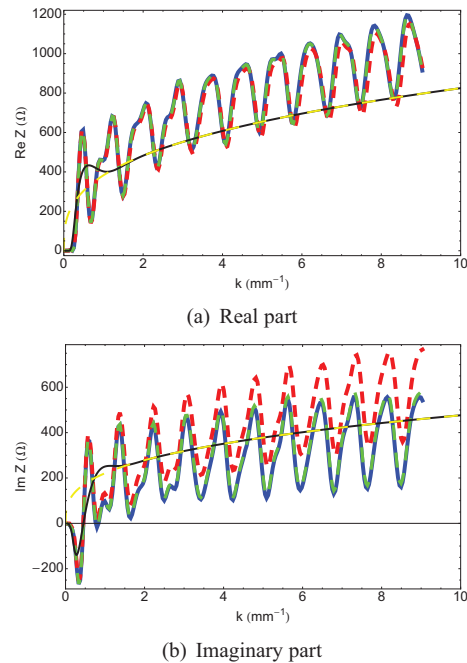


Figure 1: CSR impedance for a single bend in the cERL return loop. The CSR in the drift chamber after the exit of the bend is taken into account. Blue solid lines:  $\gamma=\infty$ ; red dashed lines:  $\gamma=68.5$  ( $E = 35$  MeV); green dashed lines:  $\gamma=244.6$  ( $E = 125$  MeV); black solid lines: steady-state parallel plates model; yellow dashed lines: steady-state free space model.

The longitudinal wake potential, indicating energy kick along a beam bunch, can be calculated from impedance with specified bunch profile. As shown in Fig. 2, first we assume Gaussian bunch lengths of  $\sigma_t = 1, 2, 3$  ps and calculate the CSR wake potentials from the impedances shown in Fig. 1. Because we only considered the normal space-charge effect in a chamber length of  $L_b = 0.7854$  m, the space-charge effect is almost invisible from the wake potentials. If we take into account the space-charge fields distributed around the whole loop, space-charge effect can become remarkable at short bunch length of  $\sigma_t = 1$  ps in the low beam energy of 35 MeV.

In Fig. 3, we compare the CSRZ results with the 1D model adopted in ELEGANT code [11, 12]. At this point, the drift CSR, which will be checked in next paragraphs, is ignored tentatively. One observes that in general CSRZ agrees with the 1D model from Saldin *et al.* in predic-

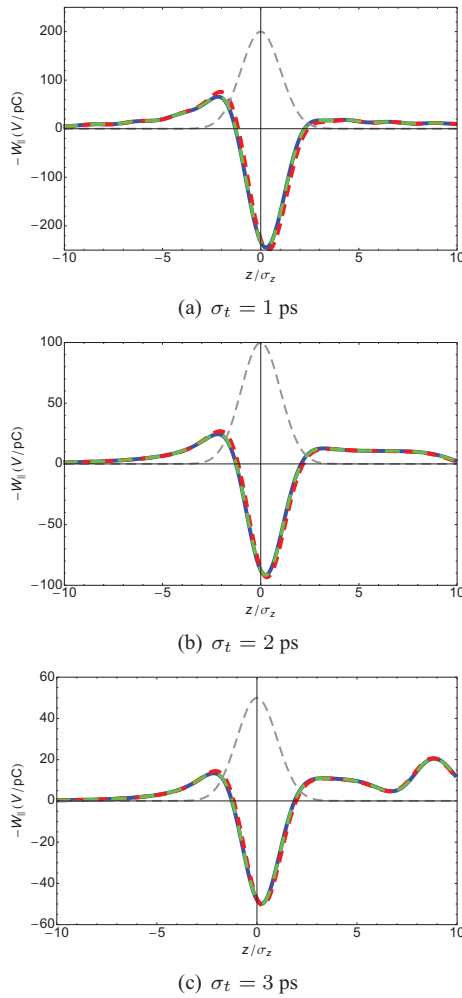


Figure 2: CSR wake potentials for a single bend in the cERL return loop with Gaussian bunch lengths of  $\sigma_t = 1, 2, 3$  ps. The drift CSR is taken into account. Blue solid lines:  $\gamma=\infty$ ; red dashed lines:  $\gamma=68.5$  ( $E=35$  MeV); green dashed lines:  $\gamma=244.6$  ( $E=125$  MeV); gray dashed lines: Gaussian bunch profile.

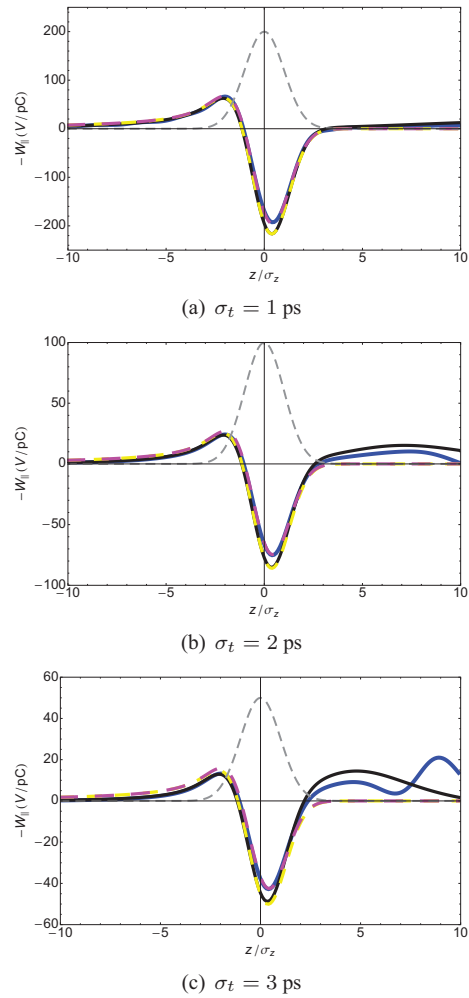


Figure 3: CSR wake potentials for a single bend in the cERL return loop with Gaussian bunch lengths of  $\sigma_t = 1, 2, 3$  ps and  $\gamma = \infty$ . The drift CSR is not taken into account. Blue solid lines: by CSRZ; magenta dashed lines: 1D model; black solid lines: steady-state parallel plates model; yellow dashed lines: steady-state free space model; gray dashed lines: Gaussian bunch profile.

tions of wakefields in the vicinity of bunch center. Meanwhile, the discrepancy of amplitudes in the same area between CSRZ and steady-state models is attributed to entrance transient. Chamber shielding slightly suppresses the CSR wakefields at the bunch head part but enhances the wakefields at the bunch tail part. That is, the particles at the bunch tail part gain energy due to chamber shielding. Only when the bunch length is short enough, i.e. much less than  $1/k_{th}$ , chamber shielding is negligible.

The effect of CSR in the drift chamber after the exit of the bend is illustrated in Figs. 4-6. As observed from Fig. 4, with drift CSR neglected, the average slope of the imaginary part of CSR impedance is close to the free-space model at high frequency. But the average slope of the real part is slightly lower than the free-space model. This is due to the transient effect at the entrance part. The drift CSR changes the slope of both real and imaginary parts of CSR

impedance under the existence of straight chamber. This feature reveals the complexity of evaluating its effects on beam dynamics. The wake potentials corresponding to the impedances of Fig. 4 are shown in Fig. 5. One can easily see that the drift CSR causes additional energy loss and gain for particles in the vicinity of bunch centroid and in the bunch tail part, respectively.

Finally, we compare CSRZ results with the free-space model for drift CSR given in Ref. [13]. The results are shown in Fig. 6. It is seen that for bunch lengths longer than 1 ps, the free-space model overestimates the energy kick at the bunch centroid, and particles at the tail part gain energy due to chamber shielding.

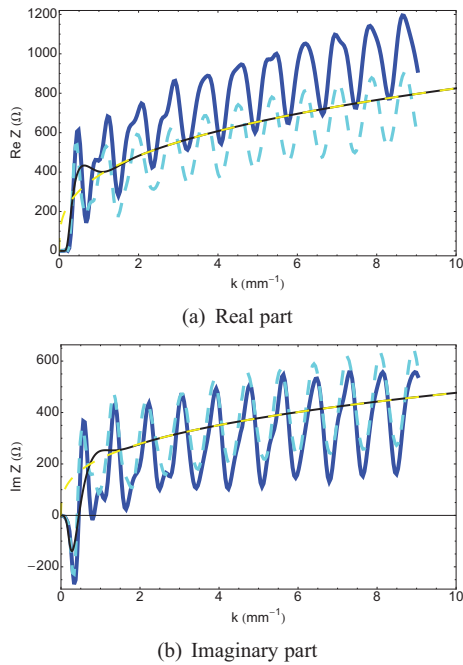


Figure 4: CSR impedance for a single bend in the cERL return loop with  $\gamma = \infty$ . Blue solid lines: with drift CSR considered; cyan dashed lines: with drift CSR neglected; black solid lines: steady-state parallel plates model; yellow dashed lines: steady-state free space model.

## DISCUSSIONS AND TENTATIVE CONCLUSIONS

In this paper, the CSRZ code was used to investigate the properties of CSR impedance of a single bending magnet in the cERL return loop. It was found that chamber shielding causes remarkable energy kick, which is comparable to that felt by the particles at the bunch head part, to the particles at the bunch tail part in the cases of  $\sigma_t > 2$  ps. When using the criterion of  $\sigma_z \ll 1/k_{th}$  to estimate the shielding effect of vacuum chamber, it is suggested that the bunch length  $\sigma_z = c\sigma_t$  should be replaced by the full bunch length, instead of the rms bunch length. Drift CSR wake is more sensitive to chamber shielding. The free-space model for drift CSR over-estimates the energy kick in the case of  $\sigma_t > 1$  ps. Under bunch compression mode, the bunch will be compressed to rms length of 0.1 ps, and chamber shielding is fairly negligible. One minor point is that normal space-charge effects can be comparable to CSR effect at beam energy of  $E = 35$  MeV or lower. More careful studies using macro-particle tracking simulations are underway to evaluate the space-charge effects and chamber shielding effects in CSR on beam dynamics.

The author would like to thank N. Nakamura for his interests in this work and M. Shimada and T. Miyajima for helpful discussions.

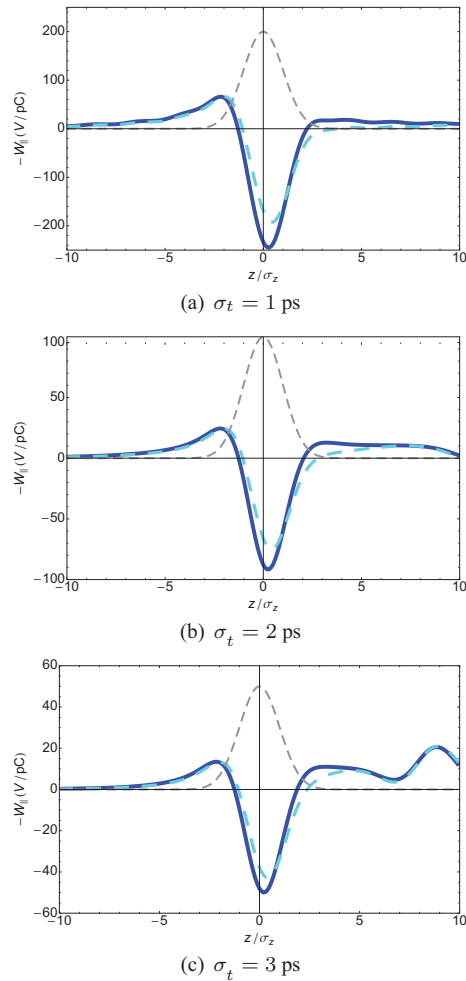


Figure 5: CSR wake potentials for a single bend in the cERL return loop with Gaussian bunch lengths of  $\sigma_t = 1, 2, 3$  ps and  $\gamma = \infty$ . Blue solidlines: with drift CSR considered; cyan dashed lines: with drift CSR neglected; gray dashed lines: Gaussian bunch profile.

## REFERENCES

- [1] T. Agoh and K. Yokoya, Phys. Rev. ST Accel. Beams, 7(5):054403 (2004).
- [2] D. Zhou, et al., IPAC'11, p.2268.
- [3] D. Zhou, et al., IPAC'11, p.604.
- [4] G. Stupakov and D. Zhou, SLAC-PUB-14332, December 9, 2010.
- [5] D. Zhou, PhD thesis, KEK/SOKENDAI, Sep. 2011.
- [6] M. Shimada, et al., IPAC'11, p.1909.
- [7] T. Agoh, Ph.D. thesis, University of Tokyo, 2004.
- [8] G. V. Stupakov and I. A. Kotelnikov, Phys. Rev. ST Accel. Beams, 12(10):104401 (2009).
- [9] A. Faltens and L. J. Laslett, Part. Accel. 4, 151. (1973).
- [10] T. Agoh, Phys. Rev. ST Accel. Beams, 12(9):094402 (2009).
- [11] M. Borland, Argonne National Laboratory Advanced Photon Source Report No. LS-287, 2000.
- [12] E. L. Saldin, et al., Nucl. Instrum. Methods Phys. Res., Sect. A, 398, 373 (1997).
- [13] G. Stupakov and P. Emma, LCLS-TN-01-12, December, 2001.

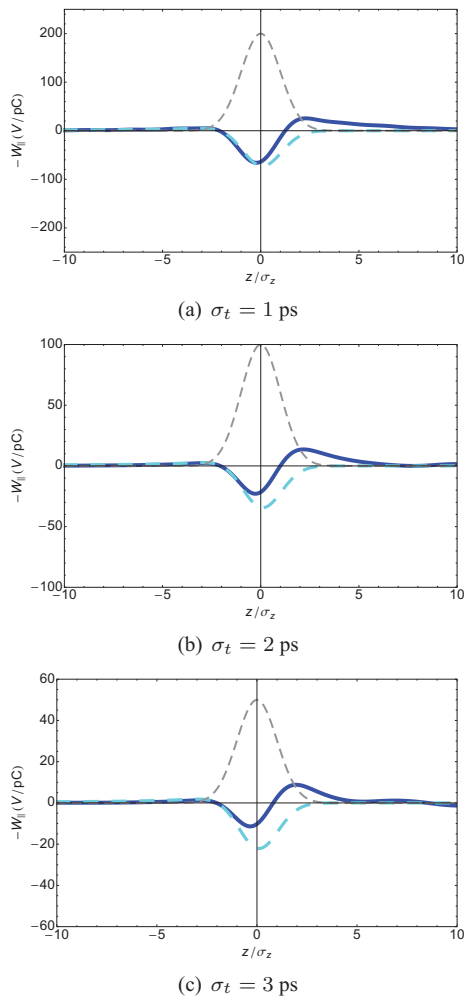


Figure 6: CSR wake potentials for a single bend in the cERL return loop with Gaussian bunch lengths of  $\sigma_t = 1, 2, 3$  ps and  $\gamma = \infty$ . Blue solidlines: drift CSR by CSRZ; cyan dashed lines: drift CSR by Stupakov and Emma's free-space model; gray dashed lines: Gaussian bunch profile.

# INTRA-BEAM SCATTERING AND ITS APPLICATION TO ERL\*

A.V. Fedotov<sup>#</sup>, BNL, Upton, NY 11973, USA

## Abstract

Treatment of Coulomb collisions within the beam requires consideration of both large and small angle scattering. Such collisions lead to the Touschek effect and Intrabeam Scattering (IBS). The Touschek effect refers to particle loss as a result of a single collision, where only transfer from the transverse direction into longitudinal plays a role. It is important to consider this effect for ERL design to have an appropriate choice of collimation system. The IBS is a diffusion process which leads to changes of beam distribution but does not necessarily result in a beam loss. Evaluation of IBS in ERLs, where beam distribution is non-Gaussian, requires special treatment. Here we describe the IBS and Touschek effects with application to ERLs.

## INTRODUCTION

A subject of Coulomb scattering within charged particle beams is well established in circular particle accelerators. In this report a brief summary is given with an emphasis on applications to the future high-current high-brightness Energy Recovery Linacs (ERLs). Here we do not attempt to produce a comprehensive list of references on existing IBS models but rather limit discussion to just a few with which we had some experience. Some specifics of the Touschek effect and IBS in ERLs are also discussed.

The effect when particles within the beam can be lost as a result of a single collision event (large-angle scattering) is called Touschek effect [1]. The cause of the Touschek effect is the transformation of the transverse momentum in longitudinal with its amplification by the relativistic factor  $\gamma$ . The particles are lost after collision if the change introduced in the longitudinal momentum is larger than the energy acceptance of accelerator.

When the scattering angles are small, random addition of such small scattering events can lead to a growth of beam dimensions. Such a multiple Coulomb scattering was first applied to explain emittance growth in electron beams [2, 3] and was called "multiple Touschek effect". The multiple Coulomb scattering was later generalized by Piwinski for proton machines without making any restrictions on the magnitude of beam temperatures, thus making it possible to transfer energy from the longitudinal into transverse via collisions [4]. This generalized treatment of multiple small-angle Coulomb scattering was also renamed as the Intrabeam Scattering (IBS) [4]. The IBS theory was later extended to include variations of the betatron functions and momentum dispersion function along the lattice of accelerator, and was summarized in reports by Martini [5] and Piwinski [6].

The different approach to IBS using the scattering matrix formalism from quantum electrodynamics was used by Bjorken and Mtingwa (B-M model) [7]. Both B-M and Martini's models are in good agreement with one another.

Note that a variety of IBS models were derived based on the original models of Bjorken-Mtingwa, Martini and Piwinski, which can produce different results, especially when used outside their region of applicability. In our experience with IBS simulations and experimental verification, exact Bjorken-Mtingwa [7] and Martini [5] models produced similar results both above and below transition energy of an accelerator.

Typical limitation of analytic models of IBS is that they are developed in an assumption of Gaussian distribution. In most situations such treatment is justified and models provide good agreement with experimental measurements (see Ref. [8], for example). However, when distribution starts to deviate from Gaussian significantly, assumption of Gaussian distribution may result in inaccurate predictions. To address this issue 1-D Fokker-Planck approach was effectively used before [9]-[10].

A more dramatic situation occurs when there is an externally applied force, like electron cooling. Since electron cooling force depends on the amplitudes of individual particles, the distribution under such force very quickly deviates from Gaussian. The problem of how to accurately account for IBS for such distributions became of special interest with a proposal to use electron cooling directly in a collider. Several approximate models were developed in the past to address this issue [11-13].

A more general description requires full treatment of kinetic problem. Such a treatment was introduced in the BETACool code [14] under the name "local IBS model" [15]. In addition to extensive numerical tests it was also benchmarked vs. experimental data with results reported in Ref. [16].

With application to ERLs, an approximate treatment using sliced-beam approach was suggested in Ref. [17]. In present report, a comparison between sliced-beam and local-IBS models is presented.

An analytic analysis of Coulomb scattering for a variety of distributions in 3-D was also performed in the past to understand possible halo formation in linear accelerators [18, 19]. These studies also discussed an extent of beam halo due to such collisions.

\*Work supported by the U.S. Department of Energy

<sup>#</sup>fedotov@bnl.gov

## TOUSCHEK EFFECT AND SCALING FOR MULTI-PASS ERL

Theoretical investigation of Touschek effect in accelerator community started with assumption of flat beams and thus transfer of only horizontal momentum into longitudinal [1, 3]. An assumption of non-relativistic velocities of colliding particles in their center of mass system was also used. The theory was further extended to take into account the cross-section valid for relativistic velocities [20]. The treatment was later generalized to 2-D to take into account transfer of both horizontal and vertical momentum with assumption of transversely round beam [21].

A more general treatment in 2-D for arbitrary ratios between horizontal and vertical amplitudes and arbitrary velocities was presented by Piwinski [22]. Piwinski's generalized expression produces other formulas by taking corresponding limits. This generalized expression of Piwinski was implemented in simulations codes and already applied for particle tracking in ERLs for APS [23] and Cornell [24] projects, for example.

For proposed eRHIC ERL [25] which is a multi-pass ERL with 6-pass acceleration to reach top energy and 6 passes to decelerate the beam, we are interested in the tails of loss distribution resulting from Touschek scattering. A net result for such distribution accumulated after total of 12 passes is shown in Fig. 1 for beam parameters shown in Table 1. For this plot we used 2-D expression for the scattering rate from Ref. [21].

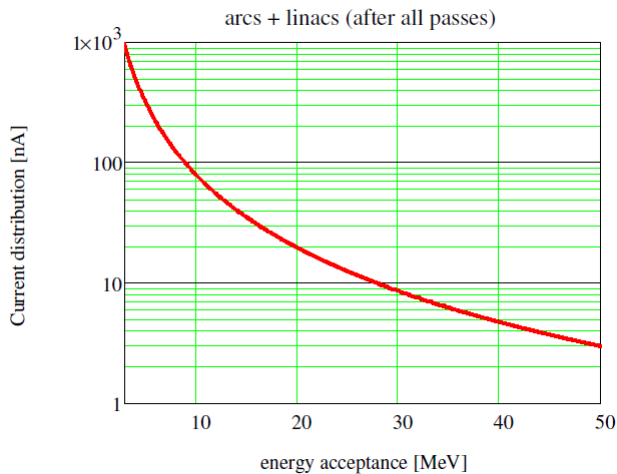


Figure 1: Resulting loss distribution from Touschek scattering after all 12 passes in eRHIC ERL expressed in terms of beam current outside energy deviation in MeV (zero on the axis is suppressed).

Table 1: Beam Parameters used for Touschek Calculations of 20 GeV eRHIC ERL

Total length of beam transport, km	46
Bunch charge, nC	3.5
RMS bunch length, mm	2
Normalized rms emittance, mm mrad	20
Average current, mA	50

In the course of these studies, the question came up whether resulting distribution in Fig. 1 is dominated by low-energy or high-energy passes in our multi-pass ERL. To understand scaling we use the same expression from Ref. [21]:

$$\frac{1}{N} \frac{dN}{dt} = \frac{2\pi}{\gamma^4} \frac{cr_c^2 NF(\varepsilon)}{(4\pi)^{3/2} \theta_y \theta_x \sigma_x \sigma_y \sigma_z (\Delta E_m / E)} \quad (1)$$

but replace function  $F(\varepsilon)$  by its approximate value

$$F(\varepsilon) = \frac{1}{\sqrt{\varepsilon}} - 6 \quad (2)$$

valid for small  $\varepsilon$  where  $\varepsilon = ((\Delta E_m / E) / (\gamma \theta_x))^2$ , and spread of the momentum in the horizontal and vertical directions is assumed the same (full coupling  $\beta_x = \beta_y$ ). Expressing in terms of the normalized emittances one gets:

$$\frac{1}{N} \frac{dN}{dt} = \frac{2\pi cr_c^2 N \gamma^{1/2}}{(4\pi)^{3/2} \varepsilon_{ny} \varepsilon_{nx} \sigma_z (\Delta E_m)^2} \sqrt{\frac{\varepsilon_{nx}}{\beta_x}} \quad (3)$$

where  $N$  is the number of particles per bunch,  $r_c$  is the classical radius of particle,  $\varepsilon_{nx}$  and  $\varepsilon_{ny}$  are transverse normalized rms emittances,  $\sigma_z$  is the rms bunch length,  $\beta_x$  is average of the lattice beta-function and  $\Delta E_m$  is energy deviation in absolute energy units. Equation (3) shows how each pass contributes to the current-loss distribution from Touschek scattering, with higher energies giving the largest contribution. Such relative contribution from different energies for eRHIC is shown in Fig. 2.

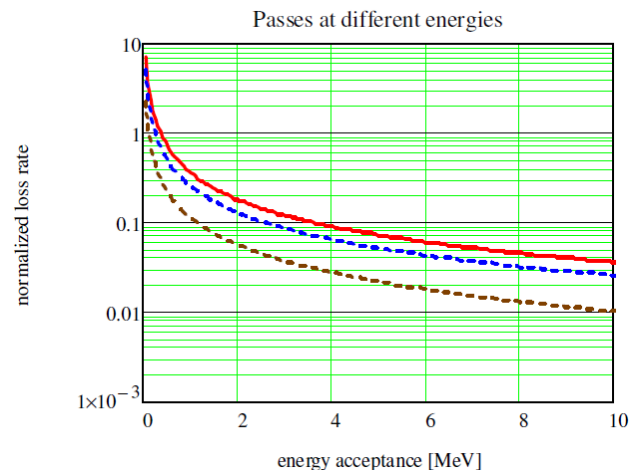


Figure 2: Relative contribution (in normalized units) to Touschek loss distribution from passes at 20 GeV (red upper curve), 10 GeV (middle blue curve) and 2 GeV (brown lower curve) for the case of eRHIC.

## IBS IN ERL

In comparison to circular accelerators, very large IBS growth rates are required to get noticeable distribution change because of a very short time the bunch spends in ERL. An order of magnitude estimate of both single and multiple scattering events can be obtained using, for example [18]:

$$\frac{1}{\tau} = K_n \frac{r_c^2 N c}{\gamma^2 \varepsilon_{ny} \varepsilon_{nx} \sigma_z \sigma_p} \Lambda_c \Lambda_n \quad (4)$$

where  $K_n$  is the normalization coefficient for a specific distribution function (less than unity),  $\sigma_p$  is rms energy spread,  $\Lambda_n$  is the logarithm needed for some singular distributions in 3-D (not needed for a Gaussian distribution), and  $\Lambda_c$  is the Coulomb logarithm (needed only for multiple scattering) the value of which varies from 10 to 15 for typical parameters of electron beams. Using parameters of some hypothetical high-brightness ERL from Table 2, and putting  $K_n = \Lambda_n = 1$  for this order-of-magnitude estimate, one gets IBS growth rates of about 1000 1/s which is large but not sufficient to cause any worry. One should note that growth rate will be significantly larger for low energies. As a result, the effect could be significant if one considers long transport of high-brightness beams at low energies.

Table 2: Beam Parameters of some Possible High-brightness ERL

Relativistic $\gamma$	1000
Bunch charge, nC	2
Bunch length $\sigma_z/c$ , ps	1
Normalized rms emittance, mm mrad	1
Rms momentum spread	0.001

However, it was recently pointed out that electron distribution in ERL is highly non-Gaussian, especially in the longitudinal plane. As a result, local IBS longitudinal rates can be very large due to small local longitudinal velocity spread within longitudinal slices of beam distribution. A simplified model of sliced-beam approach was suggested to treat such non-Gaussian distributions in ERLs [17].

A similar problem of IBS for non-Gaussian distribution was extensively studied in electron cooling community with a variety of approximate models developed. An approach based on amplitude-dependent diffusion coefficients was also implemented in BETACOOOL code [14] with extensive numerical benchmarking and comparison with experimental data [16]. Such implementation allows one to treat IBS for arbitrary distribution in 3-D, including when distribution is affected not just by IBS but also by some other amplitude-dependent force, like cooling. In the following section we present simulation comparison between such “local” IBS approach [16] and sliced-beam approximation which was also implemented in BETACOOOL code [26].

Before going into discussion of simulation results based on various models, we note that large local rate within a longitudinal slice of the beam should not necessarily lead to a significant change in beam distribution. The process of IBS is described by a diffusion in the velocity space. Since intrinsic momentum spread in typical ERL distribution is very small in each longitudinal slice of the beam, the longitudinal velocity spread in beam frame is much smaller than transverse. In such a case one can show that the longitudinal diffusion coefficient becomes almost independent of the longitudinal velocity spread (see [27, 13], for example), and thus very little growth could be expected despite the fact that local longitudinal rates are very high.

## SIMULATIONS OF IBS FOR ERL

For a test between “local” [15, 16] and “sliced-beam” approaches we use ERL beam distribution which was produced for our previous studies of high-energy electron cooling [28]. The histogram of velocities in such is shown in Fig. 3, and the longitudinal phase-space in Fig. 4.

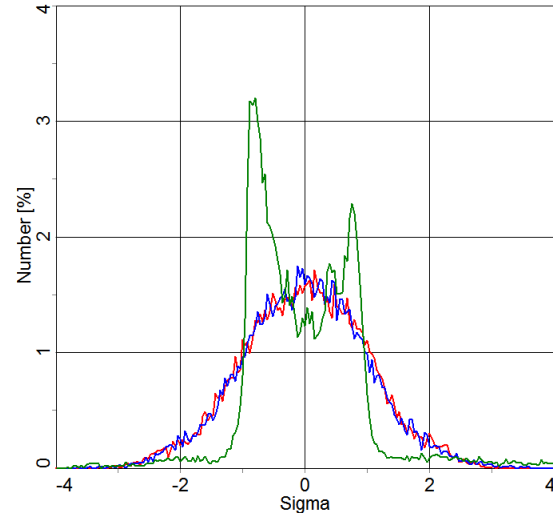


Figure 3: Histogram of velocity distribution of electrons. Red and blue – horizontal and vertical; green – longitudinal.

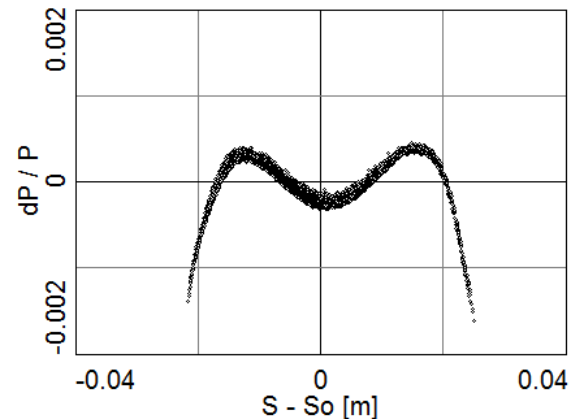


Figure 4: Initial longitudinal phase-space of distribution used in simulations.

First, we choose such beam parameters that IBS rates calculated based on rms quantities are small 15 1/s and local rates within the slices (Fig. 5) are not sufficient to cause significant distribution change. We then track such distribution over 4 km of beam transport line using the BEATCOOL code. As expected, no effect is observed both with the “local” and “sliced” beam approaches, as shown in Figs. 6 and 7, respectively.

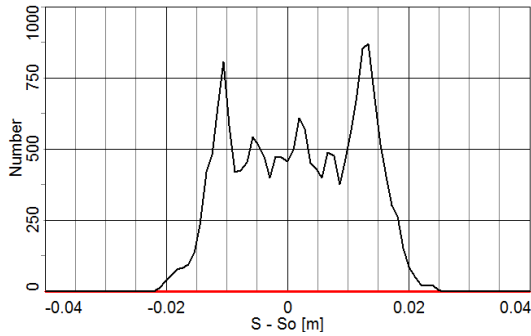


Figure 5: IBS rates within longitudinal slices of beam distribution. Vertical axis: local IBS rates [1/s].

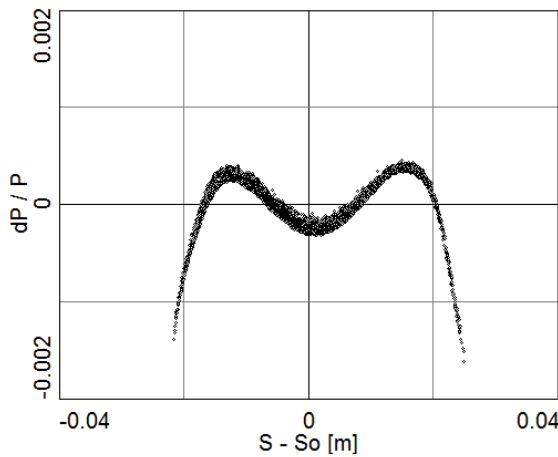


Figure 6: Longitudinal distribution after 4 km of beam transport using “sliced” approach, for local IBS rates shown in Fig. 5.

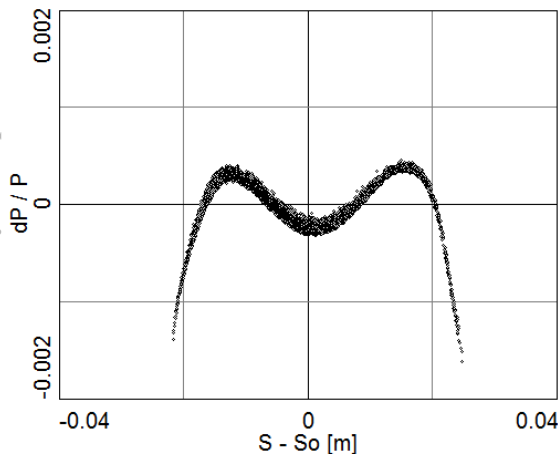


Figure 7: Longitudinal distribution after 4 km of beam transport using “local” approach, for local IBS rates shown in Fig. 5.

As a next test, we choose beam parameters for which IBS rates calculated based on rms quantities are significant: 1500 1/s and local rates within the slices are very large, as shown in Fig. 8. One can see that only modest change of distribution is observed after 4 km of beam transport both with the “sliced” and “local” beam approach, as shown in Figs. 9 and 10, respectively.

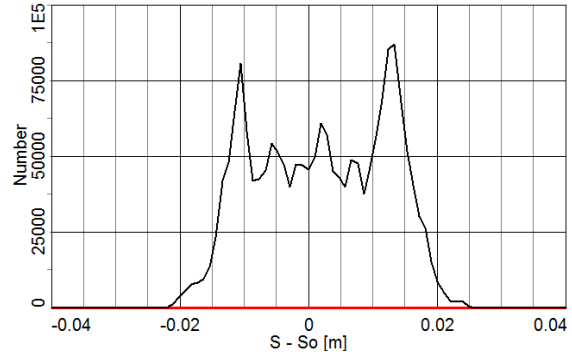


Figure 8: IBS rates within longitudinal slices of beam distribution. Vertical axis: local IBS rates [1/s].

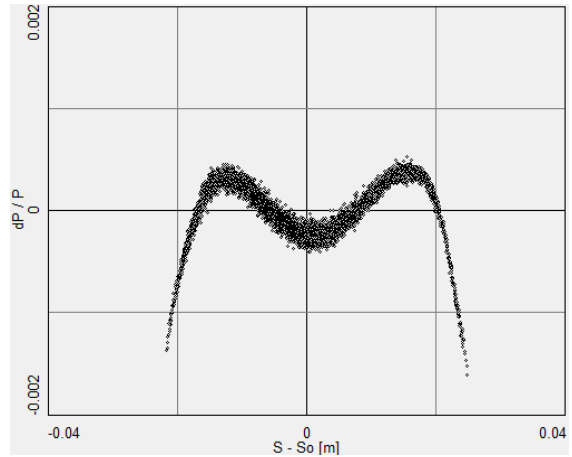


Figure 9: Longitudinal distribution after 4 km of beam transport using “sliced” approach, for local IBS rates shown in Fig. 8.

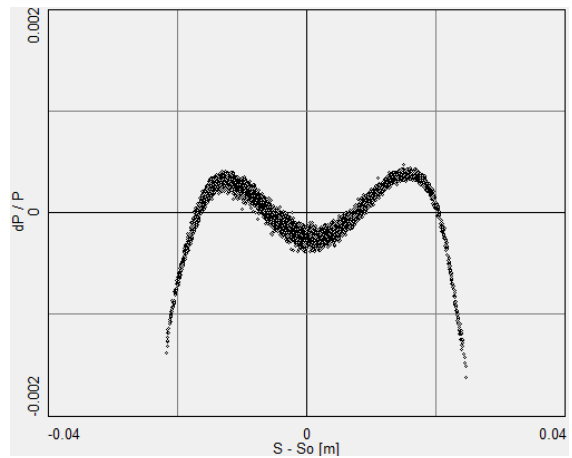


Figure 10: Longitudinal distribution after 4 km of beam transport using “local” approach, for local IBS rates shown in Fig. 8.

## SUMMARY

In circular accelerators both the Touschek effect and IBS were found important. The generalized formulas for Touschek calculations are available and are already being used in advanced tracking simulations of several ERL-based projects.

The IBS (which is diffusion due to multiple Coulomb scattering) is not expected to cause any significant effect on beam distribution in ERLs, unless one considers very long transport of high-brightness beams at low energies. Both large and small-angle Coulomb scattering can contribute to halo formation in future ERLs with high-brightness beams, as follows from simple order-of-magnitude estimates.

In this report, a test comparison between “local” and “sliced” IBS models within the BETACOOOL code was presented for an illustrative ERL distribution. We also presented accumulated current loss distribution due to Touschek scattering for design parameters of ERL proposed for the eRHIC project, as well as scaling for multi-pass ERLs.

## ACKNOWLEDGMENTS

We would like to thank D. Kayran, V. Litvinenko, V. Ptitsyn and other members of Accelerator R&D Division at Collider-Accelerator Department of BNL for useful discussions. Special thanks go to A. Smirnov (JINR, Dubna) who implemented “sliced” approach specifically to enable comparison presented in this report. We also thank members of BETACOOOL development team from JINR.

## REFERENCES

- [1] C. Bernardini et al., PRL 10, 407 (1963).
- [2] H. Bruck and J. Le Duff, Proc. of 5<sup>th</sup> Int. Conf. on High Energy Accelerators (INFN, Frascati), 1965.
- [3] H. Bruck, Circular Particle Accelerators, 1966.
- [4] A. Piwinski, Proc. 9<sup>th</sup> Int. Conf. on High Energy Accelerators, p. 105 (1974); CERN AS 1984, p. 405.
- [5] M. Martini, CERN PS/84-9 (1984).
- [6] A. Piwinski, CERN AS 1991 (CERN 92-01), p. 226.
- [7] Bjorken and Mtingwa, Part. Acc., 13, p.115 (1983).
- [8] A.V. Fedotov et al., “Experimental studies of IBS in RHIC and comparison with theories”, Proc. of HB2006 Workshop (Tsukuba, Japan, 2006), p. 259.
- [9] J. Wei et al., “IBS theory and RHIC experiments”, AIP Conf. Proc. 773 (Proc. of HB2004), p. 389.
- [10] V. Lebedev, “Single and multiple IBS in hadron colliders”, AIP Conf. Proc. 773 (HB2004), p. 440.
- [11] A. Burov, “Electron cooling against IBS for high-energy collider”, FERMILAB-TM-2213 (2003).
- [12] G. Parzen, BNL Tech Note C-AD/AP 144, 150 (2004).
- [13] A.V. Fedotov et al., “IBS for distributions under electron cooling”, Proc. of PAC05 (Knoxville, TN, 2005), p. 4263.
- [14] BETACOOOL code : <http://betacool.jinr.ru>; A. Sidorin et al., NIM A 558, p. 325 (2006).
- [15] BNL BETACOOOL report, December 2007: <http://betacool.jinr.ru/reports/>
- [16] A.V. Fedotov, A. Sidorin and A. Smirnov, Proc. of HB2010 (Morschach, Switzerland, 2010), p. 62.
- [17] A. Xiao and M. Borland, Proc. of PAC09 (Vancouver, Canada), p. 3281.
- [18] R.L. Gluckstern and A.V. Fedotov, Phys. Rev. ST Acc. Beams V. 2, 054201, 1999.
- [19] N. Pichoff, Proc. of PAC99 (New York), p. 3277.
- [20] U. Voelkel, DESY 67/5, 1965.
- [21] Y. Miyahara, Jap. Jour. of Appl. Phys. V. 24, No. 9, p. L742 (1985).
- [22] A. Piwinski, DESY 98-179, 1998.
- [23] A. Xiao and M. Borland, Proc. of PAC07 (Albuquerque, NM, 2007), p. 3453.
- [24] G. Hoffstaetter et al., Proc. of EPAC08 (Genoa, Italy), p. 1631.
- [25] V. Ptitsyn et al., Proc. of IPAC2011 (Spain), p. 3726.
- [26] Sliced-beam approach was implemented in BETACOOOL code by A. Smirnov (JINR, Dubna) specifically for benchmarking with “local” IBS model for typical distributions expected in ERLs.
- [27] A. Sorensen, Proc. CERN Accelerator School (1987).
- [28] A.V. Fedotov et al., Proc. of PAC07 (Albuquerque, NM, 2007), p. 3699.

# INVESTIGATION OF THE EFFECT OF SPACE CHARGE IN THE COMPACT-ENERGY RECOVERY LINAC

Ji-Gwang Hwang and Eun-San Kim\*,

Kyungpook National University, 1370 Sankyok-dong, Buk-ku, Daegu, 702-701, Korea

Tsukasa Miyajima,

KEK, Tsukuba, Ibaraki 305-0801, Japan

## Abstract

Compact energy recover linear(ERL) accelerator is a prototype of the 5 GeV ERL accelerator at KEK. The injector system has two SRF cavities which have the frequency of 1.3 GHz. It accelerates the bunches to the energy of 5 MeV. This beam was injected to the main ring and then it was accelerated to energy of 35 MeV at the main superconducting RF linac. Due to the low beam energy on the main ring, the investigation of the effect of space charge (SC) which causes the growth of the energy spread is important to produce the low emittance beam. For the production of the low emittance beam, the optimization of the merger was performed. To obtain smaller emittance at the exit of merger, the effect of the energy spread was also investigated by changing of the  $k_d$  which is defined by the ratio of energy spread to length of the bunch. In this calculation, we got the noralized transverse emittance of 0.735 mm-mrad at the exit of merger section.

## INTRODUCTION

The Energy Recovery Linear accelerator (ERL) is one of the candidates for the fourth generation light sources that can meet these requirements. The main feature of the ERL is production of low-emittance(  $\mu\text{m}$ ) beam with energy recovery in the main linac. The ERL requires sophisticated technology of superconducting accelerator. The generation of ultra-low emittance beams is need to demonstrate before constructing Multi-GeV ERL. The compact-ERL at KEK, in the final stage, will provide a beam energy of around 125 MeV and a bunch charge of 77 pC, which is a prototype for the future 5 GeV ERL at KEK. The layout of the compact-ERL is shown in Fig 1. The c-ERL consists of an injector system, a merger section, a superconducting RF (SRF) section, two return loops and two straight sections[3]. In the early comissioning phase of the compact-ERL, the energy is 35 MeV with a bunch charge of 7.7 pC. The electron injector system consists of a 500 kV photo cathode DC gun, two solenoid magnets, a buncher cavity, three superconducting RF cavities, seven quadrupole magnets and a merger section. In the second comissioning phase, the injector produces electron beams with a bunch charge of 77 pC, beam energy of 5 MeV and bunch length of 0.6 mm rms. The beam energy is increased by 30 MeV with two 9 cell SRF cavities. Since the beam energy in c-ERL is a

low with high charge, we need to consider the several effects, e.g., the space charge effect, the coherent synchrotron radiation (CSR) effect, the wake function, ion effects and beam break up[4]. In the case of low energy, the electric force which caused the growth of the energy spread is more stronger than the magnetic force. It called SC effect. The emittance growth due to the space charge (SC) effect is dominated for the case of low-energy, around 5 MeV [5], and causes growth of the energy spread. The energy spread induced in an achromatic cell results in the growth of projection emittance at the exit of the achromatic cell. It is known that this emittance growth can be compensated by setting the cell-to-cell betatron phase advance at an appropriate value[6].

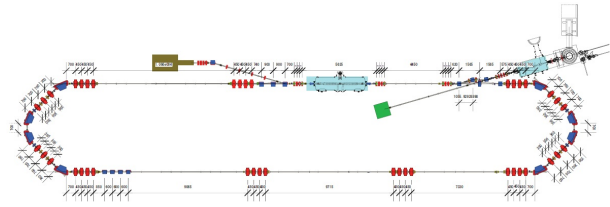


Figure 1: Layout of a compact-ERL.

## ENERGY SPREAD GROWTH DUE TO THE SC EFFECT

The low energy beam injected from the injector system merges with the circulating high energy beams. For the beam mergence, after passing the merger section, the ratio of circulating energy to injected energy should be large because the circulating beam is also kicked and needs to be bumped at the merger section. A merger section with 3-dipole was adopted for the flexible beam transport of the high energy circulating beam. The layout of the 3-dipoles merger is shown in Fig. 2.

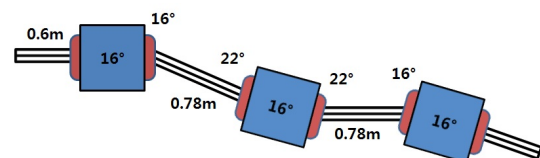


Figure 2: Layout of a merger section.

\* eskim1@knu.ac.kr

As shown in Fig. 2, the bending magnet at the center of the merger is sector type and bending magnets at the entrance and exit of the merger are rectangular type. The center bending magnet have an edge angle to achieve zero dispersion at the exit of the merger section. The space charge is dominated in the low-energy injector system. The characteristic field, which produced by the cylindrical uniform distribution, is given by Eq. 1.

$$E_z(z) = \frac{Q}{2\pi\epsilon_0 a^2} \left[ -\left| \frac{1}{2} - \frac{z}{L} \right| + \left| \frac{1}{2} + \frac{z}{L} \right| + \sqrt{\left( \frac{z}{L} - \frac{1}{2} \right)^2 + A^2} - \sqrt{\left( \frac{z}{L} + \frac{1}{2} \right)^2 + A^2} \right] \quad (1)$$

, where  $a$  is radius,  $\epsilon_0$  is permittivity,  $A = a/\gamma L$ ,  $Q$  is bunch charge and  $L = \sqrt{12}\sigma_z$  is full length of bunch. Based on the characteristic field, the growth of the energy spread due to longitudinal space charge force(LSCF) can be calculated that is shown in Fig. 3.

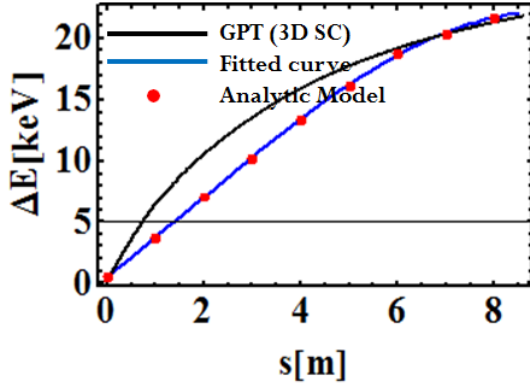


Figure 3: Growth of the energy spread due to the LSCF.

The growth of the energy spread due to the LSCF is fitted by  $\Delta E = k_0 + k_1 s + k_2 s^2 + k_3 s^3$  formula. The fitted parameter is given by  $k_0 = 0.45 \pm 0.09$ ,  $k_1 = 3.20 \pm 0.11$ ,  $k_2 = 0.092 \pm 0.033$  and  $k_3 = -0.020 \pm 0.0027$  when the charge of bunch is 77 pC, energy of bunch is 5 MeV, radius of bunch is 0.2 mm and the length of bunch is 3 ps with uniform distribution on longitudinal phase space. Based on this calculation, the analytical calculation of the emittance growth in the merger section was performed by using the first-order theory[7]. In the constant LSCF regime, the Eq. 2 can be solved analytically, and electron dynamics through an achromatic cell is calculated using the extended R-matrix [4].

$$x'' = -\frac{x}{\rho^2} + \frac{1}{\rho} \left( \delta_0 + \delta_{SC} + \frac{k_1}{E_0} (s - s_0) + \frac{k_2}{E_0} (s - s_0)^2 + \frac{k_3}{E_0} (s - s_0)^3 \right) \quad (2)$$

A vector was defined to express electron motion:

$(x, x', \delta_0, \delta_{SC}, k_1/E_0, k_2/E_0, k_3/E_0)^T$ . And an R-matrix for a sector magnet is given by

$$\begin{pmatrix} \cos \theta & \rho \sin \theta & \rho(1 - \cos \theta) & \rho(1 - \cos \theta) & \rho^2(\theta - \sin \theta) \\ -\frac{\sin \theta}{\rho} & \cos \theta & \sin \theta & \sin \theta & \rho(1 - \cos \theta) \\ 0 & 0 & 1 & 0 & 0 \\ 0 & 0 & 0 & 1 & \rho\theta \\ 0 & 0 & 0 & 0 & 1 \\ 0 & 0 & 0 & 0 & 0 \\ 0 & 0 & 0 & 0 & 0 \\ \rho^3(\theta^2 + \cos \theta - 2) & \rho^4(\theta^4 + 6 \sin \theta - 6\theta) & & & \\ 2\rho^2(\theta - \sin \theta) & 3\rho^3(\theta^2 + 2 \cos \theta - 2) & & & \\ 0 & 0 & & & \\ (\rho\theta)^2 & (\rho\theta)^3 & & & \\ 0 & 0 & & & \\ 1 & 0 & & & \\ 0 & 1 & & & \end{pmatrix} \quad (3)$$

The LSCF is the main source of the emittance growth in the low-energy beam. In the analytical calculation, we assume that the longitudinal and transverse bunch lengths and sizes are not largely changed in the merger section. The energy spread of the beam due to the SC force was induced in the upstream part of the merger section. The slice of the beam in horizontal phase space has a different position in the downstream part of the merger section, due to the energy spread. The projected emittance grew due to the SC effect, shown in Fig. 4.

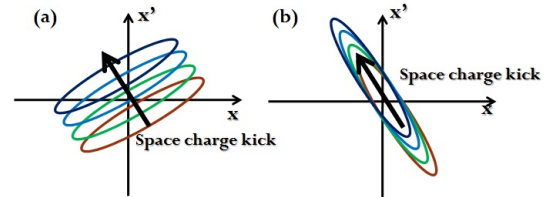


Figure 4: Growth of projected emittance due to the SC effect in merger section. (a) Maximum case of projected emittance growth (b) Minimum case of projected emittance growth.

The emittance growth due to the displacement of the bunch slices in phase space can be minimized by matching the displacement to the orientation of the phase ellipse at the exit of the merger. The first-order theory was used to calculate the space charge kick angle, because the displacement of the bunch slice is laid on the  $\zeta_x x' - \zeta'_x x = 0$ , where  $\zeta$  is the space charge dispersion,  $\zeta'$  is its derivative,  $x$  is the horizontal position and  $x'$  is its derivative. Therefore, the angle of the displacements due to the SC effect is given by

$$\phi_\zeta = \tan^{-1}(\zeta'_x / \zeta_x) \quad (4)$$

The analytical calculation of the space charge dispersion requires the space charge kick angle. The result of the space charge dispersion in the merger section is shown in Fig. 5.

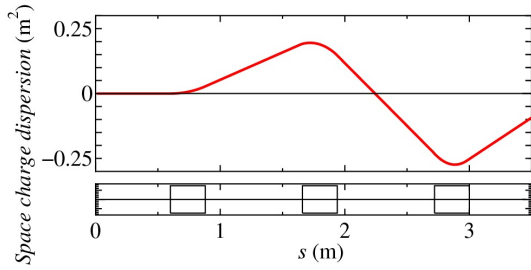


Figure 5: Space charge dispersion at the merger section.

In the analytical calculation, by using the first-order theory, the transfer matrix for each element is derived by Green's function method[8]. At the exit of the merger section, the space charge dispersion,  $\zeta_x$ , and derivative of the space charge dispersion,  $\zeta_x'$ , are  $-0.067 \text{ m}^2$  and  $0.134 \text{ m}$ , respectively. From the Eq. 4, the space charge kick angle,  $\phi_s$ , in horizontal phase space was calculated to be  $-1.11 \text{ rad}$  which is based on the first-order theory. Using the above calculation parameters, the LSCF wake potential was given by  $\Delta W_s = 13.75 \text{ [keV/m]}$ . Also,  $\kappa_s$  is the normalized space charge wake potential in the bending path and it is dependent on the space charge wake potential  $W \text{ [eV/m]}$ , and the reference energy  $E_0 \text{ [eV]}$  at  $s = s_0$ , which is the entrance of the bending magnet. It is given by  $\Delta\kappa_s = \Delta W_s / E_0 = 2.75 \times 10^{-3} \text{ [1/m]}$ . When the merger section is optimized by matching the envelope between the LSCF-induced dispersion function and the betatron function at the exit of the merger section, all the bunch slices align along the orientation of the phase ellipse and have a distribution of the displacement  $(\Delta\kappa_s\zeta, \Delta\kappa_s\zeta') = (-0.184 \text{ mm}, 0.368 \text{ mrad})$ . Based on the first-order theory, the transverse emittance growth in the merger section is given by

$$\varepsilon^2 = (\varepsilon_0\beta_x + D^2)(\varepsilon_0\gamma_x + D'^2) - (\varepsilon_0\alpha_x - DD')^2 \quad (5)$$

, where  $\varepsilon_0$  and  $\varepsilon$  are the initial and final emittance as un-normalized values, respectively, and  $(D, D') = (\Delta\kappa_s\zeta, \Delta\kappa_s\zeta')$  is the rms spread of the bunch slice displacement in  $(x, x')$  phase space. From Eq. 5, the result of analytical calculation of the emittance growth in the merger section is shown in Fig. 6.

To study the space charge effect, the particle tracking was carried out using General Particle Tracer (GPT) with mesh based method to calculate space charge effect, which includes the calculation of 3-dimensional SC force with actual electric and magnetic fields [9]. The particle tracking simulation gives the particle distribution in six dimensional phase space,  $(x, x', y, y', z, \dot{z})$ , where  $'$  and  $\dot{\phantom{x}}$  denote  $d/dz$  and  $d/dt$ , respectively. Here,  $x, y$  and  $z$  are the particle coordinates for the horizontal, vertical and longitudinal directions, respectively. When the beam consists of the  $N$  macro particles, the particle coordinate of the  $i$ -th particle is  $(x_i, x'_i, y_i, y'_i, z_i, \dot{z}_i)$ . The betatron function is defined by

$$\beta_x = \frac{\langle x_c^2 \rangle}{\varepsilon_x}, \quad (6)$$

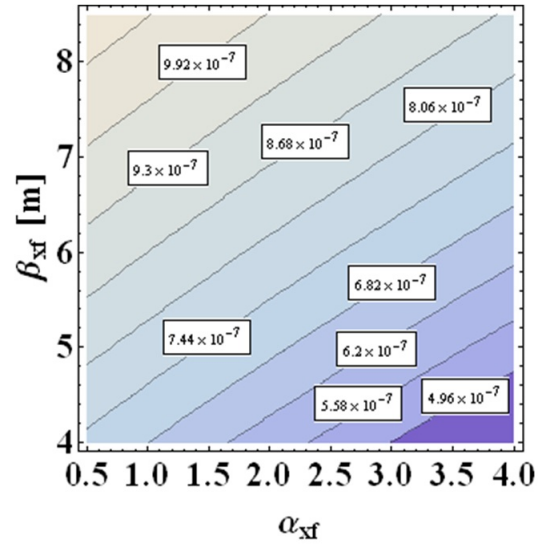
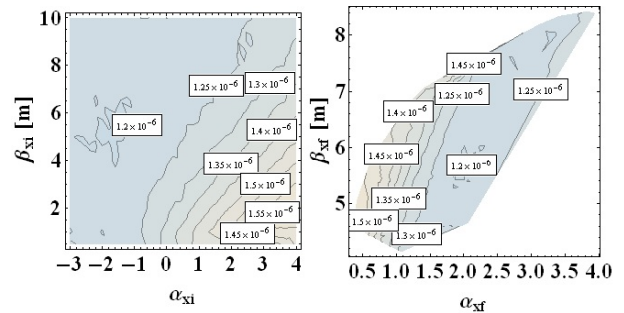


Figure 6: Analytical calculation results of emittance as function of twiss parameter at the exit of merger.

where  $x_{c,i} = x_i - \langle x \rangle$ ,  $x'_{c,i} = x'_i - \langle x' \rangle$ , and  $\varepsilon_x = \sqrt{\langle x_c^2 \rangle \langle x_c'^2 \rangle - \langle x_c x_c' \rangle^2}$ . Here,  $\langle \phantom{x} \rangle$  denotes an average, e.g.,  $\langle x \rangle = \sum x_i / N$ . In this paper, the betatron function is calculated by Eq. (6) from the calculated particle distribution. In the particle tracking simulation by using GPT code, the initial normalized transverse emittance is  $0.1 \text{ mm-mrad}$ , the bunch length is  $3 \text{ ps (rms)}$ , the beam energy is  $5 \text{ MeV}$ , radius of the bunch is  $1.5 \text{ mm}$  and the the bunch included the particle distribution of  $10000$  macroparticles. The bunch distribution was assumed to be beer-can shape, which has same vertical and horizontal emittances. The transverse emittance growth was scanned by the initial and final CS parameter at the entrance and exit of merger section. In the tracking simulation, the  $\beta_{xi}$  and  $\alpha_{xi}$  were varied from  $0.5 \text{ m}$  to  $10 \text{ m}$  by  $0.5 \text{ m}$  step and from  $-4$  to  $4$  by  $0.2$  step, respectively. Fig. 7 (a) and (b) show transverse emittances as a function of CS parameter at the entrance and the exit of the merger section.

Figure 7: Transverse emittance at the exit of the merger. (a) as function of the initial  $\alpha_{xi}$  and  $\beta_{xi}$ . (b) as function of the final  $\alpha_{xf}$  and  $\beta_{xf}$ .

As shown by Fig. 6 and 7, amount of the growth of the transverse emittance due to the SC effect is around  $1.09$

mm-mrad. Also, the growth of the transverse emittance has minimum value at the minus value of the  $\alpha_{xi}$  with small value of  $\beta_{xi}$ . But result of the growth of the emittance calculated by GPT different with result of the growth of the emittance calculated by first-order theory. These difference was caused by the 3-dimensional SC effect. In the numerical simulation by using GPT, the transverse emittance growth due to the 3-dimensional SC force in the merger section was observed. The results show that the emittance was minimized by changing the initial CS parameter. The initial CS parameter is  $\alpha_x = -1.6$ ,  $\beta_x = 5.5$  m when growth of the emittance is minimized. The growth of the transverse emittance as function of the orientation of the phase ellipse in the  $(x, x')$  phase space, which calculated by using the results of the numerical calculation as shown by Fig. 7, is shown in Fig. 8.

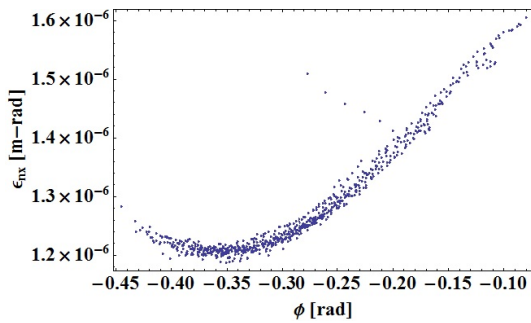


Figure 8: Transverse emittance at the exit of merger section as a function the orientation of the phase ellipse.

From the numerical calculation result, the emittance growth induced by the LSCF in the merger section was compensated by changing the orientation angle of the ellipse in horizontal phase space. We found a minimum transverse emittance growth of 1.09 mm-mrad in the merger section when the vertical CS parameter was fixed to  $\beta_y = 9$  m, with  $\alpha_y = 0$ . The CS parameters and dispersion function in merger section after compensation of the growth of the emittance due to the SC effect are shown by Fig. 9.

Also, the effect of coupled motion of the beam was investigated to minimize the emittance growth in the merger section. The vertical CS parameter was changed to investigate the effect of coupled motion. In the calculation, the horizontal CS parameter was fixed to  $\beta_x = 5.5$  m with  $\alpha_x = -1.6$  and shows a minimum emittance growth. The result is shown in Fig. 10.

As shown in Fig. 10, the minimum horizontal emittance growth at the exit of the merger becomes 0.684 mm-mrad at the  $\beta_y = 0.5$  m and  $\alpha_y = -10$ . From this result, the orientation of the phase ellipse was calculated to -0.62 rad. It is shown that the smaller angle of the phase ellipse which is calculated by the analytical model, -1.09 rad, gives the smaller growth of the emittance. To achieve the small angle of the phase ellipse, which is around -1.09 rad, it needs the small  $\beta_y$  with large  $\alpha_y$ . It causes the growth of the vertical beta-

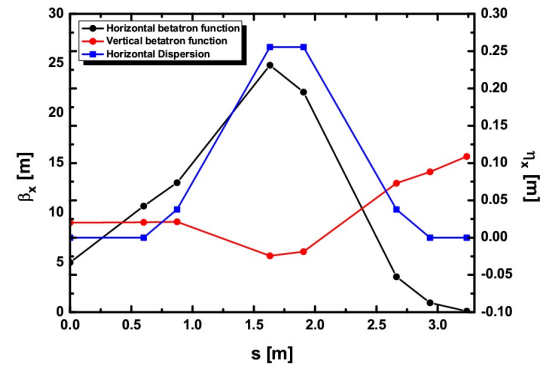


Figure 9: The envelope of the CS parameters and dispersion function in merger section after compensation of the growth of the emittance due to the SC effect.

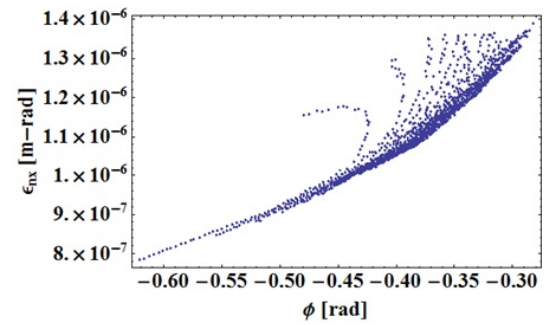


Figure 10: The change of transverse emittance at the exit of merger section as function the orientation of the phase ellipse due to the change of vertical CS parameters.

tron function after passing the merger section. Therefore, the optimum of  $\beta_x$ ,  $\alpha_x$ ,  $\beta_y$  and  $\alpha_y$  were determined to 5.5 m, -1.6, 0.5 and -10 m, respectively.

We also investigate the dependency of the energy spread in the merger section. The SC effect was reduced by the energy spread interact with the dispersion which caused by the dipole magnet. For the study of the dependency of the energy spread, the  $d_z$  was defined by ratio of the energy spread to bunch length. Also the sign of the  $d_z$  was defined by sign of gradient of the slope. The  $d_z$  was changed from the -30 MeV/m to the 50 MeV/m by 20 MeV/m step. In this tracking simulation, the length and charge of the bunch with 10k macro-particles was assumed to 0.9 mm and -80 pC, respectively. The vertical CS parameters also was fixed to  $\beta_y = 0.5$  m and  $\alpha_y = -10$ . The calculation result of the energy spread dependency of the SC effect is shown in Fig. 11

As shown by Fig. 11, the  $d_z$  caused the compression of the bunch length at the exit of merger. For longer bunch length with  $d_z > 0$ , charge density decreases, and SC effect becomes weaker. It causes the decreasing of the growth of the emittance when the beam has  $d_z > 0$ . From the calculation result, the emittance at the exit of the merger was achieved to 0.735 mm-mrad when the bunch has 27.78 MeV/m of energy spread with 0.9 mm of bunch length,  $\beta_x = 5.5$  m,  $\alpha_x = -1.6$ ,  $\beta_y = 0.5$  m and  $\alpha_y = -10$  of CS pa-

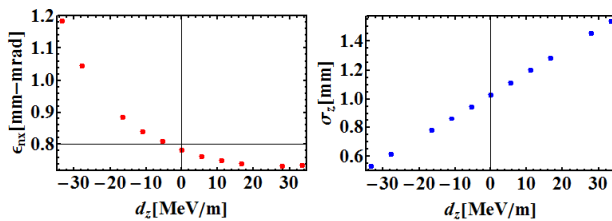


Figure 11: The energy spread dependency of the emittance(left) and bunch length (right) in the merger section.

rameters. The longitudinal phase space beam distribution at the exit of the merger section is shown in Fig. 12.

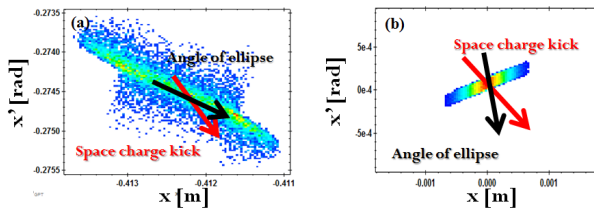


Figure 12: The longitudinal phase space beam distribution at the exit of merger section.(a)The emittance minimized by the CS parameter scan (b)The emittance minimized by changing of energy spread.

This merger system has the large emittance growth due to the SC effect. The increasing of the beam energy at the injector system was needed to achieve the small emittance growth. Because the goal of the emittance of 5 GeV ERL is 0.1 mm-mrad at the arc-section. So, the energy dependency of the transverse emittance growth is shown in Fig. 13.

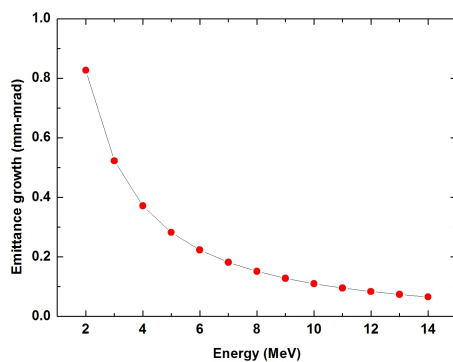


Figure 13: Energy dependency of the horizontal emittance growth in merger section.

From the analytical calculation result, the transverse emittance growth in merger section depends on the energy of beam in injector system. The both method are good to reduce the emittance growth in merger section. But, the increasing of the beam energy is more effective to achieve the smaller emittance. Therefore, the beam energy at the injector system of the 5 GeV ERL is larger than 14 MeV to achieve the 0.1 mm-mrad of transverse emittance after

passing the merger section.

## SUMMARY

The study for the compensation of emittance growth on the low energy around 5 MeV in the merger section was performed to minimize the growth of the emittance in a beam with 77 pC of bunch charge, a bunch length of 3 ps and a bunch energy of 5 MeV. Based on the first-order theory, the emittance growth due to the displacement of bunch slices in phase space was minimized by matching the orientation of the phase ellipse to the kick angle induced by the SC force at the exit of the merger. The dependency of the energy spread at the merger section was investigated. From the calculation results, we minimize the growth of the emittance. From the results, the emittance growth in the merger section was showed to be around 0.635 mm-mrad.

## REFERENCES

- [1] I. V. Bazarov and T. Miyajima, *Proceedings of EPAC'08*, Genoa, Italy, 2008, pp. 118-120.
- [2] M.Rihaoui et. al, *Phys. Rev. ST Accel. Beams* **12** 124201 (2009).
- [3] Miho Shimada et. al, *Proceedings of ERL09, USA, 2009*, WG208.
- [4] T.Miyajima et. al, *Proceedings of the Particle Accelerator Conference, Canada, 2009*, MO6RFP067.
- [5] B.Muratori et. al, *Proceedings of EPAC 2004, Lucerne, Switzerland, 2004*, MOPKF060.
- [6] D.Douglas, Thomas Jefferson, *National Accelerator Laboratory Technical Note*, JLAB-TN-98-012(1998).
- [7] R. Hajima, *Proceedings of the 1st Annual Meeting of Particle Accelerator Society of Japan, Funabashi, Japan*, 432-434 (2004).
- [8] Vladimir N. Litvinenko et. al, *Nuclear Instruments and Methods in Physics Research A* **557** 165-175 (2006).
- [9] Pulsar Physics, <http://www.pulsar.nl/gpt>.
- [10] I. V. Bazarov et. al, *Proceedings of EPAC2008, Genoa, Italy, 2008*, pp. 118-120.
- [11] J. Rosenzweig et. al, *Rev. E*, Vol49, No. 2 (1994).

# FABRICATION OF SUPERCONDUCTING RF CAVITY AT MHI

Haruki Hitomi, Fumiaki Inoue, Hiroshi Hara, Katsuya Sennyu, Kohei Kanaoka, Takeshi Yanagisawa  
 Mitsubishi Heavy Industries, Ltd, Kobe, Hyogo, 652-8585, Japan

## Abstract

We have supplied some 1.3 GHz superconducting RF cavities for STF project and cERL project for few years. Recently, we have manufactured STF phase 2.0 cavities (MHI-#12 to #22). Some of them achieved ILC specification in vertical test at KEK. We have also manufactured three sets of 2-cell cavities for injector linac modules of cERL and two sets of 9-cell cavities for main linac modules of cERL. These cavities were governed to high pressure gas safety law in Japan. We report recent activities of superconducting RF cavity at MHI in this paper.

## INTRODUCTION

MHI has supplied 1.3 GHz superconducting RF cavity for STF project (STF is a project at KEK to build and operate a test linac with high-gradient superconducting cavities, as a prototype of the main linac systems for ILC.) and ERL project (Energy Recovery Linac) for several years. Recently we have fabricated 2-types of cavity for cERL in KEK. One is 2cell cavity for injector linac, the other is 9-cell cavity for main linac as shown Figure 1.

Table 1 indicates the activities of improvement for cavity performance at MHI. We have done optimization of the design and the manufacture method for ERL cavity based on STF cavity.

We take care about cleanliness at cavity assembling, so we use clean area and air top gun. The EBW conditions were always improved. In recent vertical test at KEK, some ERL cavities show good performance [1] [2]. Furthermore STF cavities reached  $E_{acc}= 31.5$  MV/m which is the required gradient of ILC. MHI-#12 cavity

reached also over 40 MV/m [3]. All these cavities are governing the high-pressure gas safety law in Japan.

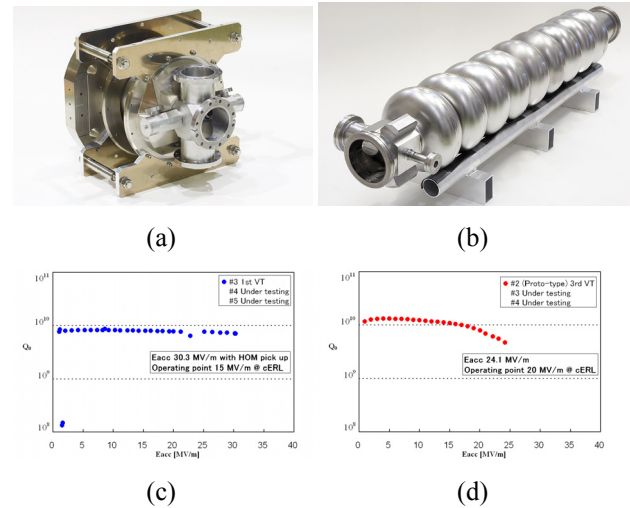


Figure 1: 1.3 GHz SRF Cavity for cERL. (a) Cavity for injector linac, (b) Cavity for main linac, (c) Q-E curve of recent vertical test of (a), (d) Q-E curve of recent vertical test of (b).

## IMPROVEMENT FOR CAVITY FABRICATION METHOD (R&D AT MHI)

Since the STF project was started, MHI has proposed some new fabricating methods for superconducting cavity [4]. Some of them were applied to production or R&D cavities. Some of them are proposal for cost reduction. Improvements in R&D cavities for cost reduction are shown in detail.

Table 1: Activities of Improvement for Cavity Performance

Project	Cavity No.	Thickness [mm]			Shape of groove	Fabrication procedure /Stiffener		Finishing of welding bead		High pressure gas safety law
		Center -cell	End -cell	Equator		Yes	No	Iris/ Equator	Yes	
Injector Linac	#1	2.8	2.8	2.0	Butt	Dumbbell	Yes	No	No	-
	#2	2.8	2.8	2.0	Butt	Dumbbell	Yes	No	No	-
	#3 to 5	3.5	5.0	2.0	Step	Dumbbell	Yes	No	No	Adapted
Main Linac	#1	2.8	2.8	2.5	Butt	Dram	No	Yes	Yes	-
	#2	2.8	3.5	2.0	Butt	Dumbbell	Yes	No	No	-
	#3 to 4	2.8	3.5	2.0	Step	Dumbbell	Yes	Yes	No	Adapted
STF	#12 to 22	2.8	3.5	2.0	Step	Dumbbell	Yes	No	No	Adapted

*Improvement Applied to Production Cavities*

- The items as following are applied to STF cavities.
- To simplify inner conductor of HOM (High Order Mode) coupler design
  - Reduction of machining of HOM cup, beam tube and base-plate by using forming

*Improvement Applied to R&D Cavities*

- The items as follows are applied to R&D cavities.
- Automatic finishing by robot for cell's inner surface (applied to MHI-B cavity)
  - Using LBW instead of EBW for stiffener and flanges (applied to MHI-A cavity)
  - Seamless dumbbell (applied to MHI-B cavity)

*Improvement under Developing*

- The items as follows are under development.
- Change of flange's material NbTi to Ti or Nb alloy
  - Brazing instead of EBW for stiffener and flanges

*Proposal for Improvement*

- The items as follows are our proposal.
- Combination of pick-up port and flanges
  - Combination of base-plate and beam-tube

**FABRICATION OF MHI-A CAVITY (R&D)**

MHI-A cavity was manufactured to establish LBW for stiffener ring and flanges and to establish deep drawing for HOM cup. The vertical test of the cavity was carried out at KEK to inspect the influences to cavity performance by new techniques. The result of the first vertical test is shown in Figure 2. MHI-A cavity achieved  $E_{acc}=29.5$  MV/m without problems at LBW points and HOM coupler. Except for No.8 cell this cavity has capacity of good performance. So we found LBW and HOM cup can be available for production of future cavities.

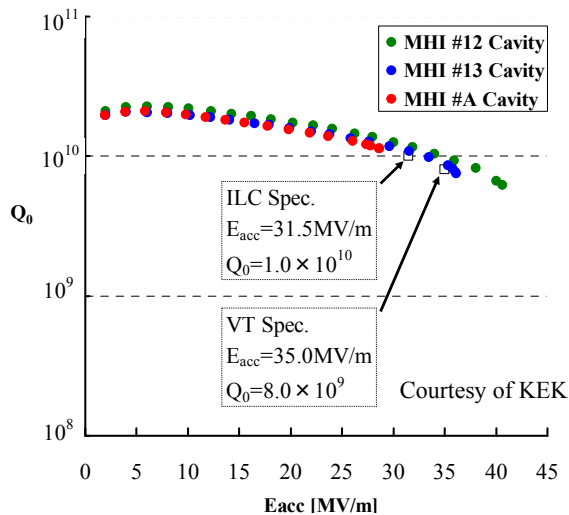


Figure 2: Q-E curve of first vertical test for MHI-A cavity at KEK.

*Feature of MHI-A cavity (shown in Figure 3)*

- Using deep drawing of HOM cup
- No finishing for inner surface of HOM cup
- Using LBW for stiffener and flanges with argon gas atmosphere and oxygen content controlled
- Same design of STF cavity.

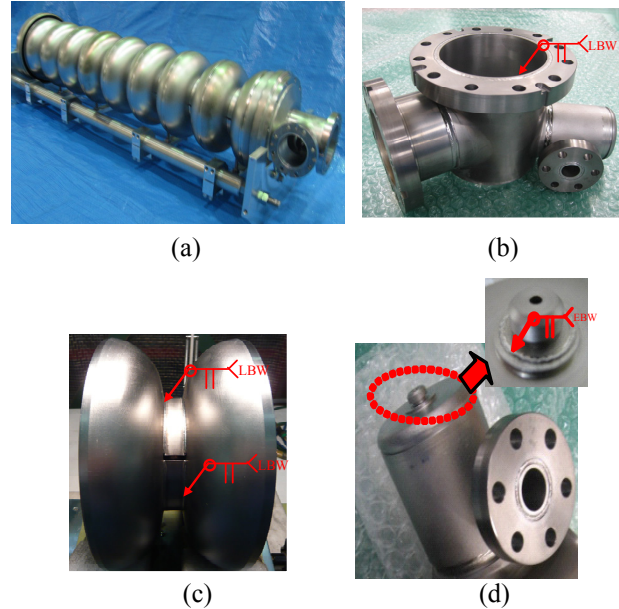


Figure 3: (a) Over view of MHI-A cavity, (b) Beam-tube, (c) Dumbbell, (d) HOM coupler.

**FABRICATION OF MHI-B CAVITY (R&D)**

MHI-B cavity is fabricated to establish a seamless dumbbell technique as shown in Figure 4. The vertical test of the cavity will be carried out to inspect the influences to cavity performance by seamless dumbbell with KEK and Jefferson laboratory. Now MHI-B is prepared for vertical test at J Lab.

*Feature of MHI-B*

- Number of cells is two.
- No welding seam on iris (seamless dumbbell).
- Finishing for inner surface of dumbbell is automatic buffing by robot.
- Cell's design is the same as STF cavity

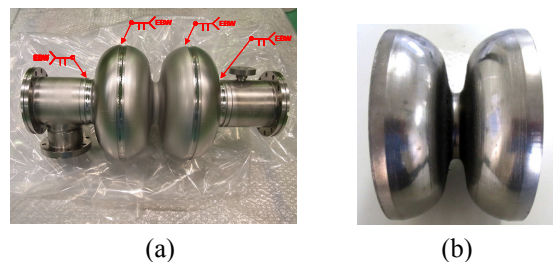


Figure 4: (a) Over view of MHI-B cavity, (b) Seamless dumbbell.

### Seamless Dumbbell

Figure 5 shows the flow of forming for seamless dumbbell. The quality of inner surface of dumbbell depends on the condition of the seamless pipe. The seamless pipe was made by deep drawing.

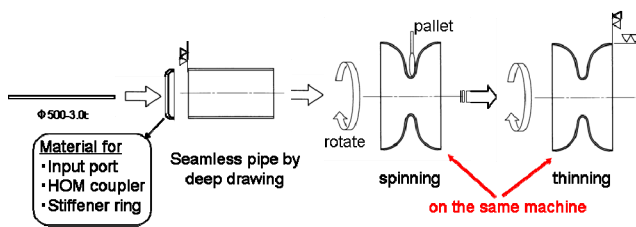


Figure 5: FlowD of seamless dumbbell.

### THINNING FOR CELL BY USING NEW CHUCKING METHOD (NEW PROPOSAL)

We have developed a new cell thinning procedure by using vacuum chucking as shown in Figure 6. Conventionally, a cell was chucked by mould clamping (a cell was fixed at the inside and the outside points with metallic mould). So this method required replacement of the mould every time the thinning part was changed. And it required a long time to set up the mould due to many bolts being used. Furthermore, much attention was necessary in order not to damage the inner surface of the cell with the metallic mould.

On the other hand, if attachment by vacuum is utilized, it facilitates setting up the chucking jig. Also, as the jig is made of resin, it seldom damages the inner surface.

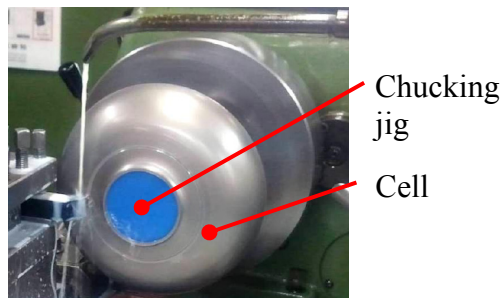


Figure 6: Image of new thinning process of cell.

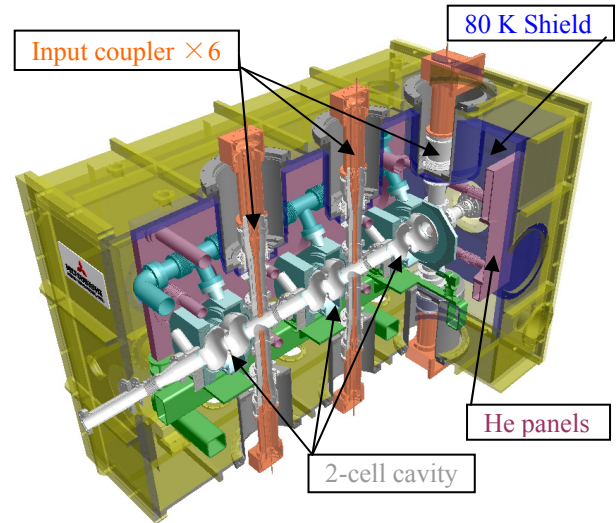
### RECENTLY STATUS OF COMPACT ERL PROJECT FOR KEK AT MHI

Now we are fabricating 2 types of cryomodule for cERL project at KEK. One is the Injector Module as shown Figure 7-(a). This module has square shape because input couplers are set from upper and lower side (double coupler system), and it has helium panels for 5 K thermal shield. This module has 3 sets of 2 cell cavities with LHe jacket and frequency tuner [5].

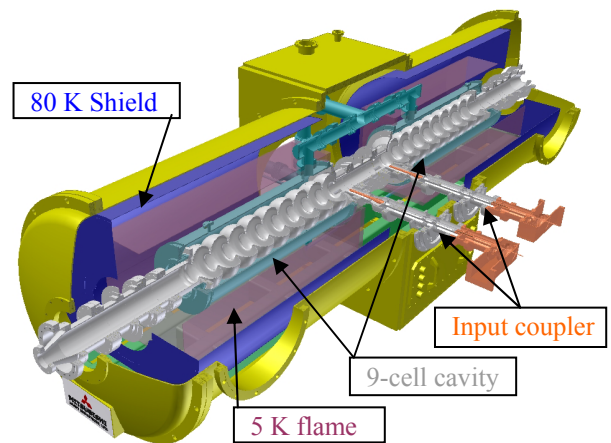
The other is the Main module which has 2 sets of 9 cell cavities with LHe jacket as shown in Figure 7-(b). Main components of this module are almost same as

Injector module. The feature of this module is that some parts are supported in center of module [6].

Some of components need to be resisting pressure, so it is required to be granted permission on high pressure gas safety law in Japan for module operation.



(a)



(b)

Figure 7: Over view of cERL modules, (a) Injector module, (b) Main module.

### CONCLUSION

- We have supplied some SRF cavities for STF and ERL projects at KEK for the last few years. The cavity performance is improving step by step.
- We have proposed some ideas for improving productivity and these methods was established step by step.
- According to MHI-A cavity, we were sure that using LBW joints instead of EBW joints for the parts of little influence to cavity performance was available.
- MHI-B cavity with seamless dumbbell is fabricated. This cavity is going to be tested at JLab after this conference.

- Now we are designing and fabricating 2 types of cryomodule for cERL at KEK. (Governed by the high pressure gas safety law in Japan)

### ACKNOWLEDGMENT

E. Kako, H. Sakai, K. Umemori, K. Watanabe, M. Satoh, S. Noguchi, T. Furuya, T. Shishido, Y. Yamamoto at KEK, M. Sawamura at JAEA, K. Shinoue at ISSP for cERL and STF activities for this paper.

### REFERENCES

- [1] K. Watanabe, et al. "Progress of cERL injector cavities at KEK", in this workshop, WG3005.
- [2] K. Umemori, et al. "Development of main linac cavity for cERL project", in this workshop, WG3.
- [3] Y. Yamamoto, et al. "Test Results of the International S1-Global Cryomodule", 15<sup>th</sup> SRF2011, Chicago, USA, (2011), THIOA01.
- [4] K. Sennyu, et al., "Improvement in Cavity Fabrication Technology", 15th SRF2011, Chicago, USA, (2011), WEIOB03.
- [5] S. Noguchi, et al., "Injector Cryomodule for cERL at KEK", in this workshop, WG3.
- [6] T. Furuya, et al., "Cryomodule of KEK-ML cavity", in this workshop, WG3.

## HOM PROPERTIES OF MAIN LINAC FOR cERL IN JAPAN

M. Sawamura<sup>#</sup>, JAEA, Tokai, Ibaraki 319-1195, Japan

T. Furuya, H. Sakai, K. Umemori, KEK, Tsukuba, Ibaraki 305-0801, Japan

K. Shinoe, ISSP, University of Tokyo, Kashiwa, Chiba 277-8581, Japan

E. Cenni, The Graduate University for Advanced Studies, Tsukuba, Ibaraki 305-0801, Japan

### Abstract

Two types of the HOM absorber models were designed and fabricated according to results of ferrites and ceramic properties measurement at low temperature. One without HIP ferrite was used to measure thermal property and the other with HIP ferrite to confirm HOM absorption property and thermal tolerance against cooling cycle. Measurement of thermal resistance in inadequate position of comb-type RF bridge suggested that the comb teeth should be modified to reduce the thermal transmission. The HIP ferrite attached to our 9-cell ERL model cavity sufficiently damped HOMs. Several cracks were observed during cooling cycle test. HOM spectrum of two cavities for cERL were measured at the vertical test and frequencies and Q-values were compared.

### INTRODUCTION

HOM damping is important for superconducting cavities, especially for high current CW machines such as ERLs. The lower Q-values of HOMs lead to the smaller capacity of a refrigeration system and the higher threshold current against the beam breakup (BBU). Enlarged beam pipes, which have lower cutoff frequencies, are effective to damp monopole and dipole HOMs [1] and the eccentric-fluted beam pipe is effective to damp quadrupole HOMs [2]. Propagating HOMs through the beam pipe are absorbed and damped by the HOM absorbers. Since the HOM absorbers are connected to the superconducting cavities in a cryomodule as shown in Fig. 1, the operating temperature of the HOM absorbers is near liquid nitrogen temperature. The HOM absorbers are required to have high thermal resistance between liquid nitrogen temperature and liquid helium temperature parts to reduce the heat load into the superconducting cavity. The HOM absorption materials are required to have good HOM absorption property as well as good tolerance against cooling cycle.

The HOM absorber models were designed and fabricated to confirm the thermal property and tolerance at liquid nitrogen temperature.

The present paper describes the measured results of thermal property and tolerance at low temperature and HOM absorption property at room temperature.

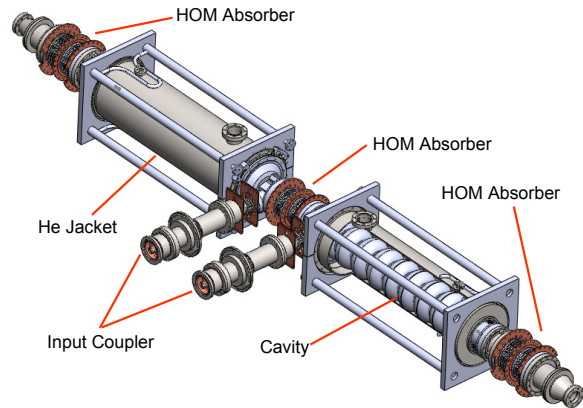


Figure 1: Layout of HOM absorbers in the cryomodule.

### HOM ABSORBER MODELS

The HOM absorber can be divided into three parts. The center part consists of the RF absorber and the 80K-anchor connected to the liquid-nitrogen-temperature line. Both end parts consist of the flange connected to the superconducting cavity and the 5K-anchor. The center part and the end part are connected with a bellows.

HIPPed (Hot Isostatic Press) ferrite is attached on the inner surface of the copper base. Since HIP can bond between the ferrite and the copper base firmly, HIP process is adopted to prevent from the ferrite falling off from the copper base. The comb-type RF bridge is adopted at the beam pipe connection between the center and the end parts [3]. The comb-type RF bridge has the advantages of low impedance and small heat conductance compared with the finger-type RF connector. The bellows is used to increase allowance of the flange connection and the heat shrink. The bellows is also used to reduce the heat transmission to the superconducting cavity when the ferrite temperature rises due to HOM power absorption.

Two types of the HOM absorber models were designed and fabricated. One was almost same structure of the HOM absorber except the HIP ferrite (Fig. 2 upper) and the other was a center part with HIP ferrite before machining for teeth of the comb-type RF bridge and the 80K-anchor (Fig. 2 lower). The former was used to measure the thermal property at 80K and the latter to measure the HOM absorption property and the cooling cycle tolerance.

<sup>#</sup>sawamura.masaru@jaea.go.jp

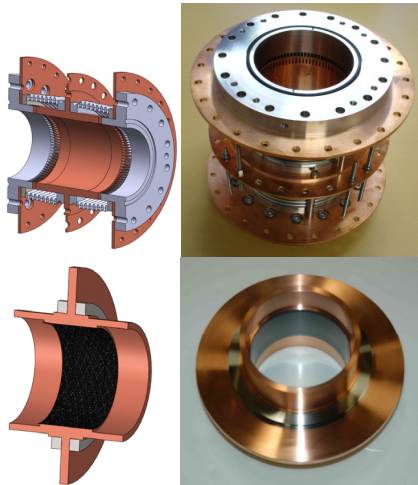


Figure 2: Schematic views and photographs of HOM absorber models without HIP ferrite (upper) and center part with HIP ferrite (lower).

### THERMAL PROPERTY

The HOM absorber model without HIP ferrite was cooled to the liquid nitrogen temperature in an adiabatic vacuum chamber. The results were presented elsewhere [4]. The thermal resistance was also measured in inadequate position where the opposite comb teeth contacted longitudinally or at a tilt. Figure 3 shows the results of thermal resistances. Though radiation can not be ignored near room temperature and small temperature changes make hard to measure accurately at low temperature, the results near middle temperature can be considered to be precise. The thermal resistances of longitudinal and tilted contact were about 1/6 and 1/2 times lower than that in the adequate position. The reason of these bad thermal resistances was considered to be caused by simple cutting of comb teeth. The comb teeth were square cut at the top and radially cut at the side. In these cases contact section is apt to increase when opposite comb teeth contact as shown in Fig. 4 left. To decrease the thermal transmission by contact with comb teeth, the shape of comb teeth should be modified to tilted cut at the top and parallel cut at the sides as shown in Fig. 4 right.

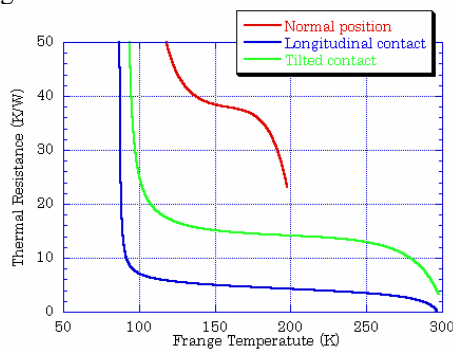


Figure 3: Thermal resistances in the normal position, with longitudinal and tilted contact.

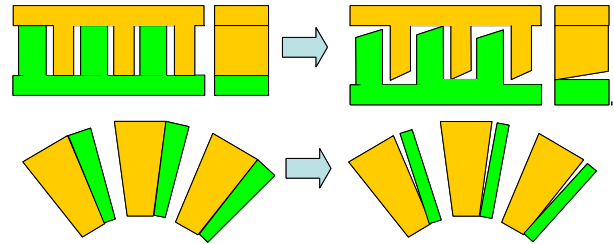


Figure 4: Schematic views of comb teeth shape cut before (left) and after (right) modification.

### COOLING CYCLE TEST

The coefficients of thermal expansion are different between ferrite and copper. When the HOM absorber is cooled down to liquid nitrogen temperature, the different coefficients of thermal expansion may cause the stress and damage to the HIP ferrite. Cooling cycle test was performed to check tolerance of the HIP ferrite. The HOM absorber model with HIP ferrite was cooled and heated by a GM refrigerator between room temperature and 80K while controlling the speed of temperature change. Figure 5 shows a schematic view of the cooling cycle test setup. Two HOM absorber models with HIP ferrite were used for the cooling cycle test. It took 2.5 days each for the models to cool and heat between room temperature and 80K to make the temperature difference between the copper base and the ferrite as low as possible.

The surface of the HIP ferrite was observed with a close-up CCD camera. The HIP ferrites initially had some linear cracks. After the first cooling cycle test, several linear cracks were observed mainly near the ferrite edge where the ferrite was tapered as shown in Fig. 6. Though one of two models with HIP ferrite chipped off a small piece of ferrite after the 2<sup>nd</sup> cooling cycle as shown in Fig. 7, the other was not observed to chip off during the five times of cooling cycle. Further inspections with ultrasonic echo will be carried out to investigate the other cracks inside the ferrite.

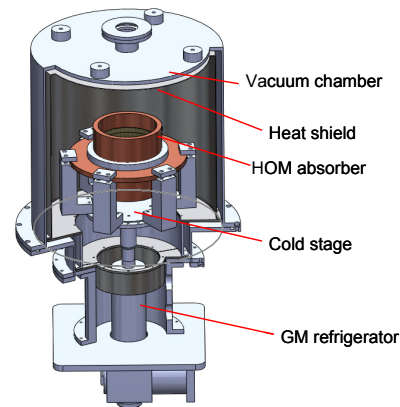


Figure 5: Schematic view of cooling cycle setup for HOM absorber model with HIP ferrite.



Figure 6: Linear cracks observed near the tapered ferrite edge.

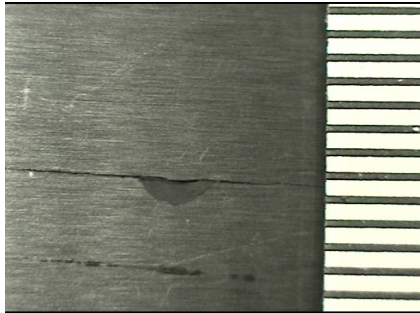


Figure 7: Trail of chipped-off piece (left) and 1mm-scale (right).

### HOM ABSORPTION PROPERTY

The HOM absorber model with HIP ferrite was attached to our 9-cell ERL model cavity to confirm HOM absorption property as shown in Fig. 8. The resonant peaks were searched with a network analyzer and Q-values were measured under two conditions with and without the HOM absorber model with HIP ferrite.

The resonant peaks and their Q-values are shown in Fig. 9. It indicates that the HOM absorber model with HIP ferrite sufficiently decreases the Q-values of both monopole and dipole modes. Some Q-values were too low to be measured with the network analyzer as plotted with blue dot only and no red dot in Fig. 9 lower.

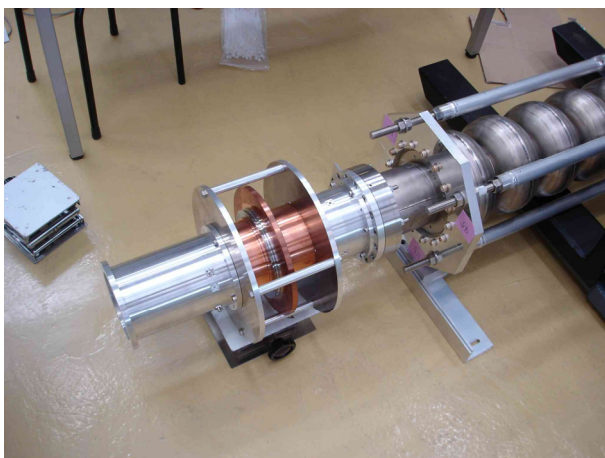


Figure 8: Setup of HOM absorption measurement with our 9-cell ERL model cavity.

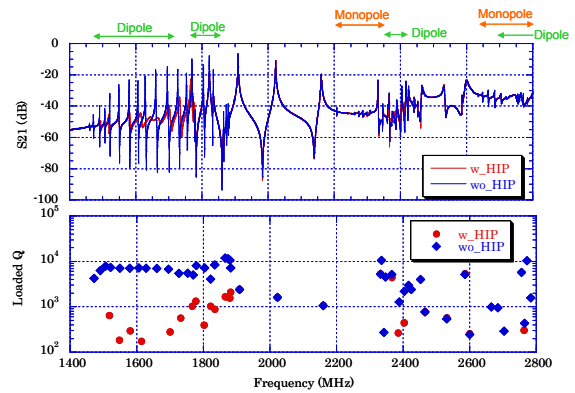


Figure 9: HOM peaks and Q-values with and without HIP ferrite.

### HOM SPECTRUM AT VERTICAL TEST

Two 9-cell cavities for compact ERL were fabricated and vertical tests were done. During the vertical test, HOM properties were also measured. The stainless steel flanges were used for beam pipes in vertical test. Since HOMs transported through the beam pipe could be dissipated at these SUS flanges, the Q-values became low so that the HOM Q-values could be measured with a network analyzer. Figure 10 shows the HOM spectrum at room temperature and 4K. HOM resonances at room temperature are broad and those at 4K become sharp and degenerate modes can be separated. Resonance frequencies are also different from room temperature and 4K. Figure 11 shows the loaded Q-values at 4K and 2K. Though the BCS resistance at 2K and 4K are different about 40 times, the Q-values at 4K and 2K are almost same. This means main power loss was at SUS flanges.

The two cavities were measured and resonance frequencies and Q-values were compared. The frequency differences are shown in Fig. 12 (upper) and frequency dispersion was  $\pm 0.73\text{MHz}$ . The Q-value differences are shown in Fig. 12 (lower) and Q-values of most modes have almost same Q-value within 3.8 times. But several modes are different more than one order.

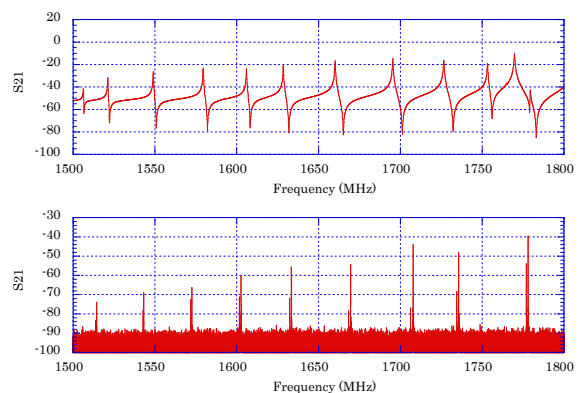


Figure 10: HOM spectrum at room temperature (upper) and 4K (lower).

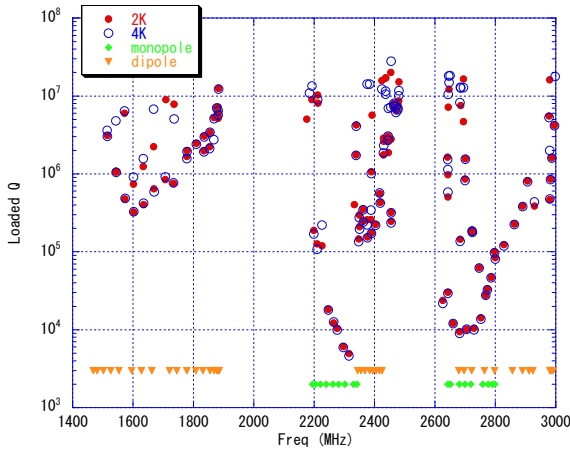


Figure 11: Loaded Q-values measured during vertical test at 4K and 2K.

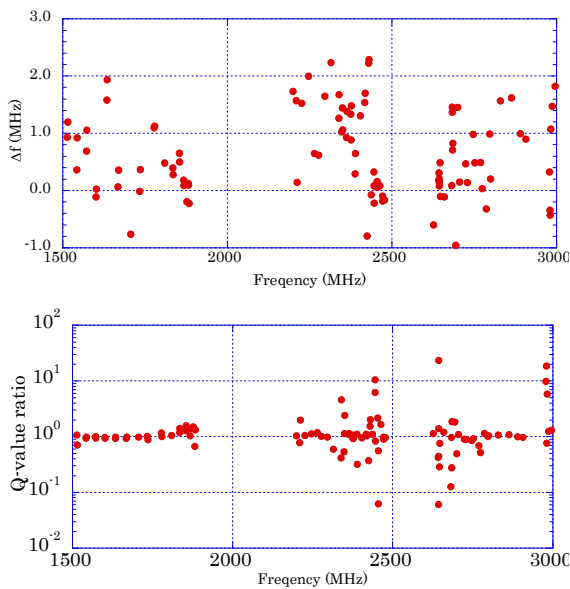


Figure 12: Frequency differences (upper) and Q-values difference (lower) with two cERL cavities.

### CONCLUSION

Two types of the HOM absorber models were fabricated and cold tests were performed. With the results of thermal resistance of the comb-type RF bridge, the shape of comb teeth is going to be modified to reduce the heat transmission. The other HOM absorber model with HIP ferrite was attached to our 9-cell ERL model cavity and both monopole and dipole HOMs were sufficiently damped. During cooling cycle test, linear cracks and small trails of chipped-off ferrite were observed. More detail inspection of ferrite surface as well as inside will be carried out.

### REFERENCES

- [1] K. Umemori et al., “Design of L-Band Superconducting Cavity for Energy Recovery Linacs”, Proc. of APAC2007, 570-572 (2007).
- [2] M. Sawamura et al., “Eccentric-fluted beam pipes to damp quadrupole higher-order modes”, Phys. Rev. ST Accel. Beams 13, 022003 (2010).
- [3] Y. Suetsugu, et al., Proceedings of the 5th Annual Meeting of Particle Accelerator Society of Japan and the 33rd Linear Accelerator Meeting in Japan, August 6-8, 2008, pp. 200-202 (in Japanese).
- [4] M. Sawamura et al., “Cooling Test of ERL HOM Absorber”, Proc. of IPAC2010, 2344-2346 (2010).

# DEVELOPMENT OF INPUT COUPLER FOR COMPACT ERL MAIN LINAC

Hiroshi Sakai<sup>#</sup>, Takaaki Furuya, Masato Sato, Kenji Shinoe, Kensei Umemori,  
KEK, Tsukuba, Ibaraki, 305-0801, Japan

Masaru Sawamura, JAEA, Tokai, Naka, Ibaraki, 319-1195, Japan

Enrico Cenni, The Graduate University for Advanced Studies, Tsukuba, Ibaraki, 305-0801, Japan

## Abstract

We fabricated the prototype of an input coupler, which has two ceramic windows to keep the inside of the superconducting cavity clean, for ERL main linac and performed the high power test. Required input power is about 20kW with standing wave condition for the cavity acceleration field of 20MV/m. In this high power test, the one ceramic window, named as a cold window, was installed into the vacuum insulating chamber and cooled by liquid Nitrogen. First, the multipacting at 10kW level prevented the power increasing. By using the pulse processing method for 8 hours, power finally reached the 25kW with standing wave condition. We could also keep feeding 20kW power into coupler for 16 hours. From these results of high power test, this prototype coupler satisfied our thermal and RF requirements. In this paper, we present the recent results about the prototype of input coupler.

## INTRODUCTION

An input coupler is one of the important items of the superconducting cavity for ERL operation [1]. Table 1 shows the parameters of the input coupler for main linac. Though the mechanism of energy recovery enables to reduce the input power of the main linac, the minimum input power will be restricted by the cavity detuning due to the microphonics from a cryomodule. Therefore, 20kW is needed for our main linac operation.

Table 1: Parameters of Input Coupler for Main Linac

Frequency	1.3GHz
Accelerating voltage	Max 20MV/m
Input power	Max CW 20kW (Standing wave)
Loaded Q ( $Q_L$ )	$1 \times 10^7 \sim 4 \times 10^7$ (variable)

Figure 1 shows the design of the input coupler for our main linac. Two coaxial disk ceramic windows are set; One, which is called as “cold window”, is set on the cold parts at 80K and the other, which is called as “warm window”, is on warm parts at 300K for safety against vacuum leak due to window break. Purity of ceramic material is 99.7% to reduce the power loss of ceramic. The impedance of coupler is 60Ω to reduce the power dissipation of inner conductor. Furthermore forced air cooling was applied to inner conductor. Detailed design strategy and parameters are expressed in Ref.[2].

<sup>#</sup> sakai.hiroshi@kek.jp

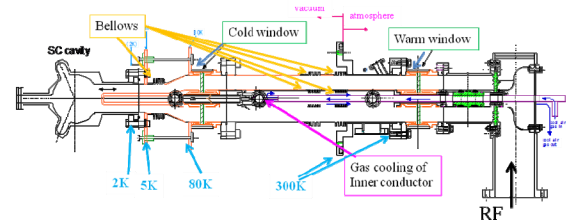


Figure 1: Schematic design of input coupler for main linac.

Previously, we fabricated input coupler components, warm ceramic windows with bellows and cold windows, and carried out the high-power test of the components by using a CW 30kW IOT power source. In these component tests, we found the resonance of the dipole mode in ceramic window made the sudden temperature rise and the break of ceramic window [3][4]. We fabricated the new ceramic window by changing the thickness of ceramic window to escape the resonance mode. We finally achieved 27kW in the high power test by using new ceramic window [5]. The high power test of the components of input coupler was successfully carried out. Therefore, we fabricated a prototype of input coupler of ERL main linac (TOSHIBA TETD). In this proceeding, we summarized the following results of prototype input coupler. First the high power test of input coupler was carried out under Liq. N<sub>2</sub> cooling. We also carried out the thermal-cycle tests of cold ceramic window by using this input coupler again. The low level test was also carried out by using ERL 9-cell cavity.

## HIGH POWER TEST OF THE PROTOTYPE OF AN INPUT COUPLER UNDER LIQUID NITROGEN COOLING

According to the components test with the high power test and the thermal cycle test, we slightly changed the parameters of ceramic window. We fabricated the first prototype of input coupler as shown in the left figure of Fig. 2. Fig. 3 shows the setup of high power test of input coupler with standing wave. RF power was fed into the input coupler from 30kW IOT via a doorknob exchangers and reflected by the end plate. The standing wave was excited, however, not to stand the peak field at the bellows and ceramic windows in high power test as shown in the right figure of Fig. 2. Especially we'd like to know the real temperature rises under vacuum insulation as same as the cryomodule by feeding the high power, the

input coupler was inserted into the vacuum insulator and the cold window was cooled by the liquid nitrogen tank via the 4 copper braid lines whose length was 200mm and total cross section was 400mm<sup>2</sup>. The cold window was surrounded by the Al cold box connected with liquid nitrogen tank to reduce thermal radiation between the cold window and the outside set on the room temperature. Other coupler components set into the vacuum insulator were also surrounded by super insulators with the enough thickness. Many temperature sensors were set to mainly monitor the temperatures of bellows and warm/cold window as shown in Fig. 3.

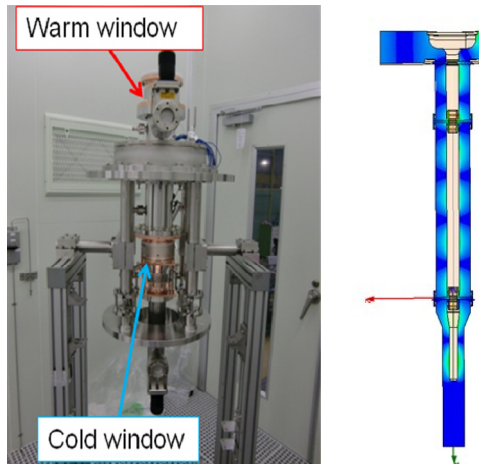


Figure 2: (Left) Picture of the prototype of the input coupler for ERL main linac. (Right) Simulation of magnetic field distribution of input coupler at test stand.

Forward RF power ( $P_{in\_for}$ ) and reflected RF power ( $P_{in\_ref}$ ) were also measured at the upstream of the doorknob exchanger. The inner conductor and bellows were cooled via rod by N<sub>2</sub> gas from the cold evaporator and the amount of gas flow was monitored. The flow of N<sub>2</sub> gas was usually kept 115 l/min in this test. Two arcs sensors were set; one was on the end plate to see the cold window (arc1), the other was on the outer conductor near the warm window (arc2). The volume between the cold window and the end plate (light blue area in the lower figure of Fig. 3) and the volume between two ceramic window (green area in the lower figure of Fig. 3) were separately pumped by each ion pump and the vacuum pressures were measured by each CCG (named as CCG1 on light blue area and CCG2 on green area), respectively. After baking over 150 °C for 24 hours, the vacuum pressures of 1.5x10<sup>-6</sup> Pa of CCG1 and 7x10<sup>-7</sup> Pa of CCG2 were achieved before high power test, respectively. Three electron probes (e-probe 1-3) were also set near the ceramic windows to detect the secondary electrons under processing as shown in the lower figure of Fig.3.

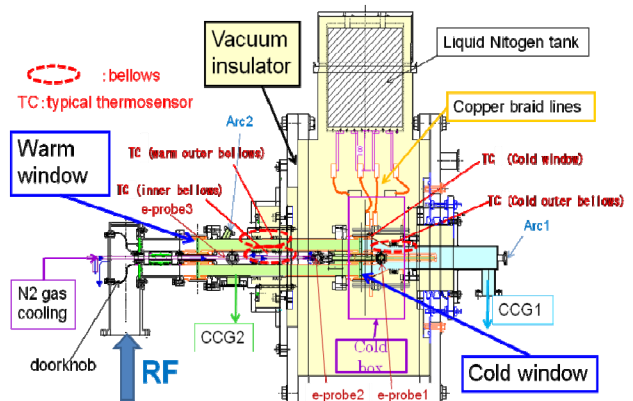
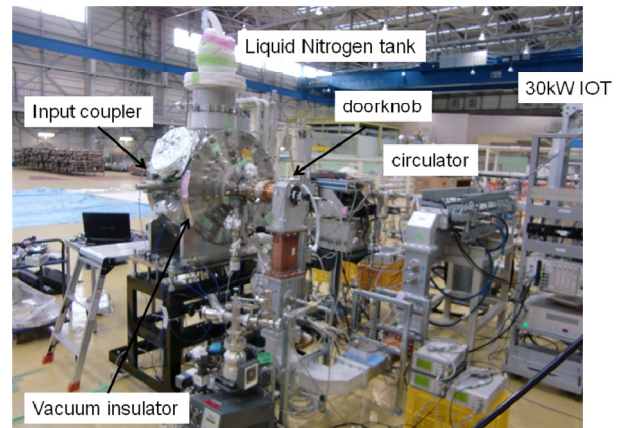


Figure 3: (upper) Picture of the setup of high power test of the input coupler under liquid nitrogen cooling. (lower) The detail of the setup of the high power test including the inside of the vacuum insulator.

We applied the RF power to this input coupler. First we could smoothly increase the RF power until 20kW. At 20kW, suddenly arc (arc2) and vacuum (CCG2) interlocks worked. Unfortunately, feeding power was down to 10kW and could not overcome 10kW level under CW power feeding. Fig. 4 shows the signal detected by electron probe set near the warm window (e-probe3). Whenever the arc interlock (arc1) worked, the vacuum of warm window increased and the e-probe signal was detected. Since the processing for one hour with same method, failed to increase the feeding power, could not be increased, we tried the pulse processing with 30μs pulse width.

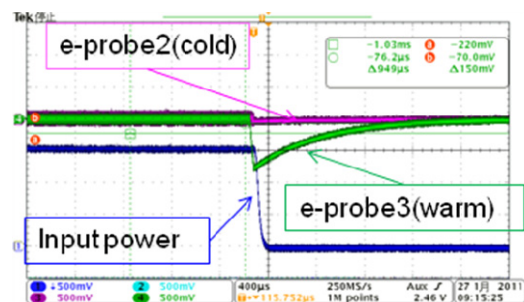


Figure 4: Signals come from electron probe (e-pick3) when the arc interlock was occurred.

Figure 5 shows the processing history up to 25kW. After searching the optimum processing condition of the pulse processing, feeding power gradually increased under keeping the lower vacuum pressure than  $1 \times 10^{-4}$  Pa for 8 hours. The vacuum of warm window (CCG2) and electron probe of warm window (e-probe3) indicated that the processing activated the area between two ceramics and finally we reached the 25kW power level. After changing to the CW power feeding at 25kW as shown in Fig. 5, the vacuum pressure of cold window (CCG1) slightly increased. The both vacuum pressures, however, gradually decreased under keeping the 25kW level. This shows the processing was in progress and finally we could not detect the secondary electron by electron probes. The processing was smoothly carried out by using the pulse processing.

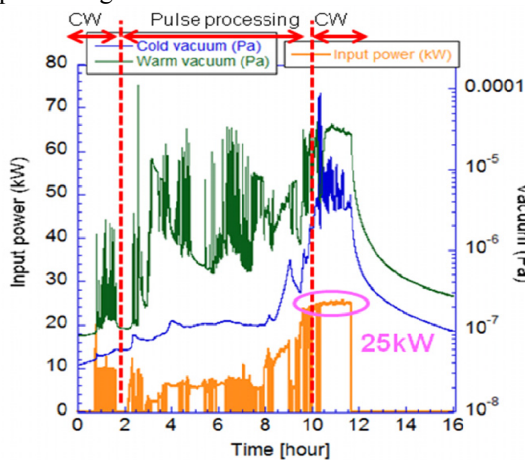


Figure 5: History of the power processing up to 25kW. The left vertical axis shows the input power ( $P_{in}$ ) (orange). The right vertical axis shows the vacuum pressure (CCG1:blue & CCG2:green). Red array shows the region of different condition of processing.

Next we kept the power at 20kW level in order to measure the temperature rise under the liquid nitrogen cooling with the vacuum insulator. Fig. 6 shows the history of the power, vacuum pressure (upper) and the temperatures (lower) whose measured positions were drawn in the lower figure of Fig. 6, by keeping 20kW standing wave to the input coupler. The power of 20kW was kept for 16 hours to become the equilibrium condition of the measured temperature. During the stable power feeding, arc interlocks worked three times. These interlocks came not from the electron activity inside the input coupler but from the unknown electrical noise of arc sensors. Furthermore, vacuum pressure increased once unless the interlock worked. This was because the lack of the liquid nitrogen in the tank. Therefore, we fed the liquid  $N_2$  to the tank soon and keep the temperature stable again. In the upper figure of Fig. 6, first the vacuum pressures increased up to  $4 \times 10^{-6}$  Pa of CCG1 and  $1 \times 10^{-6}$  Pa of CCG2. After 8 hours from 20 kW power feeding, the vacuum pressures were decreased as the temperature

reached the equilibrium condition. We stopped power feeding after 16 hours later when the temperature was stable. The maximum temperature of  $127^\circ C$  was measured at the inner conductor bellows. This temperature rise of inner conductor bellows was not so high that the vacuum would not be wrong and reasonable value compared with other experiment like Ref.[6]. We were anxious about the temperature rise ( $\Delta T$ ) of outer conductor bellows near warm window, which is shown by the black line in the lower figure of Fig. 9, to increase much higher. However, we noted that the temperature rise of 70K was not so high in spite of setting this bellows inside the vacuum insulator, compared with other experiment in Ref[7]. This is, I think, because  $150\mu m$  thick plating of the half of the warm bellows was applied and the much heat load in the bellows would transfer outside. This copper plating worked effectively.

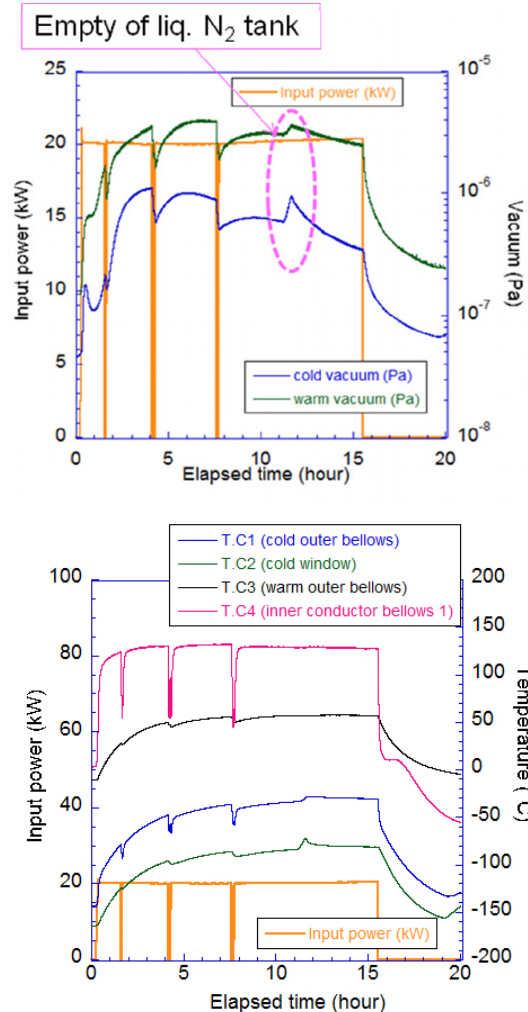


Figure 6: The history under keeping 20kW input power. (upper) The input power (orange) vs vacuum pressure (CCG1:blue & CCG2:green). (lower) The input power (orange) vs temperature rise. Blue (green, black, pink) shows the temperature at cold outer bellows (cold window, warm outer bellows, inner conductor bellows).

The temperature rise of cold window and outer bellows near cold window were 100K, which was also reasonable value. Roughly calculated heat load of the cold window from the temperature measurements of braid lines was twice bigger than expected. One reason was the poor vacuum pressure of the vacuum insulator of  $3 \times 10^0$  Pa. The cold window might be not perfectly isolated thermally from the outside.

In order to check the memory effect by processing, we warmed up the input coupler to the room temperature and exposed the inside of the input coupler to the air for 4 hours. After cooling the coupler again by liquid nitrogen with vacuum insulator, we noted that we could smoothly increase up to 24kW power level again. We did not detect the arc interlock or secondary electron by electron probes, under feeding power up to 24kW again.

### THERMAL CYCLE TESTS OF COLD CERAMIC WINDOW OF PROTOTYPE INPUT COUPLER

Previously, we carried out the thermal cycle test between 80K and room temperature by using the old cold window prior to the fabrication of the prototype of the input coupler of main linac. The cold window was gradually cooled by filling up a cooler box with evaporating  $N_2$  gas for several hours and finally reached to 80K. After keeping 80K for a few hours, the cold window was warmed up for half and/or a day and we carried out the leak check. After the fifth thermal cycle test, the leak ratio of ceramic window drastically increased from  $1 \times 10^{-10}$  Pa  $m^3/s$  to  $1 \times 10^{-4}$  Pa  $m^3/s$ . We thought that the ceramic window was broken under thermal cycle tests. After the color-check of the ceramic window to identify the leak point, we found the leak point at inner conductor as shown in Fig.7. To see the leak point precisely, we cut the ceramic window and inspected the cross section in detail. There appeared the red color line of the cross section of the ceramic window as shown in Fig.7. This broken line like the arch was typically explained by the thermal stress test under brazing between the different materials with different thermal conductivities like ceramic and metal in Ref.[8]. The thermal-stress analysis by ANSYS also explained that the edge of the ceramic window near the inner conductor have the biggest thermal stress. We continued the simulation of ANSYS to reduce the thermal stress by changing the parameters of inner copper support thickness and inner support of molybdenum thickness and length. Decreasing the thickness of copper and increasing the thickness of molybdenum mainly enabled to reduce the thermal-stress down to 78% from the original value. According to these results, we changed the brazing condition to newly calculated parameters and applied these conditions for fabrication of prototype of input coupler.

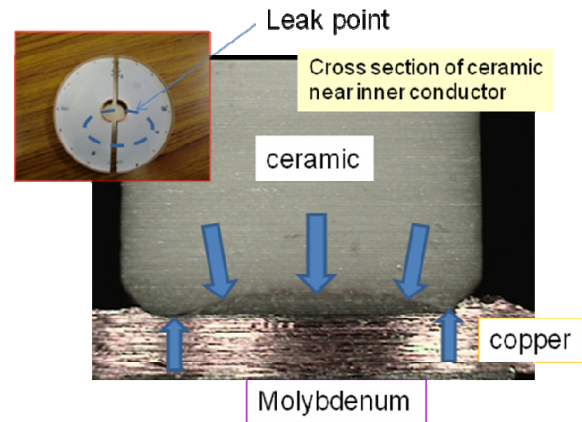


Figure 7: The pictures of ceramic window (left) and the cross section of ceramic window (center). The red arch line with blue arrows shows the broken line of the ceramic.

After high power test of prototype input coupler, we continue the liquid nitrogen cooling of the cold window by using same setup in order to carry out the thermal cycle test; we emphasized that the blazing condition of this cold window of input coupler was modified from old one. Fig. 8 shows the temperature change of cold window from the 3<sup>rd</sup> to the 10<sup>th</sup> thermal cycle test. The cold window was gradually cooled down for several hours and warmed up for more than half day not to add the sudden thermal shock to the ceramic. After the 10<sup>th</sup> thermal cycle test, we could not detect the leakage over  $1 \times 10^{-10}$  Pa  $m^3/s$  by a He leak detector. By changing the blazing condition of cold window, we found that the cold window could stand 10-times thermal cycle from liquid  $N_2$  to the room temperature. Furthermore, we found that no leaks or damages of ceramic windows and bellows were observed after this high power test.

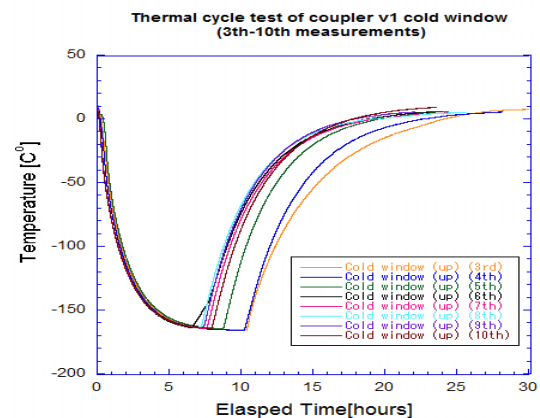


Figure 8: The temperature data from 3<sup>rd</sup> to 10<sup>th</sup> thermal cycle test. 1<sup>st</sup> and 2<sup>nd</sup> thermal cycle test were done under the high power test.

## MEASUREMENT OF COUPLING OF PROTOTYPE INPUT COUPLER

By using prototype input coupler and ERL 9cell cavity, we measured the  $Q_{ext}$  of input coupler directly as shown in Fig.9.  $Q_{ext}$  was measured by changing the distance from the cavity center. We note that we measured the coupling with doorknob exchanger.

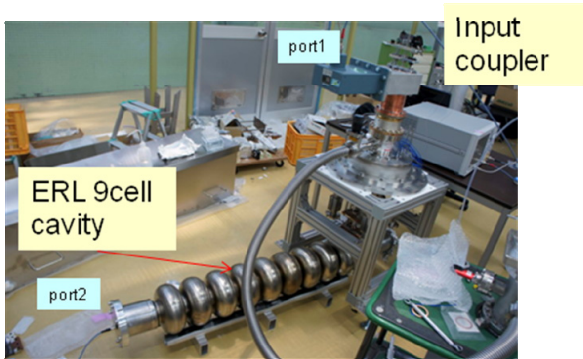


Figure 9: Measurement setup of  $Q_{ext}$  of input coupler with doorknob exchanger.

Figure 10 shows the measurement results of  $Q_{ext}$  change by changing the distance from the cavity center comparing with the calculation values of HFSS and MW-Studio[9]. Slope of  $Q_{ext}$  change with coupler length agree well with calculation. However the measured value of  $Q_{ext}$  with doorknob exchanger is 1.3 times lower than calculation. Prior to the fabrication of two input couplers for cERL cryomodule, we will change the length of 2mm shorter by using the measurement results.

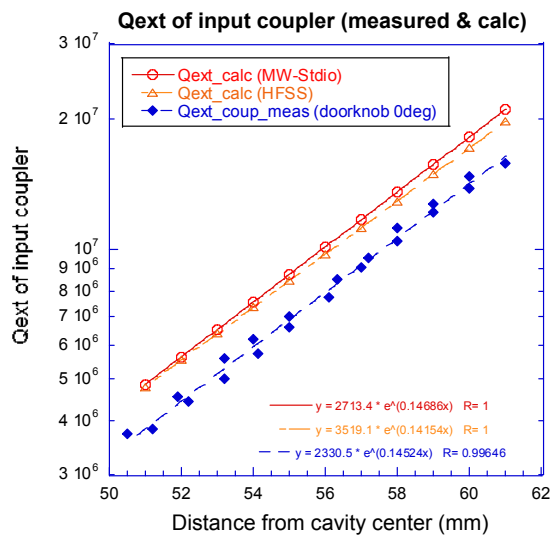


Figure 10:  $Q_{ext}$  change by changing the distance from the cavity center. Red and orange plots shows the calculation by MW-Studio (red) and HFSS (orange). Blue solid circles show the coupling measurement results by using prototype coupler with doorknob exchanger.

## SUMMARY

Prior to the fabrication of the prototype of the input coupler, we carried out the thermal cycle test of the old cold window between liquid nitrogen and room temperature. After the 5<sup>th</sup> thermal cycle test, the ceramic window near the inner conductor was cracked. This phenomenon was almost agreed well with the calculation by simulation and we applied the new brazing parameters, which reduced the thermal stress based on simulation, to the new prototype of input coupler. Next, we carried out the high power test of this input coupler under liquid nitrogen cooling with the vacuum insulator. After pulse processing for 8 hours, we finally achieved 25kW with standing wave in the high power test. By keeping 20kW input power for 16 hours, we also measured the temperature rise. The maximum temperature rise was measured at the bellows of the inner conductor. However, the temperature rise was suppressed down to 120K by N<sub>2</sub> gas cooling of 115 l/min flow. The vacuum pressure was also suppressed at  $\sim 10^{-6}$  Pa under 20kW power feeding. We noted that we could smoothly increase up to 24kW power level again after warming up to room temperature and exposing the inside of the input coupler to the air for 4 hours. In addition, after the high power test, we continued the liquid nitrogen cooling of the cold window by using the same setup in order to carry out the thermal cycle test. By changing the brazing condition of the cold window, we could increase the thermal cycles up to 10 times and no crack or leak was observed after these tests. The coupling measurement was also done by using ERL-9cell cavity directly. These values also agreed well with the expected values.

The thermal and RF power tests were successfully done with the prototype of input coupler and the basic design of the input coupler has satisfied our requirements by these tests. In this year, we will fabricate the two input couplers for the main linac to prepare the compact ERL construction.

## ACKNOWLEDGEMENT

We thank the KEK RF Group, especially T. Miura, for preparing the RF source and the KEK Cryogenic group, especially Y. Kojima for preparing the liquid nitrogen evaporator. We also thank K. Onoe from University of Tokyo for helping the measurement of the thermal cycle test of the cold window.

## REFERENCE

- [1] S. Sakanaka, et.,al, "Status of the energy recovery linac project in Japan", PAC'09, Vancouver, May (2009).
- [2] H. Sakai et al., "Development of a 1.3GHz 9-cell superconducting cavity for the Energy Recovery Linac", Proceedings of ERL07 Workshop, Daresbury, (2007).

- [3] H.Sakai et al., “Development of input power coupler for ERL main linac in Japan”, Proceedings of 14-th SRF Workshop, Berlin, (2009).
- [4] K.Umemori et al, “Observation of Resonance mode in coaxial-type input coupler”, Proceedings of IPAC2010, Kyoto, (2010).
- [5] H.Sakai et al, “Power coupler development for ERL main linac in Japan”, Proceedings of IPAC2010, Kyoto, (2010).
- [6] W.Anders et al., “CW operation of superconducting TESLA cavities”, Proceedings of 13-th SRF Workshop, Beijing, (2007).
- [7] V.Veshcherevich et al, “High Power Tests of input couplers for Cornell ERL injector”, Proceedings of 13-th SRF Workshop, Beijing, (2007).
- [8] K.Suganuma et al, “Joining of ceramics and metals”, Ann. Rev. Mater. Sci. 1988, 18: p47-73 (1988).
- [9] T.Muto et al., “The calculation of transverse kick by the input coupler of superconducting cavity for ERL main linac”, Proceedings of the 7<sup>th</sup> Annual Meeting of Particle Accelerator Society of Japan , p840-842 (THPS024), Himeji, Japan.

# LONG-TERM MONITORING OF 3<sup>RD</sup>-PERIOD EP-ELECTROLYTE IN STF-EP FACILITY AT KEK

M. Sawabe, H. Monjushiro, A. Komiya, M. Satou, T. Saeki, H. Hayano, KEK, Tsukuba, Japan

## Abstract

We have constructed an Electro-polishing (EP) Facility in the Superconducting RF Test Facility (STF) at KEK at the end of 2007. We have been operating the EP facility since January 2008 and have performed the EP-processes of cavities about 200 times up to the present. [1, 2]

We changed EP-electrolyte in the 2,000L tank three times until now. And we use the 4<sup>th</sup>-period EP-electrolyte now. We presented the long-term monitoring result of the 2<sup>nd</sup>-period EP-electrolyte so far. [3]

In this report, we present the long-term monitoring results of the 3<sup>rd</sup>-period EP-electrolyte, the correlation between EP-process data and the change of fluorine chemical species by EP-electrolyte aging, the result that we could achieve good performance by the EP-electrolyte old enough.

And we want to suggest the new EP chemical equation.

## INTRODUCTION

The electro-polishing (EP) facilities in KEK were completed at STF (Super conducting RF Test Facility) area in Dec. 2007. And we have begun to operate in Jan. 2008.

In this facility, the capacity of the electrolyte reservoir tank is 2,000 L (Figure 1), it is very large. We fill the EP-electrolyte of 2,000kg ( $\cong$  1,100L) into this tank, and use it repeatedly many times. The laboratory doing such a usage is only here.

We changed the EP-electrolyte three times until now. The 1<sup>st</sup>-period EP-electrolyte was used from Jan. 2008 to May 2009. The 2<sup>nd</sup>-period EP-electrolyte was used from May 2009 to July 2010. And the 3<sup>rd</sup>-period EP-electrolyte was used July 2010 to July 2011. And we use the 4<sup>th</sup>-period EP-electrolyte now.

The electrolyte chemical composition changes with using it repeatedly, and gives a big influence to EP-processes. Therefore its monitoring is very important.

We report the 3<sup>rd</sup>-period EP-electrolyte monitoring result and the change of chemical composition.

And we suggest the new EP equation from the long period monitoring result until now.

## THE HISTORY OF THE 3<sup>RD</sup>-PERIOD EP-ELECTROLYTE

Table 1 shows the history of the 3<sup>rd</sup>-period EP-electrolyte. We used this EP-electrolyte for about one year and performed 43 times EP-processes.

Figure 2 shows each removal weight of niobium from cavity, which was calculated from the total charge (integrated current) of each EP-process, for 43 EP-

processes. The accumulated removal weight of niobium from cavities, which was calculated from the total charge (integrated current) of all the EP-processes, was 13,032 g (Figure 3).



Figure 1: Reservoir tank of EP-electrolyte (2,000 L) in STF-EP facility at KEK.

Table 1: The History of the 3<sup>rd</sup>-period EP-electrolyte

The beginning use	July.21, 2010
The disposal	July.04, 2011
The using period	about 1 year
The number of times of EP	EP:43 times
Total removal volume	13,032g-Nb

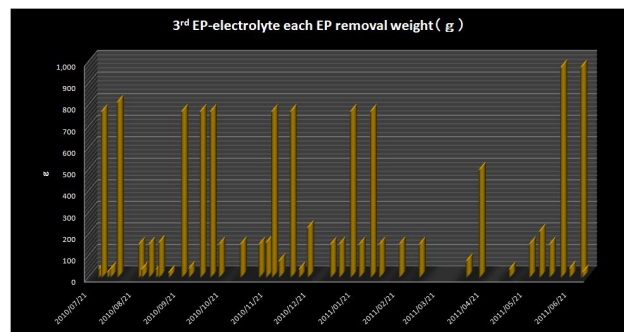


Figure 2: Each removal weight of niobium from cavity for the 43 EP-processes.

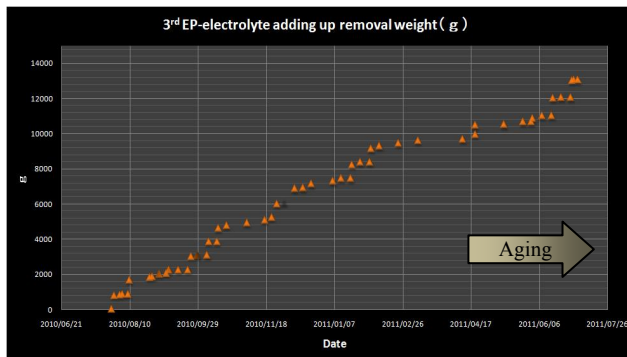


Figure 3: The accumulated removal weight of niobium calculated from the total charge (integrated current) of the 3<sup>rd</sup>-period EP processes vs. date.

### MONITORING RESULTS

#### Periodical Measurements of Niobium Concentration in EP- electrolyte

Figure 4 shows the result of the periodical measurements of the niobium concentration by ICP in the 3<sup>rd</sup>-period EP-electrolyte. The niobium concentration at the time of the disposal was 12 (g/L). In the 2<sup>nd</sup>-period EP-electrolyte, It was 9.8 (g/L) at the time of the disposal. [3]

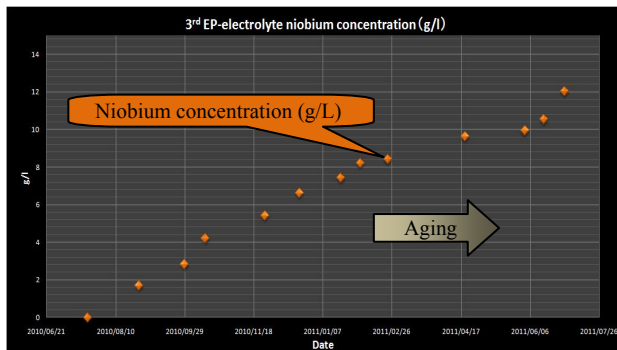


Figure 4: Periodical measurements of niobium concentration by ICP in the 3<sup>rd</sup>-period EP-electrolyte vs. date.

#### Periodical Measurements of Fluorine Concentration in EP- electrolyte

Figure 5 shows the result of periodical measurements of the fluorine concentration in the 3<sup>rd</sup>-period EP-electrolyte. Total fluorine concentration decreased to about 74% and the effective fluorine concentration ( $F^- + SO_3F^-$ ) decreased to about 50% in comparison with the initial fresh EP-electrolyte.

In the 2<sup>nd</sup>-period EP-electrolyte, total fluorine concentration decreased to about 77% and the effective fluorine concentration ( $F^- + SO_3F^-$ ) decreased to about 54% in comparison with the initial fresh EP-electrolyte. [3]

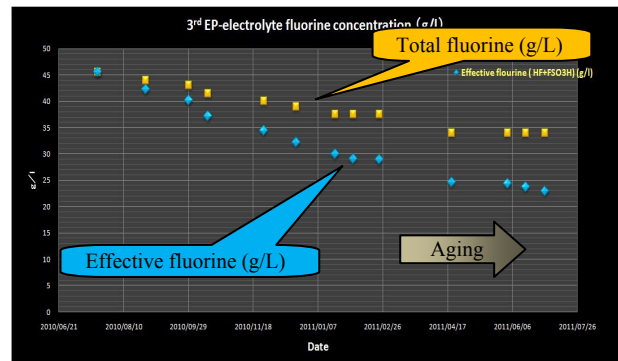


Figure 5: Periodical measurements of fluorine concentration in 3<sup>rd</sup>-period EP-electrolyte vs. date.

#### Periodical Measurements of Fluorine Chemical Species Concentration in 1/500 diluted EP - Electrolyte

Figure 6 shows the result of periodical measurements of the fluorine chemical species concentration in 1/500 diluted the 3<sup>rd</sup>-period EP-electrolyte. The fluorosulfate ion ( $SO_3F^-$ ) decreased by the aging. But the fluoride ion ( $F^-$ ) increased adversely. We were able to observe the similar change in the 2<sup>nd</sup>-period EP-electrolyte. (Figure 7) [3]

It is thought that the hydrolysis of fluorosulfuric acid in undiluted EP-electrolyte advanced by the aging.

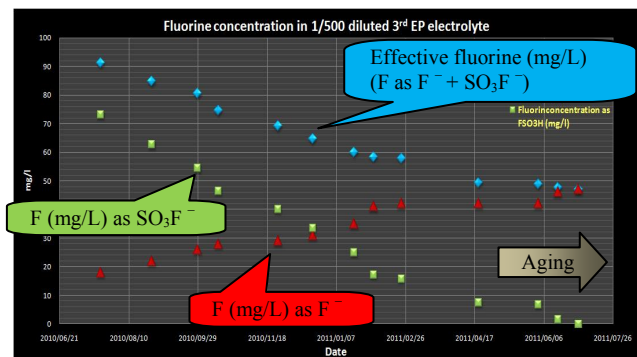


Figure 6: Periodical measurements of the fluorine chemical species concentration in 1/500 diluted the 3<sup>rd</sup>-period EP-electrolyte vs. date.

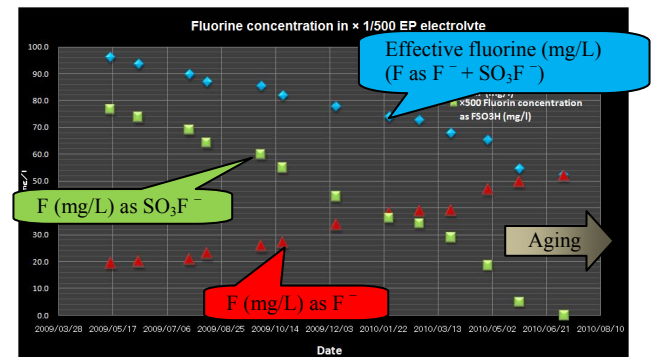


Figure 7: Periodical measurements of the fluorine chemical species concentration in 1/500 diluted the 2<sup>nd</sup>-period EP-electrolyte vs. date.

### CORRELATION BETWEEN EP-PROCESS DATA AND EP-ELECTROLYTE AGING

Figure 8 shows the logging data of current (in the unit of A) and current density (in the unit of mA/cm<sup>2</sup>) in four EP processes on 1<sup>st</sup> September 2010, 17<sup>th</sup> November 2010, 9<sup>th</sup> February 2011, and 8<sup>th</sup> Jun 2011, with the 3<sup>rd</sup>-period EP-electrolyte. The sampling rate of the data was every second. It is seen from the figure that the current oscillation became smaller when the aging of the EP-electrolyte proceeds. We calculated the Relative Standard Deviation (RSD) = Sigma /Average of current density in the unit of % for each EP process for the 3<sup>rd</sup>-period EP-electrolyte. Figure 9 is the superimposed plot of the RSD of current density and the niobium concentration vs. date for the 3<sup>rd</sup>-period EP-electrolyte. Figure 10 is the superimposed plot of the RSD of current density and the SO<sub>3</sub>F<sup>-</sup> / (F<sup>-</sup> + SO<sub>3</sub>F<sup>-</sup>) ratio vs. date. It is seen from these figures that there is a correlation between the RDS of current density and the SO<sub>3</sub>F<sup>-</sup> / (F<sup>-</sup> + SO<sub>3</sub>F<sup>-</sup>) ratio.

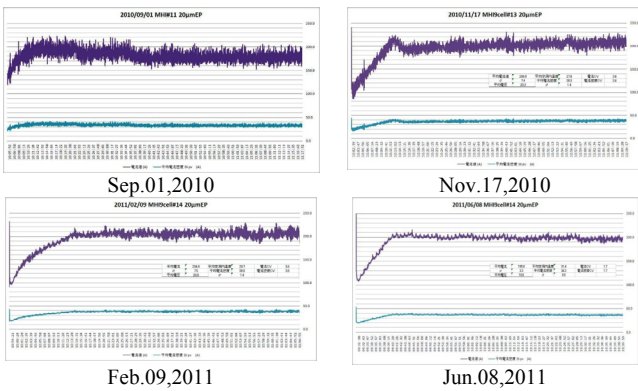


Figure 8: Logging data of current and current density in the 3<sup>rd</sup>-period EP-electrolyte.

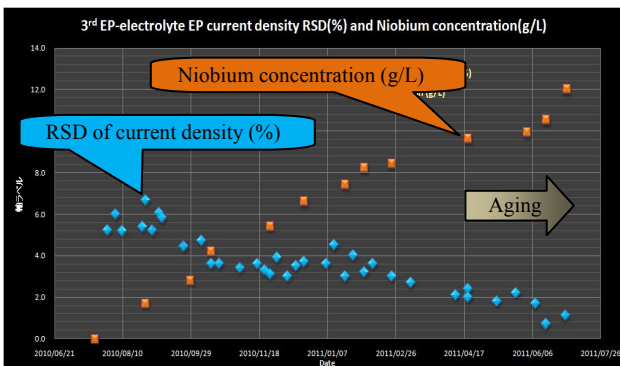


Figure 9: RSD of current density and Nb concentration in the 3<sup>rd</sup>-period EP-electrolyte vs. date.

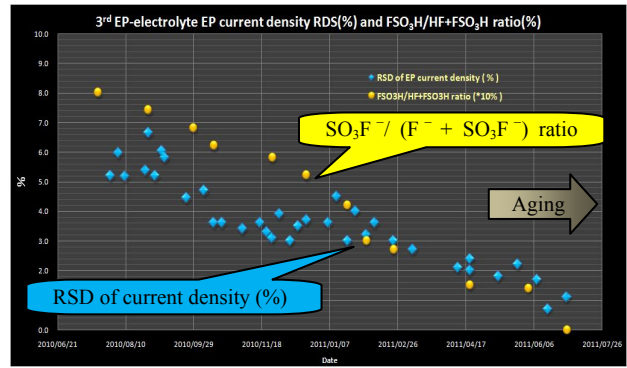


Figure 10: RSD of current density and SO<sub>3</sub>F<sup>-</sup> / (F<sup>-</sup> + SO<sub>3</sub>F<sup>-</sup>) ratio in the 3<sup>rd</sup>-period EP-electrolyte vs. date.

### Changes of the Correlation between EP-voltage and the EP-current Density by the EP-electrolyte Aging

In the case of EP2 (fine EP, about 20 μmEP), we electro-polished cavities at current density 30-40mA/cm<sup>2</sup> in the 3<sup>rd</sup>-period EP-electrolyte.

Figure 11 shows the correlation between the EP-current density and the EP-voltage in this period.

The change of correlation was not seen by the EP-electrolyte aging.

In the case of EP1 (coarse EP, about 100 μmEP), we electro-polished cavities at current density 45-50mA/cm<sup>2</sup> in this period.

Figure 12 shows the correlation between the EP-current density and the EP-voltage in this period.

The change of correlations was not seen by the aging too.

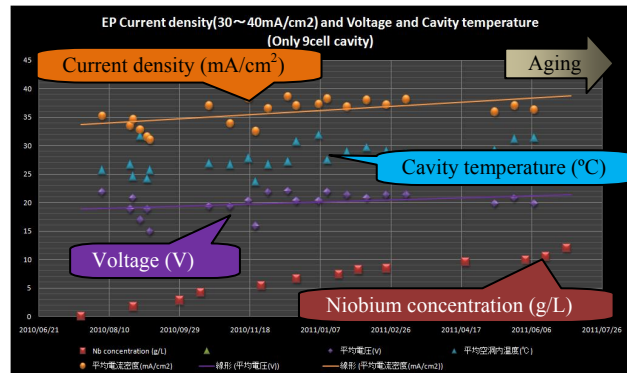


Figure 11: The changes of EP current density and EP voltage and cavity temperature and niobium concentration in the 3<sup>rd</sup>-period EP-electrolyte vs. date (at 30-40mA/cm<sup>2</sup>).

Copyright © 2013 CC-BY-3.0 and by the respective authors

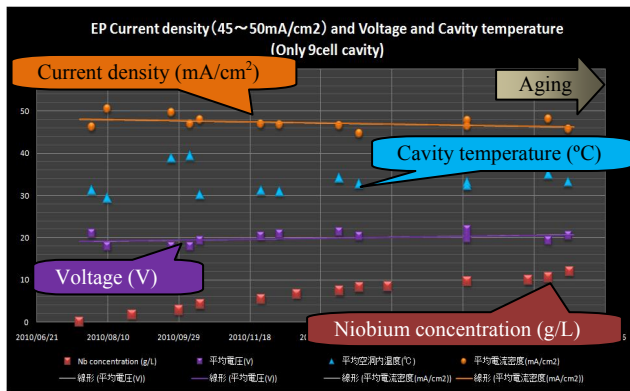


Figure 12: The changes of EP current density and EP voltage and cavity temperature and niobium concentration in the 3<sup>rd</sup>-period EP-electrolyte vs. date (at 45~50mA/cm<sup>2</sup>).

### THE CAVITIES PERFORMANCE RESULTS BY 3<sup>RD</sup>-PERIOD EP-ELECTROLYTE

Table 2 shows the cavity performance results by the 3<sup>rd</sup>-period EP-electrolyte.

We could achieve ILC spec in the four cavities by the 3<sup>rd</sup>-period EP-electrolyte.

And we could achieve it by the electrolyte old enough.

At niobium concentration is about 10 g/L.

In thinking about the life (exchange time) of EP-electrolyte, it will be the big result.

Table 2: The Cavities Performance Result by the 3<sup>rd</sup>-period EP-electrolyte

Date	Cavity	Performance (MV/m)	Notice
Jul.28,2010	ERL2cell#2	38.4	
Oct.20,2010	MHI9cell#A	29.1	Non HOM
Nov.04,2010	MHI9cell#12	37.7	
Nov.17,2010	MHI9cell#13	36.4	Achievement ILC spec
Dec.01,2010	MHI9cell#12	40.7	Achievement ILC spec
Dec.15,2010	MHI9cell#13	33.1	
May.25,2011	MHI9cell#17	39.2	Achievement ILC spec
Jun.08,2011	MHI9cell#14	36.6	Achievement ILC spec <b>Niobium concentration about 10g/L.</b>
Jun.22,2011	ERL2cell#3	30.3	

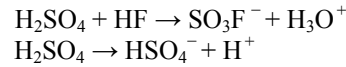
### CONSIDERATION

By the long-term monitoring results in the 2<sup>nd</sup>- and 3<sup>rd</sup>-period EP-electrolyte, we understood that fluorosulfuric acid and hydrofluoric acid exist as fluorine chemical species in EP-electrolyte and the fluorosulfuric acid is hydrolyzed to hydrofluoric acid by the aging.

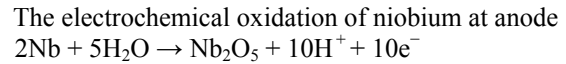
By the way, in the past EP equation, the dissolution of niobium in the EP-processes depends on only the hydrofluoric acid. There is not the existence of fluorosulfuric acid.

Therefore we want to suggest the following new chemical equation of EP-processes.

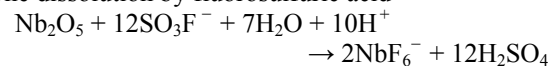
The chemical equilibrium in EP-electrolyte is thought about as follow.



The oxidation and dissolution of niobium are thought about as follows.



The dissolution by fluorosulfuric acid



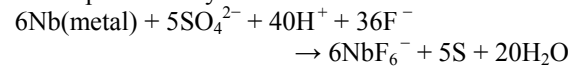
The dissolution by hydrofluoric acid



NbF<sub>6</sub><sup>-</sup> was detected by Laser Raman spectroscopy method in the used EP-electrolyte.

Side reaction (at high temperature)

Sulfur is produced by this reaction.



Sulfur was produced with niobium powder and new EP-electrolyte by our experiment. The temperature was more than approximately 40-50 degrees Celsius.

We think that the dissolution of niobium depends on the fluorosulfuric acid in the fresh EP-electrolyte and gradually depend on the hydrofluoric acid by the EP-electrolyte aging.

### SUMMARY

- In the 3<sup>rd</sup>-period EP-electrolyte, total fluorine concentration decreased to about 74% and the effective fluorine concentration decreased about 50% in comparison with the initial fresh EP-electrolyte.

- In the 1/500 diluted EP-electrolyte, the fluorine chemical species changed gradually from fluorosulfate ion (SO<sub>3</sub>F<sup>-</sup>) to fluoride ion (F<sup>-</sup>) by the EP-electrolyte aging. It is thought that the hydrolysis of fluorosulfuric acid in the undiluted electrolyte advanced by the EP-electrolyte aging.

- The EP-electric current and current density oscillation became small with the aging. It is thought that the change of oscillation is a cause of the change of fluorine species by the EP-electrolyte aging.

- We want to suggest the new EP equation. The main point is that the dissolution of niobium depends on fluorosulfuric acid and hydrofluoric acid. And we think that the dissolution product is  $\text{NbF}_6^-$ .
  - The change of correlation between the EP-voltage and the EP-current density was not seen in the 3<sup>rd</sup>-period EP-electrolyte aging.
  - We used the 3<sup>rd</sup>-period EP-electrolyte until niobium concentration became 12 g/L. And we could achieve good performance result by the EP-electrolyte old enough.
- It will become the big result in thinking about the life (exchange time) of EP-electrolyte.

## REFERENCES

- [1] M. Sawabe, et al., TTC-Meeting Apr, 2010 “Quality control of KEK STF”.  
<https://indico.fnal.gov/conferenceDisplay.py?confId=3000>
- [2] M. Sawabe, et al., Paper ID: WEPEC027, IPAC10, May 2010, “Long-monitoring of Electro-polishing Electrolyte in EP facility at KEK”.
- [3] M. Sawabe, et al., Paper ID: TUPO039, SRF2011, July, 2011, “Long-term monitoring of 2<sup>nd</sup>-period EP-electrolyte in STF-EP facility at KEK”.

# IMPROVED HEAT CONDUCTION FEEDTHROUGHS FOR HOM COUPLERS AT DESY\*

J. Sekutowicz

DESY, Notkestrasse 85, 22607 Hamburg, Germany

## Abstract

Vertical acceptance test of 808 cavities of the XFEL superconducting linac will be conducted for cavities equipped with HOM antennae, mainly to reduce the production and preparation cost. This new procedure is different from that we applied to all superconducting cavities tested in last two decades at DESY. In addition, cw and long pulse operations can be envisioned as complementary modes to the nominal short pulse operation of the XFEL facility. The new vertical test conditions and the new possible operation modes will require better cooling of the HOM couplers. In this contribution we discuss new heating conditions of the HOM antennae and present new feedthrough we ordered for the XFEL cavities.

## INTRODUCTION

The XFEL cavity and its auxiliaries were designed in early 90's for short pulse operation of the superconducting linear collider TESLA. Details of the TESLA cavity have been summarized in the Tesla Technical Design Report [1], which was published in 2001. The proposed duty factor (DF) for the TESLA collider, and presently for XFEL, is ca. 1%. This allows location of the HOM couplers outside liquid helium vessel, as shown in Figure 1. Such a design significantly reduces cost of the cavity and was an unavoidable step for 22 000 cavities of the TESLA main accelerator. Many years of operation of the FLASH linac, at present made of 56 cavities, proved that the TESLA cavity design is well suited for the nominal duty factor of XFEL. Nonetheless, the remarkable continuous improvement in performance of the TESLA cavities, both in gradients and intrinsic quality factors, raises a question, already since several years, whether or not one can increase the DF for XFEL and gain additional flexibility in time structure of the electron and photon beams [2]. As production of the XFEL cavities will begin in 2012, it is still possible to make minor changes in quality of auxiliaries to keep open the possibility of other operation modes with higher DF.

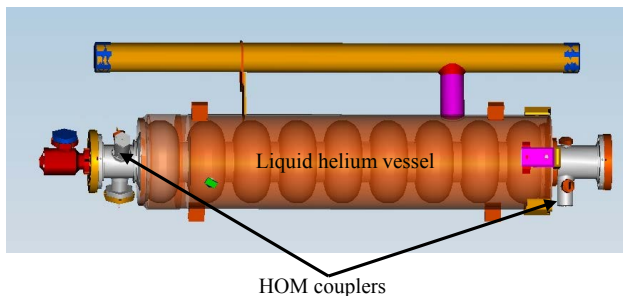


Figure 1: 9-cell TESLA cavity in liquid helium vessel.

## VERTICAL ACCEPTANCE TEST

Vertical acceptance test for all 808 XFEL cavities will take place at DESY. The cavities will have attached HOM antennae (feedthroughs) at factories before the test, mainly to lower the production and preparation cost. This new procedure is different from that we applied to all superconducting cavities tested in last two decades at DESY. The standard cw vertical acceptance test, at the specified gradient of 23.4 MV/m, would cause 100 times higher heat load for the antennae than the nominal operation with 1% DF. Unfortunately, unlike the cavity wall, removing that heat from antenna is indirect, and depends on the heat conduction of isolating window and on material it is brazed to. Two measures have been undertaken for the acceptance test to mitigate the excessive overheating.

At first, we decided to test cavities in a pulse mode with DF of ca. 10%. In that way overheating of HOM antennae will be 10 times smaller than in the standard cw vertical test. Secondly, we will replace present HOM feedthroughs with ones having higher heat conduction, because it is expected that heating of HOM antennae could be also a limitation in the linac performance for new operation modes. Design of the new feedthrough will be discussed later, but in general it follows modifications proposed first at TJNAF for cavities developed for the 12 GeV upgrade of CEBAF.

## NEW OPERATION MODES OF XFEL LINAC

Two new operation modes of XFEL are at present under discussion; the cw mode and long pulse (lp) mode. In the latter one, the linac will operate with ~100 ms long pulses, which repetition rate is 1 Hz. The intended maximum gradient for the lp mode is close to the present nominal one of 23.4 MV/m. For the cw operation, the cavities will run at 7.5 MV/m at most. Accordingly to our estimation, either of new operations will cause heating of the HOM antenna comparable to that in the pulse acceptance test.

The new modes require new RF-amplifiers with capability to run both in the cw and in long pulse mode. In addition, overall efficiency of the RF-system is an important criterion for choice of the amplifier, especially in case of the lp operation, when at the highest gradient the DF will be ~10%, and thus for 90% of time there will be no beam in the linac. We consider two candidates for the RF-source, either does not take or takes very little energy from the grid when it does not generate RF power. The first is an IOT (Inductive Output Tube), which is a

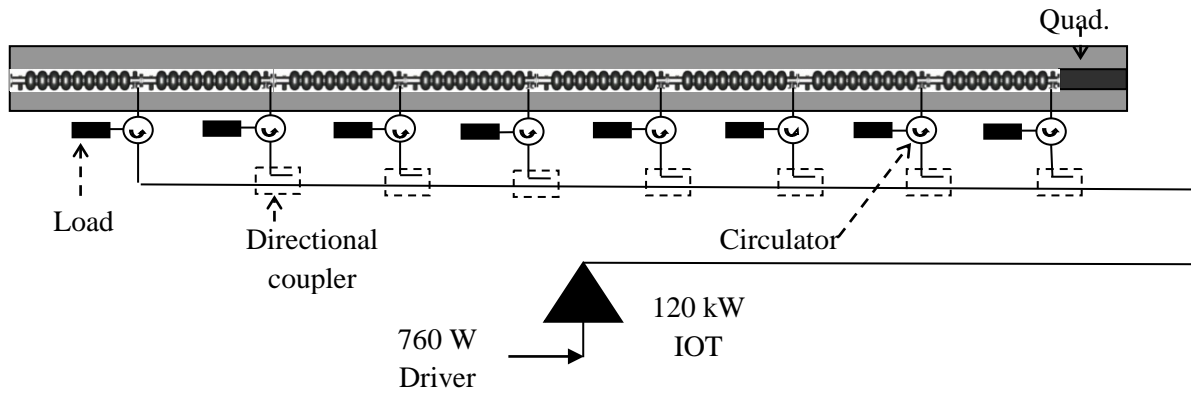


Figure 2: RF-power distribution system for a 8-cavity cryomodule with 120 kW IOT amplifier.

tetrode. The second is a solid-state amplifier. Our former studies showed that ca. 120 kW RF power per eight-cavity cryomodule will be sufficient to accelerate up to 0.25 mA beam at the nominal XFEL gradient, keeping a safety margin of the power to compensate for microphonics. For the size and cost reason an IOT seems at present to be a better choice; however we will follow the progress in the solid-state amplifier offer. The schematic configuration of the XFEL cryomodule and an IOT amplifier is shown in Figure 2.

## RESULTS OF EXPERIMENTS

### Pulse Acceptance Test

Since March 2010 we test 9-cell cavities, when they are equipped with feedthroughs, in the pulse mode. The time structure of pulse sequence is shown in Figure 3. The DF factor for the test is set to 10 % and the pulse duration of ~5 s is sufficient to reach the charging plateau for intrinsic quality factors ~2E10 (loaded Q ~1E10). Many cavities, equipped either with old “fashion” or with new prototypes of feedthroughs, have been tested and with an exception of few they performed very well. Some of these few cavities were limited by heating of the HOM couplers. That happened usually when couplers had not been well cleaned or had scratches on the surface (for example made by the electrode of EP setup). Not carefully cleaned HOM couplers showed often multipacting, which in some cases could be conditioned.

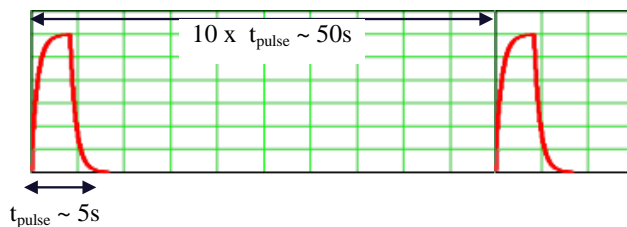


Figure 3: RF-pulses for the vertical acceptance test with DF ca. 10% and the pulse length for intrinsic quality factors ~ 2 E10.

### Operation of an 8-cavity Cryomodule with IOT

In July 2011, we have conducted the very first test of the cw and lp operations. For that test we used 85 kW IOT built by CPI in the frame of the EuroFEL program. The tested cryomodule had all eight cavities equipped with low conduction “old fashion” feedthroughs, which per purpose were not thermally connected to the 2K-tube. In that way we could test the worst case scenario for cooling conditions of the end groups.

In the test:

- 6 cavities had loaded  $Q = 1.6E7$ , one 8E6 (limit in  $E_{\text{acc}}$ ) and one 4E6 (blocked FM coupler).
- Achieved gradients were: in cw up to 5.5 MV/m and in lp mode 11 MV/m ( $t_p=300$  ms).
- Voltage vector sum stabilization was: 1E-3 (rms) with no “dedicated” LLRF system.

The result is encouraging and we will perform second test in January/February 2012 with new LLRF, dedicated to cw/lp modes, and better thermal conditions for the HOM couplers. For that test, we will have cryomodule in which 5 cavities will be equipped with high conduction and only 3 with low conduction feedthroughs. All will be thermally connected to the 2K-tube.

## HIGH THERMAL CONDUCTION FEEDTHROUGH

As already mentioned, all high conduction feedthroughs, offered by several industrial vendors, are based on the design developed at TJNAF for the cw operation of 1.5 GHz upgrade cavities. In that design, standard alumina ceramic  $Al_2O_3$  has been replaced with a sapphire crystal. In addition, the feedthroughs which we will use for the XFEL cavities will have sapphire window brazed directly to a copper fixture, allowing good heat transfer from the antenna. The antenna will be made of high purity niobium. Flange of the feedthrough will be made of titanium, which has better heat conductivity at 2K than commonly used stainless steel. The proposed feedthrough is shown in Figure 4.

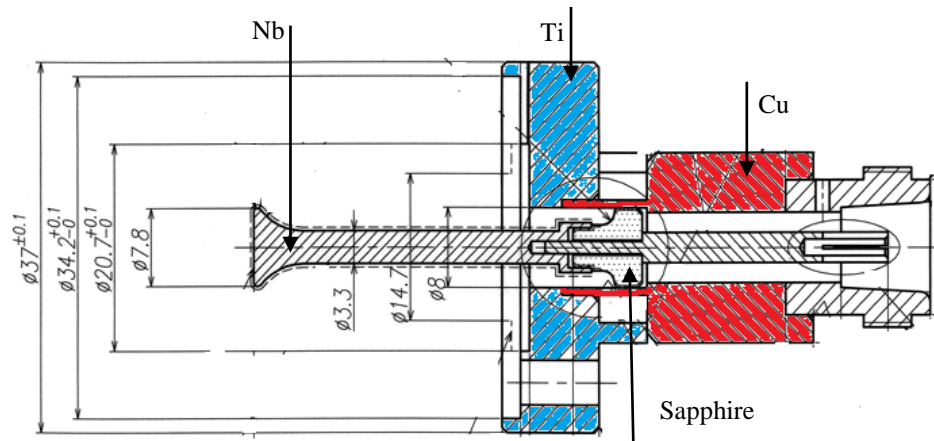


Figure 4: High conduction feedthrough with the sapphire window.

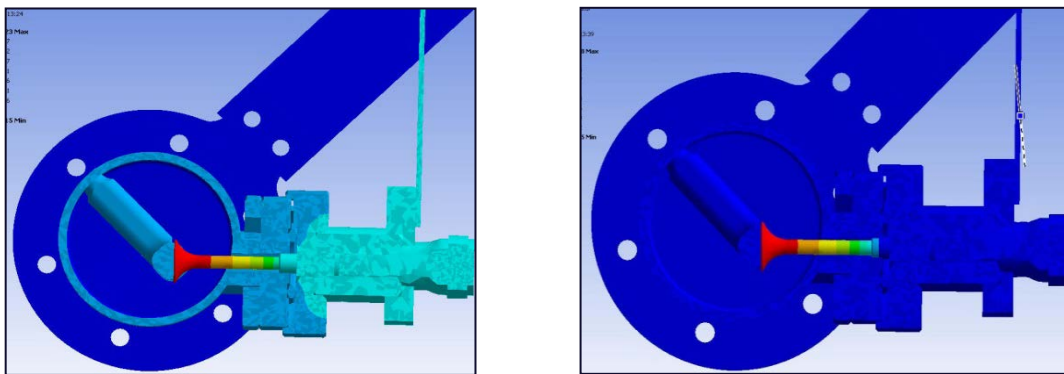


Figure 5: Calculated with ANSYS temperature profile for the HOM coupler immersed in superfluid helium (right) and when a cavity is in cryomodule (left). Dark blue color marks 2K.

We have conducted computer modeling of the antenna heating for thermal conditions in the acceptance test, when a cavity is immersed in superfluid helium and then when it is installed in a cryomodule and hence the end groups are in vacuum. For the modeling, the high conduction feedthrough was chosen. The results, T profile and T vs. dissipated heat, are shown in Figure 5 and in the Table 1 respectively. The temperatures are very similar for either condition. When the mean dissipated power on the antenna stays below 20 mW, the antenna should remain in the superconducting state. This will allow to minimize heat load for the new types of operation.

Table 1: Highest Temperature on the Antenna

Heat [mW]	T in vacuum [K]	T in superfluid He [K]
20	7.0	6.8
5	4.6	4.5
4	4.2	4.2
3	4.0	3.9
2	3.6	3.5
1	3.1	3.0

**REFERENCES**

- [1] R. Brinkmann et al. (editors), TESLA TDR, DESY-Report-2001-23 (2001).
- [2] J. Sekutowicz, "Parameter set for cw and near-cw operation of a XFEL driving superconducting linac", EUROFEL-Report-2005-DS5-003, <http://www.eurofel.org/e693/e1009/>

## CLOSING PLENARY SUMMARY OF WORKING GROUP 4 INSTRUMENTATION AND CONTROLS FOR ERL2011\*

D. M. Gassner<sup>#</sup>, BNL, Upton, NY, U.S.A.  
T. Obina, KEK, Ibaraki, Japan

### Abstract

Summary of the working group 4 activities, presented in the closing plenary session.

### OVERVIEW

Working group 4 was charged with presentations and discussions on instrumentation and controls with regards to Energy Recovery Linacs (ERL). There were 4 sessions spanning 3.5 hours in which 7 talks were delivered, the first being an invited plenary presentation. The time allotted for each talk was limited to 20-25 minutes in order to allow 5-10 minutes for discussion. Most of the talks were held in joint session with working group 5 (Unwanted Beam Loss). This format was effective for the purpose of this workshop. A final series of discussion sessions were also held with working group 5.

### PRESENTATIONS

The working group 4 presentations can be separated into 3 groups, the first being a plenary talk about the instrumentation and controls at the existing ERL at Cornell. The second group described instrumentation technology that is presently in use at other similar machines that can be applied to ERLs. The third group explained the details of two new ERLs that are under construction, and their respective instrumentation systems.

#### *B. Dunham (Cornell): Operations, Controls and Diagnostics for High Power Electron Injectors*

In this plenary talk Bruce described many aspects of the instrumentation and controls at the ERL Injector Prototype at Cornell (13MeV, 77pC/bunch, 1.3GHz bunch rate). He described the challenges ahead to provide diagnostic systems with increased resolution and wide dynamic range ( $10^6$ - $10^9$ ) that will be needed to assure beam stability and synchronization. With regards to controls systems, he described the features and advantages of EPICS and looks forward to a new version that will be released soon. He also described the DOOCS (Distributed Object Oriented Controls System) that was developed at DESY. Using this it is easy to write applications in C++, it has advantages for high data-rate DAQ streams, and it communicates well with EPICS servers.

Bruce explained techniques used at the Cornell ERL Injector to measure transverse emittance, and a new way to use two stationary slits each with a respective upstream corrector dipole pair and a downstream Faraday Cup. Slice emittance measurements were made using the

\*Work supported by the auspices of the US Department of Energy  
<sup>#</sup>gassner@bnl.gov

stationary slits, a deflection cavity, and downstream view screen as shown in Figure 1. He also described details about the deflection cavities used at Cornell and KEK, the application of these to map the time axis onto transverse coordinates, and how to make longitudinal phase space measurements. More descriptions were presented about bunch arrival time monitors, and electro-optic profile diagnostics using a laser.

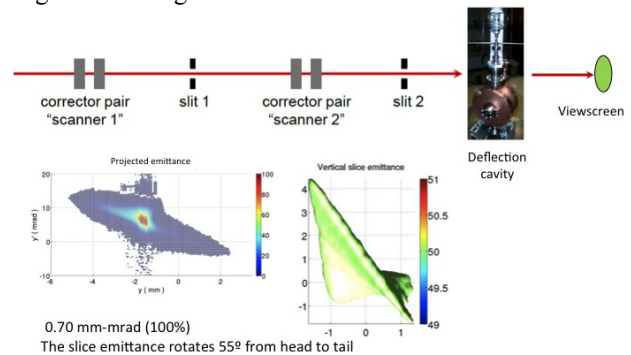


Figure 1: Slice emittance using correctors, slits, deflection cavity, and view screen.

The next topic focused on issues with regards to high current operations. The importance of the gun laser intensity and position stabilization was explained. Cornell is developing laser fast-feedback systems as a remedy; progress to date was described, as well as future plans for laser position stabilization to 10 microns.

This was followed by information about beam halo generation, causes, and methods to measure halo. Images were shown of halo measurements using the solid screens, coronagraph, screen with hole, and adaptive mapping. He emphasized the importance of minimizing the surface roughness to  $< 2$ nm rms of the mirror used to transport the laser to the photocathode.

The final topic was about valuable lessons learned, operational experiences, raster scanning, temperature monitoring, and beam diagnostics at the Cornell beam dump.

In conclusion he commented that there have been a lot of great developments for ERL diagnostics in the past 2 years, but there is still a long list of things they need and want. Some items that were requested to improve the ERL instrumentation systems include: easy to use fast DAQ and transient capture, large dynamic range CCD cameras that are inexpensive, non-intercepting emittance measurements, really fast laser monitoring to look between pulses, smarter sub-systems with more status and fault indicators, simpler non-intercepting bunch length monitors, and a more affordable streak camera.

### M. Tobiyama (KEK): Turn-by-Turn Monitor Using a Fast Gate Switch

This presentation describes the motivation and progress to employ an electronic fast gate switch to enhance the existing beam position monitoring system at the SuperKEKB facility in order to improve the control of the betatron tune during collisions. Makoto explained how his team's developments might be useful at ERLs to measure beam positions near the Linac where both low and high-energy beams are present and interleaved in time.

A variety of candidate switches were described, the Hittite HMC234C8 was chosen for integration and testing with beam. This switch is a broadband high isolation non-reflective GaAs MESFET SPDT switch in a non-hermetic surface mount ceramic package, DC–8GHz, with a 3ns switching time. The technique that was used to provide improved isolation and switching noise cancellation using several Mini Circuits MCL SBTCJ-1W power splitters/combiners was described in detail. System performance was described with scope and network analyser waveforms, an example is shown in Figure 2.

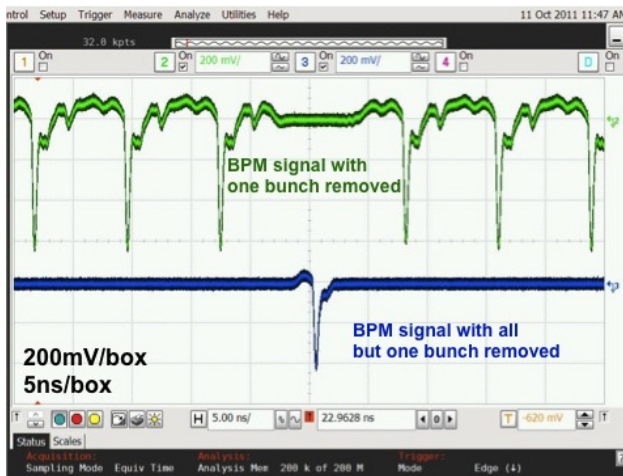


Figure 2: Fast gate switch used to gate BPM signal. The switch has two output ports, both traces are shown.

There were suggestions presented that could improve this fast switch system for ERL applications. These include the need for better time domain response from the BPM pick-ups. Stripline BPMs were used at the SuperKEKB; button electrodes will likely provide better time response. Also a switch with faster response can help, but this can be complicated by difficulties driving the switch over long cables in a noisy accelerator environment. Finally, improvements to symmetry of the printed circuit board in the noise cancellation circuit can improve performance.

### H. Maesaka (RIKEN/SPring-8): Beam Diagnostic Instruments for SACLA

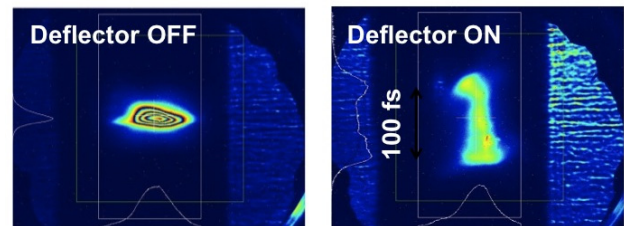
This presentation by Hirokazu described a wide variety of impressive beam diagnostic instruments used along the series of linear accelerators at this 600m long, 8GeV facility that has 3kA peak, 30fs electron bunches.

Beam position measurements are made using the RF Cavity BPM in the TM110 dipole mode, and the TM010 is used to determine the phase reference and the bunch charge. The resonant frequency of this BPM is 4.760GHz. The position resolution is < 0.6 microns rms at 7GeV, 0.1nC. The beam arrival time resolution is ~27fs.

Beam profiles are measured using YAG:Ce screens and CCD cameras. Initially the images also included undesired coherent OTR light. This was later masked using a 5mm wide shield upstream of the camera lens. There are future plans to use a fast gate CCD camera (C10042) to view only the slow (~70ns decay time) scintillation from the YAG:Ce, and ignore the prompt C-OTR radiation.

A custom designed fast differential current transformer was described that achieves a 200ps rise-time. It provides reasonable linearity, for bunch lengths > 400ps FWHM.

Details about a transverse deflection cavity that operates at 5.712GHz and 60MV were presented. Results are shown in Figure 3.



- Temporal structure of a 1.4 GeV beam was stretched to 50fs/mm at 10m downstream of the deflector cavity.  
**Resolution ~ 10fs longitudinal profile**
- YAG:Ce and OTR mask are used in the profile monitor.

Figure 3: Electron bunch data from the SACLA deflector cavity.

More details were presented about streak camera implementation, as well as the system configuration and data from a coherent synchrotron radiation monitor that employs a pyro-electric or THz diode. An electron bunch timing pick-up using an electro-optic crystal is under development. This system uses an 110fs Ti:Sapphire laser pulse, and complex optics to transport to the laser through a viewing port to a ZnTe electro-optic crystal located in the beam line vacuum chamber. They expect to achieve ~100fs timing resolution.

Many of the experiences and advances in electron beam diagnostics systems described by Hirokazu can be useful at energy recovery linacs.

*H. Maesaka: Design and Performance of the Synchronization System for SACLA*

Hirokazu's second talk described the effort to improve the synchronization system at SACLA with the purpose of providing stable x-ray lasing. System details about the optical RF signal distribution method were presented. The 2856MHz master oscillator is phase locked to 10MHz and 100MHz oven controlled crystal oscillators. Frequency dividers generate sub-harmonic signals. The distribution system employs E/O and O/E converters using an LN modulator (Mach-Zehnder interferometer), and fast photodiode, respectively. Water-cooled electronics racks were installed, as well as temperature regulated long length fiber optic cable ducts, all with stability of 0.2K (pk-pk). A low-noise linear regulated 24V DC power supply with an FFT spectrum noise floor  $\sim -140\text{dBV}/\text{root Hz}$  was used for subsystem power.

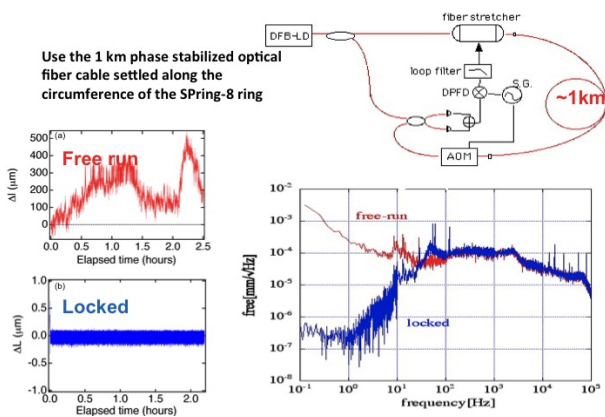


Figure 4: Experiment of fiber length control.

A fiber length control system was developed as shown in Figure 4. The system was tested using the existing 2km phase-stabilized optical fiber along the circumference of the SPring-8 ring accelerator. The displacement signal outputted from the feedback circuit is proportional to the fiber optical length change. The optical length control for the fiber worked well, and decreased the displacement to less than several micrometers of its optical length in a frequency range of less than 50 Hz.

A custom designed low-level RF control system was described. Since each facility has many unique requirements, this may not be directly beneficial for use at an ERL, but some of the subsystem techniques can be helpful.

*T. Naito (KEK): Development of Femtosecond Timing Distribution System*

Precise timing reference clock distribution is required for the new compact ERL at KEK, and also at future

accelerators such as Super KEK, and the ILC. Takashi described the previous progress at KEK, and the present similar systems at DESY and at LCLS at SLAC. A diagram of the system presently under development at KEK is shown in Figure 5. Experimental test hardware configurations were described and measurement data was presented. This included plots of long-term stability, length stability, and feedback phase versus fiber length.

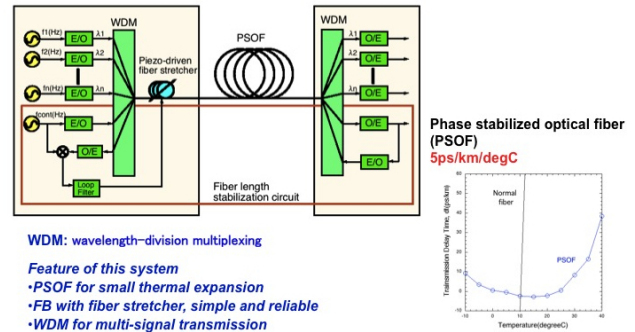


Figure 5: Femtosecond timing distribution system layout.

A precise reference clock distribution system using optical links and a feedback circuit was developed and was able to achieve stability of  $\sim 50\text{fs}$  for 900m of optical fiber, using 2856MHz clock transmission.

Efforts are underway to improve performance of several aspects of the system. In order to achieve  $<20\text{fs}$  stability, they will improve temperature stabilization of the TX/RX control box to 0.01deg C, as well as the possible use of a higher frequency 11.4GHz clock. To confirm long distance stability, a 10km long phase stabilized optical fiber will be tested. To confirm long term stability a system will be installed into the 8GeV S-band Linac.

*T. Obina (KEK): Beam Instrumentation for the Compact ERL at KEK*

Takashi provided a description of the KEK compact ERL that is presently under construction. Commissioning is planned to start in 2013. They will begin commissioning and beam tests with the gun, injection, rf cavity, and dump. Initial energy recovery operations will have a single loop at 35MeV, with a goal of 10mA. Then an rf cavity upgrade will increase the energy to 65MeV. Later a second loop is planned at 125MeV.

The standard beam diagnostics include stripline BPMs with custom processing electronics, transverse profile measurements using OTR and scintillator screens, synchrotron radiation monitors, streak camera, fast gate camera, beam loss monitors (PMT and/or Fiber) and a machine protection interlock system. Also in the design are wire scanners, and absolute and differential beam current monitors.



Figure 6: 3D Model of the KEK Compact ERL construction hall.

Special beam diagnostics include a bunch arrival monitor with precise timing distribution, deflecting cavity for longitudinal profiles and longitudinal phase space measurements, high-resolution resonant cavity BPM (low current only), and a beam halo monitor.

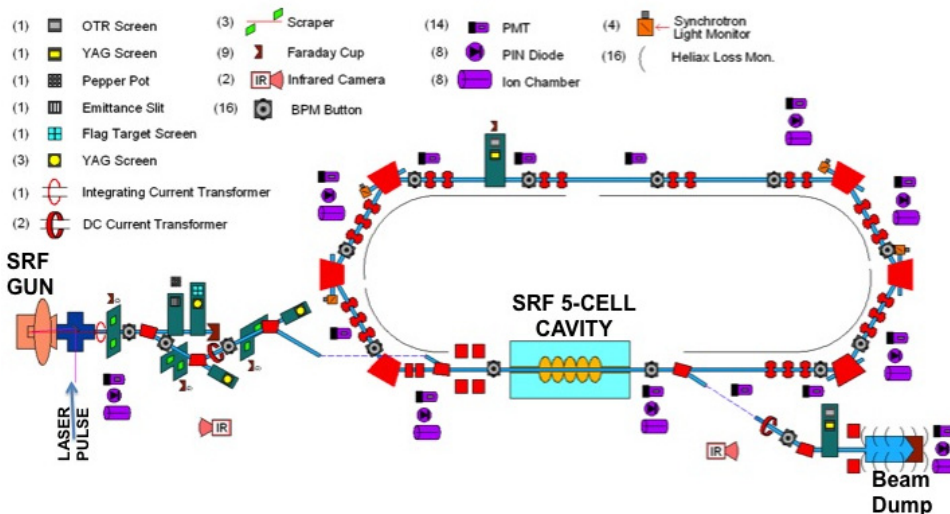


Figure 7: BNL ERL instrumentation layout.

This presentation described the present status of the diagnostic systems that will be used to meet these goals, as well as the sequence of commissioning phases planned to progress from initial gun characterization, to injection zig-zag chicane testing, to closing the beam transport loop and operations that achieve energy recovery.

## DISCUSSIONS

Together with working group 5 (Unwanted Beam Loss), discussions were held after each parallel session talk, and later at dedicated discussion sessions.

A question was raised with regards to the vulnerability of the beam current transformer ceramic gaps to charge build-up in high power CW machines with short bunches, and if a metalized coating should be applied to bleed off

The purpose of the compact ERL at KEK is to demonstrate ERL accelerator technologies, the experimental possibilities based on CSR of THz radiation, and a laser inverted Compton X-ray source.

### *D. Gassner (BNL): BNL Energy Recovery Linac Instrumentation*

The ERL project at BNL is currently under construction; first electron beams are planned for later in 2012. Energy recovery operations are expected with high intensity beams that have current up to a few hundred milliamps, while preserving the emittance of bunches with a charge of a few nC produced by a high current SRF gun. To successfully accomplish this task the machine will include beam diagnostics that will be used for accurate characterization of the beam phase space at the injection and recirculation energies, transverse and longitudinal beam matching, orbit alignment, beam current measurement, and machine protection. The distribution of instrumentation is shown in Figure 7.

charge to avoid possible damage and vacuum leaks. This is a concern since many of the ERLs under development plan unprecedented high power CW operations. One risk that was mentioned is the possibility of the coating flaking off and migrating into a nearby SRF cavity and causing a high gradient point. Shortly after the workshop it was decided to raise this topic with Julien Bergoz [1] who provides many of the CTs in use today. His conclusion was that he is not aware of any conclusive situation where damage to a ceramic break was caused by charge build-up due to the operating beam conditions. His experience is based on the deployment of several hundred CTs (FCT, ICT, NPCT, ACCT) installed in CW machines. At DESY [2] a metalization layer is sometimes applied to the ceramic of the current transformers at DESY, but it does not cover it completely. A thin gap is

left unmetalized to minimize the high frequency, high-order modes from coupling to the toroid. There were never any reported problems with suspected charge build up on any DESY current transformer ceramics.

There were discussions about measurement of dark current from SRF Cavity field emission and how to distinguish it from beam halo. More simulations would benefit the effort of trying to reduce the detrimental effects of each. It was proposed that some systematic measurements and experiments be conducted to quantify and characterize dark current and halo in operating facilities. This would assist future facilities proposing a significant increase in beam current and power to better design suitable collimation systems, and other mitigations of these issues.

There were discussions about possible methods to measure interleaved electron bunches of different energy on either side of the ERL RF cavity. This remains a challenge to the diagnostics community; it is complicated by the wide variety of bunch spacing parameters and accelerating rf frequencies specific to each ERL. The fast switch described by M. Tobiyama [3] might be a good candidate for specific ERL running modes.

Another topic was the feasibility of using a pair of NPCTs in differential mode to measure  $\sim 1\mu\text{A}$  of lost beam in an ERL. Concerns were raised about the variable bunch train lengths and intensity, bunch train gap lengths, as well as noise coupling to the signal. It was mentioned that the resonant cavity current comparison system used at CEBAF likely performed better than the PMT based BLM system, and better than their DCCT system.

The topic regarding better ways to measure electron bunch lengths was raised. The microwave spectrometer using coherent transition radiation was suggested [4].

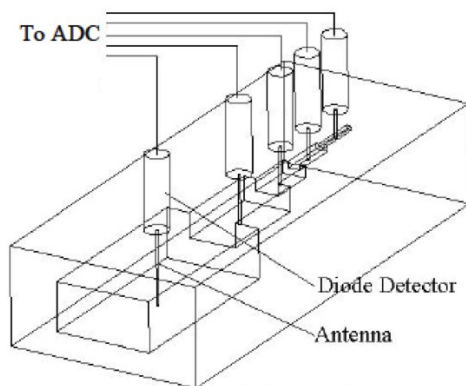


Figure 8: Microwave Spectrometer detector using coherent transition radiation for bunches  $<10\text{ps}$ .

There were discussions about loss monitor detector limitations and performance and how these aspects apply to Energy Recovery Linacs for machine protection and tuning. It was mentioned that fiber optic cable type BLM

detectors are not good candidates for CW machines due to likely radiation damage because of problems after a few MRads. Also, it is difficult to determine the specific time of a loss with a cable of significant length in this case. There were concerns that PMT type detectors might saturate in a sudden very high radiation field, and not send enough signal power to interlock the machine. This was determined to be speculation and would need testing to confirm.

There were discussions about the use of halo scrapers with electron beams, and their possible detrimental effects. The effort to measure the amount of collected electrons from a passing bunch that are intercepted by a variable position scraper jaw is typically not useful since the image charge induced on the isolated jaw is usually on the same order or larger than the signals from the collected electrons. It is difficult, if not impossible to differentiate these two signals.

## CONCLUSIONS

We had a plenary presentation on operational performance, experience, and future plans at the existing ERL injector prototype at Cornell. This included instrumentation data, controls system configurations, as well as description of future needs. This was followed by four talks from KEK and RIKEN/Spring-8 that described electron beam instrumentation already in use or under development that can be applied to ERL facilities. The final talks described the ERLs under construction at KEK and BNL. The format of having joint sessions with working group 5 was beneficial as there were a significant number of common topics and concerns with regards to the causes of beam loss, instrumentation hardware, and techniques used to measure and analyse beam loss.

## ACKNOWLEDGMENTS

The authors would like to thank the organizing committee, and all of the contributors to the working group 4 presentation and discussion sessions. Special thanks to Kevin Jordan who shared many valuable experiences, and for his contributions to the charge.

## REFERENCES

- [1] Private communication with Julien Bergoz.
- [2] Private communication with Kay Wittenburg.
- [3] Tobiyama, M. "Turn-by-Turn Monitor using a Fast Gate Switch", these proceedings.
- [4] Maesaka, H., et al. "Development of the Microwave Spectrometer for the Bunch Length Measurement using Coherent Transition Radiation at the SCSS Prototype Accelerator", Proceedings of the 3rd Annual Meeting of Particle Accelerator Society of Japan and the 31th Linear Accelerator Meeting in Japan (August 2-4, 2006, Sendai Japan), WP20.

# DESIGN AND PERFORMANCE OF THE SYNCHRONIZATION SYSTEM AND BEAM DIAGNOSTIC INSTRUMENTS FOR SACLA

Hirokazu Maesaka<sup>#</sup>, Hiroyasu Ego, Chikara Kondo, Takashi Ohshima, Tatsuyuki Sakurai, Yuji Otake, RIKEN SPring-8 Center, 1-1-1 Kouto, Sayo-cho, Sayo-gun, Hyogo, Japan

Naoyasu Hosoda, Shin'ichi Matsubara, Ken'ichi Yanagida,

JASRI/SPring-8, 1-1-1 Kouto, Sayo-cho, Sayo-gun, Hyogo, Japan

Shinobu Inoue, SPring-8 Service Co. Ltd., 1-20-5 Kouto, Shingu-cho, Tatsuno-shi, Hyogo, Japan

## Abstract

In the x-ray free electron laser (XFEL) facility "SACLA", stable timing and rf signals with less than 100 fs stability are demanded. In addition, precise beam monitors with micron-meter-level spatial resolution and femtosecond-level temporal resolution are required. For the synchronization, we employed a low-noise master oscillator, an optical rf distribution system, IQ (In-phase and Quadrature) modulators/demodulators etc. For the beam diagnostics, we developed a sub- $\mu\text{m}$  resolution rf cavity BPM, a few- $\mu\text{m}$  resolution beam profile monitor, a C-band transverse rf deflecting structure for a 10 fs resolution temporal bunch structure measurement, etc. We confirmed the performance of these instruments by using an electron beam and finally achieved XFEL lasing in the wavelength region from 0.08 nm to 0.16 nm. Some possible applications of our instruments to an ERL are also discussed.

## INTRODUCTION

The x-ray free-electron laser (XFEL) facility "SACLA" (SPring-8 Angstrom Compact Free Electron Laser) is a SASE (Self-Amplified Spontaneous Emission) FEL machine in the wavelength region around 0.1 nm. The construction of SACLA was completed in February, 2011 and the first x-ray lasing was achieved in June, 2011 [1].

The SACLA facility consists of an 8 GeV linear accelerator, in-vacuum undulators and an x-ray beamline, as shown in Fig. 1. An electron beam emitted from a thermionic gun is accelerated up to 8 GeV by 238 MHz, 476 MHz, L-band (1428 MHz), S-band (2856 MHz), and C-band (5712 MHz) accelerators. In the meantime, the temporal bunch length is compressed from 1 ns to 30 fs by three-stage bunch compressors (BC) in order to obtain the demanded peak current of 3 kA. The normalized emittance of the beam is approximately 1 mm mrad. The repetition rate of the accelerator is 60 Hz, synchronized to the AC power line frequency.

For a synchronization issue, the acceleration rf field

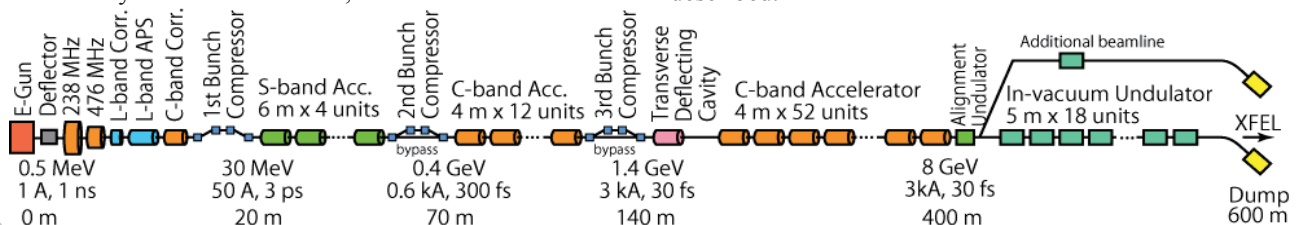


Figure 1: Schematic layout of the SACLA facility.

should be stable within  $1 \times 10^{-4}$  for the amplitude and within 100 fs for the time-equivalent value of a phase. In addition, there are about 70 acceleration rf units and 20 other rf electronics, such as beam monitor circuits and user experiment stations, along the 700 m facility. Therefore, the rf and timing signals should be distributed over 700 m. We use an optical rf and timing distribution system for this demand, because an optical fiber has much smaller attenuation than a coaxial cable. To control the rf field for each accelerator unit precisely, we developed a low-level rf (LLRF) control system. The LLRF system consists of IQ (In-phase and Quadrature) modulators and demodulators, VME D/A and A/D converter boards etc.

For beam diagnostics, high-resolution beam monitors are necessary for both spatial and temporal measurements. The beam position is demanded to be monitored with sub- $\mu\text{m}$  resolution, since an electron beam must be overlapped with x-rays within a few  $\mu\text{m}$  in the undulator section to generate SASE-FEL. The spatial resolution of a transverse beam profile image is also required with a few  $\mu\text{m}$  to see tiny electron beam of about a 10  $\mu\text{m}$  rms radius. For the temporal profile measurements, the required resolution is 10 fs level, because the bunch length is compressed up to 30 fs.

In this paper, we describe the design and performance of each component in the synchronization and beam diagnostic system. Finally, we discuss possible applications for an ERL.

## SYNCHRONIZATION SYSTEM

The synchronization system of SACLA [2] can be divided into an optical rf and timing distribution system and a LLRF system, as illustrated in Fig. 2. In the following subsections, the design and performance of these systems are described. In addition, we developed a special water-cooled enclosure and a low-noise DC power supply to reduce the temperature drift and power supply noise. The performances of these instruments are also described.

<sup>#</sup>maesaka@spring8.or.jp

### Optical RF and Timing Distribution System

A schematic block diagram of the optical rf and timing distribution system [2] is shown in Fig. 3. Low-noise rf signals of 5712 MHz and their sub-harmonics are generated by a low-noise master oscillator. Each signal is converted to a sinusoidally-modulated optical signal by an electrical-to-optical (E/O) converter consisting of a distributed feedback (DFB) laser diode and a LiNbO<sub>3</sub> Mach-Zehnder modulator. The wavelength of the carrier light is approximately 1550 nm. Trigger signals are also generated by a master trigger generator [3] and converted to a 5712 MHz phase shift keying (PSK) signal. The PSK signal is then converted to an optical signal.

These optical signals are combined into one optical fiber by wavelength-division multiplexing (WDM) technique. The combined signal is amplified by an erbium-doped fiber amplifier (EDFA) and distributed to accelerator components through phase-stabilized optical fibers (PSOF). The temperature coefficient of the PSOF is 2 ppm, which is much less than that of conventional optical fibers. At the receiver, the WDM optical signal is divided into individual wavelengths and converted to the electric rf and timing signals by fast photo-diodes in the optical-to-electrical (O/E) converter, respectively.

In addition, we are planning to install length-stabilized fiber links [4] in order to compensate for the path-length drift of the PSOFs. A frequency-stabilized laser is transmitted to a receiver as a length standard and reflected back to the transmitter with a Faraday rotator mirror. The fiber length is measured with a Michelson interferometer with sub-micron resolution. The length information is fed back to a variable delay line, such as a piezo-electric fiber stretcher. In this link, a 5712 MHz rf signal is also transmitted as a time reference. The phase drift of the signal transmitted in the PSOF is monitored at the receiver side by using an rf phase detector for 5712 MHz signals, and the PSOF length is controlled with the fiber stretcher. The length-stabilized link will be installed in 2012.

We measured the single-sideband (SSB) phase noise before and after the optical transmission in order to confirm whether the time jitter was sufficient or not. The result is plotted in Fig. 4. The time jitter after the transmission was calculated to be approximately 10 fs (rms) from the integration of the obtained phase noise spectrum.

We also tested the fiber length stabilization system by

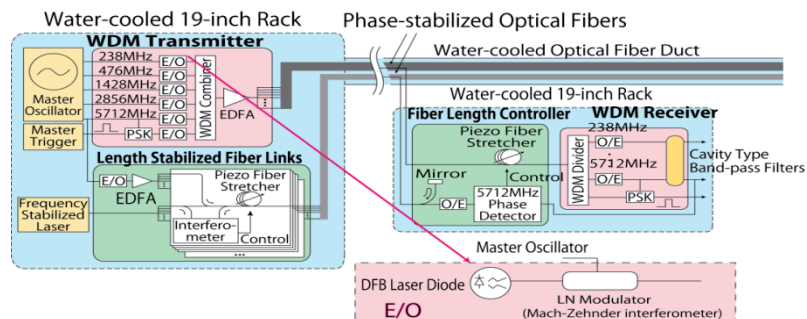


Figure 3: Block diagram of the optical rf and timing distribution system.

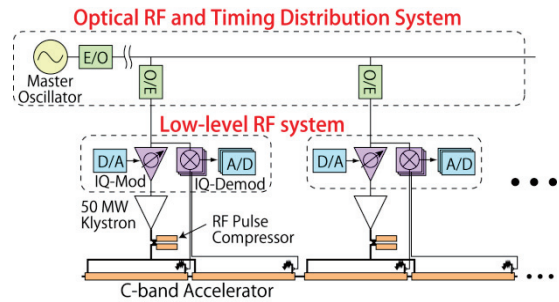


Figure 2: Schematic diagram of the synchronization system.

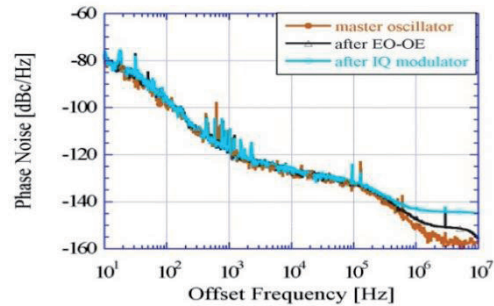


Figure 4: Phase noise spectra before and after the optical signal transmission. The carrier frequency is 5712 MHz. Brown, black and blue curves show the phase noise spectra of the master oscillator, after the E/O and O/E converters, and after the IQ modulator, respectively.

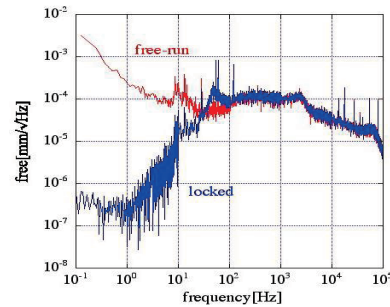


Figure 5: FFT spectra of the fiber length fluctuation from the fiber length stabilization experiment. The red line is the spectrum in the free-run case and the blue line is in the stabilized case.

using a 1 km long fiber along the SPring-8 storage ring. The spectra of the fiber length stability for a free-run case and a stabilized case are plotted in Fig. 5. The fiber length fluctuation of less than 100 Hz was significantly reduced. The fiber length drift was stabilized to be less than 1 μm.

### Low-level RF Control System

A schematic diagram of the LLRF control system for each C-band accelerator unit is shown in Fig. 6. A time-reference rf signal is provided from an O/E converter and an acceleration rf signal with appropriate phase and amplitude is generated with an IQ modulator. IQ baseband waveforms are generated with a VME 238MHz 14-bit D/A converter board [5]. The rf signal is amplified with a solid-state amplifier and a 50 MW klystron, and fed into accelerating structures. A tiny part ( $10^{-6}$ ) of the rf power around the accelerator cavity is picked up and detected with an IQ demodulator. The detected IQ baseband waveforms are recorded with a VME 238MHz 12-bit or 16-bit A/D converter board [5]. To reduce slow drifts of the acceleration rf phase, the detected signal is fed back to the D/A converter with PID (Proportional-Integral-Derivative) feedback control algorithm.

Figure 7 shows some waveforms of an acceleration rf field taken with the IQ demodulator for the C-band accelerator. For the stability issue, a trend graph of the phase of the 238 MHz sub-harmonic buncher cavity, which was taken with the IQ demodulator and the A/D converter, is plotted in Fig. 8. The rms value is 0.0067 degree for a 10-shot moving average data. This corresponds to 80 fs, which is sufficient for our requirement for SACLA.

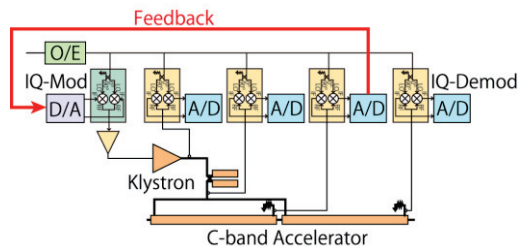


Figure 6: Schematic diagram of the LLRF system.

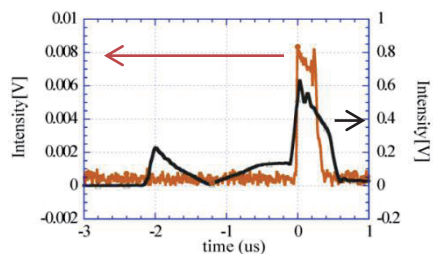


Figure 7: Rf amplitude waveforms detected by an IQ demodulator. The black curve shows an acceleration rf field of a C-band accelerator and brown one shows an beam-induced field when the klystron is off.

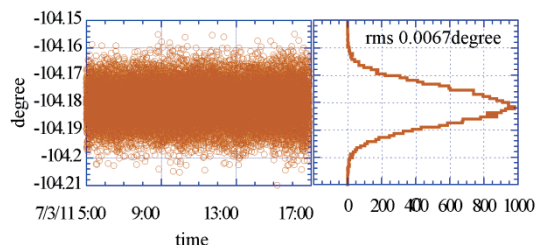


Figure 8: Trend graphs of the amplitude and phase of 238 MHz sub-harmonic buncher cavity. Each data point shows a 10-shot moving average.

### Water-cooled Enclosures and Low-noise DC Power Supply

To keep the temperatures of all the electric circuits and PSOFs, we developed a water-cooled 19-inch rack and a water-cooled fiber duct [6]. Figure 9 shows a schematic drawing and a photograph of the water-cooled 19-inch rack, and Figure 10 shows those of the water-cooled fiber duct. The water-cooled rack is equipped with a heat exchanger, which regulates the temperature of circulating air by using cooling water within a  $\pm 0.2$  K stability. The water-cooled duct consists of an inner steel duct having some water cooling channels and an outer steel duct. A thermal insulator is filled between the inner and outer ducts. PSOFs are installed in the inner ducts together with a thermal insulator.

The temperature stability of the water-cooled 19-inch rack is plotted in Fig. 11. The temperature inside the rack was kept within  $\pm 0.2$  K as expected, while the ambient temperature showed a drift of 0.5 K. The temperature stability of the water-cooled fiber duct was also confirmed to be the same level as the water-cooled 19-inch rack.

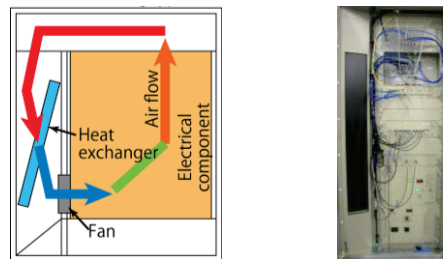


Figure 9: Cross-sectional top view of the water-cooled 19-inch rack (left) and a photograph of the rack (right).

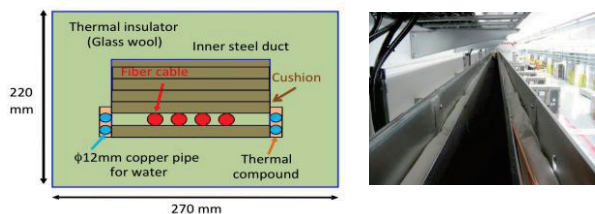


Figure 10: Schematic drawing of the water-cooled fiber duct (left) and a photograph of the duct (right).

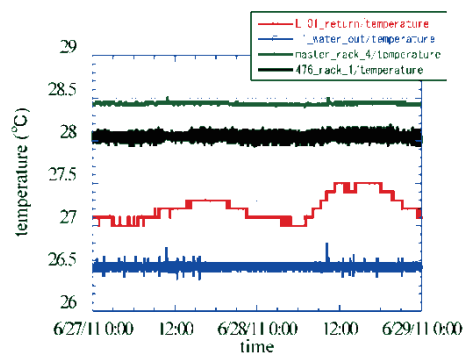


Figure 11: Temperature stability of a water-cooled 19-inch rack. Green and black lines indicate the temperature in the rack. Blue and red lines are the water temperature and the ambient temperature, respectively.

We also developed a low-noise DC power supply for the rf electronics and VME data acquisition boards. The three-phase AC power is rectified and the voltage is stabilized by a precise linear regulator. The noise floor of the output voltage was measured to be  $-150$  dBV/√Hz for 10–1000 Hz, except for the line frequency and its harmonics. Even for the line frequency, the amplitude was less than  $-100$  dBV. The voltage stability was confirmed to be less than 10 ppm pk-pk.

### BEAM DIAGNOSTIC INSTRUMENTS

We use following beam monitors in SACLA for precise beam diagnostics [7]: an rf cavity beam position monitor (RF-BPM), a beam profile monitor using OTR (Optical Transition Radiation) or YAG:Ce scintillation, a fast differential current transformer (CT), a C-band transverse rf deflecting cavity, a streak camera system, and a CSR (Coherent Synchrotron Radiation) monitor. In the following sub-sections, details of these monitors are described.

#### RF Cavity Beam Position Monitor

The RF-BPM cavity consists of two cylindrical cavity resonators, as shown in Fig. 12: a TM110 dipole resonator for the position detection and a TM010 monopole resonator for the phase reference and the bunch charge information. The resonant frequency is 4.76 GHz for both cavities. The signal from an RF-BPM is detected by an IQ demodulator.

We analyzed the position resolution of 20 RF-BPMs in the undulator section. The electron beam energy was 7 GeV and the bunch charge was 0.1 nC. The beam position at a given RF-BPM was estimated from the other 19 RF-BPMs and the position resolution was calculated from the rms of the difference between the measured value and the estimated one. Figure 13 shows a scatter plot of the measurement v.s. estimation. The measured position and estimated position were almost the same and the position resolution was calculated to be  $0.5 \mu\text{m}$  [8].

#### Beam Profile Monitor

To obtain a transverse beam profile, we use a fluorescent screen and an optical transition radiation (OTR) screen [9]. The screen attached to a pneumatic actuator in order to insert into the beam orbit remotely. The radiation from the screen is focused by a custom-made lens system to a CCD camera, as shown in Fig. 14. The optical resolution of the lens system was confirmed to be  $2 \mu\text{m}$  in case of the maximum magnification of  $\times 4$ .

The profile monitor works well for the bunch length longer than 100 fs. However, we encountered abnormal OTR radiation when the bunch length was less than 100 fs. This phenomenon is known as coherent OTR (C-OTR). Therefore, we changed the target from the OTR to the YAG:Ce in order to use scintillation light. Nevertheless, C-OTR was still observed from the YAG:Ce screen. We put an OTR mask in front of the lens, as illustrated in Fig. 15, since OTR is emitted in the forward direction. After that, an appropriate beam profile image was obtained, as shown in Fig. 16 [7].

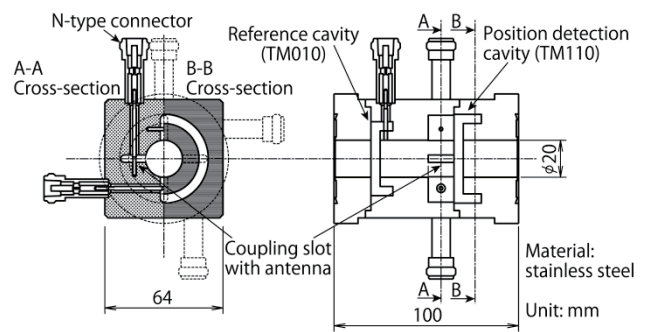


Figure 12: Drawing of the RF-BPM cavity.

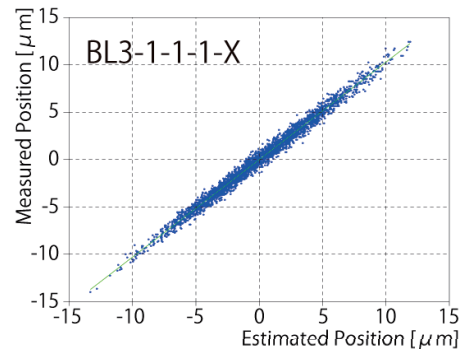


Figure 13: Scatter plot of the measured position of a BPM versus the estimated position from other BPMs.

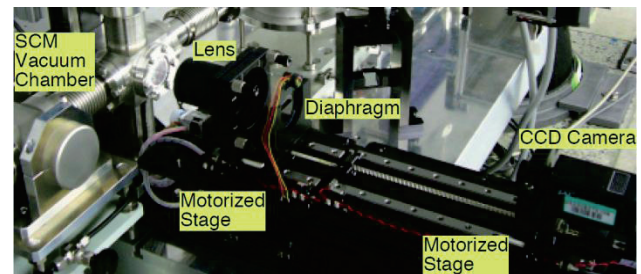


Figure 14: Photograph of the beam profile monitor.

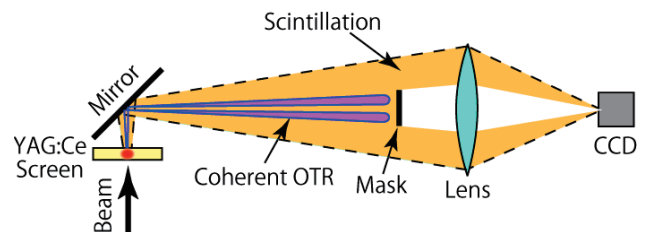


Figure 15: Setup of the profile monitor to mitigate C-OTR.

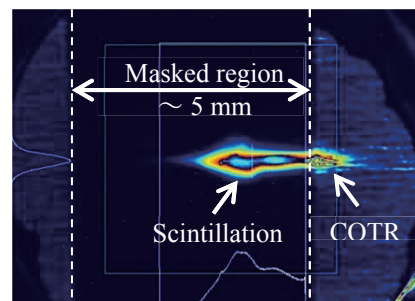


Figure 16: Beam profile image observed by the beam profile monitor with a YAG:Ce screen and an OTR mask.

### Fast Differential Current Transformer

We developed a high-speed differential CT [10], as shown in Fig. 17. This CT has four outputs: two positive and the others are negative. By subtracting a negative signal from a positive one, we can remove any common-mode noise. Since a single-turn pickup coil is used, the rise time of the output pulse is expected to be small. Raw signal waveforms from the differential CT are plotted in Fig. 18. The rise time was 0.2 ns. Therefore, this CT has a capability to measure the bunch length longer than about 0.5 ns.

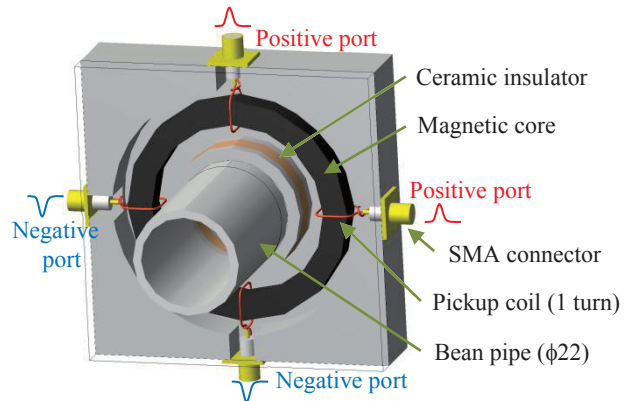


Figure 17: Schematic view of the differential CT.

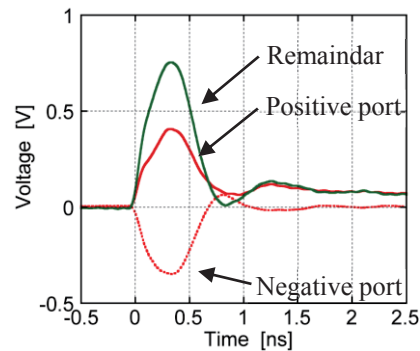


Figure 18: Waveforms of the differential CT.

### Transverse RF Deflector Cavity

We use a C-band transverse rf deflecting cavity (RFDEF) [11] to measure the temporal bunch structure of an electron beam. A schematic setup of the RFDEF system is shown in Fig. 19. An electron beam is swept by a transverse deflecting rf field and the temporal structure is converted to the transverse profile. The transverse profile is observed by a profile monitor with a spatial resolution of approximately 3μm.

Figure 20 shows a measured temporal bunch structure of a 1.4 GeV beam. The electron beam is vertically stretched by RFDEF. The temporal structure of a 100 fs long beam is appropriately obtained with approximately a 10 fs resolution.

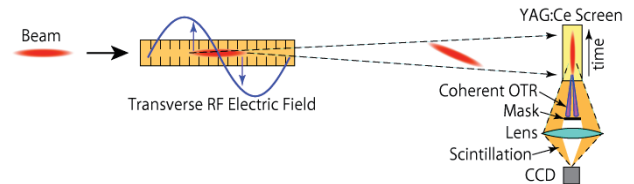


Figure 19: Schematic setup of the RFDEF system.

### Streak Camera

To measure a bunch length of longer than 300 fs, a streak camera system is also used. OTR light emitted by a stainless-steel foil is transmitted outside the accelerator tunnel and detected with a FESCA-200 [12] streak camera, which is located downstream of the BC3. Nevertheless, the bunch length after the BC1 or the BC2 can be also measured, since the BC2 and the BC3 can be bypassed.

Figure 21 shows an example of a measured bunch length after the BC2. The bunch length was 0.54 ps FWHM in this case. Thus, the streak camera system has a capability to measure the bunch length less than 1 ps.

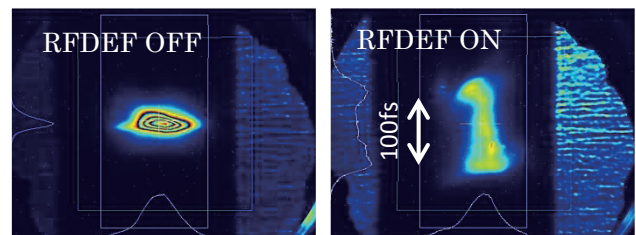


Figure 20: Beam profiles taken by the RFDEF system. The RFDEF is off in the left figure, and the RFDEF is on in the right one.

### Coherent Synchrotron Radiation Monitor

For a non-destructive bunch length monitor, a CSR monitor was developed [13]. A schematic view of the CSR monitor is illustrated in Fig. 22. CSR from the fourth dipole magnet of a bunch compressor chicane is reflected and extracted from the vacuum chamber. The CSR is then focused with a THz lens and detected with a pyro-electric detector.

Figure 23 shows a CSR intensity dependence on the bunch length. The bunch length was varied by the S-band accelerating rf phase upstream of BC2. In this data set, bunch lengths measured by the RFDEF system were 200 fs, 300 fs and 400 fs (FWHM) at -1, 0 and +1 degree, respectively. Here, the rf phase of 0 degree means the lasing condition of SACL A. Thus, the CSR monitor has sufficient sensitivity to the bunch length.

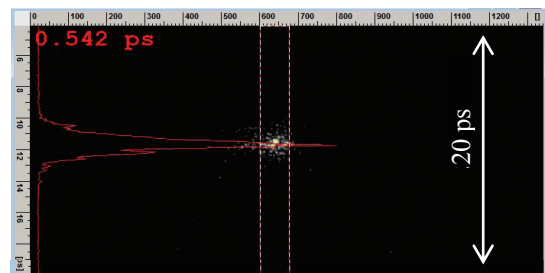


Figure 21: Example of a streak camera image. The temporal structure is stretched vertically. The full scale of the time range is 20 ps. The red line shows the projection of the image, which has the FWHM value of 0.54 ps.

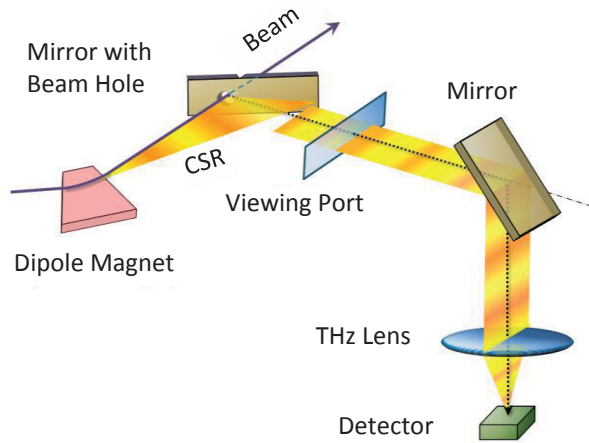
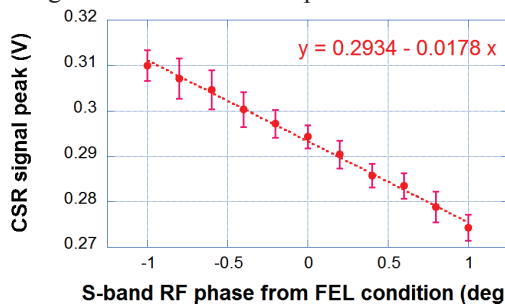


Figure 22: Schematic setup of the CSR monitor.



S-band RF phase from FEL condition (degree)

Figure 23: CSR intensity at BC2 as a function of the S-band acceleration rf phase. The origin of the horizontal axis is the phase at the XFEL lasing condition. Error bars represent the standard deviations of intensity fluctuations

### POSSIBLE APPLICATIONS TO ERL

In this section, we briefly discuss some possible applications to an ERL about our synchronization and beam diagnostic system.

For the synchronization issue, the optical system can be applied to ERL. In the ERL case, the WDM part can be removed, since all accelerator cavities have the same frequency of 1.3 GHz. On the other hand, the LLRF system cannot be used in the ERL machine without any modifications, because our LLRF system is intended for pulsed rf signals, while an ERL uses CW signal. Moreover, our LLRF system does not have an intra-pulse feedback capability, while an ERL needs a fast feedback system.

For the beam diagnostic instrument, most of our non-destructive monitors can be applied, if the repetition rate is less than 10 MHz. Since the repetition rate of the SACLA is 60 Hz, our instruments are not applicable to a 1.3 GHz operation mode of an ERL. For example, the RF-BPM cavity can be a large impedance source, when the repetition rate is more than 10 MHz. If any low-repetition bunches can be extracted from the ERL ring, all of our monitors can be used including destructive monitors.

### SUMMARY

We developed a synchronization system and a beam diagnostic system for the XFEL facility, SACLA. By using an optical rf and timing distribution system and IQ modulation/demodulation technique, acceleration rf phase and amplitude are precisely controlled. The time-equivalent value of a phase stability is less than 100 fs (rms). The optical system has capability to provide a timing signal to ERL. However, it is difficult to use our LLRF system to ERL without any modification.

For the beam diagnostics, we developed high-resolution monitors for both spatial and temporal measurements. The RF-BPM has sub- $\mu\text{m}$  resolution, and the beam profile monitor can measure a beam size of around 10  $\mu\text{m}$ . The temporal bunch structure can be measured for the bunch length from 30 fs to several picoseconds, by using a C-band rf deflector cavity, a streak camera and a CSR monitor. It is hard to use our beam monitors in an ERL ring with the repetition rate of 1.3 GHz. However, our monitors can be applied, if the repetition rate is reduced to 10 MHz or less.

### REFERENCES

- [1] H. Tanaka, *et al.*, "Status Report on the Commissioning of the Japanese XFEL at SPring-8", proceedings of IPAC'11 (2011).
- [2] H. Maesaka, *et al.*, "Recent Progress of the RF and Timing System of XFEL/SPring-8", proceedings of ICALEPCS'09 (2009).
- [3] N. Hosoda, *et al.*, "SCSS Prototype Accelerator Timing System", proceedings of APAC'07 (2007).
- [4] M. Musha *et al.*, Appl. Phys. **B** 82, 555–559 (2006).
- [5] T. Fukui *et al.*, "A Development of High-Speed A/D and D/A VME Boards for a Low Level RF System of SCSS", proceedings of ICALEPCS'05 (2005).
- [6] N. Hosoda, *et al.*, "Construction of a Timing and Low-level RF System for XFEL/SPring-8", proceedings of IPAC'10 (2010).
- [7] Y. Otake, *et al.*, "Commissioning and Performance of the Beam Monitor System for XFEL/SPring-8 'SACLA'", proceedings of IPAC'11 (2011).
- [8] H. Maesaka, *et al.*, "Performance of the RF Cavity BPM at XFEL/SPring-8 'SACLA'", proceedings of FEL'11 (2011).
- [9] K. Yanagida *et al.*, "Development of Screen Monitor with a Spatial Resolution of Ten Micro-meters for XFEL/SPring-8", Proc. of LINAC'08 (2008).
- [10] S. Matsubara, *et al.*, "Development of High-speed Differential Current Transformer Monitor", proceedings of IPAC'11 (2011).
- [11] H. Ego, *et al.*, "Transverse C-band Deflecting Structure for Longitudinal Phase Space Diagnostics in the XFEL/SPring-8 'SACLA'", proceedings of IPAC'11 (2011).
- [12] Hamamatsu Photonics K. K., <http://www.hamamatsu.com/>
- [13] C. Kondo, *et al.*, "CSR Bunch Length Monitor for XFEL/SPring-8-SACLA", proceedings of IPAC'11 (2011).

Copyright © 2013 CC-BY-3.0 and by the respective authors

## NLSL-II BEAM LOSS MONITOR SYSTEM \*

S. L. Kramer<sup>#</sup>, for the LCM Working Group  
Brookhaven National Lab., NLSL-II, Upton, NY 11973, U.S.A.

### Abstract

NLSL-II storage ring is shielded for full injected beam loss around injection point, with the remainder shielded for significantly lower losses. To insure these design levels aren't exceeded, a Loss Control and Monitoring system (LCM) was designed. The LCM will control and monitor beam losses in the injection region and monitor injection losses outside that region. In order to measure quantitative charge losses, development of new beam loss monitors using Cerenkov light produced by the electron component of the shower induced by beam particles penetrating the vacuum chamber. These Cerenkov beam loss monitors (CBLM) measure the light from electrons passing through ultra-pure fused silica rods placed close to the inner edge of the VC. These rods will give sufficient light signal to monitor beam losses from several particles lost per turn to a major fraction of the 500mA beam in one to a few turns, about a 9 decade dynamic range of signal. Design and measurements of the prototype CBLM system will be presented. Although designed for light sources, CBLMs will provide quantitative beam loss measurements for accelerators with continuous high energy electron beams, such as ERLs.

### NLSL-II DESIGN AND SPECIFICATIONS

The NLSL-II light source, which has started construction in FY2009, is a new 3<sup>rd</sup> generation light source that will replace the two operating 2<sup>nd</sup> generation light sources at BNL. It has been designed to provide major improvements in the existing beam properties from IR to hard X-rays, with leading edge electron beam properties.

The Storage Ring (SR) is a 30 cell DBA lattice with a super periodicity (SP) of 15, with alternating long (9.3m, LSS) and short (6.6m, SSS) straight sections. The ultra-low emittance ( $\leq 1\text{nm}$ ) is obtained not from breaking the achromatic condition for the lattice, but by using a novel approach of increasing the synchrotron radiation damping using damping wigglers, DW, (3-8 7m 1.8T wigglers) in the achromatic straights to reduce the lattice emittance in steps, in addition to the user undulators in the SSS's[1].

In order to maintain the high brightness for the users, the SR is designed for top-off operation with a minimum injection pulse frequency of one injection per minute, in order to maintain a  $\pm 1\%$  beam current stability. This requires a full energy booster capable of high injection efficiency.

The SR radiation shield consists of 2-cells (injection and the downstream cell) of heavy concrete shielding capable of shielding the experimental floor from the loss of the full top-off injection beam current. The remainder

of the ring will be shielded for a beam loss rate of up to  $1/12^{\text{th}}$  of the top-off injection rate at any one location in the ring. As a consequence of this shielding decision a Loss Control and Monitoring system (LCM)<sup>1</sup> has been specified that will control and monitor local beam power losses in all of the accelerators systems to less than the shielding design levels. The LCM will consist of components that will:

1. monitor and limit the beam power losses from the accelerators and transport lines
2. control a major part of beam losses in the SR to the heavily shielded injection region and
3. monitor the SR beam losses in the injection region and account for losses in the remainder of the SR.

### LCM SPECIFICATIONS [1]

The LCM specifications for the accelerators and beam transport lines are based on an analysis of the severity of the potential radiation exposure for a particular beam loss scenario which exceeds the shielding design beam loss specification. For the injection systems, the severity of the full beam power lost at any point could be high enough that engineering solutions maybe required. For example, if the full beam power of the booster were lost at any point other than the extraction region, the area above the booster shielding berm would become a high radiation area. The engineering solution is to fence off this area and post a remote area radiation monitor at this location.

The LCM system will monitor the beam current loss (difference between two consecutive current monitors) times the energy of the system transporting that beam (i.e booster dipole or transport dipole field) to determine the beam power lost. If the lost beam power exceeds the shielding design level at that location, then alarms will be issued to operators and the accelerator control system that will require action to reduce the loss level. If corrective action isn't taken within a specified time period, that insures potential radiation exposures don't exceed administrative control levels (ACL), then the LCM could prevent injection from continuing. The decisions made by the LCM are not as critical, as the Personal Protective System (PPS) and therefore will be made in a non-safety rated micro-computer that will automatically stop injection if the system fails.

This type of decision will be made for each stage of the injection accelerators and alarms sent when ACL are exceeded or are being approached. The analysis of full injection beam losses in the SR doesn't result in as high a potential radiation level as in the injector, but will have a risk of greater exposure due to the greater occupancy of the experimental floor. Therefore, in the SR the LCM

\* Work supported by U.S. DOE, Contract No. DE-AC02-98CH10886  
# [skramer@bnl.gov](mailto:skramer@bnl.gov)

1 LCM System was previously called Beam Containment System.

must insure local losses don't exceed the ACL, which as a result of the change in shielding thickness around the SR, will depend on the location of the beam loss. The LCM system for the SR will consist of beam loss control using scrapers and verification of the local beam loss using Cerenkov Beam Loss Monitors (CBLM), both in the heavily shielded injection region. The remaining unaccounted for beam loss will be attributed to losses in the remainder of the SR where the shielding isn't as thick. Each of the two regions will have different ACL values for beam loss rates and will be monitored and alarmed if exceeded. These loss rates can be exceeded during non-operational periods (i.e. commissioning and machine studies) or during operations when the SR is under administrative control.

### SR BEAM LOSS CONTROL

The LCM is planned to capture a major portion of the beam losses in the heavily shielded injection region using beam scrapers. It is planned to provide five scraper locations, each with a pair of opposing blades to define the beam aperture channel for the circulating beam at that location. The locations of the scrapers are shown in Figure 1 and were chosen to be near the location of maximum amplitude of the beam particles: two vertical scrapers (Vscraper1 & 2) are at large  $\beta_y$  locations with  $\sim 70^\circ$  phase shift between them, one horizontal scraper (HscraperX) is at a zero dispersion but high  $\beta_x$  location and the two horizontal (Hscraper1 & 2) are at high dispersion locations with a  $90^\circ$  horizontal phase shift between them.

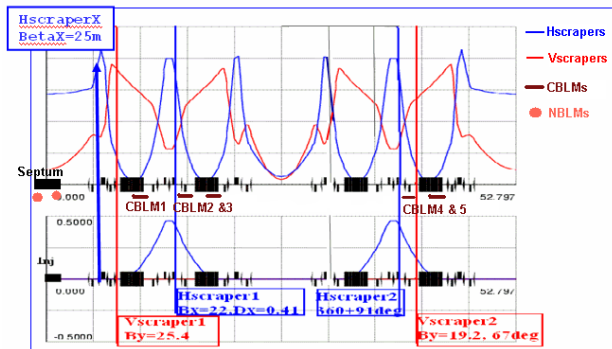


Figure 1: The SR Injection period showing Horizontal (blue) and Vertical (red) scraper locations and Twiss parameters. Also shown are the locations of the CBLM used to monitors the beam losses with or without the scrapers.

The later two, Hscraper1 and Hscraper2 are the only ones planned for use at high current operations, and only the inner blades are considered critical. They will be inserted to  $\Delta X \sim -23\text{mm}$ , which will set a closed orbit momentum aperture of  $\delta \geq -5.2\%$ . This will intercept low momentum particles from beam dumps, Bremsstrahlung, instabilities and the low energy particles from Touschek scattered electrons. The high energy Touschek scattered electrons, if they survive half a synchrotron period will

decelerated by the RF ( $\sim 60$  turns) to lower energies and intercepted at these inner blades.

The scrapers are designed to be only 10mm ( $0.7 X_{\text{rad}}$ ) thick of copper, which will absorb only enough beam energy to insure the subsequent dipole will bend these electrons out of the vacuum chamber in the injection region. For electrons with greater than 20% of their energy lost in the scraper (86% of electrons hitting scraper will loss  $> 20\%$  of their energy) they will be bent enough by the next dipole to hit the inner vacuum chamber wall (VCW) in or ahead of that dipole magnet. The 13.5% of the incident electrons that penetrate, will be lost on the VCW downstream of the dipole. The 0.5% that have  $< 1\%$  energy loss, will hit the second scraper where they undergo additional energy loss and hit the VCW. The surviving intercepted electrons that might circulate is  $< 10^{-5}$ . The thin scraper will produce lower levels of transverse radiation and neutrons off the scraper, requiring less local shielding. The beam that is dumped in the dipole will see considerable self-shielding by the dipole yoke itself, reducing the local scraper shielding[3].

The details on the beam loss control function of the scrapers were presented in Ref. [4]. The scraped beam that hits the VCW will be the source of the electron signal for the CBLM, also located in this region.

### SR BEAM LOSS MONITORING

The use of beam scrapers to intercept beam losses in the injection region was deemed insufficient and it was suggested this beam losses in the injection region needed to be verified. The beam charge loss rate will be determined from DC beam current measurements ( $I_o$ ), plus any injected charge ( $Q_{inj}$ ), during injection periods that wasn't stored will be given by:

$$Q'_{loss} = \{Q_{inj} - [I_o(t + dt) - I_o(t)] * T_o\} / dt \quad (1)$$

where  $T_o$  is the SR revolution period.

If the amount of charge that hits the scraper can be measured, then the remaining unaccounted charge loss  $Q'_{sd}$ , would be attributed to the lower shielded region of the SR. If this loss rate was below the design limit, then it doesn't matter where it is lost. Even if this limit is exceeded for short time periods, the average over administrative time periods could be maintained below this limit, by reducing the injection rate, as a last resort.

Several methods have been considered for measuring this charge hitting the scraper directly. Beam loss monitor studies from the NSLS [5] showed radiation measurements outside the magnets would not yield quantitative charge loss rates. The approach that appears most promising is to measure the electrons shower after the dipole magnet bends the electrons into the VCW. The high energy charged particles ( $e^-$  and  $e^+$ ) from this shower will have relatively small angular and spatial spread and a Cerenkov radiator placed close to the vacuum chamber (inside the magnet yokes) will provide a signal proportional to the initial charge loss, with a large signal variance due to variation in charged particles production in the shower. The NSLS-II vacuum chamber uses a

NEG pumping ante-chamber toward the outside of ring. This leaves a gap in the magnets toward the inside of the ring where a fused silica Cerenkov radiator rod (RR) can be placed in between the coils of quadrupole and sextupole magnets as shown Figure 2. A similar rod can be placed in the gap of the dipole magnet to measure charged particles that hit the scraper at that location. If these rods are placed downstream of a thin scraper, then the scraper aperture can be used to control the beam loss rate at that location and the signal output from a CBLM could be calibrated relative to the DCCT measured charge loss.

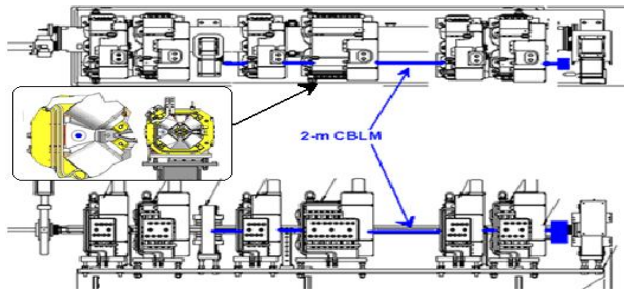


Figure 2: Two meter long CBLM placed inside quadrupole and sextupole magnets on a SR girder.

### SIGNAL GENERATION IN CBLM

If the beam electrons passed through the RR (fused silica with refractive index  $n=1.46$ ) each would produce about 900 photons per centimetre of path length with a uniform energy distribution from 1.55 eV (800nm) to 6.2 eV (200nm). With this amount of light produced for a 10mm diameter RR, a photodiode (PD) could be used as the detector rather than a photomultiplier tube (PMT). The advantage of a PD over a PMT is: higher dynamic range, greater linearity over that range, lower cost and no need of high voltage. The signal from a PD was estimated by convolving the PD sensitivity with the photon flux spectrum for Cerenkov radiation versus wavelength ( $N \sim \lambda^{-2}$ ) as shown in Figure 3. The resulting current for one electron lost per revolution of NSLS-II passing orthogonally through a 10mm RR was calculated to be  $\sim 0.02\text{nA}$ , compared to the 0.1nA dark current for the PD. However the number of electrons generated in the shower that occurs when the electron hits the vacuum chamber needs to be estimated, which could enhance this signal.

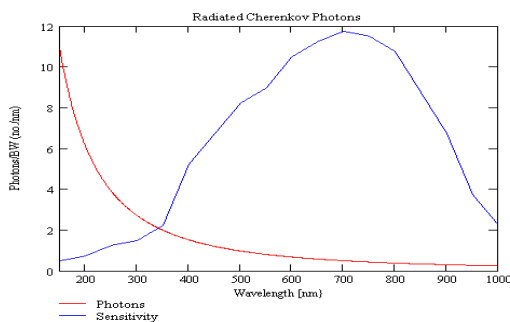


Figure 3: The Cerenkov photon flux spectrum (red curve) versus wavelength and the PD sensitivity (blue).

In order to simulate the signal produced in the CBLM RR, the electron shower was generated for beam hitting the 25mm thick inner vacuum chamber wall (VCW) using the Shower [5] interface to the EGS4 program [6]. The glancing angle of the electrons to the VCW was varied from  $1^\circ$  to  $10^\circ$  and the parameters of the  $e^-$  and  $e^+$  particles exiting the inner wall with energy  $>10\text{MeV}$  (Cerenkov energy critical energy is  $>0.7\text{MeV}$  but the magnitude of light emission and the penetration in fused silica is small below 10 MeV) were computed at the position of the RR. For incident angle,  $\theta = 3^\circ$ , the vertical position of the particles at the RR are shown in Figure 4. A 10mm diameter RR will intercept  $>30\%$  of the electrons and will reduce the sensitivity of signal variations to the vertical position and angle of the initial electron, as compared to a smaller diameter RR (e.g. a  $400\mu\text{m}$  fiber optic cable). For the  $e^-$  particles that pass through this RR ( $|y| \leq 5\text{mm}$ ) their longitudinal position and path length in the RR are computed and shown in Figure 5. For each beam particle incident on the VCW at  $3^\circ$ :  $1.66 \pm 0.13 e^-$  pass through the RR with an average path length of  $33 \pm 53\text{mm}$  and  $0.46 \pm 0.06 e^+$  with path length of  $17 \pm 4.7\text{mm}$ . This increase in number of charged particles times the increase of the photons from the increased path length of the charged particles in the RR gives a signal enhancement factor of  $6.3 \pm 1.5$  times an electron incident on the RR at  $90^\circ$ . This increase is over 11X at an angle of  $7^\circ$  as shown in Figure 6, allowing the signal to noise to exceed unity for single electron losses per turn in the CBLM with the PD module.

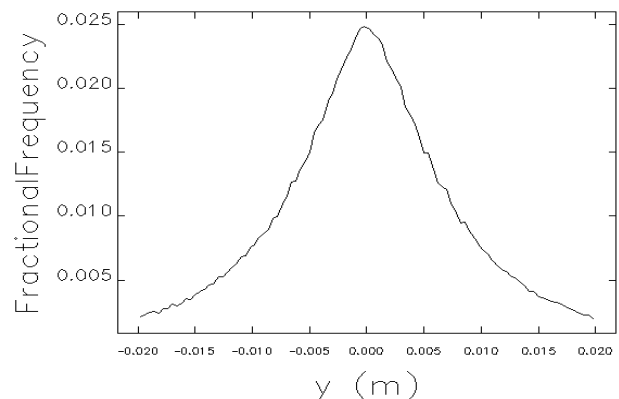


Figure 4: The vertical position of shower electrons at the RR generated in the 25mm Al VCW for a 3GeV  $e^-$  beam incident at  $3^\circ$  to the wall.

The electrons from the shower have a large spread in longitudinal position, requiring a RR that is at least 1meter long in order to capture a large part of the beam loss signal. These optical quality rods are free drawn and have a natural polished barrel that will propagate the light generated by the electrons to the PD by total internal reflection (TIR). Drawing a rod with 10mm OD longer than 1meter isn't easy, however a 25mm OD rod could be up to 2meters long [7]. NSLS-II will use 29.5mm OD rods, 1.2m long which was available from existing stock.

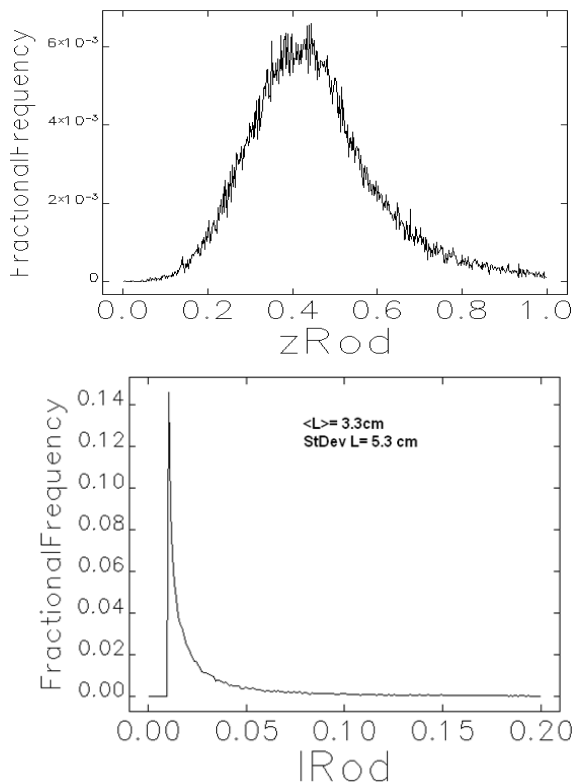


Figure 5: The longitudinal distribution of electrons with > 10 MeV energy that penetrate the VC wall and pass through the RR is shown (upper) and their path length in the 10mm RR is shown (lower).

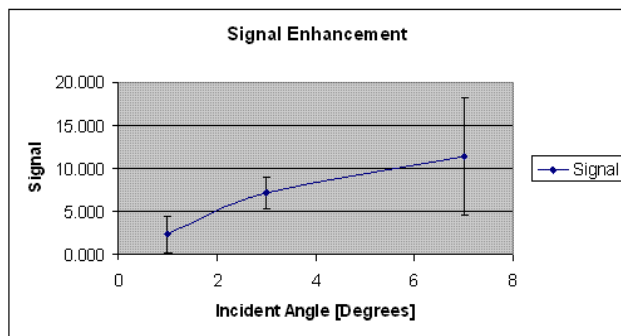


Figure 6: The signal enhancement from the electron shower in the VCW versus the incident angle of the electron.

### TESTING OF PROTOTYPE CBLM

A prototype CBLM was made using 10mm Suprasil 2B rods available from existing stock [7]. A standard Hamamatsu PD module [8] was used from to detect the light signals from this RR. The CBLM was installed in the NSLS X-ray ring and the local beam loss was controlled using a horizontal scraper near the peak dispersion point as in the NSLS-II proposal. Figure 7 shows the CBLM output voltage versus the scraper controlled local loss rate. The signal is linear over 5-

decades of dynamic range with a minimum resolution of 0.3fC/s DC loss rate. The high gain of this unit ( $10^9$  V/A and low bandwidth of 10 Hz) make this unit saturate at a rate of 60pC/sec. The lower gain setting of this PD module has a 1 KHz bandwidth has a dynamic range of 0.1 pC/s to 10 nC/s. The beam loss signal during injection had a peak loss rate that saturated the signal output but the DC coupled PD module allowed integral values during the pulse to still yield the total beam charge lost, but not the peak loss rate nor the pulse shape of the loss. The injection beam loss on the CBLM is shown in Figure 8 for the lower gain PD module with a 1 KHz BW. The integral under the injection peak showed a beam charge loss of about 85 pC or 5% of the injection current, over a 15ms period. At higher stored current a second loss signal appears about 22 ms after the injection pulse was captured, that wasn't seen at lower stored currents.

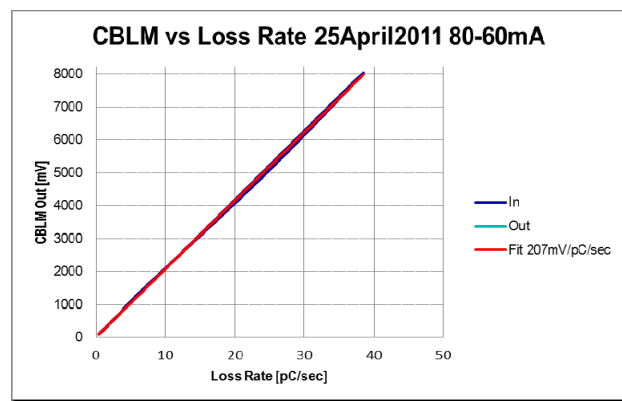


Figure 7: High gain PD module output of the CBLM versus calibrated loss rate in the X-ray ring.

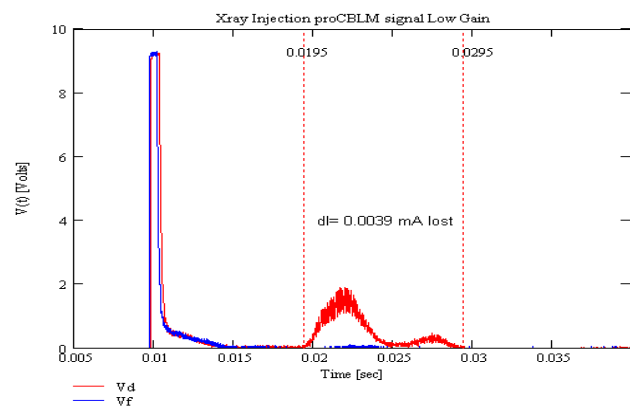


Figure 8: The injection beam loss signal from the prototype CBLM for a lower gain PD, with a 1KHz BW.

A custom PD module was obtained with a 64 KHz BW and significantly lower gain. This PD module will allow the injection peak loss rate to be measured on a turn by turn basis for NSLS-II, as well as for beam dump intensities without saturation of the peak signal, as shown in Figure 9. However the low level resolution for DC beam loss rate for this PD gain is  $\sim 80$ pC/s.

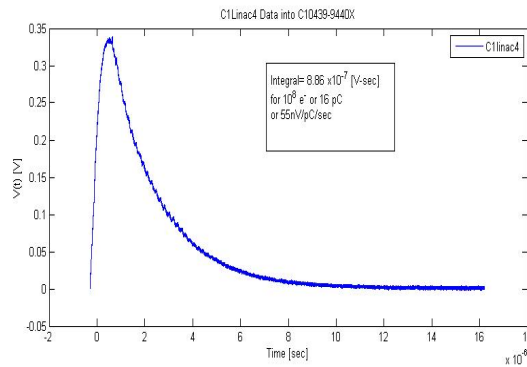


Figure 9: The CBLM beam loss signal of the 64 KHz PD module to 2nsec electron beam pulse with  $\sim 16$  pC.

## HIGH DYNAMIC RANGE CBLM

NSLS-II is developing a high dynamic range detector module that will provide the high peak intensity beam loss capabilities of the high BW low gain detector shown in Figure 9, with the low intensity beam loss of the high gain detector shown in Figure 7. This is possible with a logarithmic output amplifier using the existing PD (an 8-decade log amplifier is being tested and a 10-decade is being considered), but the large area PDs will always have low BW output. An alternative approach being pursued is to introduce a dual detector using a PMT to use the high gain and high BW of the PMT for the low intensity range using count rate to extend to the lowest beam loss rates and average current when the pulses start to pile-up but before the PMT starts to develop a nonlinear response. The two detectors will be cross calibrated in the overlap region using the installed scrapers.

Also the NSLS-II design will include a light output coupler (light pipe) to propagate the light away from the plane of radiation from the lost beam to a location under the magnet girder where the PD module will be placed. This will lower the radiation level at the PD module and reduce the amount of shielding required around the detector box. This will simplify installation and repair access to the detectors since only the RR and its light shield need to be installed prior to the magnets in the tunnel.

## CONCLUSIONS

A Cerenkov signal beam loss monitor will be used to quantify the beam charge losses in the heavily shielded injection region and used to verify that the majority of the beam losses occur in that region as controlled by the inserted beam scrapers. A prototype CBLM was built and tested in the NSLS X-ray ring which demonstrated over 8-decades of dynamic range with a switched gain photodiode system. The large diameter radiator rods yield high signal output that will verify the beam losses over an 8-10 decades of dynamic range. However, to extend the

range to the lowest loss rate (useful for diagnostics of the storage ring beam dynamics: diffusion and resonant structures) a dual detector system is being proposed.

## REFERENCES

- [1] S. Ozaki, et al., proceedings PAC07, p. 77(2007).
- [2] BCS has recently been renamed Loss Control and Monitoring system to better describe its function.
- [3] P.K. Job, et al., proceedings RADSynch09, p. (2009).
- [4] S.L. Kramer et. al, proceedings PAC11, p. (2011).
- [5] L. Emery, "User Guide to Shower...", ANL/APS (2003).
- [6] W. R. Nelson, et. al., "The EGS4 Code System," SLAC 265, SLAC (1985).
- [7] Heraeus Quartz America, Buford, GA 30518.
- [8] Hamatsu PD module C10439-03 with dual gain and a custom version with 64 KHz BW were used.

# BRIEF REVIEW OF THE APPROACHES TO ELUCIDATE THE MECHANISM OF THE RADIATION-INDUCED DEMAGNETIZATION

T. Bizen<sup>#</sup>, JASRI/SPring-8, Hyogo, Japan

## Abstract

Permanent magnets decrease their magnetic field under severe radiation environment. This radiation damage, radiation-induced demagnetization, is a great concern especially for the devices that requires very precise uniform magnetic field such as undulators. The evaluation of this field degradation is difficult because the mechanism of the radiation-induced demagnetization is not clear. Several approaches to clarify this mechanism have been made. For example, (1) the approach to examine the relations between the field degradation and the environmental factors like magnet shape, temperature and so on, (2) the approach to examine the changes of the microstructures and the properties of the magnet after irradiation, (3) the approach to compare and examine the experiments of the demagnetization and the computer simulations of the radiation. This paper reviews and summarizes these approaches and models briefly. The new point of view to consider the mechanism is presented as well.

## INTRODUCTION

The magnetic field intensity of the permanent magnet decreases when the magnets are used in a strong radiation environment. This radiation damage is called radiation-induced demagnetization. The degradation of the magnetic field is a big problem for undulators and other devices with magnet that requires precise magnetic field. The changes of the magnetic field in the undulators were observed in the storage ring in APS[1]. For this reason, many studies have been done so far. In this paper, I review and summarize the typical studies and propose the new point of view to consider the mechanism of the radiation-induced demagnetization.

## APPROACHES TO CLARIFY THE MECHANISM

Several approaches to clarify the mechanism of the radiation-induced demagnetization have been made. For example, (1) the approach to examine the relations between the field degradation and the environmental factors like magnet shape, temperature and so on, (2) the approach to examine the changes of the properties and the microstructures of the magnet after irradiation, (3) the approach to compare and examine the experiments of the demagnetization and the computer simulations of the radiation.

### *Environmental Factors*

The radiation-induced demagnetization shows the dependencies of the following environmental factors; (a)

material, chemical component, microstructure and manufacture, (b) coercivity, (c) temperature, (d) permeance coefficient that relate to magnet shape, outer magnetic field, inflection point (shape of B-H curve).

The relation of these factors looks uncertain, but these factors are similar to the factors that influence the demagnetization originated from the reversal magnetization. Especially, (b), (c), (d) are related to the coercivity decrease caused by the internal magnetic field that is described by permeance coefficient.

### *Properties and Microstructures after Irradiation*

Several researchers have tried to observe the changes in the irradiated magnets. Cost[2], Kähkönen[3], Okuda[4], Ito[5], Chen[6], Klaffky[7], and Qiu[8] examined the magnetic properties change. The damaged magnets by irradiation were remagnetized and compared the magnetic properties before irradiation. Chen observed that the recovery intensity of the remanence changed depending on the flux of a 10 MeV neutron. Qiu observed the degradation of the remanence by a 2.5 GeV electron irradiation. However, others found no changes in the remanence. Cost observed the 20 % increase of the coercivity by fast neutron irradiation. Klaffky performed a thermal neutron irradiation, and Qiu performed a 2.5 GeV electron irradiation. Though both found no changes in coercivity.

Talvite[9] and Gao[10] could not observe any microstructural changes in the magnets after irradiation by using the positron annihilation measurement or the X-ray diffraction. Yang[11, 12] found some atomic local changes by using the XAS, Mössbauer spectrometry and XAFS.

These results indicate that the radiation-induced demagnetization can occur without clear changes of the magnetic properties and the structures. The change is extremely local even if existing. This implies that the cause of the radiation-induced demagnetization in early stage should be the magnetization reversal.

### *Experiments and Computer Simulation*

Qiu, Asano and Leitner calculated the particle transport and interactions with matter using Monte Carlo simulation FLUKA, and compared the experimental results of the radiation-induced demagnetization.

Qiu[8] calculated the absorbed dose and the 1 MeV equivalent neutron fluence. "1 MeV equivalent neutron fluence, is widely used to characterize the displacement damage of the electronic devices in which the main material is Si when they are irradiated by neutrons." Qiu analysed the demagnetization caused by a 2.5 GeV electron irradiation, and proposed the fitted formula composed of two terms, the dose and the 1 MeV

<sup>#</sup>bizen@spring8.or.jp

equivalent neutron fluence. This formula requires different coefficient of the term to the different target material.

Asano[13] calculated the star densities owing to neutrons and photons. A star was defined by a hadronic inelastic interaction (spallation reaction) at energy higher than the threshold and excludes the spallation due to annihilating particles. In his calculation, the elastic scattering is included as well. He concluded, the “low-energy photoneutrons and bremsstrahlung photons are not involved in the demagnetization process, and suggest that the star density owing to the photoneutrons is strongly correlated with the demagnetization process.”

Leitner[14] indicated that “the demagnetization grows significantly with the total dose, but it increases even faster with the non-electromagnetic dose,” so the “neutrons are mostly identified as the cause of magnetization loss.” He also presumed “more noxious impact of higher energy neutrons.”

## BASIC MODEL OF MAGNETIZATION REVERSAL

The basic process of the magnetization reversal in the nucleation-type magnet as represented by  $\text{Nd}_2\text{Fe}_{14}\text{B}$  is following:

1. Heat and magnetic field decrease the coercivity.
2. Inverse magnetic moment domain nucleates where the anisotropy barrier is the lowest, such as near the grain boundary.
3. Domain wall expands in the grain immediately.

## BRIEF REVIEW AND SUMMARIZE THE PAST MODELS

Typical models of the radiation-induced demagnetization that have been proposed so far are reviewed and summarized briefly in this chapter. Blackmore[15] pointed out the similarity between a radiation damage and “a thermal heating of the sample at elevated temperature.” Cost[2] suggested that the high temperature generates the nucleus. “Collision cascade has a higher probability of nucleating a reverse domain when the temperature is closer to the Curie temperature.”

### *Brown's Model*

Brown[16] is unique for focusing on the magnetic interaction, though other researchers paid attention to the high temperature. He stated, “The decay of magnetic remanence during neutron irradiation is presumably caused by a combination of nucleation of reverse magnetic domains and depinning of domain walls, leading to domain wall motion and demagnetization.” He assumed that the “magnetic interaction of the neutron's magnetic moment with the magnetization of the material” makes a “magnetic excitation in the magnetization of a grain, thereby nucleating a reverse domain, or an excitation at a magnetic domain wall pinning site causing depinning of the domain wall, which is then free to move.” He also proposed the mechanism that the

“inelastic collisions with the atoms, causing local disruption of the crystal structure and its magnetic anisotropy” “create additional pinning sites, which is seen as increased coercivity in sintered Nd-Fe-B magnets at very high doses.”

### *Kähkönen's Model*

The process of the Kähkönen's model[3] is the following:

1. Part of the energy of the incoming particle is transferred to the primary knock-on atom.
2. The energy is then diffused into the lattice raising the temperature of a spherical region.
3. If the temperature rises above the Curie temperature and if this sphere is large enough the demagnetizing field can turn the spins and nucleation of a new domain occurs.
4. The domain immediately grows to the size of the grain.

### *Zeller's Model*

Zeller[17] pointed out that the loss of the coercivity is the reason of the demagnetization: “The sensitivity of NdFeB permanent magnet materials to radiation induced demagnetization is shown to be the result of loss of coercivity. This allows the magnet to demagnetize at locations which are subjected to the largest external and internal demagnetization fields.”

### *Makita's Model*

Makita[18] made clearer explanation of the origin of nucleation by focusing on the “decrease of the magnetic anisotropy” in place of the “loss of the coercivity”. This is because the magnetic anisotropy is the origin of the coercivity. He made the experiments of using the different coercivity magnets with same Curie temperature and concluded that nucleation occurs below the Curie temperature: “Since all of the magnets have the same Curie temperature, the difference in the demagnetization rate can be attributed to the probability of nucleation of a reverse domain in a locally heated region located around a knock-on atom, which is analogous to the thermal demagnetization of the magnets that usually starts below their Curie points.”

### *Gao's Model*

Gao[19] declared “As an external energy source,  $\gamma$ -ray irradiation will decrease the ordering of magnetic moments by disturbing the electron spin of Fe and Co atoms in the ferromagnetic phase.” and “The Curie temperature should be taken into account in high-energy particle irradiation conditions, but for  $\gamma$ -ray irradiation, coercivity mechanism is the dominant factor.”

### *Bizen's Diagram*

I propose the diagram of the process of the radiation-induced demagnetization shown in Fig. 1. If the energy from the particles supplied to the magnetic phase is sufficient, the magnetic anisotropy decreases and the nucleation occurs. There are two points to consider. The

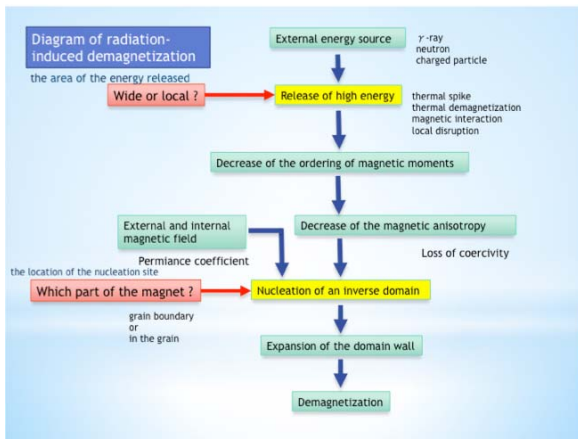


Figure 1: Diagram of the process of the radiation-induced demagnetization.

first is the area of the energy released from the particles. The second is the location of the nucleation site. From these points of view, two mechanisms were proposed [20]. These mechanisms are explained in the next chapter.

## TWO POINTS OF VIEW TO CONSIDER THE MECHANISM

### Wide Unstable Region (Magnetic Moment Instability)

Low energy radiation particles as  $\gamma$  ray, electron, and neutron transfer their energy in long range to the magnet. They act as an external energy sources like heat or magnetic field that make magnetic moment unstable in wide region. Therefore similar process of the magnetization reversal caused by heat and field would occur also in radiation (Fig. 2). The process is following:

1. Magnetic moment instability decreases the magnetic

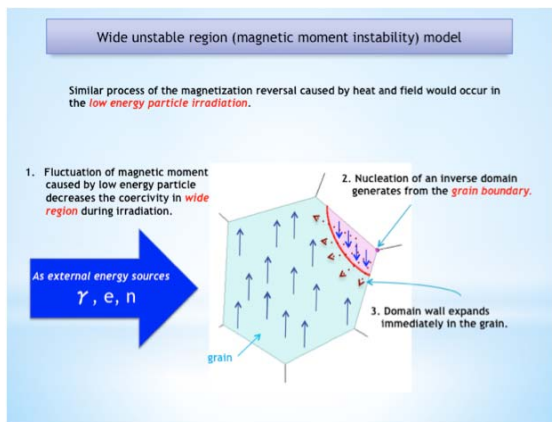


Figure 2: Wide unstable region model. Energy of  $\gamma$ ,  $e$  and  $n$  is transferred in long range to the magnet atoms as ionization and excitation. This causes the instability of the magnetic spin in the region of over the grain size. Similar process of the magnetization reversal caused by heat and field occurs by radiation.

1. anisotropy, or coercivity in wide region.
2. Inverse magnetic moment domain nucleates at the grain boundary, where the anisotropy barrier is the lowest.
3. Domain wall expands immediately in the grain.

This radiation-induced demagnetization caused by the “wide unstable region (magnetic moment instability)” mechanism is similar to the magnetization reversal caused by the magnetic moment instability originated from thermal energy. For this similarity, the engineering technique for stabilization against high temperature is effective to the radiation damage as well. The method of this stabilization technique is a partial demagnetization of the magnet by heat or magnetic field. Figure 3 shows the improvement of the radiation resistance by this stabilization[21, 22].

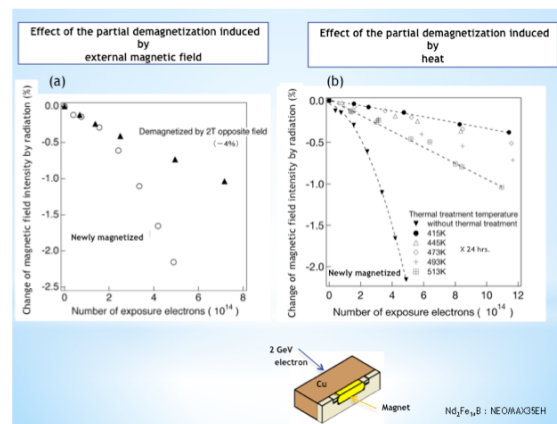


Figure 3: The effect of the engineering technique for stabilization against radiation was tested. The magnet is put behind the copper block and is irradiated with a 2 GeV electron. (a): The effect of the partial demagnetization induced by external magnetic field. The sample of partially demagnetized by magnetic field shows less demagnetization. (b): The effect of the partial demagnetization induced by heat. Black triangle is newly magnetized magnet. The others are partially demagnetized by different temperature. The samples of partially demagnetized by heat show less demagnetization.

Both different engineering stabilizing techniques are effective to the radiation.

### Local Hot Spot (Quasi-thermal Spike)

When a high-energy electron interacts with a material, high-energy photon neutrons are generated. High-energy photon neutron collides with an atom of the magnet and kicks out from the lattice. The energy of the knock-on atom transfers to the magnet atom by the process similar to the thermal spike. Thermal spike generates very high temperature over melting point instantaneously in a very small region. However, as Makita stated, demagnetization can occur below the Curie temperature of much lower

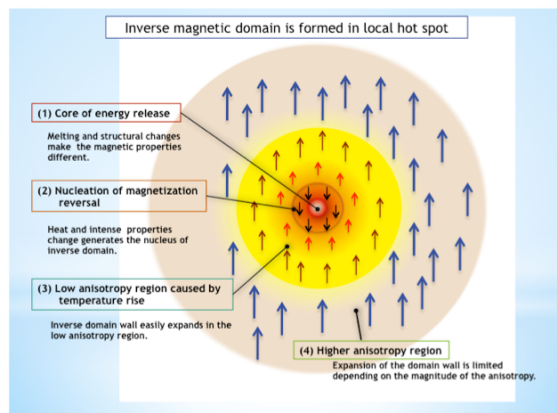


Figure 4: High-energy release point produced by the quasi-thermal-spike is made anywhere in the magnet independently of the anisotropy. This instantaneous large energy transfer generates the melted core or the structural change. The intense magnetic change in the core causes the instability of the magnetic spin around the core and produces the nucleus of inverse magnetization. Low coercivity region is generated around the core as well. The inverse domain wall of the nuclei easily expands in this region, but this expansion is limited when it enters into the high coercivity region.

than the thermal spike temperature. Therefore, the term of "quasi-thermal-spike" is used here instead of the "thermal spike". Quasi-thermal spike generates hot spots everywhere, such as near the grain boundary where the anisotropy barrier is low, and in the grain where the anisotropy barrier is high. Figure 4 shows the image of the local hot spot. The process is following:

1. In the center of the hot spot, there is a core of energy release where the temperature is very high. If the released energy is very high, the temperature rises over the melting point. Melting and structural changes make the magnetic properties different.
2. Around the core, heat and intense properties change decreases the magnetic anisotropy and generates the nucleus of inverse domain.
3. Inverse domain wall easily expands in the low anisotropy region caused by the temperature rise.
4. In the higher anisotropy region, expansion of the domain wall is limited depending on the magnitude of the anisotropy.

In this "local hot spot (quasi-thermal spike)" mechanism, the nucleation can occur in the middle of the grain where the magnetic anisotropy is high, because the temperature of the hot spot is very high with the high-energy electron irradiation. Under the same irradiation condition, the amount of the nucleation should be same in all magnets, though the demagnetization shows the coercivity dependence. This is because the expansion of the inverse domain wall is regulated especially in the high coercivity magnet (Fig. 5).

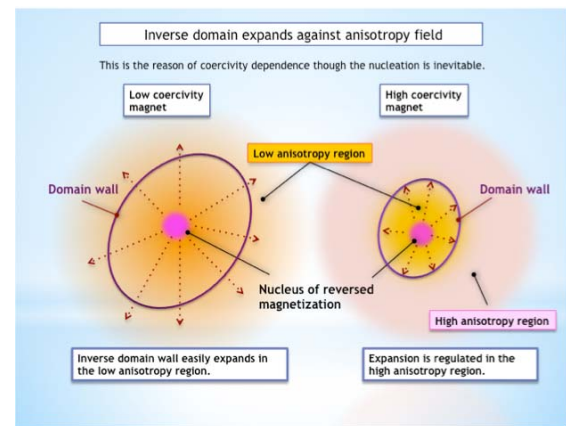


Figure 5: Temperature generated by the quasi-thermal-spike is extremely high so that the nuclei are produced in any magnet. In contrast, the easiness of the expansion of the inverse domain wall depends on the properties of the magnet. In the low coercivity magnets, the domain wall expands easily and the inverse domain grows to the whole grain, consequently this leads large demagnetization. In the large coercivity magnets, the coercivity around the nucleus is so large that the domain wall can hardly expand therefore the demagnetization is small.

The experimental results of the demagnetization caused by the high-energy electron irradiation were compared to the computer calculation. Asano calculated the neutron collision density distribution by using FLUKA code as shown in Fig.6 [13]. In the neutron energy below 1 MeV, the collision density at the center of the magnet irradiated with a 2 GeV electrons to the copper target is smaller than that at the end of the magnet with an 8 GeV to the tantalum target. But the demagnetization experiment shows opposite result as shown in Fig.7. Little demagnetization is observed at the end of the magnet irradiated with an 8 GeV electrons to the tantalum target. This implies that the neutron in the low energy region is not effective to demagnetization of the thermally stabilized magnet.

The calculation results of the absorbed doses are shown in (a) of Fig. 8. Experimental result of the tantalum target is different from the calculation. The right hand graph is the star densities that include elastic and inelastic interactions owing to high-energy photon neutrons. Both experimental results of copper and tantalum target are better fit to the calculation. This indicates that the absorbed dose is not strongly connected to the demagnetization of the thermally stabilized magnet. On the contrary, the interactions owing to high-energy photon neutrons are strongly correlated with the demagnetization process. These results could be explained by the mechanism of the local hot spot. The demagnetization caused by the high-energy electron is well indicated by the star densities than the dose. For the example of this application, Asano performed the estimation of the demagnetization quantitatively as



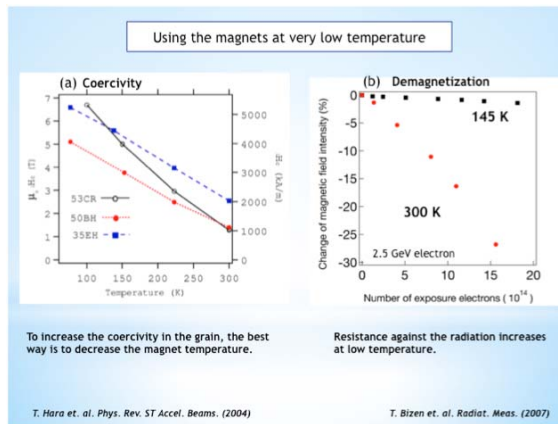


Figure 9: To increase the coercivity in the grain, the best way is to decrease the magnet temperature. (a) The coercivity increases with the temperature decrease. (b) Resistance against the radiation remarkably increases at low temperature.

mechanism, and the second is the “local hot spot (quasi-thermal spike)” mechanism.

The demagnetization cannot be estimated sufficiently by a calculation of the dose alone, because the mechanism of the demagnetization depends on the particle energy. The simulation of the star density is in good agreement with the demagnetization of the stabilized magnet with high-energy electron irradiation. The star density can be used for estimation of the radiation-induced demagnetization.

## REFERENCES

- [1] S. Sasaki et al., “Radiation Damage to Advanced Photon Source Undulators”, PAC’05, Knoxville, Tennessee, May 2005, p. 4126 (2005).
- [2] J. R. Cost et al., “Effects of Neutron Irradiation on Nd-Fe-B Magnetic Properties”, IEEE T. Magn., 24 (3), p. 2016 (1988).
- [3] O. -P. Kähkönen et al., “Temperature Dependence of Irradiation-Induced Magnetic Flux Loss in Nd<sub>2</sub>Fe<sub>14</sub>B Permanent Magnets”, Europhys. Lett., 12 (5), p. 413 (1990).
- [4] S. Okuda et al., “Effects of Electron-Beam and  $\gamma$ -ray Irradiation on the Magnetic Flux of Nd-Fe-B and Sm-Co Permanent Magnets”, Nucl. Instrum. Meth. B, 94, p. 227 (1994).
- [5] Y. Ito et al., “Radiation Damage of Materials due to High-Energy Ion Irradiation”, Nucl. Instrum. Meth. B, 191, p. 530 (2002).
- [6] C. H. Chen et al., “The Effect of Neutron Irradiation on Nd-Fe-B on Sm<sub>2</sub>Co<sub>17</sub>-Based High Temperature Magnets”, IEEE T. Magn., 41 (10), p. 3832 (2005).
- [7] R. Klaffky et al., “Thermal Neutron Demagnetization of NdFeB Magnets”, EPAC’06, Edinburgh, Scotland, July 2006, THPLS130 (2006).
- [8] R. Oiu et al., “Radiation Damage of Nd<sub>2</sub>Fe<sub>14</sub>B Permanent Magnets at 2.5 GeV Electron Accelerator”, Nucl. Instrum. Meth. A, 594, p. 111 (2008).
- [9] M. Talvitie et al., “Magnetic Flux Loss in Nd-Fe-B Magnets Irradiated with 20 MeV Protons”, J. Magn. Magn. Mater., 102, p. 323 (1991).
- [10] R. S. Gao et al., “Study of  $\gamma$ -ray Irradiation Effect on Permanent Magnets”, J. Appl. Phys., 103, 07E136-1 (2008).
- [11] L. Yang et al., “Effects of Proton Irradiation on Electronic Structure of NdFeB Permanent Magnets”, Nucl. Instrum. Meth. B, 267, p. 3084 (2009).
- [12] L. Yang et al., “Effects of Proton Irradiation on Structure of NdFeB Permanent Magnets Studied by X-ray Diffraction and X-ray Absorption Fine Structure”, J. Magn. Magn. Mater., 323, p. 4 (2011).
- [13] Y. Asano et al., “Analyses of the Factors for Demagnetization of Permanent Magnet Caused by High Energy Electron Irradiation”, J. Synchrotron. Radiat., 16, p. 317 (2009).
- [14] M. S. Leitner et al., “Radiation Protection Studies for LCLS Tune up Dump”, SLAC-PUB-14020 (2010).
- [15] E. W. Blackmore, “Radiation Effects of Protons on Samarium-Cobalt Permanent Magnets”, IEEE T. Nucl. Sci., NS-32, No.5, p. 3669 (2010).
- [16] R.D. Brown, “Neutron Irradiation Study of Nd-Fe-B Permanent Magnets Made from Melt-Spun Ribbons”, J. Appl. Phys., 64 (10), p. 5305 (1988).
- [17] A. F. Zeller, “Radiation Damage Mechanisms in NdFeB”, The Eleventh International Workshop on Rare-Earth Magnets and Their Applications, Pittsburg, PA, October 1990, W6.2 (1990).
- [18] K. Makita et al., “Flux Loss of Nd-Fe-B Sintered Magnets Placed Near a Proton Synchrotron”, J. Magn. Soc. Jpn., 28, p. 326 (2004).
- [19] R. S. Gao et al., “Effect of  $\gamma$ -ray Irradiation on the Magnetic Properties of NdFeB and Fe-Cr-Co Permanent Magnets”, J. Magn. Magn. Mater., 302, p. 156 (2006).
- [20] T. Bizen et al., “Radiation-Induced Demagnetization Model for Undulator Magnets”, Particle Accelerator Society Meeting 2009, Tokai, Ibaraki, August 2009, p. 133 (2009).
- [21] T. Bizen et al., “Radiation Damage in Permanent Magnets for ID”, Radiat. Meas., 41, S260 (2007).
- [22] T. Bizen et al., “Baking Effect for NdFeB Magnets Against Demagnetization Induced by High-Energy Electrons”, Nucl. Instrum. Meth. A, 515, p. 850 (2003).
- [23] Y. Asano et al., “Estimation for Demagnetization of ID Permanent Magnet due to Installation of OTR”, IPAC’11, San Sebastian, Spain, THPC165 (2011).
- [24] T. Bizen et al., “Radiation Damage in Magnets for Undulator at Low Temperature”, EPAC’04, Lucerne, July 2004, WEPLT103, p. 2089 (2004).
- [25] T. Hara et al., “Cryogenic Permanent Magnet Undulators”, Phys. Rev. ST Accel. Beams., 7, 050702 (2004).

# LATTICE DESIGN AND BEAM DYNAMICS OF ERL-TF IN IHEP, BEIJING

Xiaohao Cui, Jiuqing Wang, Shuhong Wang, IHEP, Beijing, China

## Abstract

Energy Recovery Linac is considered as a potential candidate type of the next generation light source. A 35MeV ERL test facility (ERL-TF) is proposed in IHEP, Beijing, in order to test the technology and study the beam dynamics of ERL. In this paper, the lattice design and some beam simulations of the ERL-TF are described, with the focal points on the bunch length compression, emittance suppression, and energy spread compression.

## INTRODUCTION

ERL can provide high current and low emittance electron beams, and is considered to be a potential candidate for the next generation light source. But to build a qualified operational ERL, many accelerator issues and technologies are still have to be studied. In order to study the machine physics and to develop some key components, such as photo-cathode high voltage electron gun and high average CW super conducting cavity, we are planning to design and construct a 35 MeV ERL-TF in IHEP, Beijing[1, 2].

The layout of the ERL-TF is as shown in Figure 1. The ERL-TF consists of a photo-cathode 500 kV DC gun, an energy booster of 5 MeV with 2 x 2cell 1.3 GHz SC cavities, a merger, a main SC linac with 2 x 7-cell 1.3 GHz cavities, two TBA arcs, and an undulator. For simplicity, a lattice with compact racetrack shape is employed. The 500 keV electron beam is accelerated to 5MeV by the booster, and then injected into the main Linac. Downstream the linac, the 35MeV electron beam is transported to the undulator by the first TBA arc to produce THZ wave with high average power. Then the electron beam is re-injected into the main linac at a deceleration phase for energy recovery. The main parameters of the ERL-TF are listed in Table 1.

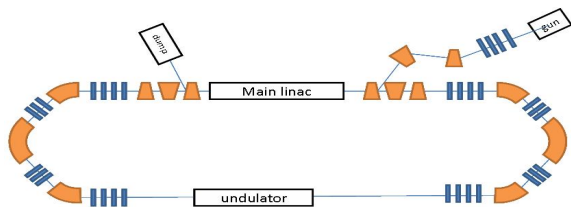


Figure 1: Layout of ERL-TF.

In the design of the ERL-TF, linear beam optics are simple, and structures of mergers and arcs are well known [3, 4]. Twiss parameters are set to meet several criteria: small beta functions throughout the loop, suitable in the arcs, dispersion free in the linac and undulator sections, etc. Nonlinear optics and collective effect play the important roles in the ERL-TF performance. In the following sections, our concern will be on beam dynamics in the first and second arcs.

Table 1: Main Parameters of the ERL-TF

Injection Energy	5 Mev
Maximum Energy	35 Mev
Normalized Emittance at the undulator	2.4 mm.mrad
Normalized Emittance after the injector	1.5 mm.mrad
Beam Current	10 mA
RF Frequency	1.3 GHz
Nominal Bunch Charge	77 pC
Bunch Length	0.23 ps
Injection rate	130 MHz

## BUNCH COMPRESSION

In our ERL-TF design, short bunches are generated by magnetic bunch compression in the 1st TBA arc, because the bunch at the merger and in the main linac must be sufficiently long to avoid significant emittance growth and high-order-mode (HOM) effects, respectively. We choose the bunch length at the entrance of the merger to be 2ps, and it is compressed to ~200fs by the first TBA arc.

The mechanism of magnetic compression is well-known[3]. In the ERL-TF, the electron bunch is accelerated in the main linac with an off-crest phase  $\Phi$ . After acceleration, electrons in the bunch will get an energy spread of

$$\delta = \frac{\Delta E}{E_f} = \frac{E_0}{E_f} \left( \cos\left(\phi + \frac{\omega z}{c}\right) - \cos(\phi) \right) . \quad (1)$$

Where  $\omega$  is the frequency of the main linac,  $c$  the velocity of light, and  $z$  the longitudinal position of the electron relative to the reference particle. Then the electrons pass through an arc with non-zero. At the exit of the arc, the deviation of longitudinal path length will be

$$\Delta z = R_{56} \delta + T_{566} \delta^2 + U_{5666} \delta^3 + \dots \quad (2)$$

The optimum can be approximately expressed as

$$R_{56} \approx \frac{c}{\omega \tan \phi} . \quad (3)$$

In our design, we use a TBA structure for its recirculator arcs because The R56 of TBA can be easily changed. The TBA consists of three 45-90-45 dipoles and three families of quadrupoles. To optimize the parameters of the first arc to get short bunchlength and small normalized emittance at the entrance of the undulator, we used ELEGANT[4] for numerical simulation. In our simulation, the CSR and space-charge effects are considered. Results are listed in Table 2. To achieve the minimum bunchlength, We choose the linac phase and R56 of the first arc to be 13deg and 0.16, respectively. Twiss parameters of the first arc are shown in Fig. 2.

Table 2: Main Parameters of the ERL-TF

Linac phase(degree)	Normalized Emittance(mm.mrad)	Bunch length(ps)
13	2.65	0.178
12.6	2.4	0.25
12.3	2.26	0.33
12	2.16	0.41
11	1.97	0.7

### SUPPRESSION OF THE CSR INDUCED EMITTANCE

Low emittance at the undulator is the most important feature of ERL, and it can be deteriorated by Coherent Synchrotron Radiation (CSR) if bunches are very short. Hence, in the design of the first arc, suppression of the CSR induced emittance is of great importance.

There are several ways for the emittance compensation, and in our design we used the envelope matching method. In this method, we make the orientation of the phase ellipse parallel to the CSR kick by scanning Twiss parameters at the exit of the arc[5]. Parameters optimization is done by simulation code ELEGANT with CSR calculation. We set  $\alpha_x = 0.202$ , and scan  $\alpha_x$  in the range of  $-5 < \alpha_x < 5$ . Normalized emittance at the entrance of the undulator as a function of  $\alpha_x$  are as shown in Figure 3. It shows that the emittance can be suppressed greatly by envelope matching. Particle distributions in the phase space are seen in Figure 4.

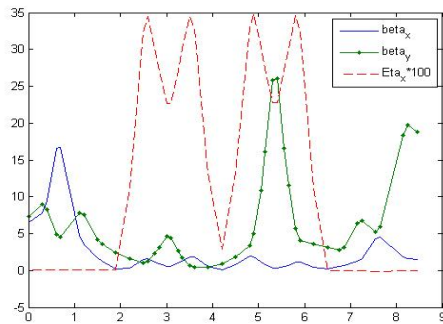


Figure 2: Twiss Parameters of the first arc.

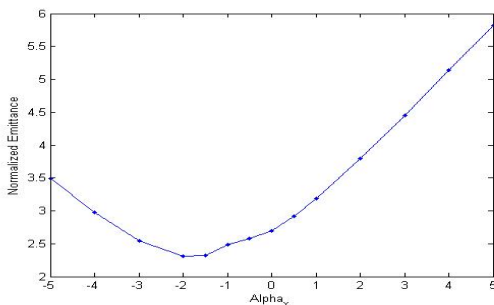


Figure 3: Normalized emittance at the entrance of the undulator.

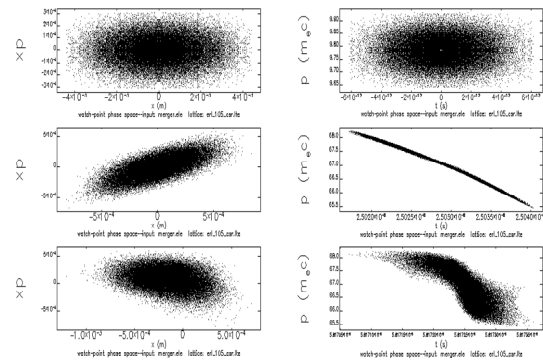


Figure 4: Beam distributions in the x and t phase space. The upper figures is taken at the entrance of Merger, the middle figures at the entrance of the first arc while lower ones at the entrance of the undulator.

### ENERGY COMPRESSION

Downstream of the undulator, the emittance of the ERL-TF is not very important unless it causes beam loss. One of the features must be considered in the return loop is energy compression. Interactions in the undulator will cause large energy spread in the electron bunch. When the electron bunches with large energy spread is decelerated through the Linac, relative energy spread will become quite large. This energy spread can be reduced by rotating the bunch in the longitudinal phase space, as so called Energy compression[6]. In our ERL-TF, energy compression is done by setting the return arc (or say 2nd TBA arc) non-isochronous, and tuning the deceleration phase in the linac. To stretch the bunch length, is set to be -0.16 in the return arc. Linac phase is optimized by numerical simulation in Fig 5. With these optimizations, we got a beam of energy-spread 1.5% at the exit of the main linac for a 1% energy-spread beam out of undulator.

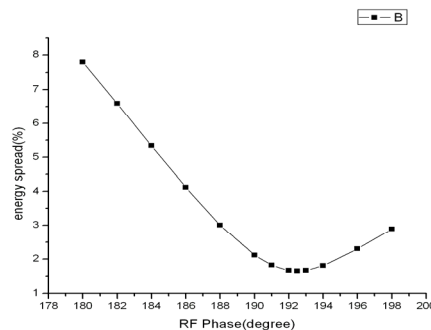


Figure 5: Energy spread after deceleration as a function of the phase in the linac.

### SUMMARY

In this paper, some preliminary beam dynamics studies on the ERL-TF in IHEP, China are presented. With the simulation of ELEGANT, we performed bunch compression, CSR suppression and energy compression. With these optimization, we got a beam with bunch length 200fs and normalized emittance 2.5mm.mrad in the undulator.

**REFERENCES**

- [1] CHEN Senyu, ZHU Xiongwei and WANG Shuhong, “Towards one machine two purposes: using a common SC linac for XFEL and ERL simultaneously,” Chinese Physics C 34. 1, 2010, January.
- [2] S. H. Wang, et al, paper submitted to Chinese Physics C.
- [3] V.N. Litvinenko, R. Hajima and D. Kayran, NIM A 557 (2006) 165.
- [4] R. Hajima, NIM A 557(2006) 45.
- [5] T. Shiraga, K. Yokoya, T. Suwada, A. Enomoto, NIM A 575(2007) 315.
- [6] M. Borland, ELEGANT: “A flexible SDDS-Compilant Code for Accelerator Simulation,” APS LS-287, September 2000.
- [7] R. Hajima, in: Proceedings of the APAC 2004, Gyeongju, Korea.
- [8] P. Pilot, D. R. Douglas, G. A. Krafft, Phys. Rev. ST. Accel. Beams 6(2003)0.0702.

# INDIVIDUAL HALF-CELLS FREQUENCY MEASUREMENTS OF A DUMBBELL CAVITY \*

Valery Shemelin<sup>†</sup>, Paul Carriere

Cornell Laboratory for Accelerator-based Sciences and Education (CLASSE), Ithaca, NY 14853, USA

## Abstract

Precise dumbbell fabrication is a critical step in the manufacture of multi-cell SRF cavities. The resonant frequency of each individual half-cell can be determined by perturbing the welded dumbbell and measuring the  $TM_{010}$  0- and  $\pi$ -mode. A correction to a previously derived formulae for  $\pi$ -mode frequency of each individual half-cell is presented and compared to SLANS simulations. The RF fixture and data acquisition hardware was designed and validated during 7-cell cavity fabrication. The system comprised of a mechanical press with RF contacts, a network analyzer, a load cell and custom LabVIEW and MATLAB scripts.

## INTRODUCTION

Production of the first superconducting cavities for the Cornell University Energy Recovery Linac (ERL) is complete. In order to minimize cavity tuning, a mid-process quality control step is introduced during the cavity fabrication when the half-cells (or cups) are welded together to form “a dumbbell”. Variability in the raw niobium, deep-drawing and weld shrinkage results in increased deviations in the dumbbell shape. These errors can be compensated by fabricating cups with an extended equators, determining the supplementary length using frequency measurements and, finally, machining each equator to the target length and hence frequency. We used the wealth of SC cavity experience published by DESY and JLab [1, 2, 3]. Both labs used measurement fixtures with a perturbing body to identify dumbbell asymmetry. There are no direct references in the DESY publications of how this asymmetry is used to define cup frequencies, but in the JLab publication the measured frequencies with and without perturbation were used to determine the individual  $\pi$ -modes of the cups.

## CALCULATION OF HALF-CELLS FREQUENCIES FROM DUMBBELL MEASUREMENTS

The formula for the frequencies of two coupled oscillators used by [3] is derived in [4, 5]:

$$\begin{aligned} f_{\pi,U} &= \sqrt{\frac{f_{\pi}^2 + f_0^2}{2} + \frac{(f_{\pi}^2 - f_0^2) \cdot (2 + R)}{2\sqrt{R} + 4}}, \\ f_{\pi,D} &= \sqrt{\frac{f_{\pi}^2 + f_0^2}{2} + \frac{(f_{\pi}^2 - f_0^2) \cdot (2 - R)}{2\sqrt{R} + 4}}, \end{aligned} \quad (1)$$

with the substitution

$$R = \sqrt{\frac{f_{\pi}^2 - f_{\pi,P,U}^2}{f_{\pi}^2 - f_{\pi,P,D}^2}} - \sqrt{\frac{f_0^2 - f_{0,P,U}^2}{f_0^2 - f_{0,P,D}^2}}. \quad (2)$$

Here “0” and “ $\pi$ ” denote the 0-mode or  $\pi$ -mode respectively and half-cells are distinguished by their location in the fixture with indices “U” for up and “D” for down. Frequencies measured with the perturbation are additionally marked with the index “P”. One can see that both (1) and (2) are asymmetric relative to a swap of indices “U” and “D”. Analysis of the derivation of the formula in [4] shows that there should be  $R^2$  in the denominators of (1):

$$\begin{aligned} f_{\pi,U}^* &= \sqrt{\frac{f_{\pi}^2 + f_0^2}{2} + \frac{(f_{\pi}^2 - f_0^2) \cdot (2 + R)}{2\sqrt{R^2 + 4}}}, \\ f_{\pi,D}^* &= \sqrt{\frac{f_{\pi}^2 + f_0^2}{2} + \frac{(f_{\pi}^2 - f_0^2) \cdot (2 - R)}{2\sqrt{R^2 + 4}}}. \end{aligned} \quad (3)$$

Now, the formulae in (3) are symmetric if  $R$  in (2) changes its sign when the dumbbell is turned upside-down. However, this can happen only if both right components in (2) are close to a unity:

$$\begin{aligned} R &= \sqrt{\frac{f_{\pi}^2 - f_{\pi,P,U}^2}{f_{\pi}^2 - f_{\pi,P,D}^2}} - \sqrt{\frac{f_0^2 - f_{0,P,U}^2}{f_0^2 - f_{0,P,D}^2}} \approx \\ &\approx (1 + \alpha) - (1 + \beta) = \alpha - \beta, \\ R' &= \sqrt{\frac{f_{\pi}^2 - f_{\pi,P,D}^2}{f_{\pi}^2 - f_{\pi,P,U}^2}} - \sqrt{\frac{f_0^2 - f_{0,P,D}^2}{f_0^2 - f_{0,P,U}^2}} \approx \\ &\approx \frac{1}{1 + \alpha} - \frac{1}{1 + \beta} \approx \beta - \alpha \approx -R. \end{aligned} \quad (4)$$

This, in its turn, can happen when the shift caused by the extra length of the cell is less than the shift due to perturbation.

One could transform the formula for  $R$  so that it would be symmetrical, e. g. by taking a mean arithmetic of  $R$  and  $-R'$ , or using an expansion by the small parameter mentioned above. But the original formula (2) is rather compact and the transformed formula would be presumably more cumbersome and hardly more accurate. A verification of (2) and (3) was done with SLANS [6] using a dumbbell with pre-defined equator lengths. We assume SLANS gives exact frequency values of a dumbbell with and without perturbations. We can also determine the relationship

\* Supported by NSF award DMR-0807731

<sup>†</sup> vs65@cornell.edu

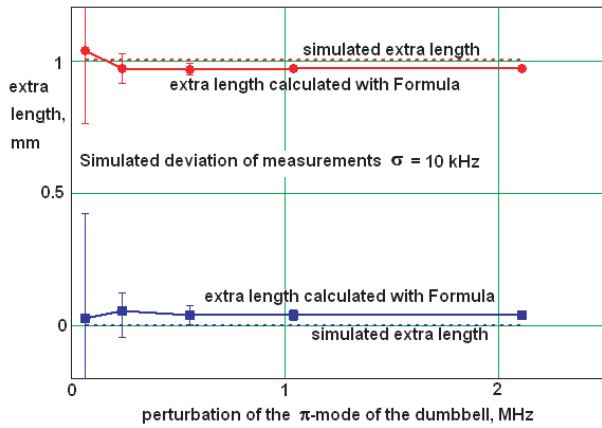


Figure 1: Simulation of a dumbbell with extra lengths 0 and 1 mm.

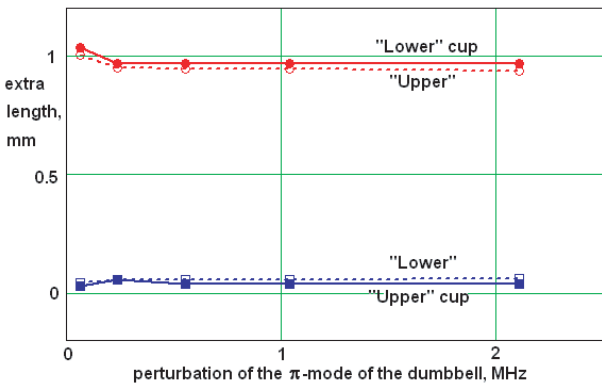


Figure 2: Extra length calculated with Formula.

between the extra equator length and frequency, commonly referred to as the trimming parameter,  $t$ . In our case, we determined that  $t = 5.1$  MHz/mm. Knowing the frequency of an “ideal” cup, or the target frequency,  $f_{target}$ , we can determine the extra equator lengths

$$\Delta_U = \frac{f_{target} - f_{\pi,U}^*}{t}, \text{ and } \Delta_D = \frac{f_{target} - f_{\pi,D}^*}{t} \quad (5)$$

to be trimmed. SLANS outputs frequencies for a dumbbell of known length, thereby giving us a means of validating formulae (3). We can also analyze how measurement errors of the dumbbell frequencies influence the accuracy of the found extra length. For this purpose, we can generate random values of frequencies around the values calculated by SLANS and use again the formulae (2) and (3) but now for 6 arrays of “measured” frequencies. Repeated measurements show that the standard deviation of each resonant frequency is about  $\sigma = 10$  kHz. Let the dumbbell have an extra lengths on one cup only:  $\Delta_1 = 1$  mm,  $\Delta_2 = 0$ . The perturbation used in this calculation was such that the frequency shift of the  $\pi$ -mode when inserted from the “ideal” side ( $\Delta_2 = 0$ ) is 60 kHz to 2.1 MHz, Fig. 1.

One can see that very small perturbations lead to uncertainty of extra length due to the errors of measurements.

Conversely, large perturbations do not reproduce the exact extra lengths as calculated with (5).

We can treat the cup with the extra length  $\Delta_1 = 1$  mm as an “Upper” or “Lower” cup. The choice of the cup location is conditional.  $R$  changes its sign when the dumbbell is turned over but also slightly changes its absolute value. The values of extra lengths calculated for these two possibilities are shown in Fig. 2.

We will have practically the same graph if  $\Delta_1 = 2$  mm,  $\Delta_2 = 1$  mm (the numbers on the ordinate axis will increase by 1). Therefore, we conclude that *the error is always smaller if the cup with bigger deviation of the  $\pi$ -mode is taken as the lower cup*. As is seen from the graph, the accuracy is improved by a factor of two.

If the cups have similar dimensions, this difference between frequencies defined with swapped upper and lower cups becomes small (no difference if  $R = 0$ ).

## A DUMBBELL MEASURING FIXTURE

To measure the resonant frequencies of a fabricated niobium dumbbell, a fixture with supporting hardware and software was constructed, Fig. 3. The system was inspired by the JLab system, with the most notable difference being the operating frequency (1300 MHz instead of 1500 MHz) [3]. The fixture was designed to accommodate completed end group measurements. In the case of end groups, no perturbation was used since the cavity was comprised of a single half-cell. Two feedthroughs with antennas were placed in the upper and lower plates, and the RF measurement was done in transmission. For the end group, one antenna was replaced by a flexible conductor such that it was easily inserted into the cavity. In each case, the antenna length was trimmed such that the cavity was heavily undercoupled with a  $Q_{ext} \approx 10^6$ , giving  $Q_l \approx Q_0$ .

The measurement system consists of a HP85047A network analyzer (NA), a RF dumbbell fixture with copper contact fingers, and a Transducer Techniques load cell with analog readout. The NA and load cell were connected to a LabVIEW program which logs the frequency ( $f_0$ ), quality factor ( $Q_0$ ) and applied force.  $Q_0$  and  $f_0$  were determined by fitting the amplitude of  $S_{21}$  to the Lorentzian function while accounting for a constant direct transmission between antennas. LabVIEW was chosen to increase the measurement accuracy while simplifying the measurement and processing procedure.

The six measured frequencies comprised the 0 and  $\pi$ -mode, with and without perturbation in the upper and lower half-cells. These values were written to a file and then processed using MATLAB. The script calculates the individual  $\pi$ -mode frequencies according to the modified formulae (3). The program recognizes which half-cell has the biggest  $\pi$ -mode deviation and assigns this cup as ‘lower,’ in spite of its physical location. The program also incorporates a correction for ambient conditions: humidity, temperature and atmospheric pressure [7].

The value of the frequency perturbation should be bigger

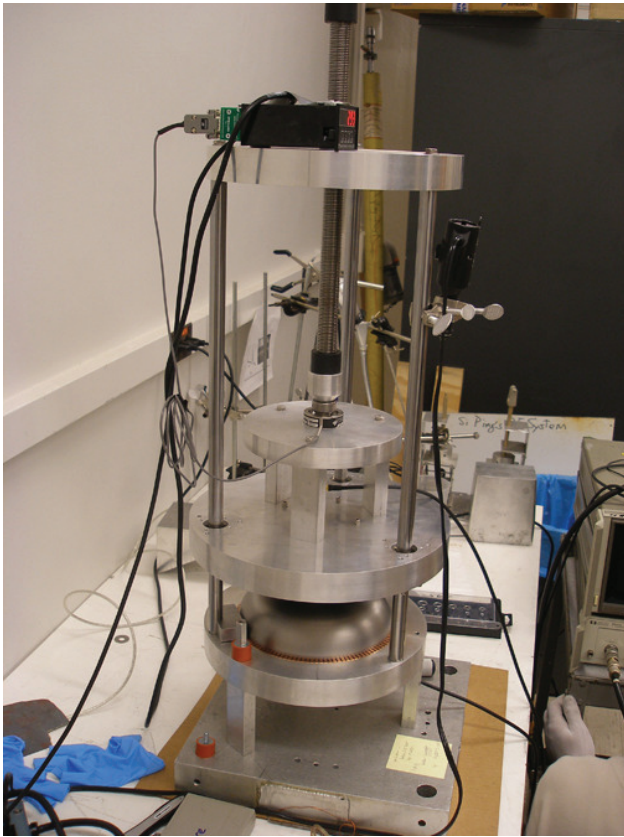


Figure 3: Dumbbell measuring fixture.

than the error in measurement (10 kHz) but less than the difference between the 0 and  $\pi$ -mode frequencies (about 26 MHz). We have chosen our perturbation such that  $\Delta f \approx 0.5$  MHz. The perturbing body is a cylinder 3.175 mm in diameter with a spherical top, and the total length of 6.5 mm. In order to guarantee reliability, the perturbation was fastened with a torque wrench to 10 inch-lb.

To obtain a reliable RF contact at the Nb/Cu joint, the fixture must compress the dumbbell between copper plates. The mechanical press comprised of linear bearings mounted on aluminum plates, sliding on case-hardened shafts. The press was manually driven by a 1-inch ACME screw. ANSYS simulations show that the force applied to the dumbbell should be kept below 350 lbs, in order to prevent inelastic deformation. Therefore, our operating pressure was 300 lbs. Plastic deformation will affect the resonant frequency of the cavity, but a linear extrapolation to zero pressure of the  $f_0$  versus  $F$  curve found this deviation to be negligible compared to our machining tolerance. To overcome the dry-contact friction between components, a small mechanical vibrator was attached to the fixture. It was also helpful to gently rub the niobium dumbbell against the copper contact using a circular motion. To exclude the copper contamination of the niobium, a 30 minute nitric acid etch of the equators was performed prior electron-beam welding.

These measures resulted in  $Q_0$ 's between 5000 and

7000. The theoretical value simulated in SLANS was about 7500 for both 0- and  $\pi$ -modes, given our geometry and material. We assumed that a  $Q_0$  greater than 5000 indicates a reliable RF contact. Using the methods outlined above, we demonstrated repeatable frequency measurements with  $\sigma=10$ kHz, regardless of cavity orientation or re-insertion.

## CONCLUSION

Dumbbell cavities for the Cornell ERL multicell cavity were measured in a measuring fixture constructed for this purpose to determine equator trimming lengths. Corrections were introduced into the formulae for calculation the individual half-cell frequencies. LabVIEW and MATLAB software was written for a semi-automatic measurements with a network analyzer, load cell, and RF dumbbell fixture. Our system helped to control individual cell frequencies to within narrow limits: the first completed Cornell ERL 7-cell cavity has a frequency deviation of 360 kHz, and a field flatness of 88 %. This corresponds to an average deviation of less than 0.003 inches (75  $\mu$ m) per cell.

## REFERENCES

- [1] G. Kreps et al. Half-cell and dumb-bell frequency testing for the correction of the TESLA cavity length. Proceedings of the SRF'99, Santa Fe, New Mexico, November 1999, p. 499.
- [2] J. Iversen et al. Development and design of a RF-measurement machine for the European XFEL cavity fabrication. Proceedings of the SRF2009, Berlin, Germany, September 2009, p. 786.
- [3] F. Marhauser. JLab SRF cavity fabrication errors, consequences and lessons learned. JLab-TN-10-021, August 2010.
- [4] S. An et al. A method to measure the frequencies of the individual half cells in a dumbbell cavity. Rev. Sci. Instr. **79**, 104701, 2008.
- [5] S. An et al. PEPF dumbbell frequency and length tuning of a low-beta SRF cavity. Proceedings of the EPAC'08, Genoa, Italy, July 2008, p. 823.
- [6] D. G. Myakishev, V. P. Yakovlev. The New Possibilities of SuperLANS Code for Evaluation of Axisymmetric Cavities. Proc. of the PAC'95, pp. 2348–2350.
- [7] V. Shemelin. Correction of a superconducting cavity shape due to etching, cooling down, and tuning. Presented at SRF11 Workshop, Chicago, IL, 2011.

# CHARGE LIFETIME, EMITTANCE, AND SURFACE ANALYSIS STUDIES OF $K_2CsSb$ PHOTOCATHODE IN A JLAB DC HIGH VOLTAGE GUN\*

J. L. McCarter<sup>#</sup>, University of Virginia, Charlottesville, VA 22904, U.S.A.

T. Rao, J. Smedley, BNL, Upton, NY 11973, U.S.A.

R. Mammei, M. Poelker, R. Suleiman, TJNAF, Newport News, VA 23606, U.S.A.

## Abstract

For the past year, BNL and JLab groups have been collaborating to study the characteristics of  $K_2CsSb$  photocathodes inside a DC high voltage photogun. Although the first set of runs at 1 mA and at 100 kV bias voltage indicated disappointing charge lifetime, comparable to values obtained with GaAs photocathodes, subsequent measurements indicate that both the QE and charge life time increased significantly. This improvement could be attributed to the change in the chemical composition of the cathode due to UV irradiation. The charge life time measurements do not indicate any QE decay for currents of 10 mA with 350 micron FWHM spot, slight decay at 16 mA and significant decay at 20 mA for this spot size. When the spot size was increased to 850 micron, the lifetime at 20 mA increased significantly, implying local heating due to high laser intensity. Additional measurements with laser alone, without the HV, support this argument. These results as well as emittance and surface science measurements will be presented.

## INTRODUCTION

Photoelectron guns are well suited to provide the high brightness, and often high average current, electron beams required for light sources and energy recovery LINAC accelerator applications. Two popular photocathode choices are GaAs:Cs and  $K_2CsSb$ . The GaAs:Cs photocathode can exhibit very high QE and can produce a beam with small thermal emittance [1]; however, it requires strict adherence to procedures that limit the effects of its fragility. Once inside the photogun, GaAs is prone to rapid QE loss that can result from many situations such as poor vacuum and field emission. The  $K_2CsSb$  photocathode can exhibit high QE has complications of its own in practice. GaAs can be purchased from numerous reliable vendors while the  $K_2CsSb$  photocathode is an amorphous compound that must be grown while in vacuum via successive application of the elemental species on a suitable substrate and then transported and installed into the photogun also entirely under vacuum. Consistent results depend on consistent adherence to proper growth procedures. While the  $K_2CsSb$  photocathode has larger thermal emittance [1,2] as compared to GaAs:Cs, it is considered to be a prompt emitter because of its positive electron affinity nature, producing shorter bunches than

GaAs:Cs. The biggest advantage of  $K_2CsSb$  however is the photocathode's ability to survive under markedly harsher vacuum conditions as compared to GaAs:Cs.

The purpose of this work was to expand on prior measurements done on the performance of a  $K_2CsSb$  photocathode. The performance directly compares to that of GaAs:Cs, which was characterized in the same 100kV DC photogun [3]. Early results indicated that the charge lifetime while illuminated at 532nm was no better than GaAs [4]; however after a major vacuum event, the lifetime at 440nm greatly improved, along with the QE of almost the entire photocathode [5]. This work revisits the initial lifetime results at 532nm and measures the beam emittance, as well as provides some insight into what factors affect the performance of a  $K_2CsSb$  cathode by using SEM techniques.

## EQUIPMENT

$K_2CsSb$  was grown at BNL on a JLab style photocathode puck [6] and was then transported via car to JLab, roughly 450 miles away, in an ultrahigh vacuum transfer vessel ( $10^{-11}$  Torr). After growth at BNL, the  $K_2CsSb$  photocathode was installed in the DC high voltage photogun within approximately 2.5 days. No appreciable QE decay was observed, which indicates a very long dark lifetime.

### Cathode Fabrication

The  $K_2CsSb$  cathode was prepared at BNL in a UHV chamber by depositing sequentially high purity Sb, K and Cs onto a puck, similar to the standard JLab puck but made of aluminium with a thin layer of stainless steel (SS) explosion bonded to the top surface to accept the coating. Stainless steel was chosen as previous measurements at BNL indicate it provides high QE at 532 nm. Two sequential depositions were executed on the same substrate, as the first evaporation did not produce satisfactory QE. Specifics to the BNL  $K_2CsSb$  deposition system and process can be found in these proceedings [7]. During the second evaporation process the potassium dispenser was prematurely exhausted, which decreased the expected QE at wavelengths above 300nm [4, 5].

### Load-Lock DC High Voltage Photogun

The CEBAF load-locked DC photogun [6] is composed of four vacuum chambers separated by all-metal gate valves: the high voltage chamber, where the electron

\*Work supported by the U.S. DOE under Contracts No. DE-AC05-84ER40150 and DE-AC02-98CH10886 and partially by DE-FG02-97ER41025.

<sup>#</sup>jlm2ar@virginia.edu

beam is generated, the preparation chamber, which is normally used to heat and activate GaAs:Cs photocathodes and was instead used here as a transfer and storage area, and a small-volume loading chamber. The fourth chamber, the Suitcase, is attached to the photogun only when photocathodes are replaced. The Suitcase was used to deliver the  $K_2CsSb$  from BNL.

The DC JLab photogun was outfitted with a large grain niobium cathode electrode that was both mechanically and chemically polished and HV conditioned in order to allow 200 kV operations with no field emission. Photoelectrons were accelerated in the gun chamber and then steered through a diagnostic beam line ending in a Faraday cup  $\sim 5$  m downstream. Charge lifetime, defined as the amount of charge that can be extracted before the QE falls to  $1/e$  of its initial value, was measured by monitoring the QE evolution as a function of accumulated charge. Measurements are made at a particular electron beam current by continually adjusting the laser power striking the photocathode to ensure a constant current measured in the faraday cup. Beam emittance was measured using wire scanners along the beam line.

## CATHODE PERFORMANCE AND DISCUSSION

### Previous Lifetime Measurements

Initial measurements made with a 532 nm, 350  $\mu$ m FWHM (Gaussian) DC laser running 1 mA at 100 kV showed charge lifetimes around 100 C, which were comparable to an unmasked GaAs:Cs photocathode [4]. Measurements made with a 440 nm, 850  $\mu$ m FWHM (Gaussian) DC laser were presented at IPAC 11 [5]. The initial QE scan of the photocathode, shown in Figure 1, with 440 nm light roughly agrees with the QE at 440 nm originally measured at BNL. The QE scan was accomplished by extracting  $\sim 1$   $\mu$ A from the grounded photocathode, with the anode biased at  $\sim 375$  V, while scanning the laser across the photocathode by translating a focusing lens mounted to x/y stepper motor stages.

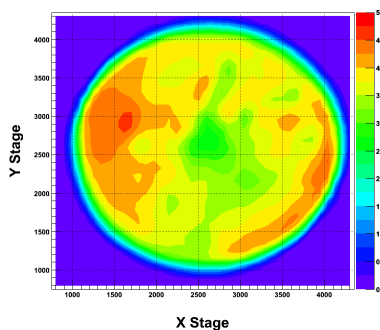


Figure 1: QE scan along the photocathode with 440 nm.

Charge lifetime measurements were performed at a 1 mA beam current with 100 and 200 kV gun voltages and at different positions on the photocathode. Each measurement was allowed to run for 24 hr, and no QE degradation was observed, even from beam extracted

from the electrostatic center of the cathode. While further stressing the photocathode by running higher current, a power failure cause the electron beam to impact a section of beamline, causing a major vacuum event which decreased the QE by a half. During this time, neither the laser nor HV supply were affected and about 1.5 mA of beam was extracted from the photocathode for  $\sim 2$  hr in a  $5 \times 10^{-10}$  Torr environment. Again a vacuum event of this magnitude would have quickly degraded the QE of GaAs:Cs, but this is not the case for  $K_2CsSb$ .

A subsequent QE scan over the photocathode, shown in Figure 2, showed that only the EC was severely damaged and there were still useable extraction sites around the EC. 5 mA was extracted for 24 hr and no permanent QE decay was observed, despite several vacuum events that temporarily lowered the QE in a manner similar to earlier runs [5].

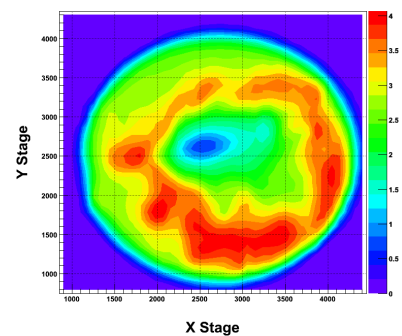


Figure 2: QE scan after a major vacuum event caused beam to be extracted in a  $5 \times 10^{-10}$  environment for  $\sim 2$  hr. Visual inspection of the puck after the event seems to indicate that the  $K_2CsSb$  material at the EC was sputtered away leaving the stainless steel substrate.

### Laser Heating

All charge lifetime measurements with 440 nm light indicated that QE did not decay with extracted charge; for the higher current runs, the QE actually increased. The QE continued to increase merely while illuminating several spots along the photocathode without a bias voltage for various periods of time and laser powers. Up to a maximum power density of  $0.37$  W/mm<sup>2</sup> at 440 nm the QE at any illuminated spot increases, which indicated that the stoichiometry of the photocathode is improving locally at the illuminated spot with 440 nm. Of note is that this behaviour was not observed during previous charge lifetime measurements made with 532 nm. This suggests an absorption depth and/or surface chemistry dependence for  $K_2CsSb$  [5].

### Redone Charge Lifetimes at 532 nm

The QE of the photocathode at 532 nm was increased relative to its value before the 440 nm runs after the occurrence of the major vacuum event previously mentioned. Figure 3 shows the typical QE evolution as function of charge for 5 mA at 532 nm and 200 kV, with a 350  $\mu$ m laser spot. The initial QE was higher than before the vacuum event, and then continued to rise over time, similarly to the 440 nm lifetime runs.

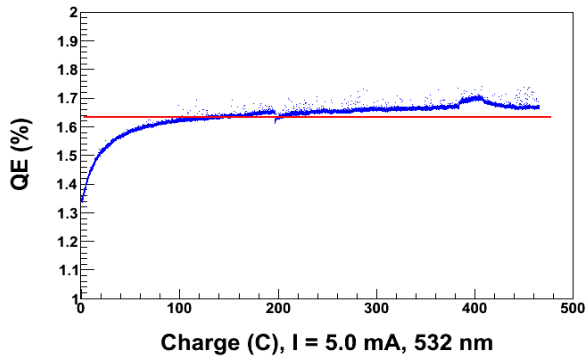


Figure 3: QE evolution vs. accumulated charge when using a 532 nm/350 μm (FWHM) Gaussian laser spot.

Taking advantage of a seemingly indestructible photocathode, maximum current was extracted from the cathode, using maximum laser power. Figure 4 shows the QE vs time of this run. Up to 10 mA, the QE seemed to either rise over time, or at least was constant; however, at 16 mA the QE started to slowly decline. At 20 mA, the QE sharply dropped.

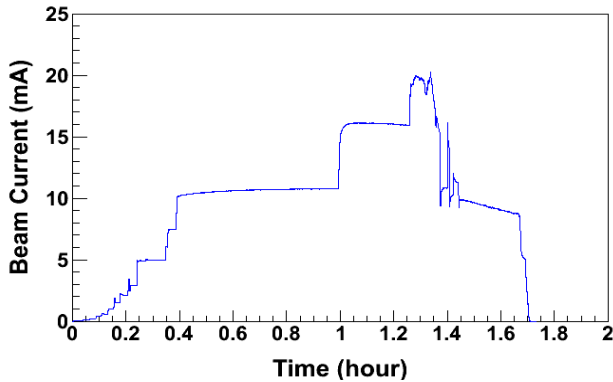


Figure 4: QE evolution vs. time while trying to extract maximum current using a 532 nm/350 μm (FWHM) Gaussian laser spot.

Because laser heating seemed to help improve QE at 440 nm, it was suspected that too much heating was occurring due to high laser power densities. QE scans indicated that the QE surrounding the area that beam was extracted from actually increased, which was likely a result of the extreme heating being primarily localized to the location of the laser. In addition, lowered laser powers were noted to locally increase the QE of the cathode in a similar way to the 440 nm light. To check suspicions of a heating threshold being reached that hurt the cathode, 20 mA was again run, but with a laser spot of 800 μm, and the resulting QE evolution is shown in Figure 5(b), along with the 200 mA 350 μm run, which is Figure 5(a).

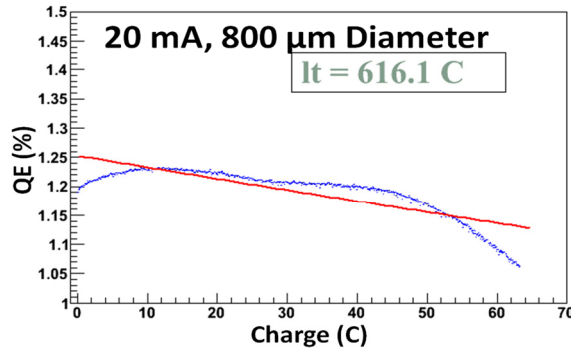
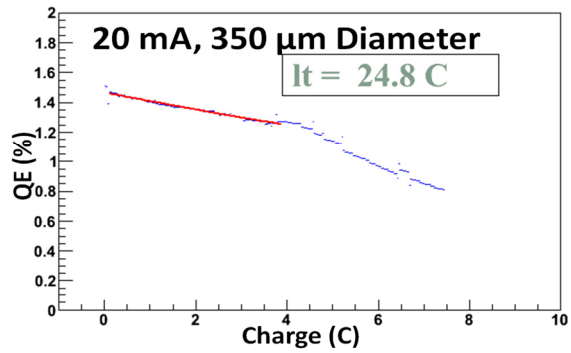


Figure 5: QE evolution vs. charge at 20 mA for (a) 350 μm spot and (b) 800 μm spot. Lifetimes per a 1/e fit are indicated in boxes.

*Emittance*

The emittance of the K<sub>2</sub>CsSb photocathode was measured using a solenoid scan technique. 3 μA of beam was run at both 100 kV and 200 kV and also at both 440 nm and 532 nm in order to measure the emittance. Table 1 shows the results of these measurements. The emittance is roughly twice that measured in previous measurements at Cornell, although the following SEM analysis provides a possible explanation for this discrepancy.

Table 1: Emittance for K<sub>2</sub>CsSb for Varying Wavelengths and Bias Voltages

Laser Wavelength (nm)	Laser FWHM (um)	HV (kV)	Normalized Emittance (mm mrad/mm(rms))
440	850	100	1.11 +/- 0.10
440	850	200	0.97 +/- 0.18
532	330	100	1.25 +/- 0.08
532	330	200	1.12 +/- 0.35
532	700	100	1.01 +/- 0.08
532	700	200	1.19 +/- 0.27

### SEM Analysis

After all lifetime and emittance measurements were conducted, an attempt was made at measuring the lifetime in a poor vacuum setting. In order to simulate a high  $H_2$  environment, the NEG pumps in the gun were heated in order to release gases. During this heating, 1 mA was run from the cathode and the QE rapidly decayed. The QE of the entire cathode fell by a factor of 3, which indicated that the high heat caused by the hot NEGs negatively impacted the cathode.

Visual inspection of the photocathode surface revealed several features that were not present initially. Figure 6 shows the cathode upon removal from the gun. Location 1 refers to the spot of complete QE loss due to the major vacuum event, and visually appears to be the stainless steel substrate. Location 4 was masked by the cathode from being exposed directly to the gun vacuum. Locations 2 and 3 refer to spots of the photocathode that were exposed to beam related events. This area is partially frosted to the eye, as seen in location 2.

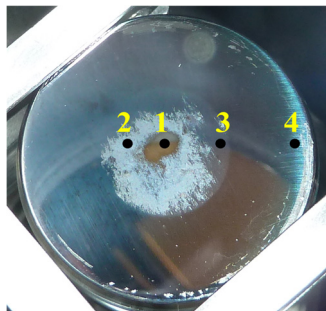


Figure 6: The  $K_2CsSb$  puck after removal from the JLab DC gun.

An attempt was made to restore the QE of the cathode by withdrawing it from the DC gun to place it in the JLab preparation chamber, which is usually used to heat and activate GaAs. The puck was brought to  $130^\circ C$  while Cs was evaporated onto it; however, the QE of the cathode dropped to zero in this time.

The cathode was moved into the transport suitcase at this time for transfer to a SEM. A glove bag filled with argon was used for the hand off between the suitcase and the vacuum vessel of the SEM. The SEM confirmed that Location 1 was indeed stainless steel, which indicates that the vacuum event was severe enough to sputter away the entire photocathode layer. Importantly, the rest of the cathode survived this major event, which would have been completely destroyed a GaAs cathode.

Figure 7 shows two of the SEM images, with (a) referring to location 2 and (b) referring to location 3. The frosted region, location 2, is comprised of islands of Cs, K, and Sb, with SS and some Sb in between. While smooth to the eye, location 3 shows some cracking of the photocathode film, with SS located in the cracks. The rough surface of the photocathode possibly contributed to the higher than expected measured emittance.

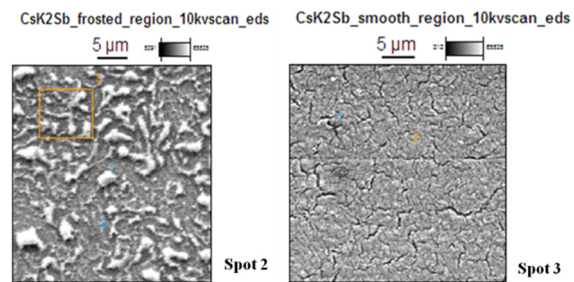


Figure 7: SEM images of the  $K_2SbCs$  puck taken at 20 keV electron energy of (a) location 2 on the puck and (b) location 3.

### SUMMARY CONCLUSIONS

A  $K_2CsSb$  photocathode was prepared at BNL and transported to JLAB with no QE degradation. At JLab, beam was extracted in a 100 and 200 kV DC CEBAF load locked gun. Charge lifetime measurements made with a 440 nm/850  $\mu m$  (FWHM-gaussian) laser showed no QE decay, even when extracting charge from the EC. While extracting beam, a vacuum event modified the surface of the photocathode, which restored QE at 532 nm. Charge lifetime at 532 nm was subsequently greatly improved due to either the vacuum event or from laser irradiation at 440nm. At both 532 nm and 440 nm, it was possible to locally improve QE via laser heating the cathode. Maximum current run was 20 mA at 532 nm, and was limited by too much laser heating of the cathode. Decreasing the power density of the drive laser improved lifetime at 20 mA. Emittance was measured and was slightly higher than expected, which was potentially due to the rough surface of the cathode that was seen via SEM analysis.

### REFERENCES

- [1] D. Dowell, *et al.* Nucl. Instrum. Methods Phys. Res. A 622 685 (2010).
- [2] I. Bazarov, *et al.* Appl. Phys. Lett. 98, 224101 (2011).
- [3] J. Grames, *et al.* Phys. Rev. ST Accel. Beams 14, 043501 (2011).
- [4] J. L. McCarter, *et al.* PAC11, Proceedings of 2011, WEP284.
- [5] R. Mammei, *et al.* IPAC11, Proceeding of 2011.
- [6] P. A. Adderley, *et al.* Phys. Rev. ST Accel. Beams 13, 010101 (2010).
- [7] J. Smedley, M. Osés, *et al.* IPAC11, Proceedings of 2011.

# RECENT PROGRESS OF AN Yb-DOPED FIBER LASER SYSTEM FOR AN ERL-BASED LIGHT SOURCE

I. Ito, ISSP, University of Tokyo, Kashiwa, Chiba, 277-8581, Japan

R. Kasahara, S. Nakamura, Ibaraki University, Hitachi, Ibaraki, 316-8511, Japan

D. Yoshitomi, K. Torizuka, AIST, Tsukuba, Ibaraki, 305-8568, Japan

N. Nakamura, KEK, Tsukuba, Ibaraki, 305-0801, Japan

## Abstract

We have been developing an Yb fiber laser system for an ERL photocathode gun. The Yb fiber laser system is expected to have both high stability and high output power required for the drive laser. We have improved the output power of the Yb fiber laser system up to 31 W at 85 MHz by installing a preamplifier and keeping the wavelength of pump light and the temperature of a photonic crystal fiber. We also have demonstrated wavelength conversion from 1  $\mu\text{m}$  to 800 nm with a conversion efficiency of 9.5% by generating a supercontinuum light, which is planned to be amplified by optical parametric amplification (OPA) in future. In addition, we are developing a Nd:YVO<sub>4</sub>-based mode-locked oscillator that can operate at the same frequency as the RF frequency of a superconducting accelerating cavity. We report our recent progress in this development.

## INTRODUCTION

An electron source significantly contributes to the performance of an Energy Recovery Linac (ERL) because an electron beam goes around it only one or a few times not to reach the equilibrium between the radiation damping and quantum excitation. A 500kV DC electron gun with a negative electron affinity (NEA) GaAs photocathode is being developed as an ERL gun [1,2]. In order to produce ultra-low emittance and high-charge beam by the photocathode gun, a drive laser system requires leading-edge technology.

Figure 1 shows the schematic of the drive laser system. The drive laser system is MOPA (Master Oscillator and Power Amplifier) type with an Yb fiber laser oscillator and two Yb fiber laser amplifiers. The Yb fiber laser is expected to have high stability and high output power. In addition, the optical parametric amplification (OPA) is done to convert the wavelength of the Yb fiber laser (1030nm) to the wavelength equal to the band gap of the photocathode NEA-GaAs (700-800nm). Firstly, two lights are diverged from the light amplified by the Yb fiber laser amplifier. One is converted to a second harmonic (SH, 515nm) by a nonlinear optical crystal and the other to a supercontinuum light (SC, 800 $\pm$ 50nm) by a high nonlinear photonic crystal fiber (PCF). Finally, OPA is done using SH as the pumping light and SC as the seed light.

In this paper, we report the development of the Yb fiber laser amplifier and the demonstration experiment of wavelength conversion from 1  $\mu\text{m}$  to 800 nm by the

supercontinuum generation. Additionally we report the development of a Nd:YVO<sub>4</sub>-based mode-locked oscillator that can operate at the same frequency as the RF frequency of a superconducting accelerating cavity.

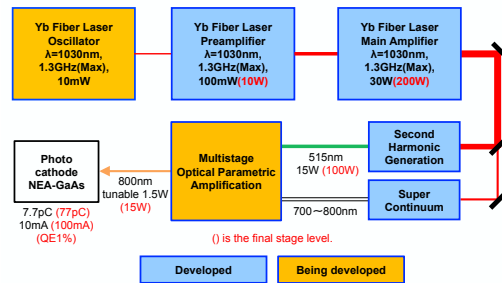


Figure 1: Schematic of drive laser system.

## LASER AMPLIFIER

We previously developed an Yb doped phonic crystal fiber laser amplifier and amplified an 85MHz seed pulse up to 10W [3]. This time, we have improved the output power of the amplifier system up to 31 W at 85 MHz.

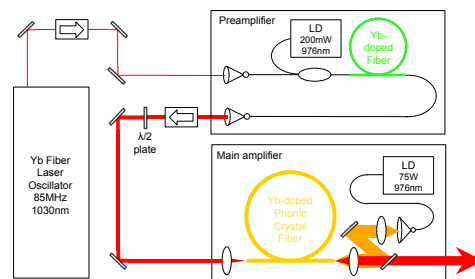


Figure 2: Schematic of Yb fiber laser amplifier system.

Figure 2 shows the schematic of the Yb fiber laser amplifier system. An 85MHz seed pulse is made by an Yb fiber oscillator and amplified to 60mW by a preamplifier. The preamplifier is composed by the Yb doped fiber (core diameter:5  $\mu\text{m}$ , length:5m). The preamplifier can amplify 10mW pulse up to 100mW without nonlinear optical effect. The 85MHz seed pulse from the preamplifier is then amplified by a main amplifier. The main amplifier is composed of an Yb doped photonic crystal fiber (PCF, core diameter: 40 $\mu\text{m}$ , length:1.2m). Because the PCF has a large core doped with Yb ions and a clad having periodically allocated air holes, it can significantly amplify the seed pulse without nonlinear optical effect. If a pump power becomes much higher, various troubles happen. First of all, the PCF is at risk of burning by much

higher pump power. So we installed a cooling fan near the PCF tail edge into which pump light is input. Additionally, the amplified efficiency decreases due to the shift of the center wavelength of the laser diode (LD) output by its heating. As a result we kept the center wavelength of the LD output at 976nm by controlling the LD temperature.

We performed evaluation of the amplified pulse. Fig. 3 shows the amplifier slope efficiency. The slope efficiency is about 40%. The 85MHz pulse can be amplified to 31W and have almost the same pulse energy as required at 1.3-GHz repetition rate for the ERL. Fig.4 shows spectra of the seed pulse and amplified pulses. A dot line shows the seed pulse and solid lines the amplified pulses. FWHMs of the amplified pulse spectra are about 10nm, and significant bandwidth broadening does not appear. Fig. 5 shows the autocorrelation traces of the seed pulse and amplified pulses. The autocorrelation trace is the convolution of two pulses into which a pulse is divided. FWHMs of the autocorrelation traces are about 10ps and almost unchanged. Therefore, we can confirm that nonlinear optical effect that causes the pulse distortion is suppressed in the main amplifier.

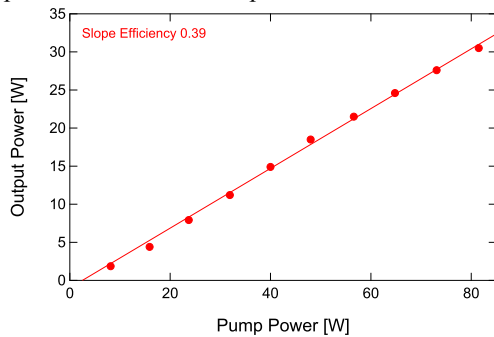


Figure 3: Amplifier slope efficiency.

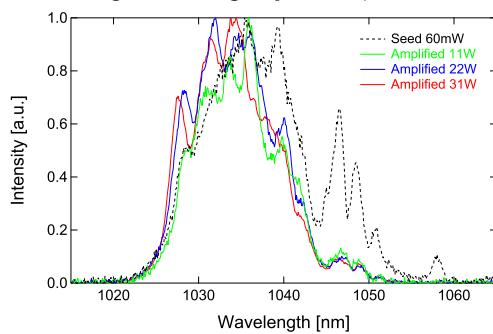


Figure 4: Optical Spectrum.

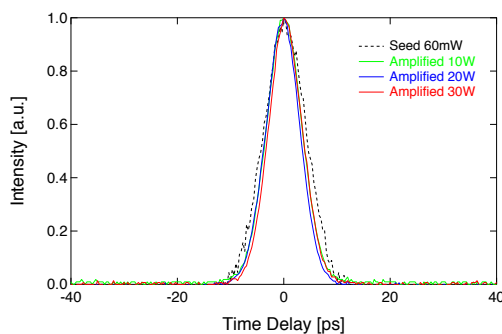


Figure 5: Autocorrelation trace.

## SUPERCONTINUUM GENERATION

In order to use as a seed light of the optical parametric amplification (OPA), we generated the supercontinuum (SC) by the high nonlinear PCF (NKT Photonics, NL-1050-ZERO-2). Fig. 6 shows the schematic of the experiment setup. The 85MHz amplified pulse (2W) was input into the high nonlinear PCF. Because the high nonlinear PCF has low dispersion around the wavelength 1μm, the input pulse whose wavelength is 1030nm can propagate with its peak intensity kept and the broadband SC can be generated efficiently. In order to extract frequency component around 800nm from the SC, the broadband SC is reflected by two mirrors that have the center wavelength of 800nm and the bandwidth of 80nm.

Figure 7 shows the spectrum of the SC. The center wavelength is 800nm and the bandwidth is 85nm. The average power is 190mW and the conversion efficiency is 9.5% (0.19W/2W). At the present stage, the wavelength of the SC can satisfy the specification required by the ERL.

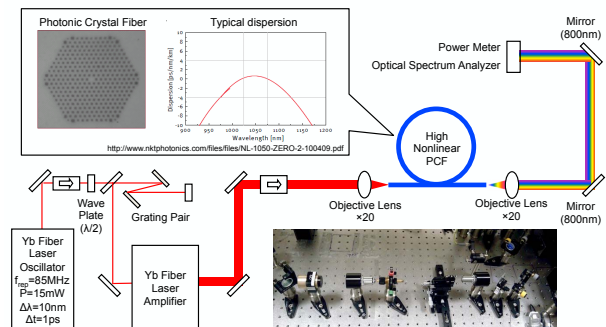


Figure 6: Setup of supercontinuum generation.

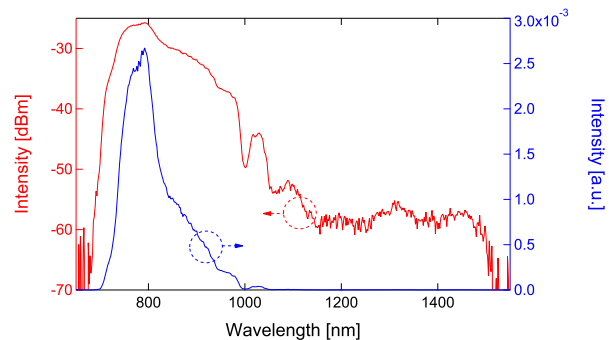


Figure 7: Spectrum of supercontinuum light.

## TOWARD THE 1.3GHz LASER SYSTEM

We have developed the Nd:YVO<sub>4</sub> laser oscillator for the 1.3GHz laser system. Fig. 8 shows the schematic of the Nd:YVO<sub>4</sub> laser oscillator. The fiber coupled laser diode (center wavelength: 808nm) is used as the pumping light source. The core diameter of the fiber is 105 μm. Because the center wavelength of the LD depends on temperature, we have developed the temperature controller that holds the LD temperature and keeps the center wavelength at 808nm. The lens (f=25mm) is used to focus pumping light. Nd:YVO<sub>4</sub> crystal has 0.5% doped

density and 8mm crystal length. The dichroic mirror (DM) is coated with the anti-reflective 808nm and high-reflective 1064nm. The output coupler (OC) is the concave mirror that has 99% reflection ratio and 1% transition ratio and 50mm curvature radius. The semiconductor saturable mirror (SESAM) is used for mode locking. The spontaneous light output from Nd:YVO<sub>4</sub> crystal pumped by the LD is locked in the cavity by DM and SESAM. This locked light turns around in the cavity and the induced emission happens. This induced emission light is amplified in the cavity and mode locking happens. One percent of this mode locked pulse light is extracted by the OC.

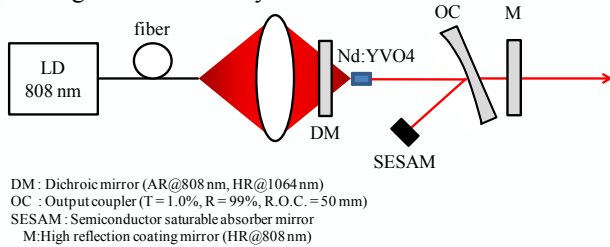


Figure 8: Schematic of Nd:YVO<sub>4</sub> oscillator.

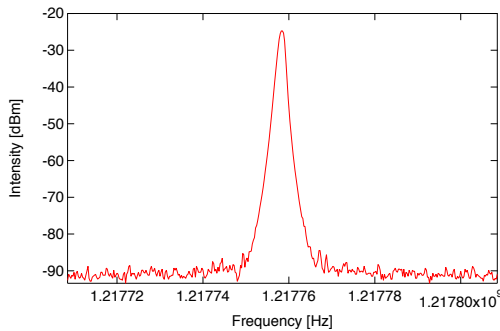


Figure 9: RF spectrum of Nd:YVO<sub>4</sub> oscillator pulse.

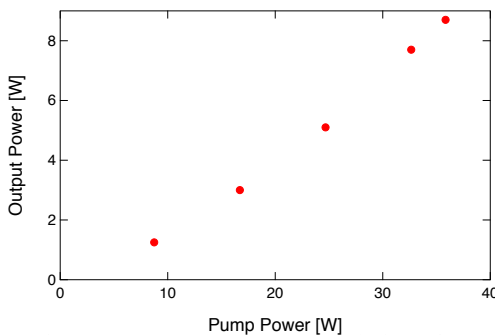


Figure 10: Input and output characteristics of the 1.2GHz laser system.

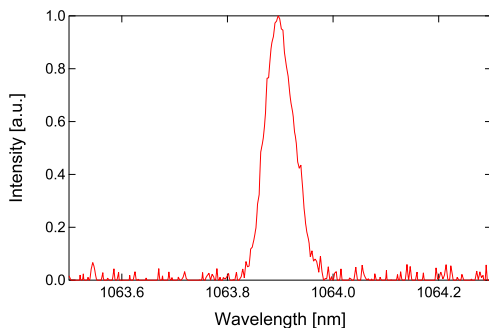


Figure 11: Optical spectrum of 1.2GHz pulse.

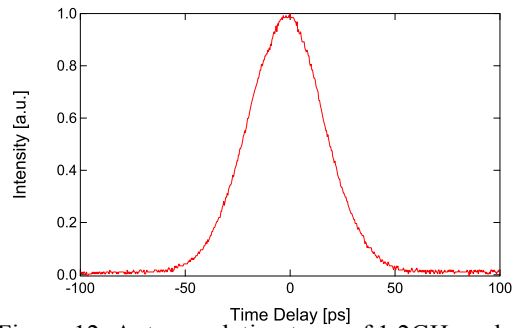


Figure 12: Autocorrelation trace of 1.2GHz pulse.

Figure 9 shows the RF spectrum of the seed pulse from the Nd:YVO<sub>4</sub> oscillator. We can find the peak at about 1.2GHz due to the mode locked pulse.

We amplified the mode locked pulse by the photonic crystal fiber laser amplifier. Fig. 10 shows the input and output characteristics of the 1.2GHz laser system. The 1.2GHz laser system can amplify 1.2GHz mode locked pulse to 8W by 33W pumping light.

Figure 11, 12 show the optical spectrum and the autocorrelation trace of the amplified pulse. In the optical spectrum, the center wavelength is 1063.9nm and the bandwidth is 0.067nm, which is almost the same as the resolution of the optical spectrum analyzer (0.05nm). The FWHM of the autocorrelation trace is 42ps, from which the pulse width is estimated at 27ps by fitting sech<sup>2</sup> type pulse.

## SUMMARY

We have been developing an Yb fiber laser system for an ERL photocathode gun.

We improved the Yb doped photonic crystal fiber laser amplifier by installing the Yb fiber preamplifier and keeping the temperature of the LD and the PCF. The improved amplifier can amplify the 85MHz seed light up to 30W that is the first goal in compact ERL laser system.

We demonstrated the supercontinuum generation for OPA. We could convert wavelength from 1 μm to 800 nm with a conversion efficiency of 9.5%.

We are developing a Nd:YVO<sub>4</sub>-based mode-locked oscillator that can operate at the same frequency as the RF frequency of a superconducting accelerating cavity. The band width is 0.067nm and the pulse width is 27ps. Additionally, we could amplify pulse light of Nd:YVO<sub>4</sub> oscillator up to 8W by the photonic crystal fiber laser amplifier.

## REFERENCES

- [1] R. Hajima et al. (ed.), KEK Report 2007-7/JAEA-Research 2008-032 (2008) (in Japanese).
- [2] R. Nagai et al., Rev. Sci. Instr. 81, (2010) 33304.
- [3] I. Ito et al., Proceedings of IPAC10, 2141-2143 (2010).

## DESIGN OF ERL SPOKE CAVITY FOR NON-DESTRUCTIVE ASSAY RESEARCH

M. Sawamura<sup>#</sup>, R. Hajima, R. Nagai, N. Nishimori, JAEA, Tokai, Ibaraki 319-1195, Japan

### Abstract

We are proposing non-destructive assay system of nuclear materials with laser Compton scattering combined with an energy-recovery linac and a laser. To construct this system for nuclear safeguards and security purpose, it is important to make the accelerating cavity small. The spoke cavity has advantages over the elliptical cavity to adopt for our proposing system. We are designing a spoke cavity favorable to compact cavity. Design optimization calculation of the spoke cavity shape is being carried out using 3D electro-magnetic field simulation code with multi-objective genetic algorithm. The results will be presented.

### INTRODUCTION

Energy Recovery-Linac (ERL) can accelerate low emittance and high current beam, which generates high brightness and high quality light source. The high quality beam of ERL combined with lasers can also significantly improve brightness and monochromaticity of X/ $\gamma$ -ray generated by laser Compton scattering (LCS). Nuclear resonance fluorescence (NRF) with the LCS- $\gamma$  ray can be utilized to nondestructively inspect nuclear materials such as Uranium, Plutonium and minor actinoid elements in spent reactor fuels. This method is significant technology for nuclear safeguards and security. We are proposing non-destructive assay system of nuclear materials by LCS combined with an ERL and a laser.[1]

Practical use of this system requires downsizing the ERL so that it is important to compact the accelerating cavity.

Since the beam instability due to higher-order modes (HOMs) limits the beam current of the ERL, HOM damping is significant for the ERL cavities. Elliptical cavities have tendency to increase the total accelerator length since HOM absorbers, HOM couplers and input couplers are attached to the beam pipes. On the contrary, spoke cavities have an advantage of shortening the total accelerator length [2]. The spoke cavity design suitable for ERL has been being multi-objectively optimized with electro-magnetic simulation code. The present paper describes the results of calculation.

### ADVANTAGES OF SPOKE CAVITY

The superconducting spoke cavity used for ERL has following advantages.

- 1) A superconducting cavity requires HOM absorbers or HOM couplers to damp HOM and input couplers to feed RF power into the cavity. These elements can be installed along the side of the spoke cavity so that the total length of spoke cavity can get shorter than that of elliptical cavity and the distance between the cavities can be decreased.(Fig. 1)

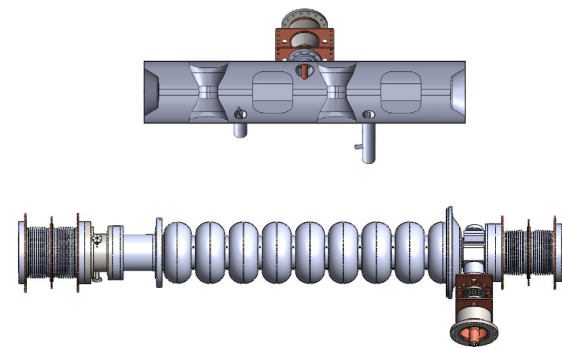


Figure 1: Schematic views of spoke cavity (upper) and elliptical cavity (lower).

- 2) The resonant frequency of spoke cavity mainly depends on the spoke length, and high cavity stiffness reduces the fluctuation of cavity resonant frequency due to microphonics. The ERL cavity of small frequency fluctuation can decrease the required RF power and tolerance of the input coupler. This results in making the RF power supply compact.
- 3) When the outer size of spoke cavity is similar to that of elliptical cavity, the resonant frequency of spoke cavity is nearly half of elliptical cavity. Lower frequency can decrease the energy spread because of the narrow accelerating phase spread for the same bunch length beam. Small energy spread beam can increase the brightness of LSC X/ $\gamma$ -ray.
- 4) Cell coupling of spoke cavity is stronger than that of elliptical cavity since the outer size of the tank is almost same along the axis. Stronger cell coupling makes the field flatness easier to adjust and less disturbed to increase number of cells. This increases the effective accelerating length.

<sup>#</sup>sawamura.masaru@jaea.go.jp

## SPOKE CAVITY SHAPE

The spoke cavity consists of three parts; a spoke, a tank and an end nose as shown in Fig. 2.

The spoke shape used for calculation has three different cross-sections, which deforms from a rectangle through a round corner rectangle to an ellipse. The center part is created by extruding one cross-section and the other parts by smoothly deforming the adjacent cross-sections. The bore for beam acceleration is located in the center of spoke and the corners are rounded to prevent sharp edges.

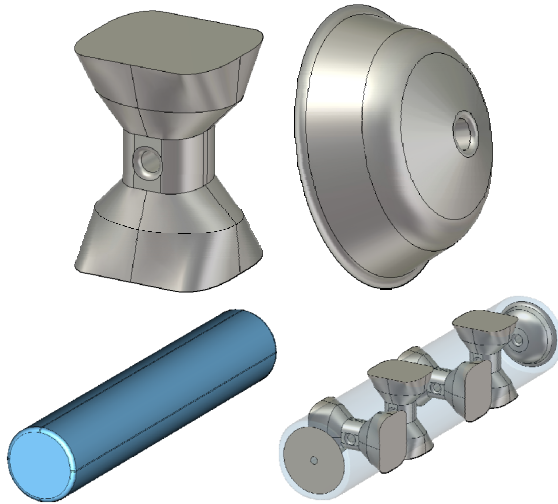


Figure 2: Example of parts of spoke cavity; spoke (upper left), tank (lower left) and end nose (upper right) and their assembly (lower right).

The tank involves the spokes. The tank cross-section varies from a square through a round corner square to a circle. The corner between the tank and the end plate is rounded.

The end nose is combined with circular truncated cone and circular cone and the bore for beam acceleration is located along the axis. The corners of the bore, boundary of the cones, and boundary between cone and end plate are rounded and smoothly deformed.

The resonant frequency of the spoke cavity is assumed to 650 MHz so that the outer size of spoke cavity become almost same as that of widely fabricated 1.3 GHz elliptical cavity. This frequency enables the superconducting spoke cavity to operate at 4K liquid helium temperature.

The cell number is set to five so that the cavity length is nearly same as that of 1.3GHz 9-cell elliptical cavity. The 5-cell spoke cavity has four spokes and each spoke is installed orthogonally to the adjacent spoke.

## OPTIMIZATION PROCEDURE

When the spoke cavity shape is optimized with electro-magnetic simulation code, three objectives should be noted; the ration of maximum electric field to accelerating field ( $E_{peak}/E_{acc}$ ), the ration of maximum magnetic field to accelerating field ( $H_{peak}/E_{acc}$ ), and the ratio of shunt

impedance to Q-value ( $R/Q$ ). The accelerating field is defined as

$$E_{acc} = \frac{\int_0^L E_z e^{jkz} dz}{L} \quad (1)$$

where  $L$  is the cavity length given by multiplying half wave length by number of cell and  $k$  is wave number.

We deal with three objectives of  $E_{peak}/E_{acc}$ ,  $H_{peak}/E_{acc}$  and  $1/(R/Q)$  to treat as optimization problem. The procedures of optimization with genetic algorithm are as follows.

- 1) Assume the minimum and maximum values and bit length which corresponds to resolution within the range to encode each shape parameter.
- 2) A set of shape parameters called individual is converted to an array of bits called chromosome.
- 3) Initially many chromosomes are randomly generated to form an initial population.
- 4) Decode one chromosome to model the cavity shape and calculate the fields with electro-magnetic simulation code.
- 5) Select the  $TM_{010}$   $\pi$ -like mode among the calculated modes by analyzing electric field distribution along the axis.
- 6) When the frequency is out of  $650 \text{ MHz} \pm 5 \text{ MHz}$ , adjust the outer size of the tank and repeat until the frequency converges within the range.
- 7) Search the maximum accelerating field of each cell from the axial field distribution. When difference between the maximum and minimum among the data of all cells is more than 10%, adjust the height of end nose and repeat until the cell field difference converges within the range.
- 8) Obtain the accelerating field, maximum electric and magnetic fields and  $R/Q$ .
- 9) Repeat above procedures from 4) to 8) for all chromosomes
- 10) The fitness function is defined with the rank-based fitness assignment method [3], which counts the superior individuals to itself. This method evaluates the closer individuals to the Pareto front to be better regardless of the values.
- 11) Individuals are selected among the existing population according to the fitness function to breed a new generation.
- 12) Preferentially select a given number of elite individuals which have superior fitness function.
- 13) Select the required number of individuals with the roulette of which selection probability varies according to the fitness function.
- 14) Select a pair of parent from the pool selected previously with a new roulette based on the selected individuals.
- 15) Produce a pair of children from a pair of parent using uniform crossover method.
- 16) Repeat above procedures from 14) to 15) until the next generation population reaches the required number.

- 17) Mutation is operated to the children with a constant probability.
- 18) Repeat above procedure from 4) to 17) until successive iterations no longer produce better results.

### RESULTS OF OPTIMAZATION

Three parameters of  $E_{peak}/E_{acc}$ ,  $H_{peak}/E_{acc}$  and  $1/(R/Q)$  were used for the fitness function at first. Since the value of  $1/(R/Q)$  was strongly optimized and the other two values of  $E_{peak}/E_{acc}$  and  $H_{peak}/E_{acc}$  were hardly optimized around the 10<sup>th</sup> generation, the fitness function was estimated with  $E_{peak}/E_{acc}$  and  $H_{peak}/E_{acc}$  by omitting  $1/(R/Q)$  after the 15<sup>th</sup> generation. After this operation  $E_{peak}/E_{acc}$  and  $H_{peak}/E_{acc}$  became decreasing again with increasing  $1/(R/Q)$ .

The distributions and the Pareto fronts of  $E_{peak}/E_{acc}$  and  $H_{peak}/E_{acc}$  at some generations are shown in Fig. 3. With the passage of generation Pareto fronts were improving and the individuals were gradually approaching near Pareto front.

The typical shapes of spoke cavity close to the Pareto front are shown in Fig. 4. The  $E_{peak}/E_{acc}$ -dominant shape as shown in Fig. 4(A) has longer width than thickness of the spoke center and thick base of the spoke. In contrast the  $H_{peak}/E_{acc}$ -dominant shape as shown in Fig. 4(C) has shorter width than thickness and slim base. Their medium shape as shown in Fig. 4(B) is intermediate between the two.

Comparison of the designed values of  $E_{peak}/E_{acc}$  and  $H_{peak}/E_{acc}$  with other designs of spoke cavities [4, 5] is shown in Fig. 5.  $E_{peak}/E_{acc}$  trends upward slightly with increasing beta and  $B_{peak}/E_{acc}$  also appears to increase relatively more quickly with increasing beta than the electric fields. Though there exist no spoke cavities of high beta, our spoke design of  $\beta=1$  seems to be as good as any other spoke designs.

### COMPARISON WITH ELLIPTICAL CAVITY

Table 1 shows some parameters for the elliptical cavity and spoke cavity. The parameters of the 9-cell cavity for cERL[6] were used for elliptical cavity. The surface resistance was assumed to get the Q-value of elliptical cavity of 1.3GHz to be  $1 \times 10^{10}$  at 2K. The accelerating field or number of cavities was given to get energy gain of about 30MeV. When the total length is almost same, the power loss of the spoke cavity is about 60% of that of the elliptical cavity. When the power loss is same, the total length of spoke cavity is about 75% of that of the elliptical cavity.

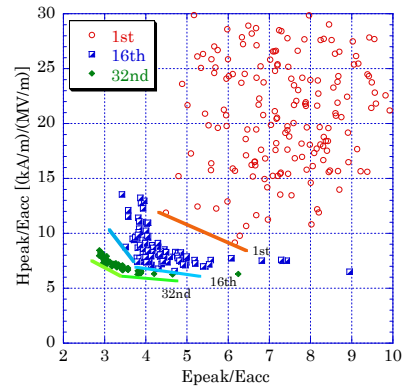


Figure 3: Distribution (dots) and Pareto fronts (lines) of  $E_{peak}/E_{acc}$  and  $H_{peak}/E_{acc}$  at some generations.

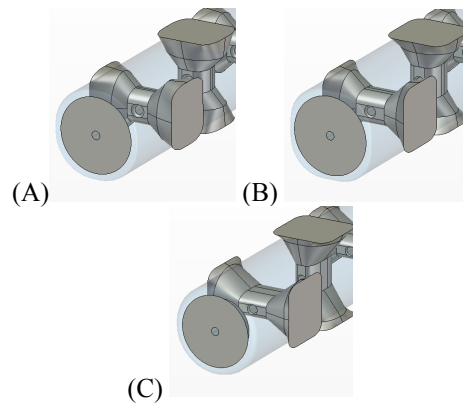


Figure 4: Typical shapes of spoke cavity near Pareto front of  $E_{peak}/E_{acc}$ -dominant (A),  $H_{peak}/E_{acc}$ -dominant (C) and their medium (B).

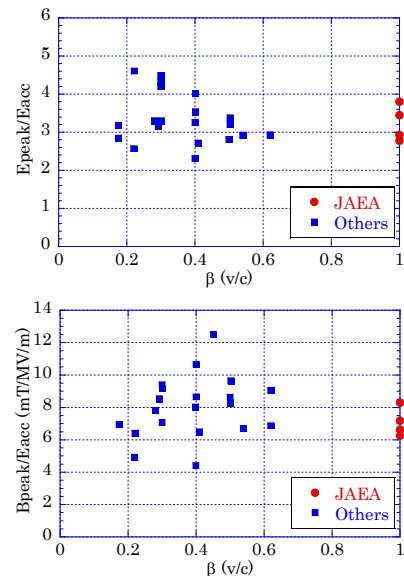


Figure 5:  $E_{peak}/E_{acc}$  (upper) and  $B_{peak}/E_{acc}$  (lower) as a function of  $\beta$ . Solid circles: our spoke cavity design and solid squares: other spoke cavities shown in references [4-5].

Table 1: Comparison with Spoke and Elliptical Cavity

	Elliptical (9cell)	Spoke (5cell)	
Frequency (MHz)	1300	650	650
Temperature (K)	2.0	2.0	2.0
$R/Q \cdot G (\Omega^2)$	$2.5 \cdot 10^5$	$1.8 \cdot 10^5$	$1.8 \cdot 10^5$
Surface Resistance	28n $\Omega$	20n $\Omega$	20n $\Omega$
$Q_0$	$1.0 \cdot 10^{10}$	$7.6 \cdot 10^9$	$7.6 \cdot 10^9$
No. of Cavity	2	3	2
Packing Factor	0.65	0.95	0.95
Eacc (MV/m)	14.4	8.7	13
Power loss (W)	50.4	33.7	50.6
Total Length (m)	3.2	3.6	2.4

G: geometrical factor

## CONCLUSION

We have been designing the spoke cavity shape using the genetic algorithm with multi-objective optimization method. As the new generation is produced, the Pareto

front improves and the results are approaching close to the Pareto front. The current results are as good as any other spoke design and the optimization calculation is in progress.

Since HOM damping is also significant for the ERL cavity, HOM property of the cavity must be investigated and the design of HOM couplers will be carried out.

## REFERENCES

- [1] T. Hayakawa et al., Nucl. Instr. and Meth. A621 (2010), pp. 695-700.
- [2] F. Krawczyk, Proc. of 11<sup>th</sup> Workshop on RF-Superconductivity (SRF2003), Sept. 8-12, 2003, WeO05.
- [3] C. M. Fonseca and P. J. Fleming, Proceedings of the Fifth International Conference on Genetic Algorithms, pp. 416-423, 1993.
- [4] J. R. Delayen, Proc. of the 10<sup>th</sup> Workshop on RF superconductivity (SRF2001), pp. 152-161, 2001.
- [5] M. Kelly, Proc. of the 13<sup>th</sup> Workshop on RF superconductivity (SRF2007), pp. 414-418, 2007.
- [6] K. Umemori et al. Proc. of APAC2007, pp. 570-572(2007).



*List of Authors*

**Bold** papercodes indicate primary authors

<b>— A —</b>		<b>WG1008, WG1019</b>
Abo-Bakr, M.	WG2008	
Adachi, S.	<b>PLT011</b>	
Adelmann, A.	<b>WG2016</b>	
Anders, W.	WG1003, <b>WG3047</b>	
Andrews, A.	WG1015	
Andrews, H.L.	WG1012	
Andrianov, A.V.	WG2002	
Aoyagi, H.	<b>WG5001</b>	
Arnold, A.	WG1000, <b>WG1002</b>	
Asano, Y.	WG5001, WG5006	
Aulenbacher, K.	<b>WG2004</b>	
<b>— B —</b>		
Barday, R.	WG1003	
Bazarov, I.V.	WG1005, WG1019	
Belomestnykh, S.A.	WG1000, <b>WG1001</b> , WG1016, <b>WG3001</b> , <b>WG3026</b> , <b>WG3031</b>	
Benson, S.V.	WG1000, <b>WG2001</b> , <b>WG2026</b>	
Ben-Zvi, I.	WG1016, WG3001	
Bishopberger, K.	PLT004, WG2021	
Bizen, T.	WG5001, <b>WG5005</b>	
Bluem, H.	<b>WG1010</b>	
Bogacz, S.A.	WG2006	
Bondarenko, A.V.	WG2024	
Buckley, S.R.	<b>WG5004</b>	
Büchner, A.	WG5002	
Büttig, H.	WG1002	
<b>— C —</b>		
Cao, J.	WG2009	
Carlsten, B.E.	<b>PLT004</b> , <b>WG2021</b>	
Carriere, P.R.	PSP007	
Cash, R.J.	WG1017	
Cenni, E.	WG3003, WG3006, <b>WG3043</b>	
Chang, X.	WG1016	
Chanlek, N.	WG1011, WG1017	
Chen, J.E.	PLT003, WG2007	
Chen, S.Y.	WG2009	
Chi, Y.L.	WG2009	
Conway, J.V.	WG1019	
Cui, X.	WG2009, <b>PSP001</b>	
Cultrera, L.	WG1019	
<b>— D —</b>		
Dale, D.	WG1015	
DeSanto, L.	WG4003	
Douglas, D.	WG2001	
Dowell, D.	WG1010	
Duffy, L.D.	WG2021	
Dunham, B.M.	<b>PLT007</b> , <b>WG1000</b> , WG1005,	
<b>— E —</b>		
Eckman, C.F.	WG1015	
Ego, H.	WG4001	
Enami, K.	<b>WG3023</b>	
<b>— F —</b>		
Fedotov, A.V.	<b>WG2014</b> , <b>WG2019</b>	
Fell, B.D.	WG1017	
Fernández-Hernando, J.	WG5004	
Forest, E.	<b>WG2018</b>	
Fukuda, S.	<b>WG3048</b>	
Furuya, T.	WG3003, WG3006, <b>WG3037</b> , <b>WG3054</b>	
<b>— G —</b>		
Gao, J.	WG2009	
Gassner, D.M.	<b>WG4000</b> , <b>WG4003</b>	
Getmanov, Ya.V.	WG2002, WG2013	
<b>— H —</b>		
Haga, K.	WG4002	
Hahn, H.	WG3001	
Hajima, R.	WG1007, WG2010, <b>WG2012</b> , WG2022, PSP021	
Hannon, F.E.	WG1009	
Hao, J.K.	PLT003	
Hao, Y.	WG2005, WG2015, WG5007	
Hara, H.	WG3002	
Harada, K.	WG2010, WG2022	
Hasegawa, D.	WG1014	
Hayakawa, T.	<b>PLT008</b>	
Hayano, H.	WG3016, <b>WG3051</b>	
Heath, C.E.	WG1012	
Hernandez-Garcia, C.	WG1000, <b>WG1009</b>	
Hill, C.	WG1017	
Hitomi, H.	<b>WG3002</b>	
Hoffstaetter, G.H.	<b>PLT001</b> , <b>PLT010</b> , <b>WG2020</b> , <b>WG3039</b>	
Honda, T.	WG4002	
Honda, Y.	WG1007, WG4002	
Hosoda, N.	WG4001	
Hosoyama, K.	<b>WG3045</b>	
Huang, C.	PLT004	
Huang, S.	PLT003, <b>WG2007</b>	
Hunt, A.W.	WG1015	
Hwang, J.G.	WG2022, <b>WG2025</b>	
<b>— I —</b>		
Iijima, H.	WG1007	

Inoue, F. WG3002  
 Inoue, S.I. WG4001  
 Ito, I. PSP020  
 Itoga, T. WG5001, WG5006

— J —

Jackson, F. WG2003, WG2023  
 Jankowiak, A. WG1003  
 Jones, J.K. WG2003  
 Jones, L.B. WG1011, WG1017  
 Jordan, K. WG5009  
 Justus, M. WG1002, WG5002

— K —

Kako, E. PLT006, WG3005, WG3046, WG3052  
 Kamps, T. WG1002, WG1003  
 Kanaoka, K. WG3002  
 Karkare, S.S. WG1019  
 Kasahara, R.K. PSP020  
 Kayran, D. WG2005, WG2014, WG2015, WG4003  
 Kim, E.-S. WG2025  
 Kim, K.-J. PLT005  
 Kim, Y. WG1015  
 Kitamura, H. WG5001  
 Kneisel, P. WG1002, WG1003  
 Knobloch, J. WG1003  
 Kobayashi, Y. WG2010, WG2022  
 Kolobanov, E.I. WG2002  
 Komiya, A. WG3016  
 Kondo, C. WG4001  
 Kosolobov, S.N. WG1017  
 Kramer, S.L. WG5003  
 Krawczyk, F.L. WG1012  
 Kugeler, O. WG1003  
 Kulipanov, G.N. WG2002, WG2013  
 Kuriki, M. WG1007  
 Kuske, B.C. WG2008  
 Kuwahara, M. WG1007  
 Kwan, T.J. PLT004

— L —

Lehnert, U. WG1002, WG5002  
 Lewellen, J.W. WG1012  
 Li, X.P. WG2009  
 Li, Y. WG1019  
 Liang, X. WG1016  
 Liepe, M. WG3044, WG3049  
 Lin, L. PLT003, WG2007  
 Litvinenko, V. PLT002, WG2005, WG2015, WG2027, WG5007  
 Liu, K.X. PLT003, WG2007, WG3038  
 Liu, S. WG2009  
 Liu, W.B. WG2009

Liu, X. WG1019  
 Lu, H.H. WG2009  
 Lu, X.Y. PLT003

— M —

Maesaka, H. WG4001  
 Mahler, G.J. WG3001, WG4003  
 Mammei, R.R. WG1016, PSP019  
 Mantimin, M. WG1015  
 Maréchal, X.-M. WG5006  
 Marksteiner, Q.R. WG2021  
 Masuzawa, M. WG3055  
 Matsuba, S. WG4002  
 Matsubara, S. WG4001  
 Matveenko, A.N. WG1003, WG2008, WG2024  
 Maxson, J.M. WG1019  
 Mayes, C.E. PLT009, WG2000, WG2011  
 McCarter, J.L. WG1016, WG1020, PSP019  
 McKenzie, J.W. WG1017, WG2003, WG2023  
 Medvedev, L.E. WG2002  
 Michel, P. WG1002, WG5002  
 Michizono, S. WG3021  
 Michnoff, R.J. WG4003  
 Middleman, K.J. WG1017, WG1011  
 Milityn, B.L. WG1011, WG1017  
 Miller, T.A. WG4003  
 Miyajima, T. WG1007, WG2010, WG2022, WG2025, WG4002  
 Monjushiro, H. WG3016  
 Moody, N.A. WG1012  
 Morita, Y. WG3027  
 Muller, E.M. WG1016  
 Murcek, P. WG1002

— N —

Nagai, R. WG1007, PSP021  
 Naito, T. WG4005  
 Nakai, H. WG3019  
 Nakamura, N. WG2000, WG2010, WG2022, WG3006, PSP020  
 Nakamura, S. PSP020  
 Nakanishi, T. WG1007  
 Nariyama, N. WG5001  
 Nassiri, R. WG3004  
 Neumann, A. WG1003  
 Nguyen, D.C. WG1000, WG1012  
 Nietubyc, R. WG1003  
 Nishimori, N. WG1000, WG1007, PSP021  
 Noguchi, S. WG3005, WG3053

— O —

Obina, T. WG2022, WG4000, WG4002  
 Ohshima, T. WG4001  
 Okumi, S. WG1007  
 Otake, Y. WG4001

— P —

Piot, P. PLT004  
 Poelker, M. WG1016 , PSP019  
 Prokop, C.R. PLT004  
 Ptitsyn, V. WG2005 , WG2015 , WG5007

— Q —

Quan, S.W. PLT003 , WG2007  
 Quast, T. WG1000 , WG1003

— R —

Rao, T. WG1000 , WG1004 , WG1016 ,  
 PSP019  
 Renneke, R.M. WG1012  
 Rudolph, J. WG1002  
 Ruiz-Osés, M. WG1016  
 Ryne, R.D. PLT004 , WG2021

— S —

Saeki, T. WG3016  
 Sakai, H. WG3003 , WG3006  
 Sakanaka, S. WG2010 , WG2022  
 Sakurai, T. WG4001  
 Sato, M. WG3006  
 Satou, M. WG3016  
 Saveliev, Y.M. WG1011 , WG2003 , WG2023 ,  
 WG3007  
 Sawabe., M. WG3016  
 Sawamura, M. WG3006 , PSP021 , WG3003  
 Scheglov, M.A. WG2002  
 Scheibler, H.E. WG1017  
 Schneider, Ch. WG1002  
 Schubert, S.G. WG1003  
 Schulte, D. WG2006  
 Schurig, R. WG5002  
 Sekutowicz, J.K. WG1003 , WG3036  
 Sennyu, K. WG3002  
 Serednyakov, S.S. WG2002  
 Setiniyaz, S. WG1015  
 Shemelin, V.D. PSP007  
 Shevchenko, O.A. WG2002 , WG2013  
 Shimada, M. WG2010 , WG2022  
 Shin, I. WG2006  
 Shinoe, K. WG3003 , WG3006  
 Shishido, T. WG3005  
 Skrinsky, A.N. WG2013  
 Smedley, J. WG1003 , WG1016 , PSP019  
 Smolenski, K.W. WG1019  
 Suleiman, R. WG1000 , WG1018 , WG1016 ,  
 PSP019

— T —

Tadano, M. WG4002

Takai, R. WG4002  
 Takeuchi, Y. WG3028  
 Tanaka, T. WG5001  
 Tanimoto, Y. WG4002  
 Teichert, J. WG1002 , WG5002  
 Terekhov, A.S. WG1017  
 Than, R. WG3001  
 Titberidze, M. WG1015  
 Tobiyama, M. WG4002 , WG4006  
 Todd, A.M.M. WG1010  
 Torizuka, K. PSP020  
 Trbojevic, D. WG2005 , WG2015  
 Tribendis, A.G. WG2013  
 Tsoupas, N. WG2005  
 Tuzel, W.M. WG1012

— U —

Uchiyama, T. WG4002  
 Umemori, K. WG3003 , WG3005 , WG3006 ,  
 WG3042

— V —

Valles, N.R.A. WG3041  
 Vinokurov, N. WG2002 , WG2013  
 Völker, J. WG1003  
 Volkov, V. WG2013

— W —

Wang, E. WG1016  
 Wang, F. PLT003  
 Wang, G.W. WG2009  
 Wang, J.Q. WG2009 , PSP001  
 Wang, S.H. WG2009 , PSP001  
 Wang, Y.C. WG1015  
 Watanabe, K. WG3005  
 Wells, D.P. WG1015  
 Wilinski, M. WG4003  
 Will, I. WG1002 , WG1003  
 Wolski, A. WG2003  
 Wu, Q. WG1016

— X —

Xiang, R. WG1002  
 Xiao, Q. WG2009  
 Xie, H.M. PLT003  
 Xin, T. WG1016  
 Xu, J.Q. WG2009  
 Xu, W. WG2015 , WG3001

— Y —

Yamada, H. WG1014  
 Yamamoto, M. WG1000 , WG1007  
 Yamamoto, Y. WG3050  
 Yampolsky, N.A. PLT004 , WG2021

Yanagida, K.	WG4001	Zhai, J.Y.	WG3040, WG2009
Yanagisawa, T.	WG3002	Zhang, B.C.	PLT003
Yano, Y.	WG4004	Zhao, K.	PLT003
Yoshitomi, D.	PSP020	Zhao, Z.	WG1005
Young, L.M.	WG1010	Zhou, D.	WG2017
<hr/>			
— Z —			
Zaigraeva, N.S.	WG2002	Zhou, Z.S.	WG2009
		Zhu, F.	PLT003, WG2007
		Zimmermann, F.	WG2006

## *Institutes List*

### **AES**

Princeton, New Jersey, USA

- Bluem, H.
- Dowell, D.
- Todd, A.M.M.
- Young, L.M.

### **AIST**

Tsukuba, Japan

- Torizuka, K.
- Yoshitomi, D.

### **ANL**

Argonne, USA

- Kim, K.-J.
- Nassiri, R.

### **BINP SB RAS**

Novosibirsk, Russia

- Andrianov, A.V.
- Getmanov, Ya.V.
- Kolobanov, E.I.
- Kulipanov, G.N.
- Medvedev, L.E.
- Scheglov, M.A.
- Serednyakov, S.S.
- Shevchenko, O.A.
- Skrinsky, A.N.
- Tribendis, A.G.
- Vinokurov, N.
- Volkov, V.
- Zaigraeva, N.S.

### **BNL**

Upton, Long Island, New York, USA

- Belomestnykh, S.A.
- Ben-Zvi, I.
- Chang, X.
- DeSanto, L.
- Fedotov, A.V.
- Gassner, D.M.
- Hahn, H.
- Hao, Y.
- Kayran, D.
- Kramer, S.L.
- Litvinenko, V.
- Mahler, G.J.
- Michnoff, R.J.
- Miller, T.A.
- Ptitsyn, V.
- Rao, T.
- Smedley, J.
- Than, R.
- Trbojevic, D.
- Tsoupas, N.
- Wang, E.

- Wilinski, M.
- Wu, Q.
- Xu, W.

### **CERN**

Geneva, Switzerland

- Schulte, D.
- Zimmermann, F.

### **CLASSE**

Ithaca, New York, USA

- Bazarov, I.V.
- Carriere, P.R.
- Conway, J.V.
- Cultrera, L.
- Dunham, B.M.
- Hoffstaetter, G.H.
- Li, Y.
- Liepe, M.
- Liu, X.
- Mayes, C.E.
- Shemelin, V.D.
- Smolenski, K.W.
- Valles, N.R.A.
- Zhao, Z.

### **Cockcroft Institute**

Warrington, Cheshire, United Kingdom

- Jones, L.B.
- McKenzie, J.W.
- Middleman, K.J.
- Saveliev, Y.M.

### **Cornell University**

Ithaca, New York, USA

- Karkare, S.S.
- Maxson, J.M.

### **DESY**

Hamburg, Germany

- Sekutowicz, J.K.

### **Hiroshima University, Graduate School of Science**

Higashi-Hiroshima, Japan

- Matsuba, S.

### **HU/AdSM**

Higashi-Hiroshima, Japan

- Iijima, H.

### **HZB**

Berlin, Germany

- Abo-Bakr, M.
- Anders, W.

- Barday, R.
- Bondarenko, A.V.
- Jankowiak, A.
- Kamps, T.
- Knobloch, J.
- Kugeler, O.
- Kuske, B.C.
- Matveenko, A.N.
- Neumann, A.
- Quast, T.
- Rudolph, J.
- Schubert, S.G.
- Völker, J.

#### **HZDR**

Dresden, Germany

- Arnold, A.
- Büchner, A.
- Büttig, H.
- Justus, M.
- Lehnert, U.
- Michel, P.
- Murcek, P.
- Schneider, Ch.
- Schurig, R.
- Teichert, J.
- Xiang, R.

#### **IAC**

Pocatello, IDAHO, USA

- Andrews, A.
- Dale, D.
- Eckman, C.F.
- Kim, Y.
- Mamtimin, M.
- Titberidze, M.
- Wang, Y.C.
- Wells, D.P.

#### **Ibaraki University**

Hitachi, Ibaraki, Japan

- Kasahara, R.K.
- Nakamura, S.

#### **IHEP Beijing**

Beijing, People's Republic of China

- Cao, J.
- Chen, S.Y.
- Chi, Y.L.
- Cui, X.
- Gao, J.
- Li, X.P.
- Liu, S.
- Liu, W.B.
- Lu, H.H.
- Wang, G.W.
- Wang, J.Q.
- Wang, S.H.

- Xiao, Q.
- Zhai, J.Y.
- Zhou, Z.S.

#### **IKP**

Mainz, Germany

- Aulenbacher, K.

#### **Institute of High Energy Physics (IHEP)**

People's Republic of China

- Xu, J.Q.

#### **ISP**

Novosibirsk, Russia

- Kosolobov, S.N.
- Scheibler, H.E.
- Terekhov, A.S.

#### **ISSP/SRL**

Chiba, Japan

- Ito, I.
- Shinoe, K.

#### **ISU**

Pocatello, Idaho, USA

- Hunt, A.W.
- Setiniyaz, S.

#### **JAEA/ERL**

Ibaraki, Japan

- Sawamura, M.

#### **JAEA**

Ibaraki-ken, Japan

- Hajima, R.
- Hayakawa, T.
- Nagai, R.
- Nishimori, N.
- Sawamura, M.

#### **Japan Atomic Energy Agency (JAEA), Gamma-ray Non-Destructive Assay Research Group**

Tokai-mura, Ibaraki-ken, Japan

- Sawamura, M.

#### **JASRI/SPRING-8**

Hyogo, Japan

- Aoyagi, H.
- Bizen, T.
- Hosoda, N.
- Itoga, T.
- Maréchal, X.-M.
- Matsubara, S.
- Nariyama, N.
- Yanagida, K.

**JLAB**

Newport News, Virginia, USA

- Benson, S.V.
- Bogacz, S.A.
- Douglas, D.
- Hannon, F.E.
- Hernandez-Garcia, C.
- Jordan, K.
- Kneisel, P.
- Mammei, R.R.
- McCarter, J.L.
- Poelker, M.
- Shin, I.
- Suleiman, R.

**KEK**

Tsukuba, Japan

- Adachi, S.
- Enami, K.
- Forest, E.
- Fukuda, S.
- Furuya, T.
- Haga, K.
- Harada, K.
- Hayano, H.
- Honda, T.
- Honda, Y.
- Hosoyama, K.
- Kako, E.
- Kobayashi, Y.
- Komiya, A.
- Kuriki, M.
- Masuzawa, M.
- Michizono, S.
- Miyajima, T.
- Monjushiro, H.
- Morita, Y.
- Naito, T.
- Nakai, H.
- Nakamura, N.
- Noguchi, S.
- Obina, T.
- Saeki, T.
- Sakai, H.
- Sakanaka, S.
- Sato, M.
- Satou, M.
- Sawabe., M.
- Shimada, M.
- Shishido, T.
- Tadano, M.
- Takai, R.
- Takeuchi, Y.
- Tanimoto, Y.
- Tobiyama, M.
- Uchiyama, T.
- Umemori, K.
- Watanabe, K.
- Yamamoto, M.
- Yamamoto, Y.
- Yano, Y.

- Zhou, D.

**Kyungpook National University**

Daegu, Republic of Korea

- Hwang, J.G.
- Kim, E.-S.

**LANL**

Los Alamos, New Mexico, USA

- Andrews, H.L.
- Bishofberger, K.
- Carlsten, B.E.
- Duffy, L.D.
- Heath, C.E.
- Huang, C.
- Krawczyk, F.L.
- Kwan, T.J.
- Marksteiner, Q.R.
- Moody, N.A.
- Nguyen, D.C.
- Renneke, R.M.
- Tuzel, W.M.
- Yampolsky, N.A.

**LBNL**

Berkeley, California, USA

- Ryne, R.D.

**MBI**

Berlin, Germany

- Will, I.

**MHI**

Kobe, Japan

- Hara, H.
- Hitomi, H.
- Inoue, F.
- Kanaoka, K.
- Sennyu, K.
- Yanagisawa, T.

**Nagoya University**

Nagoya, Japan

- Kuwahara, M.
- Nakanishi, T.
- Okumi, S.

**NCBJ**

Świerk/Otwock, Poland

- Nietubyc, R.

**Northern Illinois University**

DeKalb, Illinois, USA

- Piot, P.
- Prokop, C.R.

**NPS**

Monterey, California, USA

- Lewellen, J.W.

**PKU**

Beijing, People's Republic of China

- Chen, J.E.
- Hao, J.K.
- Huang, S.
- Lin, L.
- Liu, K.X.
- Lu, X.Y.
- Quan, S.W.
- Wang, F.
- Xie, H.M.
- Zhang, B.C.
- Zhao, K.
- Zhu, F.

**PPL**

Omihachiman, Japan

- Hasegawa, D.

**PSI**

Villigen PSI, Switzerland

- Adelman, A.

**RIKEN SPring-8 Center**

Sayo-cho, Sayo-gun, Hyogo, Japan

- Asano, Y.
- Ego, H.
- Kitamura, H.
- Kondo, C.
- Maesaka, H.
- Ohshima, T.
- Otake, Y.
- Sakurai, T.
- Tanaka, T.

**SBU**

Stony Brook, New York, USA

- Muller, E.M.

**SES**

Hyogo-pref., Japan

- Inoue, S.I.

**SLLS**

Shiga, Japan

- Yamada, H.

**Sokendai**

Ibaraki, Japan

- Cenni, E.

**STFC/DL/ASTeC**

Daresbury, Warrington, Cheshire, United Kingdom

- Buckley, S.R.
- Cash, R.J.
- Fell, B.D.
- Fernández-Hernando, J.L.
- Hill, C.
- Jackson, F.
- Jones, J.K.
- McKenzie, J.W.
- Middleman, K.J.
- Militsyn, B.L.
- Saveliev, Y.M.

**Stony Brook University**

Stony Brook, USA

- Ben-Zvi, I.
- Liang, X.
- Ruiz-Osés, M.
- Xin, T.

**The University of Liverpool**

Liverpool, United Kingdom

- Wolski, A.

**UMAN**

Manchester, United Kingdom

- Chanlek, N.

**UVa**

Charlottesville, Virginia, USA

- McCarter, J.L.